

Transport of Ultrasonic Waves in Strongly Scattering or Absorbing Heterogeneous Media

by

Sébastien O. Kerhervé

A Thesis submitted to the Faculty of Graduate Studies of

The University of Manitoba

in partial fulfilment of the requirements of the degree of

Doctor of Philosophy

Department of Physics and Astronomy

University of Manitoba

Winnipeg

Copyright © 2018 by Sébastien O. Kerhervé

Abstract

Propagation of ultrasonic waves in disordered heterogeneous media was studied experimentally, using samples composed of aluminum beads and viscoelastic samples consisting of noodle dough. Even if they look very different, all these samples have in common some resonating constituents: the aluminum beads are resonators as are the bubbles trapped inside a dough. The strong influence of the resonances on the propagation of ultrasonic waves is observed in two different contexts. In the case of aluminum bead samples, the resonators are coupled together and enable a propagation pathway that leads to anomalous transport. For noodle dough, the propagation in the viscoelastic matrix is modified by the resonances of the bubbles.

Measurements of the transport of ultrasound in a 3D sample of loose aluminum beads immersed in a liquid has led to the first observation and quantitative analysis of multiply scattered waves travelling together through two weakly coupled pathways. A model was developed to explain and understand the properties of wave propagation in this sample, showing that one of the two propagating waves is diffusive while the other is sub-diffusive. The diffusive wave travels in the liquid and scatters off the beads whereas the sub-diffusive wave uses the network of beads as its medium of propagation. One of the key features of sub-diffusive transport is the dependence on position and frequency of the diffusion coefficient. A second experiment was designed to study this effect. This experiment was performed on a single layer of brazed aluminum beads, allowing ultrasonic measurements to be performed as a function of position inside this 2D sample (this is not possible inside a 3D aluminum sample). The wave field on the surface of the sample was measured using a laser interferometer, giving access to the three

components of displacement. The same set of measurements was also used to investigate energy equipartition in a multiply scattering medium. In a complementary set of experiments, a non-contact ultrasonic technique was developed to characterize the mechanical properties of Asian noodle dough and investigate the influence of dough composition and processing parameters. This work demonstrated the potential for online quality control during noodle production.

Acknowledgements

First, I need to thank my Ph.D. supervisor Dr. John H. Page for his guidance and support during the past 6 years working in his group. His attention to every detail and his perseverance have largely participated in the improvement of the content of this thesis.

I would like to thank all the past and present members of the Ultrasonics Research Laboratory, in particular Dr. Anatoliy Strybulevych for all his help in conducting the different experiments described in this thesis and Dr. Reine-Marie Guillermic, without whom this thesis would have been very different. She is a colleague but also become a close friend.

I am very grateful to Dr. Sergey Skipetrov for the discussions we had about the self-consistent theory and how to solve it.

Many thanks also to the members of my examining committee: Dr. Byron Southern, Dr. Johan van Lierop, Dr. Martin Scanlon and Dr. Alexey Yamilov. I also want to thank all the support staff of the Department of Physics and Astronomy; my life as a graduate student at the University would have been more difficult without them, and their support is really appreciated.

Funding for this thesis research is gratefully acknowledged from NSERC, the Faculty of Graduate Studies, the Faculty of Science, and the Graduate Student Association of the University of Manitoba.

Finally, I would like to thank my family who supported me from France during this research. Thanks to the French and Francophone communities of Winnipeg, without whom my life in Winnipeg would have been less exciting, and to the wonderful people of the Manitoba Orienteering Association, who helped me to discover the province of Manitoba.

Table of contents

Abstract.....	i
Acknowledgements.....	iii
Table of contents.....	v
List of Tables	ix
List of Figures	xi
List of copyrighted material for which permission was obtained.....	xxi
Chapter 1 Introduction	1
Chapter 2 Background concepts and theory	13
2.1 Waves in Complex Media.....	15
2.2 Wave equations in inhomogeneous media.....	19
2.2.1 Wave equation.....	19
2.2.2 Helmholtz equation	22
2.3 Green's function for multiply scattered waves	22
2.3.1 Definition of the Green's function	22
2.3.2 Green's function in a complex medium [8,13]	24
2.3.3 The T-matrix [8,13].....	26
2.3.4 The scattered wave	28
2.3.5 Born approximation [13].....	28
2.4 Propagation of the average amplitude [8,13,14].....	31
2.4.1 Dyson equation.....	32
2.4.2 Effective medium (coherent potential approximation) [8].....	33
2.4.3 Experimental measurement of the ballistic signal.....	35
2.5 Propagation of the average intensity [8,14]	37
2.5.1 Calculation of the intensity	38
2.5.2 Transport equations [14]	45
2.5.3 Diffusion approximation [13]	48
2.6 Renormalized diffusion and Anderson Localization	51
2.6.1 Renormalized diffusion and self-consistent theory	52
2.6.2 Position-dependent diffusion coefficient	54

Chapter 3 Resonances of aluminum beads	57
3.1 Introduction.....	59
3.2 Natural frequencies of a sphere [34].....	60
3.2.1 First “breathing” mode.....	63
3.2.2 Pure shear modes.....	64
3.2.3 Mixed mode.....	65
3.3 Experimental determination of the resonant frequencies.....	66
3.3.1 Experimental setup.....	66
3.3.2 Analysis and results.....	68
3.4 Simulation of the resonant frequency	71
3.5 Dwell time of aluminum beads	77
3.6 Density of states and pass-band	82
3.7 Conclusion	83
 Chapter 4 Anomalous wave transport in a biphasic disordered medium.....	 85
4.1 Introduction.....	87
4.2 Sample description and fabrication.....	90
4.2.1 Aluminum beads	90
4.2.2 Liquid surrounding the beads	92
4.2.3 How the sample is made.....	93
4.3 General experimental setup.....	96
4.3.1 Transverse confinement setup.....	96
4.3.2 Electronics.....	98
4.3.3 Plane wave experiment.....	103
4.4 Results.....	104
4.4.1 Ballistic Measurement.....	104
4.4.2 Transverse confinement experiment	109
4.5 Analysis.....	120
4.5.1 Two coupled diffusive modes of transport.....	121
4.5.2 Coupled diffusive and slow renormalized transport	129
4.6 Comparison between experimental results and simulations	164
4.6.1 650 kHz	165
4.6.2 1000 kHz	168
4.6.3 1225 kHz	170

4.7	Conclusions.....	172
Chapter 5 Propagation of ultrasound in a single-layer sample of beads..... 177		
5.1	Introduction.....	179
5.2	Measurement Technique.....	180
5.2.1	Experimental setup.....	180
5.2.2	Laser Interferometer.....	182
5.3	Sample fabrication.....	186
5.3.1	How to obtain a 2D-random compact system.....	186
5.3.2	How the sample is made.....	190
5.4	Theory: position-dependent diffusion coefficient and equipartition.....	194
5.4.1	Position-dependent diffusion coefficient.....	194
5.4.2	Equipartition of the energy.....	200
5.5	Experimental results.....	203
5.5.1	In-plane signal filtering.....	203
5.5.2	Scan of the entire sample.....	205
5.5.3	Acquisition of three components of the displacement.....	216
5.6	Analysis of the results.....	219
5.6.1	Estimation of the scattering mean free path.....	219
5.6.2	Position-dependent diffusion coefficient.....	221
5.6.3	Equipartition of the energy.....	226
5.7	Finite Element Simulations.....	232
5.7.1	Resonance frequencies of truncated beads.....	232
5.7.2	Simulation of the propagation in a 2D sample.....	236
5.8	Conclusions.....	239
Chapter 6 Measurement of the mechanical properties of noodle dough with ultrasound..... 243		
6.1	Introduction.....	245
6.2	Influence of the dough properties on the ultrasonic signal.....	247
6.2.1	Effect of bubbles in the propagation of acoustic waves.....	247
6.2.2	Propagation of ultrasound in a viscoelastic medium.....	251
6.3	Experimental setup.....	254
6.3.1	Transducers.....	255
6.4	Analysis.....	261
6.4.1	Theory.....	261

6.4.2	Experimental technique.....	264
6.5	Results and Interpretation	266
6.5.1	Noodle dough making [76,100]	267
6.5.2	Comparison of the acoustical properties of different doughs	269
6.6	Conclusions.....	291
Chapter 7 Conclusions		295
Bibliography		303
Chapter 8 Appendices		313
8.1	Einstein notation	315
8.2	Voigt notation	315
8.3	Wave equation in a solid.....	316
8.4	Signal processing in SIA-7	320
8.5	Transmission analyser.....	323

List of Tables

Table 3.1: Experimental values of the resonant frequencies (average) of a single bead	69
Table 3.2: Resonant frequencies obtained from Comsol with their degeneracy and the type of resonances.	72
Table 3.3: Resonant frequencies, with their degeneracy, of a bead surrounding by hexamethyldisiloxane (see section 4.2.3) obtained from Comsol.	73
Table 3.4: Measured mechanical properties of the aluminum beads used in different samples of this thesis. The values of the velocities and density are very close to the literature values in reference [40] [$\rho = 2700 \text{ kg/m}^3$, $v_l = 6380 \text{ m/s}$ and $v_s = 3120 \text{ m/s}$].....	84
Table 4.1: The 9 deciles of the bead diameter distribution. The smallest bead has a diameter of 3.08 mm and the biggest diameter is 4.21 mm.	91
Table 4.2: Acoustic properties of the different constituents of the sample	95
Table 4.3: Characteristics of the plane wave transducers.	106
Table 4.4: Parameters of the coupled diffusion simulations.....	127
Table 5.1: Average and standard deviation of the noise for two components.....	207
Table 5.2: First resonance frequencies of a truncated bead	233
Table 6.1: Parameters used to obtain Figure 6.1 and Figure 6.2. f is the frequency in Hz.....	250
Table 6.2: Characteristics of VN instrument transducers	259
Table 6.3: Separation between the rolls of the noodle machine for the different reduction steps (after the lamination steps).....	268
Table 6.4: Thickness and density of the different doughs on which ultrasonic measurement was performed during the production (Atm: Atmospheric mixing, Vac: Vacuum mixing).....	285

List of Figures

Figure 2.1: Speckle patterns obtained at two different times: at a short time (left), before the wave can fill the full scanned area, and at a longer time (right), after the wave reaches the boundary of the scanned area. To obtain these speckle patterns, the source was a short point-like pulse centred at $x = y = 0$ on one side of the sample, and the wave intensity close to the opposite side of the sample was determined as a function of position. In the left picture, the effect of the point source is still visible as there is no signal at long distances from the centre. A full speckle pattern is observable on the right. These results have been obtained for the sample of aluminum beads in liquid described in the next part of this thesis, with a 500 kHz transducer. 17

Figure 2.2: Setup of an experiment on wave transport in a multiple scattering medium. Here, the source is focused on the surface of the sample. Other source configurations can also be used. From [11], with kind permission of Società Italiana di Fisica. 18

Figure 2.3: A plane wave, travelling in the direction of the unit vector u_{inc} , is scattering off a single scatterer (yellow object). The scattered wave is observed in the direction u_{obs} and can be measured. 29

Figure 2.4: On the left: wave field for 3025 different source positions. The white line in the middle is the average of all these wave fields (coherent signal). On the right: close-up on the coherent signal. The signal inside the black box is taken to be the ballistic signal. These signals have been obtained on a sample of aluminum beads in a low-loss fluid with a 500 kHz transducer. 36

Figure 2.5: Example of a time-signal with two different time scales: one for the variation of the envelope ($1/\Delta\omega$) and one for the frequency of the wave ($1/\omega$)..... 39

Figure 2.6: Diagrammatic representation of the reducible vertex Γ as a function of the irreducible vertex U . The circles represent U and the dots are the four variables (two inputs, two outputs). Γ is the infinite sum of the scattering events described by U ; the lines represent the Green's functions [8]. 42

Figure 2.7: Example of scattering processes with two paths (one for each Green's function): a) the two paths are completely independent, b) the two paths are identical, and c) the two paths have opposite directions..... 43

Figure 2.8: Loop path participating in the reduction of the diffusion coefficient in the Self-Consistent theory 52

Figure 3.1: Picture of the experimental setup. A bead was placed between two transducers. 67

Figure 3.2: Pulse "Gauss2" with a central frequency of 1 MHz 67

Figure 3.3: Recorded signal through a single bead at 1 MHz. The inset is zoomed in to show the phase variation of the signal. 68

Figure 3.4: Fourier transform of a signal going through a single bead. Two acquisitions at two different frequencies have been done to cover a larger frequency band (Blue: 1 MHz, Red: 1.3 MHz). 69

Figure 3.5: Simulation of the first breathing mode obtained with Comsol at 1.37 MHz. The color of the sphere represents the amplitude of the displacement and the arrows indicate the direction. For this mode, the displacement is purely radial. 74

Figure 3.6: Simulation of the $n=1$ torsional mode obtained with Comsol at 1.38 MHz. The color of the sphere represents the amplitude of the displacement and the arrows indicate the direction. For this mode, the displacement is along the surface of the sphere. 75

Figure 3.7: Simulation of the $n=2$ torsional mode obtained with Comsol at 0.60 MHz. This is the lowest resonant frequency for an aluminum bead. The color of the sphere represents the amplitude of the displacement and the arrows indicate the direction. For this mode the displacement is along the surface of the sphere. 76

Figure 3.8: Simulation of the lowest frequency mixed mode obtained with Comsol at 0.64 MHz. The color of the sphere represents the amplitude of the displacement and the arrows indicate the direction. 77

Figure 3.9: Top Left: Normalized emitted signal in the liquid. Other three pictures: amplitude of the particle velocity at three different times. The color scale is adjusted for each image. Top right: $t = 2.6 \mu\text{s}$, $max = 20.2$, bottom left: $t = 10.4 \mu\text{s}$, $max = 23.0$ and bottom right: $t = 15.6 \mu\text{s}$, $max = 0.9$ 78

Figure 3.10: Evolution of the energy with time inside the bead; the two figures represent the same data obtained with Simsonic. On the left, it is shown that after $30 \mu\text{s}$ the energy inside the beads is still several orders of magnitude above zero. The figure on the right shows that the variation of kinetic and potential energies compensates each other to give a total energy decaying at all times. 80

Figure 3.11: Total Energy in a bead as a function of time: blue, one bead in the system, red, a second bead is placed behind the first one. The energy represented is the energy of the first bead. 81

Figure 3.12: Example of the frequency transmission coefficient in a sample made of brazed aluminum beads (diameter $4.11 \pm 0.03 \text{ mm}$) for a sample with a thickness of 14.5 mm. The red arrows represent the resonance frequencies of a single bead [3]. Figure shown with kind permission from Springer Nature. 83

Figure 4.1: Picture of 1008 beads used to measure the diameters of the beads (9 pictures were used). Beads were placed on a clear plastic plate with little holes in it and a light was put behind the plate. 91

Figure 4.2: Distribution of the diameter of the beads used in the sample (data for 8143 beads) . 92

Figure 4.3: Picture of the sample. At the top of the picture there is the tube used to flow the liquid between the beads and to control the pressure in the sample. 94

Figure 4.4: Position of the 13 acquisitions on the output side of the sample for each source position. The on-axis position is in front of the source, which is on the other side of the sample. The distances between the on-axis position and the other points are 15, 20 and 25 mm. 97

Figure 4.5: Block diagram of the electronic equipment used for transverse confinement experiments. The sample is placed between the transducer and the hydrophone, immersed in a water tank. Sample and hydrophone positions are controlled by multi-axis translation stages with step motor controllers, not represented here.	98
Figure 4.6: Example of a "Gauss2" signal at 1MHz.	99
Figure 4.7: Schematic diagram of a piezoelectric focusing transducer used in the transverse confinement experiments.	100
Figure 4.8: Coherent plane wave signal going through the sample at 1 MHz. (Red: ballistic signal, blue: average signal for the entire transmitted pulse, Inset: reference signal). The time zero corresponds to the emission time.	106
Figure 4.9: Phase velocity of ultrasonic waves propagating in the sample of aluminum beads in liquid obtained from the ballistic signal recorded during plane wave experiments.	107
Figure 4.10: The attenuation coefficient obtained from the same set of data as was used to determine the phase velocity in Figure 4.9.	108
Figure 4.11: Frequency dependence of kl_s obtained from the ballistic signal. kl_s is calculated from the phase velocity and attenuation shown in Figure 4.9 and Figure 4.10.	109
Figure 4.12: Effect of the filtering on the Fourier transform of a wave (blue). Two different Gaussian filters ($f_c = 1.18$ MHz or $f_c = 1.40$ MHz) are applied to the original wave (dashed red lines). The result of the first filter (black) is centred at 1.18 MHz, the result of the second filter (orange) is centered at 1.38 MHz. The bandwidth of both filters is 50 kHz. For this figure, the signal going only through water is used (no multiple scattering).	111
Figure 4.13: Example of four different signals obtained during a transverse confinement experiment on the sample of aluminum beads in liquid, filtered at 1.00 MHz with a bandwidth of 25 kHz.	112
Figure 4.14: Intensities measured at 375 kHz (bandwidth of the filter: 25 kHz)	114
Figure 4.15: Normalized width squared at 375 kHz. The black curve is a linear fit of the average of the three curves (equation of the fit: $y = 0.024t + 0.073$, R-square = 0.988).....	115
Figure 4.16: Intensities measured at 1000 kHz (bandwidth of the filter: 25 kHz)	116
Figure 4.17: Normalized width squared at 1000 kHz. The black curve is a linear fit of the average of the three curves for the first 80 μ s (equation of the fit: $y = 0.024t + 0.13$, R-square = 0.985)	116
Figure 4.18: Schematic diagram illustrating a two-component mechanism for wave transport through the sample: a) waves travelling through the liquid scattering off the beads, b) waves travelling through the solid network of beads using resonances.	117
Figure 4.19: Intensities measured at 800 kHz (bandwidth of the filter: 25 kHz)	119
Figure 4.20: Normalized width squared at 800 kHz. The black curve is a linear fit of the average of the three curves (equation of the fit: $y = 0.028t - 0.06$, R-square = 0.982).....	119
Figure 4.21: Example of the space used for the FDTD simulations. For clarity, only the points on the outside of the drawing are labelled.	122

Figure 4.22: Width squared obtained for three different sets of parameters (described in Table 4.4) obtained from the coupled diffusion simulations	127
Figure 4.23: $T(q_{\perp}, \Omega)$ represented in the complex plane of Ω . The blue dots represent the poles of the function.	134
Figure 4.24: $T(q = 0, \alpha)$ for almost diffusive transport. A small imaginary part is added to α to be just off the imaginary axis corresponding to a green line of Figure 4.23, to avoid being exactly at the poles of the function.	137
Figure 4.25: Comparison between the results of the simulation for uncoupled propagation (dashed) of the fast component and the equivalent component in the coupled case (line). The color code is the same for both cases.....	156
Figure 4.26: Comparison between the results of the calculation for uncoupled propagation (dashed) and the equivalent component in the coupled case (line). The color code is the same for both cases.	157
Figure 4.27: Time of flight of the two individual components (with coupling): fast diffusive component (dot) and slow renormalized component (dashed), as well as the total intensity (solid line).	159
Figure 4.28: Width squared for four different values of $L\xi_1$. The width squared is calculated for $\rho = 15$ mm.	160
Figure 4.29: Width squared for three different values of R_1 . The width squared is calculated for $\rho = 15$ mm.	161
Figure 4.30: Width squared for three different values of θ . The width squared is calculated for $\rho = 15$ mm.	162
Figure 4.31: Width squared for three different values of γ . The width squared is calculated for $\rho = 15$ mm.	163
Figure 4.32: Width squared for $\rho = 15$ mm at three different frequencies: 650 kHz (blue line), 1000 kHz (red line) and 1225 kHz (green line).	165
Figure 4.33: Comparison of the experimental values (solid line) of the width squared at 650 kHz with the theoretical predictions (dashed line) for three different values of ρ . The colors have the same meaning for experiment and theory.	166
Figure 4.34: Comparison of the experimental values (solid lines) of the time-of-flight profiles at 650 kHz and the theoretical predictions (dashed lines) for four different values of ρ . The colors have the same meaning for experiment and theory.....	167
Figure 4.35: Comparison of the experimental values (solid lines) of the width squared at 1000 kHz with a theoretical calculation (dashed lines) for three different value of ρ . The colors have the same meaning for experiment and theory.	168
Figure 4.36: Comparison of the experimental values (solid lines) of the time of flight profiles at 1000 kHz with theory (dashed lines) for four different values of ρ . The colors have the same meaning for experiment and theory.....	170

Figure 4.37: Comparison of the experimental values (solid lines) of the width squared at 1225 kHz with theoretical predictions (dashed lines) for three different values of ρ . The colors have the same meaning for experiment and theory.	171
Figure 4.38: Comparison of the experimental values (solid lines) of the time of flight profiles at 1225 kHz with theoretical predictions (dashed lines) for four different ρ values. The colors have the same meaning for experiment and theory.	172
Figure 5.1: Picture of the sample between the two transducers. In this chapter, we will define the x -axis as the axis going along the long side of the sample, the y -axis along the short side of the sample and the z -axis as being perpendicular to the surface of the sample.....	181
Figure 5.2: The interferometer measures the reflected signal and also the scattered light due to the roughness of the surface. An array of photodiodes acquires the signal: the array is symmetric with the axis of the lens. The elements of the array are numbered from $-i$ to i	182
Figure 5.3: Example of an in-plane signal, displacement along the x -axis (blue), and an out-of-plane signal, along the z -axis (red). The pre-trigger signals allow the noise levels to be compared.....	184
Figure 5.4: Diagram representing the electronic equipment used during the experiment. The black lines represent the connection between the different pieces of equipment. The green line represents the laser light.....	185
Figure 5.5: Example of patterns obtained with the “classic”: techniques used to create 2D random patterns. On a) the final packing fraction is 54 % and in b) 61 %. For both cases, the programs stop after trying 10^6 times to add a new disk.	187
Figure 5.6: Example of a pattern obtained with 650 4-mm-diameter disks with a final packing fraction of 80 %. The red lines represent the box in which the simulation was performed.	188
Figure 5.7: Histogram of the distances between each pair of beads for two patterns of 650 4-mm-diameter disks, with each bin representing 1 mm, and the number of distances between pairs of disks being 210925. In red, histogram for a perfect arrangement of beads (hexagonal compact), for which some sharp peaks appear. In blue, histogram obtained for the pattern shown in Figure 5.6.....	189
Figure 5.8: Picture of the mold used in the furnace to make the one-layer of beads sample	191
Figure 5.9: In-plane signal measured 4 mm away from the transducer, before (blue) and after (red) filtering. The blue signal is identical to the blue signal in Figure 5.3. The central frequency of the filter is 1 MHz and its bandwidth 400 kHz.....	204
Figure 5.10: Absolute value of the out-of-plane displacement in pm at four different times: a) 5 μ s, b) 20 μ s c) 100 μ s and d) 250 μ s. The pulse is emitted at the top of the sample. The color scale is logarithmic. The central frequency and bandwidth are 1 MHz and 400 kHz, respectively.	205
Figure 5.11: Absolute value of the in-plane displacement signals in the y -direction in pm at four different times: a) 5 μ s, b) 20 μ s c) 100 μ s and d) 250 μ s. The experimental data have been filtered to remove the high frequency noise.	206

Figure 5.12: Absolute value of the amplitude of the out-of-plane displacement (a) and the in-plane displacement (b) 5 μ s after the emission of the pulse for the beads far away from the transducer (the color scale is identical for both pictures and is the identical to the one of Figure 5.10).....	207
Figure 5.13: Transmission coefficients of the out-of-plane displacements for different distances from the transducer.	209
Figure 5.14: Transmission coefficients of the in-plane displacements for different distances from the transducer.	209
Figure 5.15: Absolute value of the out-of-plane displacement, in pm, for a frequency inside a band gap (850 kHz) at four different times: a) 5 μ s, b) 20 μ s c) 100 μ s and d) 250 μ s. The pulse is emitted at the top of the sample. The color scale is logarithmic.	211
Figure 5.16: Absolute value of the in-plane displacement, in pm, for a frequency inside a band gap (850 kHz) at four different times: a) 5 μ s, b) 20 μ s c) 100 μ s and d) 250 μ s. The pulse is emitted at the top of the sample. The color scale is logarithmic.....	211
Figure 5.17: Absolute value of the out-of-plane displacement, in pm, for a frequency inside a pass band (1000 kHz) at four different times: a) 5 μ s, b) 20 μ s c) 100 μ s and d) 250 μ s. The pulse is emitted at the top of the sample. The color scale is logarithmic.	212
Figure 5.18: Absolute value of the in-plane displacement, in pm, for a frequency inside a pass band (1000 kHz) at four different times a) 5 μ s, b) 20 μ s c) 100 μ s and d) 250 μ s. The pulse is emitted at the top of the sample. The color scale is logarithmic.	212
Figure 5.19: Absolute value of the amplitude (a. u.) of the Fourier transform of the out-of-plane displacement for three different frequencies: a) 850 kHz, b) 880 kHz and c) 1000 kHz. The color scale is logarithmic.	214
Figure 5.20: Absolute value of the three components of the field for four different times (time value indicated at the top of each column) obtained with a 1 MHz transducer. First and second rows show the x and y components (in-plane); the third row shows the z -component (out-of-plane). The color scale is in pm.....	217
Figure 5.21: Absolute value of the three components of the field for four different times (time value indicated at the top of each column) obtained with a 500 kHz transducer. First and second rows show the x and y components (in-plane); the third row shows the z -component (out-of-plane). The color scale is in pm.....	218
Figure 5.22: Transmission for each component obtained with the 500 kHz transducer 17 mm away from the transducer. Blue: x -component (in-plane), red: y -component (in-plane) and green: z -component (out-of plane).	219
Figure 5.23: Averaged amplitude of the out-of-plane signal at the output of the transducer (blue) and 10 mm away from the transducer (red). The thicker, darker solid lines represent the ballistic signals; the thinner, lighter colored lines, represent the scattered signal. Experiments are performed at 1 MHz.....	220
Figure 5.24: Scattering mean free path obtained from the out-of-plane signal for the 1 MHz experiment.....	221

Figure 5.25: Energy density for three different frequencies as a function of the distance from the transducer (blue: 850 kHz, red: 1000 kHz and green: 1170 kHz).	223
Figure 5.26: x -component of the flux (Poynting vector) for three different frequencies as a function of the distance from the transducer (blue: 850 kHz, red: 1000 kHz and green: 1170 kHz). The inset is a zoom at the long distances.	224
Figure 5.27: Diffusion coefficient calculated as a function of distance away from the transducer for three different frequencies (blue: 850 kHz, red: 1000 kHz and green: 1170 kHz).	224
Figure 5.28: Shear (blue) and compressional (red) energies as a function of time in the bead in the centre of the white square in the right image (emitting transducer is at the top of the image) at 850 kHz.	227
Figure 5.29: Shear (blue) and compressional (red) energies in the same bead as Figure 5.28 at 1000 kHz, as a function of time.	228
Figure 5.30: Shear (blue) and compressional (red) energies in the bead in the centre of the white square on the right image (transducer is at the top of the image) at 850 kHz, as a function of time.	228
Figure 5.31: Shear (blue) and compressional (red) energies in the same bead as Figure 5.30 at 1000 kHz, as a function of time.	229
Figure 5.32: Ratio of the shear energy to the compressional energy for a bead at 8 mm from the source at 850 kHz (blue) and at 1000 kHz (red).	230
Figure 5.33: Ratio of the shear energy to the compressional energy for a bead at 14 mm from the source at 850 kHz (blue) and at 1000 kHz (red).	230
Figure 5.34: Simulation of the displacement field of the 0.677 MHz resonance of a truncated bead. The displacement field is completely along the surface of the object.	234
Figure 5.35: Simulation of the displacement field of the 0.704 MHz resonance of a truncated bead. The displacement field is mainly radial at this frequency.	235
Figure 5.36: Simulation of the displacement field of the 0.492 MHz resonance of a truncated bead. At this frequency, the flat part of this object is deformed.	235
Figure 5.37: Displacement fields at 750 kHz in the three directions: along x (left), along y (centre) and along z (right). Here, the y direction is going from top to bottom of the images, and the z direction is the out-of-plane direction. The color scale is expressed in arbitrary units of displacement.	237
Figure 5.38: Amplitude transmission coefficient of the magnitude of the out-of-plane displacement obtained from the Comsol simulation. The transmission is obtained 27 mm away from the transducer.	238
Figure 6.1: Phase velocity obtained using the model described by equation (6.6) with the parameters of Table 6.1.	250
Figure 6.2: Attenuation obtained using the model described by equation (6.6) with the parameters of Table 6.1.	251
Figure 6.3: Transducers from Microacoustics.	256

Figure 6.4: Typical signal obtained with the BAT-1 transducers (central frequency: 200 kHz).	257
Figure 6.5: Air-coupled transducer from the Ultrason Group.	258
Figure 6.6: Typical signal obtained with the Ultrason transducers (central frequency: 200 kHz).	259
Figure 6.7: VN instruments transducer.	260
Figure 6.8: Typical signal obtained with the pair of CAP 3 transducers.	261
Figure 6.9: Multiple reflections inside a layer of noodle dough (image courtesy of R.-M. Guillermic).	262
Figure 6.10: Left: dough crumbs at the end of mixing. Right: Dough going through the rolls during a lamination step (the dough has been folded in two). Pictures taken at the Grain Research Laboratory by Dr. Daiva Daugelaite.	268
Figure 6.11: Reference signal obtained with the Microacoustics transducers at 250 kHz. The separation between the two transducers is 16 cm.	270
Figure 6.12: Signal going through a noodle dough made with a water absorption level of 34%, 1% of NaCl salt and 1% of kansui salt. This dough was made with 9 lamination steps. The thickness of the dough was 1.75 mm.	270
Figure 6.13: Velocity of ultrasound as a function of frequency for dough with 38% water made with 1 lamination step (blue circles) and 9 lamination steps (red open triangles). The thickness of the 1-lamination noodle dough was 1.64 ± 0.03 mm and the thickness of the 9-lamination noodle dough was 1.69 ± 0.03 mm.	273
Figure 6.14: Attenuation of ultrasound as a function of frequency for dough with 38% water and 1 lamination step (blue circles) and 9 lamination steps (red open triangles).	273
Figure 6.15: Velocity of ultrasound as a function of frequency for dough with 34% water and 1 lamination step (orange triangles) and 9 lamination steps (green open squares). The thickness of the 1-lamination noodle dough was 1.72 ± 0.03 mm and the thickness of the 9-lamination noodle dough was 1.80 ± 0.05 mm.	274
Figure 6.16: Attenuation of ultrasound as a function of frequency for dough with 34% water and 1 lamination step (orange triangles) and 9 lamination steps (green open squares).	274
Figure 6.17: Velocity of ultrasound as a function of frequency for dough with 34% (green open squares) and 38 % (blue circles) water and 9 lamination steps. The thickness of the 34% water noodle dough was 1.80 ± 0.05 mm and the thickness of the 38% water noodle dough was 1.69 ± 0.03 mm.	275
Figure 6.18: Attenuation of ultrasound as a function of frequency for dough with 34% (green open squares) and 38 % (blue circles) water and 9 lamination steps.	275
Figure 6.19: Velocity of ultrasound as a function of frequency for dough with 34% (orange triangles) and 38 % (red open triangles) water and 1 lamination step. The thickness of the 34% water noodle dough was 1.72 ± 0.03 mm and the thickness of the 38% water noodle dough was 1.64 ± 0.03 mm.	276
Figure 6.20: Attenuation of ultrasound as a function of frequency for dough with 34% (orange triangles) and 38 % (red open triangles) water and 1 lamination step.	276

Figure 6.21: Real part of the complex longitudinal modulus (storage modulus) as a function of frequency for dough with 34% (orange triangles) or 38 % (red open triangles) water and 1 lamination step.	278
Figure 6.22: Imaginary part of the complex longitudinal modulus (loss modulus) as a function of frequency for dough with 34% (orange triangles) or 38 % (red open triangles) water and 1 lamination step.	279
Figure 6.23: Ratio of the imaginary and real parts of the longitudinal modulus, $\tan(\delta) = M''/M'$ as a function frequency for dough with 34% (orange triangles) or 38 % (red open triangles) water and 1 lamination step.	279
Figure 6.24: Velocity of ultrasound as a function of frequency for dough with 1% NaCl salt (green open triangles) or 1% kansui + 1% NaCl salt (blue squares).....	280
Figure 6.25: Attenuation of ultrasound as a function of frequency for dough with 1% NaCl salt (green open triangles) or 1% kansui + 1% NaCl salt (blue squares).....	281
Figure 6.26: Real part of the longitudinal modulus M as a function of frequency for dough with 1% NaCl salt (green open triangles) or 1% kansui + 1% NaCl salt (blue squares).....	282
Figure 6.27: Imaginary part of the longitudinal modulus M as a function of frequency for dough with 1% NaCl salt (green open triangles) or 1% kansui + 1% NaCl salt (blue squares).....	282
Figure 6.28: Ratio of the imaginary and real parts of the longitudinal modulus, $\tan(\delta) = M''/M'$ as a function of frequency for dough with 1% NaCl salt (green open triangles) or 1% kansui + 1% NaCl salt (blue squares).....	283
Figure 6.29: Ultrasonic transducers placed on opposite sides the dough sheet as it moves between two sets of rolls at the CIGI pilot plant. The transducers used are the Ultran transducers (section 6.3.1.2).....	284
Figure 6.30: Velocity measured at 200 kHz for different noodle doughs measured during production.	285
Figure 6.31: Attenuation measured at 200 kHz for different noodle doughs measured during production.	286
Figure 6.32: Signals obtained with the 200-kHz transducers from VN instruments. Left: reference signal through air. Right Signal through a noodle dough with a thickness of 1.31 mm and containing 36 %fwb of water and 2% of salt. 1 lamination step was performed.	287
Figure 6.33: Image of a noodle dough sheet obtained by X-ray microtomography (experiment done at the Canadian Light Source in Saskatoon). The white elements of the image represent the voids (air) inside the noodle. The noodle was made with 34% water, 1% salt and 1 lamination step (picture courtesy of R.-M. Guillermic).....	289
Figure 6.34: Velocity obtained over a large frequency band with contact experiments (red: 500 kHz transducers, blue: 10 MHz transducers). The inset is a zoom at low frequency to compare the air-coupled results (orange) obtained on a similar dough.	290
Figure 6.35: Attenuation obtained over a large frequency band with contact experiments (red: 500 kHz transducers, blue: 10 MHz transducers). The inset is a zoom at low frequency to compare the air-coupled results (orange) obtained on a similar dough.	291

Figure 8.1: Definition of the components of the stress tensor.	317
Figure 8.2: A chirp signal (blue, left scale) and the results of the cross-correlation of the chirp by itself (red, right scale).	321
Figure 8.3: Example of the improvement of the signal-to-noise ratio, using the pulse compression technique. In blue, a random signal has been added to a chirp. In red, the cross-correlation of the blue signal with the chirp from Figure 8.2 is shown.	322
Figure 8.4: Example of the envelope detection using demodulation. Blue: experimental signal after pulse compression; red: envelope of the blue signal obtained by demodulation.	322
Figure 8.5: First panel of the GUI displaying the time signals.	323
Figure 8.6: Second panel of the GUI displaying the velocity and attenuation.	324

List of copyrighted material for which permission was obtained

Figure 2.2: Setup of an experiment on wave transport in a multiple scattering medium. Here, the source is focused on the surface of the sample. Other source configurations can also be used. From [11], with kind permission of Società Italiana di Fisica. 18

Figure 3.12: Example of frequency transmission coefficient in a sample made of brazed aluminum beads (diameter 4.11 ± 0.03 mm) for a sample with a thickness of 14.5 mm. The red arrows represent the resonance frequencies of a single bead [3]. Figure shown with kind permission from Springer Nature. 83

Chapter 1

Introduction

The propagation of waves is important in many different areas of physics and has been extensively studied for centuries. It is also important in many different aspects of daily life. Communications, for example, rely mainly on waves, either spoken communication (acoustic waves), visual communication via images (electromagnetic waves in the visible spectrum) or, of course, modern communication technologies such as Wi-Fi or cellphones (electromagnetic GHz waves). In these different examples it is assumed that waves travel mainly in straight lines and few scattering events cause their direction of propagation to deviate from the incident direction or decrease their amplitude. The study of wave propagation in multiple scattering media, *i.e.*, when waves scatter in all directions, has gained a lot of interest over the past century and has led to the explanation of different natural phenomena. For example, the crust of the earth acts as a multiple scattering medium for the elastic (seismic) waves (e.g., produced by an earthquake) travelling in it, leading to a long coda, which is due to the scattered waves that travel for a long time in the earth after the initial direct pulse arrives at the detector. Another example of multiple scattering is the origin of the white color of milk (or white paint), which is due to the scattering of the light by proteins in it (or TiO_2 particles in the paint). While all types of waves can be multiply scattered, this thesis focuses exclusively on acoustic and elastic waves.

Interesting cases of light scattering can be seen in the sky where scattering explains why the sky is blue and why the clouds are white. This example also serves to illustrate the important characteristic lengths in a scattering problem. The light from the sun is scattered by the molecules in air, mainly N_2 , which are much smaller than the wavelength of the light. When a scattering particle is much smaller than the wavelength, the scattering is isotropic, so that the scattered intensity is the same in all directions, and the intensity of the scattered light depends strongly on the wavelength. This phenomenon is called Rayleigh scattering. The blue is more

strongly scattered than the red, so the sky is seen as being blue: blue light is coming from all directions in the sky. In a cloud, the light is scattered by droplets of water, which are larger than the visible wavelength, so the scattering is no longer isotropic, and the scattering no longer depends strongly on frequency. After several scattering events, the direction of propagation is completely randomized; this occurs at a distance called the transport mean free path. The scattered radiation then has no preferred directionality, and since the scattering is essentially independent of frequency in the visible spectrum, clouds appear white in color (the white color of milk is due to the scattering of light off the proteins). The same phenomenon happens in fog: inside a fog, it is possible to have an idea of the distance the light needs to travel before the direction of propagation is randomized; it corresponds to how far we can see clearly in the fog, and depends a lot on the concentration of droplets. The blue color of the sky and the white color of the cloud are both explained by scattering but due to different length scales the final observations are different.

The phenomena described for light in the example of the sky and clouds depend only on the wave nature of light, and the same phenomena can happen for acoustic waves (on different scales, since the wavelengths are typically much longer). The two examples described in the last paragraph show the importance of the different lengths involved in the propagation of waves in a multiple scattering medium. The first important one is the wavelength λ characterizing the wave, depending on the frequency f and of the speed of propagation of the wave in the medium v ($\lambda = v/f$). The scattering mean free path l_s represents the average distance travelled by the wave between two scattering events and the transport mean free path l^* represents the distance travelled by the wave to become randomized. l_s and l^* depend on the properties of the scatterers, in particular on their sizes. The second important length in a scattering problem is the size of the

sample L . When L and l_s are comparable, the wave cannot undergo a lot of scattering events and the propagation is mainly ballistic (the wave travels straight through the medium without scattering away from the forward direction). On the other hand, when the sample is large compared to l_s and λ , waves become multiply scattered and randomized due to the large number of scattering events along the path of the wave. As a result of the large number of scattering events encountered by the waves in multiple scattering media, the waves take longer to travel through a sample. In a pulsed experiment, these multiply scattered waves form a “coda” that arrives after the direct ballistic signal. Rather than focussing on the specific details of these coda waves for a particular configuration of scatterers and detector position, a probabilistic approach to describe the average energy density of the wave is more useful, leading to the diffusion approximation. In this approximation, the transport of energy by the waves undergoes a random walk through the medium, and the wave energy spreads out, on average, from a point source as the square root of time, instead of the distance traveled being proportional to time like in the case of ballistic propagation.

The diffusion approximation starts to break down when the wavelength λ of the wave is comparable to or smaller than the scattering mean free path l_s . The wave transport can then be described as sub-diffusive, a regime in which the transport of the energy is, on average, slower than in the classic case of diffusive transport. In the most extreme case, Anderson localization can occur. Waves are then trapped in the sample by interference effects. Diffusion or localization can, in principle be observed for different types of waves: acoustic, light, electrons or matter waves. The focus of much of this thesis is on such “anomalous” transport of acoustic or elastic waves.

Acoustic and elastic waves¹ have several advantages compared to the other types of waves to perform experiments in strongly scattering media. First, in ultrasonics, all the length scales are more manageable, as it is convenient to work in the frequency range where the wavelength is of the order of a millimeter. This leads to centimetre-sized samples, which are easier to manipulate than the much smaller sized samples appropriate for optics experiments (where the wavelength is more than three orders of magnitude smaller) or matter wave experiments. Another advantage is that the measurement instruments used in acoustics allow direct access to the field of the wave including the phase, which is difficult in optics where only the intensity is easy to measure and, therefore, where all information about the phase is often lost. Lastly, because the scattering “strength” of a scatterer depends on the contrast of impedance between the exterior medium and the scatterer, and because higher contrasts of impedance are accessible in acoustics than in optics, experiments with ultrasonic waves have an additional advantage for exploring physical phenomena for which very high scattering contrast is needed.

In this thesis, ultrasonic wave propagation is investigated in a range of heterogeneous materials that have been selected to illustrate and probe how transport can be radically altered by the two main characteristics: scattering and absorption. The different experiments reported in this thesis explore wave transport and its relation to material properties in two contrasting situations: 1) very strong scattering and low absorption, in order to study how wave transport is affected by strong scattering without complications from absorption, or 2) the combination of strong scattering and large absorption, in order to study how the very different character of wave transport in this regime is affected by the medium’s mechanical properties. In the first case, the

¹ “Acoustic” and “elastic” waves refer to sonic or ultrasonic waves in fluids and solids, respectively. Acoustic waves involve only compressional waves (pressure waves) whereas elastic waves have three displacement polarizations, one longitudinal (compressional) and two transverse (shear) to the direction of propagation.

constituents have well known properties, and the interest is in studying how novel wave properties can be discovered, while in the second case, the constituents are more complex, and the interest is in learning about the material properties from transport measurements.

A key parameter that determines in which regime an ultrasonic experiment is being performed is the wavelength relative to the characteristic size of the scatterers present in the medium. In the first case of the strong scattering regime, the ultrasonic wavelength is comparable to the size of the scatterers inside the sample. This regime is explored in samples made of aluminum beads. Aluminum is a low absorption material for elastic waves and these samples are surrounded by various media with very different acoustic properties, meaning that a long coda can be observed and studied. Two different types of samples were constructed from the aluminum beads. A three-dimensional (3D) sample made of aluminum beads immersed in a low-loss liquid was expected to be a simple model system for exploring the multiple scattering of ultrasonic waves. Indeed, apart from this sample's extremely low losses, it is very similar to samples of glass beads in a liquid that were studied approximately two decades ago. These pioneering studies were the first to show that the transport of energy by multiply scattered ultrasonic waves can be described by the diffusion approximation [1], and to examine in detail the parameters governing diffusive transport of acoustic waves [2]. A natural question to ask is if the much lower losses in the 3D aluminum bead sample would permit previously unexplored aspects of the transport of multiply scattered waves in such a solid/fluid system to be discovered. The answer to this question, provided by an extensive set of new experiments and the development of a theoretical model that has permitted a quantitative analysis of the experimental results, is a major focus of this thesis.

Another way of constructing low-loss strongly scattering samples from aluminum beads is to braze the beads together to form a disordered solid network of beads. Then, no surrounding medium is necessary to support the structure, and strong multiple scattering of waves confined to the solid network of beads can be studied. Previous studies of 3D samples of brazed aluminum beads have provided the first clear evidence of the Anderson localization of ultrasonic waves [3], and enabled the experimental investigation of remarkable wave properties due to Anderson localization [4,5,6,7]. However, in such 3D samples, it is impossible to measure the wave field *inside* the sample, and information on the transport properties has to be obtained from transmission or reflection (backscattering) measurements. To overcome this limitation, I have made and studied (quasi-) two dimensional (2D) samples consisting of a monolayer of brazed aluminum beads. The 2D nature of this sample means transport properties inside the sample can be investigated using a laser interferometer to measure the ultrasonic displacements on the surfaces of the beads. These experiments have the potential to answer fundamental questions about how the diffusion coefficient varies with position in an open system close to Anderson localization, and how the total wave energy is partitioned between longitudinal and shear energies.

The second case of a heterogeneous material with strong scattering and very large absorption was studied on samples for which the absorption was so strong that no multiple scattering coda could be measured; only the ballistic signal could be studied. Typically, this situation is encountered in the low frequency regime (large wavelength), where the scattering is weak and a heterogeneous material can be seen as a uniform effective medium, with average properties that reflect the properties of the constituents and how they are put together. Then, the measured velocity and attenuation give access to the mechanical properties of the medium. This aspect of

wave propagation was studied with experiments on noodle dough because of the importance of developing new methods for quality control in noodle production. From the physics perspective, noodle dough is also an interesting complex material in which both scattering and absorption are significant even at wavelengths much larger than the sizes of the heterogeneities; this occurs because of the presence of bubbles, which have a strong low-frequency acoustic resonance. An important challenge for assessing the mechanical properties of such a soft material using ultrasound is to develop a method for doing experiments noninvasively. To address this challenge, this thesis describes the development of a method for measuring the mechanical properties of noodle dough using non-contact, air-coupled ultrasonic transducers, with a view towards demonstrating the capability of doing such measurements online during production.

Chapter 2 of this thesis introduces background concepts in wave physics that are needed to interpret the data obtained from all the experiments described in the thesis. In particular, the theory of multiply scattering is summarized, with a focus on explaining why (and when) the diffusion approximation can be used in the case of strongly scattering media. The terms “probabilistic” or “on average” used earlier in this introduction will be explained. Some theoretical concepts about the transition to localization are also introduced at the end of the chapter.

Chapter 3 focuses on the vibrational resonances of aluminum beads. These resonances occur at the natural frequencies of oscillation of a given object. Aluminum beads are the main constituents of the samples described in chapters 4 and 5 and their resonances strongly influence the transport in these two types of samples. In a sample made of coupled resonators, the scattering mean free path l_s and the transport mean free path l^* depend on the resonances.

Chapters 4, 5 and 6 explain the different experiments I conducted during my thesis research. Each of these three chapters starts with an explanation of which phenomena I want to study. This is followed by a description of the samples studied for each of the three sets of experiments, along with a description of the experimental techniques used. Chapter 4 describes the propagation of acoustic waves in a biphasic medium composed of aluminum beads in a liquid. The propagation of waves in this sample is different from any other recorded experiment, as I have observed two coupled multiply scattered modes of propagation, including one sub-diffusive one, travelling together in the sample.

In chapter 5, the sample studied is a single layer of brazed aluminum beads. This experiment was designed to study a specific phenomenon of sub-diffusive or localized waves in open media - the variation with position of the diffusion coefficient. At the same time, the equipartition of elastic waves was studied; equipartition is a signature of the randomization of the waves by the scattering events and states that after many such events all modes and directions of propagation are equally probable. To investigate this effect, the amplitude of the elastic wave was recorded on the surface of the sample using a laser interferometer. The two experiments described in chapters 4 and 5 focus mainly on understanding the scattering properties of the samples using the long-time coda of the recorded signals, meaning the part of the wave which undergoes a lot of scattering events.

The experiment described in chapter 6 is different from the two others in several ways. First, the samples studied, noodle dough, have not been designed specifically for an acoustic experiment that is aimed at understanding new aspects of wave physics. Secondly, in this sample, a coda cannot be observed due to the higher absorption in the dough compared to the aluminum bead samples. Here, the properties of the samples are studied via the ballistic signal,

the part of the signal going directly through the sample without being deviated by scattering. The propagation of ultrasound through the dough is strongly influenced by the resonances of the bubbles present in it, as well as by the elastic properties of the other constituents of the dough. Another feature of this experiment is the use of air-coupled transducers; because of the large impedance mismatch between air and the dough, extracting accurately the acoustic properties of the sample is quite challenging, and the development of a robust analysis technique was needed.

Overall, the work presented in this thesis is a step towards a more complete understanding of the propagation of acoustic or elastic waves in complex heterogeneous media, in which either or both strong scattering and absorption play significant roles.

Chapter 2

Background concepts and theory

2.1 Waves in Complex Media

In this chapter, I will discuss the propagation of waves in complex media, but first I should define what a complex medium is and what we can observe in these media. In general, a complex material is a medium with some internal structure on a length scale between atoms and bulk that can give rise to a variety of interesting properties. In the context of wave physics, the focus is on wave properties, and the first, very simple definition of a complex medium is a medium in which waves cannot travel only in straight lines: the waves will have to undergo scattering events inside the sample. This definition is not sufficient as it is often important to consider the idea of randomness in these media. The behaviour of the waves will be different if the medium is ordered (such as in a crystal) or disordered. In the rest of this thesis, a complex medium will be taken to be a medium composed of randomly placed scatterers; such a medium will also be called an inhomogeneous medium or a multiple scattering medium.

Wave transport in a multiple scattering medium is often treated as a random walk process. On “average”, the transport of energy by the waves will follow the same behaviour as Brownian motion of particles. Even though the random walk process neglects all effects of interference, which is an important phenomenon for waves, it describes wave transport in a complex medium remarkably well for a wide range of multiple scattering strengths [1,8,9]. Of course, the “average” has to be defined: here the average is done on different samples having the same properties of scattering but not the same disorder; it is a configurational average. Theoretically, to perform this “averaging”, the sample is considered as the realization of a random process. At the end, the transport through the sample is described by the “probability” of a “walker” to travel a distance r .

On average, the effect of interference might not be seen, but if there is only one realization of the disorder (only one wave field is measured), the interferences between the different paths of the wave are visible and lead to a speckle pattern. Figure 2.1 shows an example of an ultrasonic speckle pattern measured when a short pulse is incident on the sample and the intensity of the wave field is determined as a function of position near the opposite surface of the sample. The speckle pattern is often random, but it is always the same for a given realization of the disorder of the sample at a given time. It appears due to the different path lengths taken by the wave reaching a given point in the sample. If different wave paths are in phase, the interference is constructive (bright spot), otherwise, the interference is destructive (black spot). In the case of a point source experiment, the full pattern is observable only after the waves have filled the entire sample. As the speckle pattern is a representation of a given realization of the disorder of a sample, averaging the intensity over different disorder configurations will cause the spatial fluctuations in a speckle pattern to be smoothed out, giving the average “probability” for the wave to reach a given point following a random walk process. The average pattern will have a Gaussian shape.

The Gaussian profile is obtained for a medium in which the scattering is not “too strong”. At the end of this chapter, I will discuss situations for which this is not true anymore: instead of diffusive-like transport, the transport can slow down, leading to sub-diffusive or even localized behaviour [3,8,9,10]. In this situation, the interference effects become important.

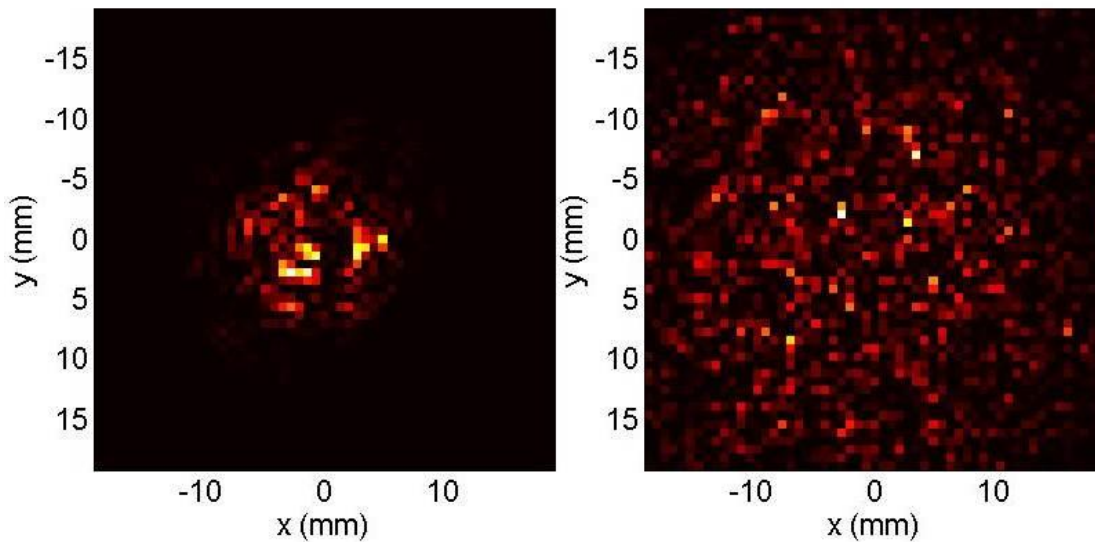


Figure 2.1: Speckle patterns obtained at two different times: at a short time (left), before the wave can fill the full scanned area, and at a longer time (right), after the wave reaches the boundary of the scanned area. To obtain these speckle patterns, the source was a short point-like pulse centred at $x = y = 0$ on one side of the sample, and the wave intensity close to the opposite side of the sample was determined as a function of position. In the left picture, the effect of the point source is still visible as there is no signal at long distances from the centre. A full speckle pattern is observable on the right. These results have been obtained for the sample of aluminum beads in liquid described in the next part of this thesis, with a 500 kHz transducer.

It is interesting to look at how the speckle patterns in Figure 2.1 were obtained. The sample, used for these acquisitions was in the form of a slab (large dimensions in the $x - y$ plane compared to the thickness in z). On one side of the sample, there was a source emitting a short pulse (a couple of periods at the working frequency). On the other side of the sample, there was a sub-wavelength-sized detector recording the signal in time (sometimes several hundred times longer than the emitted pulse) and in space, as the detector was moved to different positions as shown in Figure 2.2.

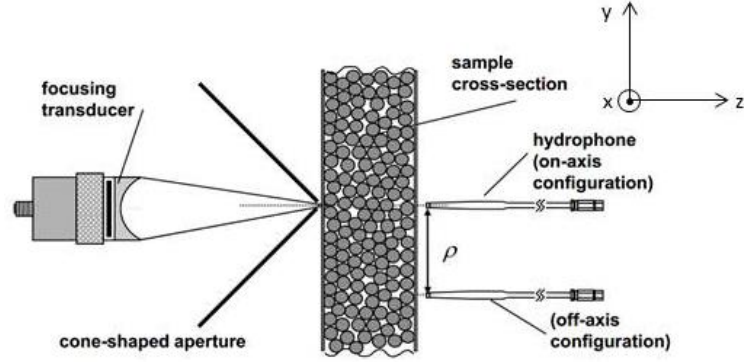


Figure 2.2: Setup of an experiment on wave transport in a multiple scattering medium. Here, the source is focused on the surface of the sample. Other source configurations can also be used. From [11], with kind permission of Società Italiana di Fisica.

This wave field can be recorded for different realizations of the disorder. The different moments (average or variance) of the field give access to information about the propagation in the sample. The wave field going through the sample can be decomposed into two parts:

$$\psi = \langle \psi \rangle + \delta\psi, \quad (2.1)$$

where ψ is the total wave field, $\langle \psi \rangle$ is the coherent wave and $\delta\psi$ is the incoherent part of the wave, by definition $\langle \delta\psi \rangle = 0$ ($\langle \dots \rangle$ represents the average over different realizations of disorder). In this chapter, we will first look at what information can be extracted from the coherent wave, *i.e.*, the wave resulting from the average of the field over the different realizations of the disorder. Then, we will look at the information that can be obtained from the incoherent part of the waves. This is done by looking at the average of the intensity I over the disorder:

$$I \propto \langle \psi^2 \rangle = \langle (\langle \psi \rangle + \delta\psi)^2 \rangle. \quad (2.2)$$

Before looking at the properties of the wave field and intensity in a disordered medium, some concepts about wave propagation in a complex medium need to be introduced. First, we will

look at the wave equation in inhomogeneous media, and then a solution of this equation will be found by introducing the Green's function. From the Green's function, the properties of the wave field and wave intensity will be obtained.

2.2 Wave equations in inhomogeneous media

2.2.1 Wave equation

The wave equation can be written for different physical quantities. For an acoustic wave in a fluid, the wave field can be described in terms of the acoustic pressure in the liquid or the particle velocity. In a solid, those physical quantities will be the stress or the displacement [12]. As is well known, the wave equation is written in terms of a double derivative in time and a double derivative in space of one of these physical quantities. The two derivative terms are linked by the velocity of the wave in the medium:

$$\frac{\partial^2 \varphi(\vec{x}, t)}{\partial t^2} - c_0^2 \vec{\nabla}^2 \varphi(\vec{x}, t) = 0. \quad (2.3)$$

The previous equation is the classical wave equation: $\varphi(\vec{x}, t)$ is the relevant physical quantity and c_0 is the velocity of propagation of sound in the medium. A source term can be added in the right-hand side of the equation. In a fluid, the wave velocity depends on the density (ρ_0) and on the compressibility (χ_s) of the fluid²:

$$c_0 = \frac{1}{\sqrt{\rho_0 \chi_s}}. \quad (2.4)$$

² In a solid, the velocity will depend on the density and on elastic constants.

The two previous equations are true if the medium is homogeneous, *i.e.*, if the density and the compressibility are independent of the position. When the medium is not homogenous, we cannot obtain an equation as simple as equation (2.3). To obtain the new wave equation, we need to go back to basic equations, the conservation of mass (2.5) and the Euler equation (2.6):

$$\frac{\partial \rho_a}{\partial t} + \vec{\nabla} \cdot (\rho_0 \vec{v}) = 0 \quad (2.5)$$

and

$$\frac{\partial \vec{v}}{\partial t} + \frac{1}{\rho_0} \vec{\nabla} p_a = 0. \quad (2.6)$$

The density ($\rho = \rho_0 + \rho_a$) is the sum of the equilibrium density (ρ_0), which is position dependent (because of the inhomogeneity of the medium) but time independent, and the time- and position-dependent density modification due to the wave (ρ_a). The pressure in the medium ($p = p_0 + p_a$) is the sum of the equilibrium pressure (p_0) and the acoustic pressure (p_a). The two acoustic terms (with the subscript “a”) are very small compared with their respective equilibrium values. The particle velocity (\vec{v}) is also a small quantity. The two previous equations have been linearized so there is no product of these small terms.

One additional equation is needed, which links the pressure with the compressibility (χ) and the displacement. By definition, the compressibility is equal to the infinitesimal limit of the relative variation of the volume ($\delta V/V$) divided by the pressure variation δp :

$$\chi_0 = \lim_{\delta p \rightarrow 0} \left(-\frac{1}{V} \frac{\delta V}{\delta p} \right) = -\frac{1}{V} \frac{dV}{dp}. \quad (2.7)$$

For an acoustic wave the pressure variation δp is p_a . The relative variation of the volume can be expressed in terms of the displacement \vec{u} :

$$\frac{\delta V}{V} = \vec{\nabla} \cdot \vec{u} = -\chi_0 p_a. \quad (2.8)$$

As for the density ρ_0 , the compressibility χ_0 is position dependent, but time independent. Using equations (2.5), (2.6) and (2.8), we can obtain the wave equation for inhomogeneous media:

$$\frac{\partial^2 p_a}{\partial t^2} = -\frac{1}{\chi_0} \frac{\partial^2 \vec{\nabla} \cdot \vec{u}}{\partial t^2} = -\frac{1}{\chi_0} \vec{\nabla} \cdot \left(\frac{\partial \vec{v}}{\partial t} \right) = \frac{1}{\chi_0} \vec{\nabla} \cdot \left\{ \frac{1}{\rho_0} \vec{\nabla} p_a \right\}. \quad (2.9)$$

In equation (2.9), we can see one of the main characteristics of the wave equation, the double derivatives in time and in space. This equation cannot be as simple as equation (2.3) due to the spatial variation of the density. The equation for the particle velocity is a little different from the one for pressure [equation (2.9)]:

$$\frac{\partial^2 \vec{v}}{\partial t^2} = \frac{1}{\rho_0} \vec{\nabla} \cdot \left\{ \frac{1}{\chi_0} \vec{\nabla} \cdot \vec{v} \right\}. \quad (2.10)$$

Equation (2.9) [and (2.10)] can be written differently and allow the classical wave equation to be retrieved. It is necessary to expand the right-hand side of these two equations. For example, equation (2.9) becomes

$$\vec{\nabla}^2 p_a - \frac{1}{c^2(\vec{r})} \frac{\partial^2 p_a}{\partial t^2} = \frac{1}{\rho_0} \vec{\nabla} \rho_0 \cdot \vec{\nabla} p_a, \quad (2.11)$$

where the velocity c , is position dependent. We can see that the heterogeneity of the medium acts as a source term in the new wave equation [equation (2.11)].

2.2.2 Helmholtz equation

For monochromatic harmonic waves, equation (2.11) can be used to obtain the Helmholtz equation. If we assume

$$p_a(\vec{r}, t) = \psi(\vec{r})e^{-i\omega t}, \quad (2.12)$$

the wave equation becomes

$$\vec{\nabla}^2\psi + \frac{\omega^2}{c^2(\vec{r})}\psi = \frac{1}{\rho_0}\vec{\nabla}\rho_0 \cdot \vec{\nabla}\psi. \quad (2.13)$$

2.3 Green's function for multiply scattered waves

2.3.1 Definition of the Green's function

Green's functions are often introduced since they provide a powerful way to solve the wave equation [8]. The Green's function G , represents the response of a system for a point source at a given point \vec{r}_s , at a given time t_s . In a homogeneous infinite medium, the Green's function G_0 is defined by the following equation:

$$\left(\frac{\partial^2}{\partial t^2} - c_0^2\vec{\nabla}^2\right)G_0(\vec{r}, \vec{r}_s, t, t_s) = \delta(\vec{r} - \vec{r}_s)\delta(t - t_s), \quad (2.14)$$

and is equal to

$$G_0^\pm(\vec{r}, \vec{r}_s, t, t_s) = \frac{-1}{4\pi} \frac{\delta(t - t_s \pm |\vec{r} - \vec{r}_s|/c_0)}{|\vec{r} - \vec{r}_s|}. \quad (2.15)$$

The Green's function can also be defined for monochromatic waves:

$$(\nabla^2 + k_0^2)G_0^\pm(\omega, \vec{r}, \vec{r}_s) = \delta(\vec{r} - \vec{r}_s), \quad (2.16)$$

and

$$G_0^\pm(\omega, \vec{r}, \vec{r}_s) = \frac{-1 \exp(\pm ik_0 |\vec{r} - \vec{r}_s|)}{4\pi |\vec{r} - \vec{r}_s|} = G_0^\pm(\omega, \vec{r} - \vec{r}_s). \quad (2.17)$$

The wave number $k_0 = \omega/c_0$ has been defined in the two previous equations. We should note that, in a homogeneous medium, the Green's function only depends on $|\vec{r} - \vec{r}_s|$, the distance from the source, and not on the actual position of the observation point. Two solutions can be defined from these equations: G_0^+ and G_0^- . These two solutions exist because the system is time-reversal invariant. In the frequency domain these two solutions are complex conjugates of each other ($G_0^+ = G_0^{-*}$) and in the time domain, we can write $G_0^+(t) = G_0^-(-t)$. We can define the Fourier Transform in space of the Green's function:

$$G_0(\omega, \vec{r} - \vec{r}_s) = \int G_0(\omega, \vec{k}) e^{i\vec{k} \cdot (\vec{r} - \vec{r}_s)} d\vec{k} \quad (2.18)$$

Equations (2.17) and (2.18) lead to the Fourier transform of the Green's function:

$$G_0(\omega, \vec{k}) = \frac{1}{k_0^2 - k^2}. \quad (2.19)$$

Once the Green's function is known, we can express the solution of the wave equation for any distribution of sources $f(\vec{r})$, inside the medium. The wave field, $\psi(\vec{r})$, in the medium will be the convolution product of the source with the Green's function:

$$\psi(\omega, \vec{r}) = (G_0 * f)(\vec{r}) = \int G_0(\omega, \vec{r} - \vec{r}_s) f(\vec{r}_s) d\vec{r}_s. \quad (2.20)$$

2.3.2 Green's function in a complex medium [8,13]

The transport in an inhomogeneous medium can also be described by a Green's function. The first step is to re-write equation (2.13) to obtain the classical wave equation on the left-hand-side. The velocity in the medium can be written as $c(\vec{r}) = c_0 + \delta c(\vec{r})$, where c_0 is the average velocity in the medium. The definition of c_0 allows equation (2.13) to be rewritten as a wave equation in a homogenous medium with a source term:

$$(\vec{\nabla}^2 + k_0^2)\psi = V(\omega, \vec{r})\psi. \quad (2.21)$$

$V(\vec{r})$ is a position-dependent scattering potential describing the heterogeneity of the medium. In the most general case, we can assume that V is random and describes the disorder of the medium. The equation (2.21) shows that the disorder will act like a source inside the medium. The potential operator is

$$V(\omega, \vec{r}) = k_0^2 \left(1 - \frac{c_0^2}{c^2(\vec{r})} \right) + \frac{1}{\rho_0} \vec{\nabla} \rho_0 \cdot \vec{\nabla}. \quad (2.22)$$

As has been done for the case of the wave in a homogeneous medium, the Green's function can be defined for equation (2.21) via

$$(\vec{\nabla}^2 + k_0^2)G(\omega, \vec{r}, \vec{r}_s) = V(\omega, \vec{r})G(\omega, \vec{r}, \vec{r}_s) + \delta(\vec{r} - \vec{r}_s) \quad (2.23)$$

This equation can be solved using equation (2.20). Here the source term is the right-hand side of equation (2.23):

$$\begin{aligned}
G(\omega, \vec{r}, \vec{r}_s) &= \int G_0(\omega, \vec{r} - \vec{r}_1) [V(\omega, \vec{r}_1) G(\omega, \vec{r}_1, \vec{r}_s) + \delta(\vec{r}_1 - \vec{r}_s)] d\vec{r}_1 \\
&= G_0(\omega, \vec{r} - \vec{r}_s) + \int G_0(\omega, \vec{r} - \vec{r}_1) V(\omega, \vec{r}_1) G(\omega, \vec{r}_1, \vec{r}_s) d\vec{r}_1
\end{aligned} \tag{2.24}$$

The Green's function in an inhomogeneous medium, $G(\omega, \vec{r}, \vec{r}_s)$, is composed of two parts. The uniform medium Green's function G_0 describes the propagation from the source to a position \vec{r} , which could be for example the location of the detector. The second term describes the propagation from the source to a scatterer at \vec{r}_1 and then from this scatterer to \vec{r} , described by the scattered Green's function in the integral. It is possible to substitute equation (2.24) into itself; this new equation gives us a better understanding of the different scattering events happening in the medium:

$$\begin{aligned}
G(\omega, \vec{r}, \vec{r}_s) &= G_0(\omega, \vec{r} - \vec{r}_s) + \int G_0(\omega, \vec{r} - \vec{r}_1) V(\omega, \vec{r}_1) G_0(\omega, \vec{r}_1 - \vec{r}_s) d\vec{r}_1 \\
&+ \int G_0(\omega, \vec{r} - \vec{r}_1) V(\omega, \vec{r}_1) G_0(\omega, \vec{r}_1 - \vec{r}_2) V(\omega, \vec{r}_2) G_0(\omega, \vec{r}_2 - \vec{r}_s) d\vec{r}_1 d\vec{r}_2 \tag{2.25} \\
&+ \dots
\end{aligned}$$

Equation (2.25) is called the Born expansion. The different integrals describe the number of scattering events that a wave is going through. The first integral corresponds to a wave going from the source to a scatterer at \vec{r}_1 , and then going directly to the detector (single scattering). Then, the second integral describes a wave going through two scattering events, at \vec{r}_1 and \vec{r}_2 , before going to the detector (double scattering). The ballistic signal is described by the first term in the equation (G_0). The expansion for G in equation (2.25) can be done for as many scattering events as are needed.

a) Matrix notation [8]

It is useful to introduce matrices to express equation (2.25) or (2.24) as it will simplify some of the calculations. First, we need to define a two-position variable potential V :

$$V(\omega, \vec{r}_1, \vec{r}_2) = V(\omega, \vec{r}_1)\delta(\vec{r}_1 - \vec{r}_2), \quad (2.26)$$

with this new potential, equation (2.24) becomes

$$G(\omega, \vec{r}, \vec{r}_s) = G_0(\omega, \vec{r} - \vec{r}_s) + \iint G_0(\omega, \vec{r} - \vec{r}_1)V(\omega, \vec{r}_1, \vec{r}_2)G(\omega, \vec{r}_2, \vec{r}_s)d\vec{r}_1d\vec{r}_2 \quad (2.27)$$

This equation can be rewritten using matrices. This is equivalent to doing discrete summations over the position of each scatterer instead of doing the double integrals:

$$\mathbf{G} = \mathbf{G}_0 + \mathbf{G}_0\mathbf{V}\mathbf{G}, \quad (2.28)$$

where the matrices have been defined such as: $(\mathbf{M})_{i,j} = M(\vec{r}_i, \vec{r}_j)$, for the two Green's functions, and the potential, \mathbf{V} , is a diagonal matrix. These matrices can be seen as operators acting on the incident waves in the medium. This new notation gives a very compact way to write the Born expansion [equation (2.25)]:

$$\mathbf{G} = \mathbf{G}_0 + \mathbf{G}_0\mathbf{V}\mathbf{G}_0 + \mathbf{G}_0\mathbf{V}\mathbf{G}_0\mathbf{V}\mathbf{G}_0 + \mathbf{G}_0\mathbf{V}\mathbf{G}_0\mathbf{V}\mathbf{G}_0\mathbf{V}\mathbf{G}_0 + \dots \quad (2.29)$$

2.3.3 The T-matrix [8,13]

The T-matrix, also known as the scattering matrix, is an operator containing information about all the scattering events in the system, including the multiple scattering events. The definition of the T-matrix is

$$\mathbf{T} = \mathbf{V} + \mathbf{V}\mathbf{G}_0\mathbf{V} + \mathbf{V}\mathbf{G}_0\mathbf{V}\mathbf{G}_0\mathbf{V} + \dots \quad (2.30)$$

The first term of the right-hand side of equation (2.30) represents the single scattering events; the second term represents the double scattering events, and so on... For most experimental situations, the T-matrix cannot be calculated exactly. However, it can be obtained exactly in the case of single scattering by using the scattering cross section of the scatterer. This cross section is well known for some simple geometries (sphere, cylinder). In the situations with a lot of scatterers, in which the scattered wave from one of them will influence all the other scatterers, it is not possible to calculate the T-matrix exactly. The best way to obtain information about the scattered waves in such a medium is to use averaged properties of this medium. Here the “averaged properties” should be understood as the result of a configurational average, meaning an average over different realizations of the disorder (see section 2.4).

With the definition of the T-matrix, we can write:

$$\mathbf{G} = \mathbf{G}_0 + \mathbf{G}_0\mathbf{T}\mathbf{G}_0. \quad (2.31)$$

This last equation is very similar to equation (2.28), but all the terms on the right-hand-side are either a characteristic of the medium (the T-matrix) or of propagation in the uniform medium (\mathbf{G}_0). Equation (2.31) represents the Green’s function of the system, taking into account all the possible scattering events between all the different scatterers. It is easier to explain the meaning of this equation if we write it in the continuous form:

$$G(\omega, \vec{r}, \vec{r}_s) = G_0(\omega, \vec{r} - \vec{r}_s) + \iint G_0(\omega, \vec{r} - \vec{r}_1)T(\omega, \vec{r}_1, \vec{r}_2)G_0(\omega, \vec{r}_2 - \vec{r}_s)d\vec{r}_1d\vec{r}_2. \quad (2.32)$$

$T(\vec{r}_1, \vec{r}_2)$ represents all the possible ways for the waves to go from a position \vec{r}_2 to a position \vec{r}_1 and the two uniform-medium Green’s functions in the integral represent the wave travelling from

the source to \vec{r}_2 and from \vec{r}_1 to the observation point. The integrals allow the wave to cover all the space in the medium.

2.3.4 The scattered wave

Now that we have the Green's function of the wave equation in a heterogeneous medium [equation (2.11)] in which we have defined a scattering potential [equation (2.22)], we can look at the wave propagating through such a medium. According to Green's theorem, we have

$$\psi(\omega, \vec{r}) = \int G(\omega, \vec{r}, \vec{r}_s) f(\omega, \vec{r}_s) d\vec{r}_s, \quad (2.33)$$

with f the distribution of sources in or outside the medium. Equation (2.32) representing the Green's function in the heterogeneous medium can be used in this last equation (2.33) to obtain an expression for a wave travelling in a heterogeneous medium:

$$\psi(\omega, \vec{r}) = \psi_0(\omega, \vec{r}) + \iint G_0(\omega, \vec{r} - \vec{r}_1) T(\omega, \vec{r}_1, \vec{r}_2) \psi_0(\omega, \vec{r}_2) d\vec{r}_1 d\vec{r}_2. \quad (2.34)$$

$\psi_0(\vec{r})$ is the wave travelling directly to the observation position as in a homogeneous medium. The second term of this last equation is the scattered wave, ψ_s , in the heterogeneous medium.

2.3.5 Born approximation [13]

A very common approximation, which can be done at this stage, is the Born approximation or single scattering approximation. This approximation consists in taking only into account the first scattering term in the Born expansion [equation (2.25) or (2.29)]. In this approximation, the Born expansion and the T-matrix become:

$$\mathbf{G} = \mathbf{G}_0 + \mathbf{G}_0 \mathbf{V} \mathbf{G}_0 \quad (2.35)$$

and
$$\mathbf{T} = \mathbf{V}. \quad (2.36)$$

In this case, it is possible to determine the scattering matrix exactly as it is only given by the potential of each scatterer. This approximation is used, for example, for imaging purposes, such as medical imaging or non-destructive testing. In these situations, it is assumed that echoes coming back to the probe (in the case of reflection measurements) correspond to a pulse which has been reflected once by one inclusion in the medium.

The T-matrix can be determined for a single scatterer, and even if it will not be helpful to solve problems for a medium with a high density of scatterers, it will nonetheless help to understand the meaning of the T-matrix. We can imagine an experiment in which we send a plane wave on a scatterer and observe the scattered wave in all the directions.

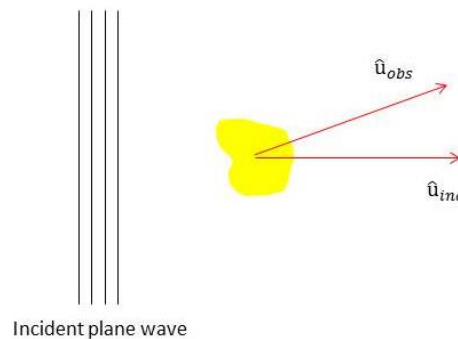


Figure 2.3: A plane wave, travelling in the direction of the unit vector \hat{u}_{inc} , is scattering off a single scatterer (yellow object). The scattered wave is observed in the direction \vec{u}_{obs} and can be measured.

The resultant wave of the measurement described in Figure 2.3 is given by equation (2.34). Here, we will look only at the second term of this equation, the scattered wave ψ_s . The scattered wave will be observed in the far field ($r \gg r_s$) and the expression for the Green's function G_0 can be simplified:

$$G_0(\omega, \vec{r}, \vec{r}_s) = \frac{-1 \exp(ik_0|\vec{r} - \vec{r}_s|)}{4\pi |\vec{r} - \vec{r}_s|} \approx \frac{-1 \exp(ik_0r)}{4\pi r} \exp(-ik_0 \hat{u}_{\text{obs}} \cdot \vec{r}_s). \quad (2.37)$$

Here \hat{u}_{obs} is a unit vector in the direction of observation. Similarly \hat{u}_{inc} is a unit vector in the direction of incidence. With this approximation and the expression for the incident plane wave [$\psi_0(\omega, \vec{r}) = \exp(ik_0 \hat{u}_{\text{inc}} \cdot \vec{r})$], we can obtain a formula for the scattered wave:

$$\begin{aligned} \psi_d(\omega, \vec{r}) &= \frac{-1 \exp(ik_0r)}{4\pi r} \iint \exp(-ik_0 \hat{u}_{\text{obs}} \cdot \vec{r}_s) T(\omega, \vec{r}_1, \vec{r}_2) \exp(ik_0 \hat{u}_{\text{inc}} \cdot \vec{r}) d\vec{r}_1 d\vec{r}_2 \\ &= \frac{\exp(ik_0r)}{r} \cdot \frac{-1}{4\pi} \tilde{T}(k_0 \hat{u}_{\text{obs}}, k_0 \hat{u}_{\text{inc}}). \end{aligned} \quad (2.38)$$

In the last equation, \tilde{T} is “almost” a 2D Fourier transform of the scattering matrix. It is not the real Fourier transform as a minus sign is missing for one of the two variables. The last line of the equation shows us that \tilde{T} represents the scattering amplitude at a given direction for a given direction of the incident wave. For simple objects, such as a sphere, this amplitude is well known. Moreover, thanks to the optical theorem [8], linking the forward scattering to the scattering cross section, we can express the scattering cross section, σ_T , as a function of the scattering matrix:

$$\sigma_T = -\frac{1}{k_0} \text{Im} \left(\tilde{T}(k_0 \hat{u}_{inc}, k_0 \hat{u}_{inc}) \right). \quad (2.39)$$

2.4 Propagation of the average amplitude [8,13,14]

For situations in which the Born approximation cannot be used, which will be the case for all the experiments described in this thesis, it is necessary to find another way to evaluate the properties of the scattering matrix (T-matrix). This will be done by looking at the averaged properties of the medium. Until now, we have been considering a heterogeneous medium without specifying precisely the nature of the heterogeneity. Now, the medium will be considered to be the result of a random process. By looking at a lot of realizations of this random process, the average amplitude travelling through such a medium can be obtained. Here, the average will be done on different configurations of the “disorder” of the medium.

The randomness of the medium can come, for example, from the positions of the scatterers (which define where the potential $V(\vec{r})$ is non-zero) or the strength of the scatterers (magnitude of $V(\vec{r})$). In practice, a lot of different samples will not be built to be able to perform a real configurational average: instead, an average over the disorder of a given sample will be performed by moving the source (and/or detector) position. Two adjacent source positions will be chosen such that they are independent of short-range C_1 correlations (i.e., at positions that are at least one speckle spot away from each other, or approximately a wavelength apart in the near field of the sample).

2.4.1 Dyson equation

Propagation of the average wave field is described by the configurationally averaged Green's function $\langle G \rangle_c$. Because this is an average over different realization of a random process, this Green's function is invariant under translation, *i.e.*, it depends only on the separation between the source position and the observation position, as is the homogeneous medium Green's function G_0 [equation (2.17)]:

$$\langle G(\omega, \vec{r}, \vec{r}_s) \rangle_c = \langle G(\omega, \vec{r} - \vec{r}_s) \rangle_c \quad (2.40)$$

No averaging is needed for G_0 , as it is not the result of a random process. The averaging of equation (2.27) gives:

$$\begin{aligned} \langle G(\omega, \vec{r} - \vec{r}_s) \rangle_c &= G_0(\omega, \vec{r} - \vec{r}_s) \\ &+ \iint G_0(\omega, \vec{r} - \vec{r}_1) \Sigma(\omega, \vec{r}_1 - \vec{r}_2) \langle G(\omega, \vec{r} - \vec{r}_s) \rangle_c d\vec{r}_1 d\vec{r}_2. \end{aligned} \quad (2.41)$$

This equation (2.41) is known as the Dyson equation. Σ is the self-energy operator, which has to be invariant under translation, as all the other operators in this equation are. At this point, it is convenient to go to the Fourier domain in space. The Fourier Transform of equation (2.41) is easy to perform, as the double integral is two convolution products, so that in the Fourier domain, it involves simple multiplication. Also, as the only variable is $(\vec{r} - \vec{r}_s)$, the Fourier transform of the operator will have only one variable, \vec{k} .

$$\langle G(\omega, \vec{k}) \rangle_c = G_0(\omega, \vec{k}) + G_0(\omega, \vec{k}) \Sigma(\omega, \vec{k}) \langle G(\omega, \vec{k}) \rangle_c. \quad (2.42)$$

The Fourier Transform of the homogeneous medium Green's function is known [equation (2.19)], so it is possible rewrite the last equation as:

$$\langle G(\omega, \vec{k}) \rangle_c = \frac{1}{k_0^2 - \Sigma(\omega, \vec{k}) - k^2}. \quad (2.43)$$

The self-energy and the scattering matrix can be linked. By taking the average and the Fourier transform of equation (2.32), and using equation (2.42), we obtain:

$$\Sigma(\omega, \vec{k}) = \frac{\langle T(\omega, \vec{k}) \rangle_c}{1 + \langle T(\omega, \vec{k}) \rangle_c G_0(\omega, \vec{k})}. \quad (2.44)$$

2.4.2 Effective medium (coherent potential approximation) [8]

If the self-energy $\Sigma(\omega, \vec{k})$ is independent of \vec{k} for a given frequency band, it is straightforward to define an effective medium, which is a uniform medium with effective parameters that describe coherent propagation through the medium. In this description, we can replace k_0 by a new effective wave number k_e (both wave numbers are frequency dependent), which takes into account the renormalization of the wave number by the self-energy. The wave number of the effective medium is

$$k_e^2 = k_0^2 - \Sigma(\omega). \quad (2.45)$$

A space-dependent Green's function $G_e(\omega, \vec{k})$ can then be obtained in this new effective medium,

$$G_e(\omega, \vec{r} - \vec{r}_s) = \langle G(\omega, \vec{r} - \vec{r}_s) \rangle_c = \frac{-1 \exp(ik_e |\vec{r} - \vec{r}_s|)}{4\pi |\vec{r} - \vec{r}_s|}. \quad (2.46)$$

As the self-energy $\Sigma(\omega)$ is a complex number, so is k_e . The imaginary part of the wave number leads to a decrease in amplitude with the distance travelled through the medium. This is

only due to the scattering, as no absorption has been added to the model. The decrease in amplitude is due to scattering loss, the part of the wave which is not going in the original direction of propagation. The scattering mean free path can be expressed as a function of the imaginary part of k_e :

$$l_s = \frac{1}{2\text{Im}(k_e)}, \quad (2.47)$$

where the factor 2 has to be introduced because the scattering mean free path describes the decay of the intensity of the waves, not the decrease of the amplitude.

It is also informative to look at the scattering matrix, or T-matrix, T_e in the effective medium. We can start by rewriting equation (2.43) to isolate the self-energy:

$$\langle G(\omega, \vec{k}) \rangle_c^{-1} = G_0(\omega, \vec{k})^{-1} - \Sigma(\omega, \vec{k}) = G_e(\omega, \vec{k})^{-1} \quad (2.48)$$

From equations (2.43) and (2.45), the effective medium Green's function, $G_e(\omega, \vec{k}) = 1/(k_e^2 - k^2)$, has the form of a uniform Green's function [equation (2.19)], so that relative to the effective medium, the self-energy Σ_e is equal to zero. All information about the scattering that is contained in the self-energy $\Sigma(\omega, \vec{k})$ has been introduced into the effective medium Green's function via the effective wave number k_e . Since the self-energy Σ_e is equal to zero, $\langle T_e \rangle_c$ is also equal to zero according to equation (2.44). In this effective medium, there is no scattering on average (scattering still exists as $\langle T_e^2 \rangle_c \neq 0$). The signal described by the effective medium Green's function G_e is a signal which, on average, does not encounter any scattering event. This signal corresponds to the ballistic signal, which travels coherently straight through the medium without scattering away from the forward direction.

In which cases can we use the approximation of the self-energy being independent of \vec{k} ? The first case, in which we can use it, is the low frequency limit, when the wavelength is much larger than the size of the scatterers (Rayleigh scattering). The scatterers will then appear as points for the wave and will not have any spatial structure, so the scattering properties will be independent of \vec{k} . A second case, in which the approximation can be done, is when the scattering is not very strong and the renormalization of k_0 is small [$k_0^2 \gg \Sigma(\omega, \vec{k})$].

2.4.3 Experimental measurement of the ballistic signal

Experimentally, the ballistic signal will be measured to obtain information about the scattering properties of a sample. The ballistic signal is the coherent signal, the part of the transmitted wave field which is not cancelled by the configurational average. Ideally, the configurational averaging should be performed on different samples with the same scattering properties, but with different realizations of the disorder. In practice, as it would be too difficult to create thousands of different samples to perform the average, the average will be done over the disorder of a given sample by moving the source position (Figure 2.4). As the ballistic signal will have a similar shape to the input pulse, so long as dispersion over the pulse bandwidth is not too extreme, the ballistic signal is identified as the part of the average signal that arrives the earliest, thereby exploiting temporal resolution to exclude the rest of the average, where the multiple scattering component is larger, and therefore may not be completely cancelled in the averaging process.

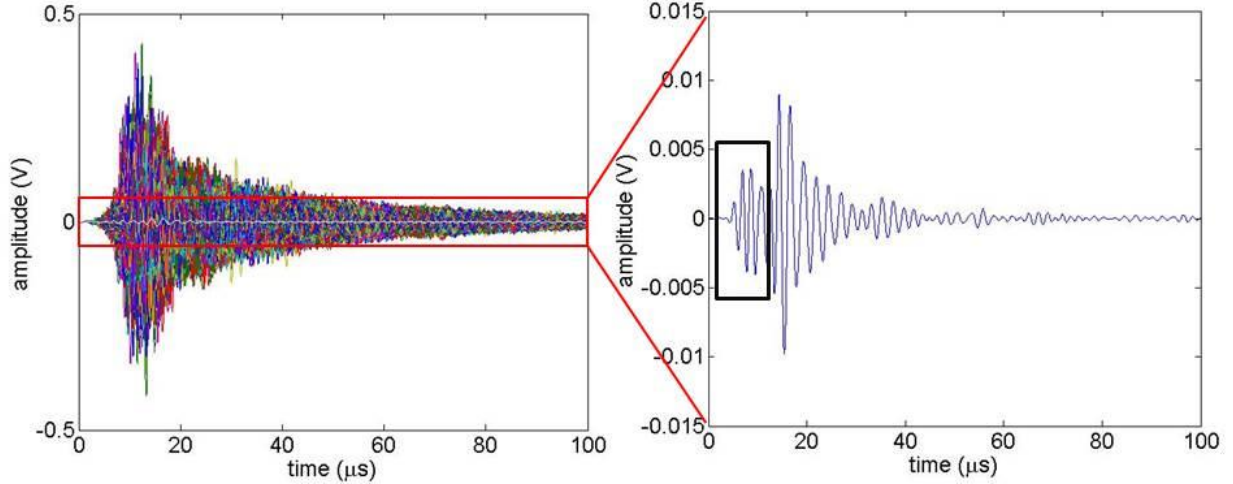


Figure 2.4: On the left: wave field for 3025 different source positions. The white line in the middle is the average of all these wave fields (coherent signal). On the right: close-up on the coherent signal. The signal inside the black box is taken to be the ballistic signal. These signals have been obtained on a sample of aluminum beads in a low-loss fluid with a 500 kHz transducer.

To obtain the ballistic signal, the experiment is performed in transmission; the emitter and the receiver face each other on each side of the sample. After each acquisition, the sample is moved by at least half a wavelength, so that adjacent source positions are essentially independent. A great number of acquisitions are done (typically around 3000) and the field is averaged for all these source positions (Figure 2.4). The signal obtained after averaging contains the coherent ballistic signal and a residual of the multiply scattered coda that survives the averaging process. Different information can be extracted from the ballistic signal by looking at the amplitude and the phase; this information is obtained from the complex wave number k_e of the sample. Then,

$$v_\varphi = \frac{\omega}{\text{Re}(k_e)}, \quad v_g = \frac{d(\omega)}{d(\text{Re}(k_e))} \quad \text{and} \quad l_e = \frac{1}{2\text{Im}(k_e)}. \quad (2.49)$$

The two different velocities are the phase velocity v_φ , and the group velocity v_g . l_e is the extinction length, which takes into account the different mechanisms that reduce the amplitude of the wave. These mechanisms are scattering, as seen in equation (2.47), and absorptive losses of

energy due to, for example, viscous effects. Characteristic lengths can be defined for these two mechanisms: the scattering mean free path l_s , and the absorption length l_a . These lengths add “in parallel” to give the extinction length:

$$\frac{1}{l_e} = \frac{1}{l_s} + \frac{1}{l_a}. \quad (2.50)$$

Depending on the experiment, and on the sample, a particular mechanism can be more important than the others. For example, in the case of the sample of aluminum beads in a low-loss fluid, the absorption is very weak and l_a is very large, in this situation $l_e \approx l_s$. On the other hand, in the case of wave propagation in noodle dough, the viscous effects are very important and l_a is small ($l_e \approx l_a$).

2.5 Propagation of the average intensity [8,14]

Until now, we have looked at the propagation of the average amplitude which has been denoted the coherent wave. At long times, when the distance travelled by the wave is larger than several scattering mean free paths, most of the energy of the wave is not in the coherent signal anymore. At each scattering event, a portion of the energy remains coherent (forward scattering), and the rest of the energy is deviated to another direction. After another scattering event, some of the deviated energy can go back in the “forward” direction, but because the phase will be different, it will not participate in the coherent signal. As soon as some energy has been taken away from the coherent signal, it cannot go back. The study of the incoherent signal is done using the average intensity of the signal instead of the average amplitude as was done in section 2.4.

2.5.1 Calculation of the intensity

The intensity is calculated using the square of the wave field $|\psi|^2$ and, the wave field being complex, the intensity is written using the complex conjugate of the field (ψ^*). As for the calculation of the amplitude, a configurational average should be taken:

$$\langle I(t, \vec{r}, \vec{r}_s) \rangle_c = \langle |\psi(t, \vec{r}, \vec{r}_s)|^2 \rangle_c = \langle \psi(t, \vec{r}, \vec{r}_s) \psi^*(t, \vec{r}, \vec{r}_s) \rangle_c. \quad (2.51)$$

As was done previously, the calculation of the intensity will be done using the Green's function. To do so, equation (2.31) [or (2.32) for the continuous form] in the effective medium will be used³:

$$\mathbf{G} = \mathbf{G}_e + \mathbf{G}_e \mathbf{T}_e \mathbf{G}_e \quad (2.52)$$

and

$$\mathbf{G}^* = \mathbf{G}_e^* + \mathbf{G}_e^* \mathbf{T}_e^* \mathbf{G}_e^*. \quad (2.53)$$

These two equations are written in the frequency domain, so it is simplest to work with the Fourier transform of the intensity:

$$I(\omega_0, \vec{r}, \vec{r}_s) = \int_{-\infty}^{+\infty} I(t, \vec{r}, \vec{r}_s) \exp(i\omega_0 t) dt \quad (2.54)$$

and

$$\begin{aligned} & G(t, \vec{r}, \vec{r}_s) G^*(t, \vec{r}, \vec{r}_s) \\ &= \frac{1}{(2\pi)^2} \iint_{-\infty}^{+\infty} G(\omega_1, \vec{r}, \vec{r}_s) G^*(\omega_2, \vec{r}, \vec{r}_s) \exp(-i\omega_1 t) \exp(i\omega_2 t) d\omega_1 d\omega_2 \\ &= \frac{1}{(2\pi)^2} \iint_{-\infty}^{+\infty} G(\omega_1, \vec{r}, \vec{r}_s) G^*(\omega_2, \vec{r}, \vec{r}_s) \exp(-i\Delta\omega t) d\omega_1 d\omega_2. \end{aligned} \quad (2.55)$$

³ We have $G_e = \langle G \rangle_c$, but $G = G_e + G_e T_e G_e$

The two previous equations can be used to obtain an expression for the Fourier transform of the intensity:

$$I(\Delta\omega, \vec{r}, \vec{r}_s) = \frac{1}{2\pi} \int_{-\infty}^{+\infty} G\left(\omega + \frac{\Delta\omega}{2}, \vec{r}, \vec{r}_s\right) G^*\left(\omega - \frac{\Delta\omega}{2}, \vec{r}, \vec{r}_s\right) d\omega. \quad (2.56)$$

The last equation is expressed in terms of two new quantities: $\omega = (\omega_1 + \omega_2)/2$ and $\Delta\omega = \omega_1 - \omega_2$. In the expression for the intensity, there are now two different time scales: $\Delta\omega$ corresponds to variation of the envelope of the intensity and ω is the frequency of the wave, i.e. the frequency corresponding to the fast variation of the phase inside the envelope (see Figure 2.5).

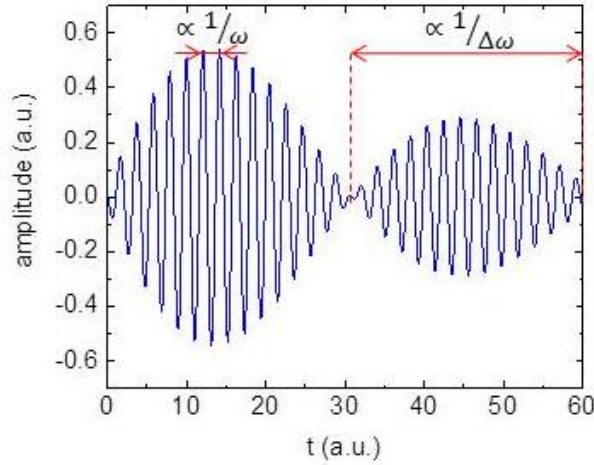


Figure 2.5: Example of a time-signal with two different time scales: one for the variation of the envelope ($1/\Delta\omega$) and one for the frequency of the wave ($1/\omega$).

The product of equations (2.52) and (2.53) can now be taken: $\mathbf{G} \otimes \mathbf{G}^*$. Here, the product of these two matrices is done element by element and will give a tensor of dimension 4: $(\mathbf{G} \otimes \mathbf{G}^*)_{ijkl} = G_{ik}G_{lj}^*$ [13].

$$\langle \mathbf{G} \otimes \mathbf{G}^* \rangle_c = \mathbf{G}_e \otimes \mathbf{G}_e^* + \langle \mathbf{G}_e \mathbf{T}_e \mathbf{G}_e \otimes \mathbf{G}_e^* \mathbf{T}_e^* \mathbf{G}_e^* \rangle_c \quad (2.57)$$

The cross terms are not present in the average equation because $\langle \mathbf{T}_e \rangle_c = 0$. It is useful to look at the equation for each term of the tensor to be able to reorganize equation (2.57):

$$\begin{aligned} (G \otimes G^*)_{ijkl} &= (G_e \otimes G_e^*)_{ijkl} + \sum_{m,n,p,q} (G_e)_{im} (T_e)_{mn} (G_e)_{nk} (G_e^*)_{lp} (T_e^*)_{pq} (G_e^*)_{qj} \\ &= (G_e \otimes G_e^*)_{ijkl} \\ &+ \sum_{m,n,p,q} (G_e)_{im} (G_e^*)_{qj} (T_e)_{mn} (T_e^*)_{pq} (G_e)_{nk} (G_e^*)_{lp} \\ &= (G_e \otimes G_e^*)_{ijkl} \quad (2.58) \\ &+ \sum_{m,n,p,q} (G_e \otimes G_e^*)_{ijmq} (T_e \otimes T_e^*)_{mqnp} (G_e \otimes G_e^*)_{npkl} \\ &= (G_e \otimes G_e^*)_{ijkl} + ((G_e \otimes G_e^*) (T_e \otimes T_e^*) (G_e \otimes G_e^*))_{ijkl}. \end{aligned}$$

Now that the elements of the tensor have been reorganized in this way, it is convenient to summarize the results by going back to the operator notation:

$$\langle \mathbf{G} \otimes \mathbf{G}^* \rangle_c = \mathbf{G}_e \otimes \mathbf{G}_e^* + (\mathbf{G}_e \otimes \mathbf{G}_e^*) \mathbf{\Gamma} (\mathbf{G}_e \otimes \mathbf{G}_e^*). \quad (2.59)$$

In equation (2.59), the “vertex” operator $\mathbf{\Gamma} = \langle \mathbf{T}_e \otimes \mathbf{T}_e^* \rangle_c$ has been introduced. The vertex function is a four-variable function which contains all the information about the multiple scattering. It is the analog of the T-matrix for the amplitude [equation (2.31)]. In the integral notation, equation (2.59) becomes:

$$\begin{aligned}
\langle G \left(\omega + \frac{\Delta\omega}{2}, \vec{r}, \vec{r}_s \right) G^* \left(\omega - \frac{\Delta\omega}{2}, \vec{r}, \vec{r}_s \right) \rangle_c = \\
G_e \left(\omega + \frac{\Delta\omega}{2}, \vec{r}, \vec{r}_s \right) G_e^* \left(\omega - \frac{\Delta\omega}{2}, \vec{r}, \vec{r}_s \right) + \\
\int d\vec{r}_1 d\vec{r}_2 d\vec{r}_3 d\vec{r}_4 G_e \left(\omega + \frac{\Delta\omega}{2}, \vec{r}, \vec{r}_1 \right) G_e^* \left(\omega - \frac{\Delta\omega}{2}, \vec{r}, \vec{r}_2 \right) \Gamma(\vec{r}_1, \vec{r}_2, \vec{r}_3, \vec{r}_4,) \\
G \left(\omega + \frac{\Delta\omega}{2}, \vec{r}_3, \vec{r}_s \right) G^* \left(\omega - \frac{\Delta\omega}{2}, \vec{r}_4, \vec{r}_s \right).
\end{aligned} \tag{2.60}$$

As the vertex function Γ contains all the information about multiple scattering, it is easy to see with the integral expression that all the possible scattering events are taken into account in this expression for both Green's functions. Two of the variables of the vertex function correspond to the input position [\vec{r}_3 and \vec{r}_4 in equation (2.60)] in the sample of the wave coming from the source; one for each Green's function. The two other variables [\vec{r}_1 and \vec{r}_2 in equation (2.60)] are the output positions of the vertex for the waves going to the detector position, via the two Green's functions on the left side of the integral.

By analogy with the self-energy for the amplitude, an “irreducible vertex” \mathbf{U} can be introduced that satisfies the following equation for $\langle \mathbf{G} \otimes \mathbf{G}^* \rangle_c$:

$$\langle \mathbf{G} \otimes \mathbf{G}^* \rangle_c = \mathbf{G}_e \otimes \mathbf{G}_e^* + (\mathbf{G}_e \otimes \mathbf{G}_e^*) \mathbf{U} \langle \mathbf{G} \otimes \mathbf{G}^* \rangle_c. \tag{2.61}$$

The equation (2.61) is called the Bethe-Salpeter equation. It is the equivalent of the Dyson equation for the amplitude [equation (2.42)]. The irreducible vertex \mathbf{U} and the “reducible vertex” $\mathbf{\Gamma}$ are linked, with the relationship between them being given by

$$\mathbf{\Gamma} = \mathbf{U} + \mathbf{U}(\mathbf{G}_e \otimes \mathbf{G}_e^*) \mathbf{U} + \mathbf{U}(\mathbf{G}_e \otimes \mathbf{G}_e^*) \mathbf{U}(\mathbf{G}_e \otimes \mathbf{G}_e^*) \mathbf{U} + \dots \tag{2.62}$$

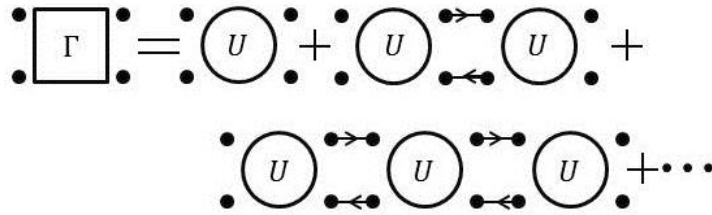


Figure 2.6: Diagrammatic representation of the reducible vertex Γ as a function of the irreducible vertex U . The circles represent U and the dots are the four variables (two inputs, two outputs). Γ is the infinite sum of the scattering events described by U ; the lines represent the Green's functions [8].

U is called the “irreducible” vertex because it cannot be decomposed in any way, as represented in Figure 2.6. Of course it will contain single scattering events, but also scattering events which cannot be decomposed as the sum of independent scattering events. In Figure 2.7, we can see different scattering processes contributing in the different parts of equation (2.61). Sketch a) represents two completely independent paths, which will not contribute to the total intensities as they are out of phase [9]. Sketch b), in which the paths have all the scatterers in common, will participate in the reducible vertex Γ . These two paths can be decomposed into a sequence of individual scattering events each of which contributes to the irreducible vertex U . The sketch c) represents two paths going through the same scatterers but in reverse order. In this situation, the whole path is contributing to U as it is not possible to decompose these paths into independent scattering events (each scatterer has to be visited in a specific order by each path).

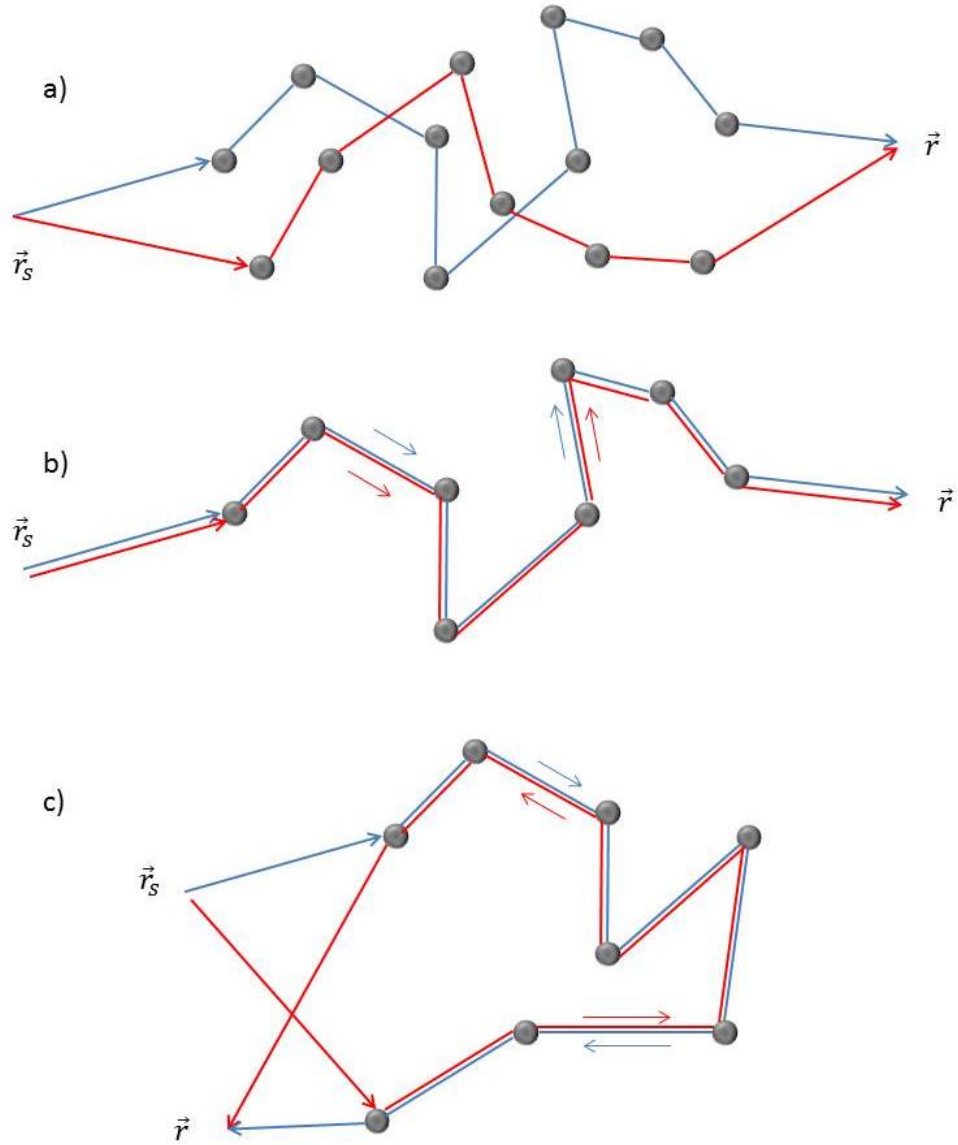


Figure 2.7: Example of scattering processes with two paths (one for each Green's function): a) the two paths are completely independent, b) the two paths are identical, and c) the two path have opposite directions.

As for the Dyson equation [equation (2.41) or (2.42)], it is desirable to work with in the Fourier domain for the position variables. First, the Fourier transform of the intensity is defined, and as for the amplitude, the Bethe-Salpeter equation is rewritten in the Fourier domain. The spatial Fourier transform of the Green's function is

$$G(t, \vec{r}, \vec{r}_s) = \sum_{\vec{k}_1, \vec{k}_2} G(t, \vec{k}_1, \vec{k}_2) \exp(i(-\vec{k}_1 \cdot \vec{r} + \vec{k}_2 \cdot \vec{r}_s)), \quad (2.63)$$

so the Fourier transform of the intensity is

$$\begin{aligned} I(\Delta\omega, \vec{r}, \vec{r}_s) = \\ \frac{1}{2\pi} \int_{-\infty}^{+\infty} d\omega \sum_{\vec{k}_1, \vec{k}_2, \vec{k}_3, \vec{k}_4} G\left(\omega + \frac{\Delta\omega}{2}, \vec{k}_1, \vec{k}_2\right) G^*\left(\omega - \frac{\Delta\omega}{2}, \vec{k}_3, \vec{k}_4\right) * \\ \exp(i[\vec{r} \cdot (\vec{k}_3 - \vec{k}_1) + \vec{r}_s \cdot (\vec{k}_2 - \vec{k}_4)]) \end{aligned} \quad (2.64)$$

We are interested in the configurational average of the intensity, and as for the amplitude, the average intensity will depend only on the distance between the source and the observation point:

$$\langle I(\Delta\omega, \vec{r} - \vec{r}_s) \rangle_c = \langle I(\Delta\omega, \vec{r}, \vec{r}_s) \rangle_c \quad (2.65)$$

and $\langle I(\Delta\omega, \vec{r} - \vec{r}_s) \rangle_c =$

$$\begin{aligned} \frac{1}{2\pi} \int_{-\infty}^{+\infty} d\omega \sum_{\vec{k}_1, \vec{k}_2, \vec{k}_3, \vec{k}_4} \langle G(\omega + \Delta\omega/2, \vec{k}_1, \vec{k}_2) G^*(\omega - \Delta\omega/2, \vec{k}_3, \vec{k}_4) \rangle_c * \\ \exp(i[\vec{r} \cdot (\vec{k}_3 - \vec{k}_1) + \vec{r}_s \cdot (\vec{k}_2 - \vec{k}_4)]) \end{aligned} \quad (2.66)$$

Finally, we can write the Fourier transform of the intensity as (knowing that the right and side of equation (2.66) depends only on $\vec{r} - \vec{r}_s$):

$$\begin{aligned} \langle G\left(\omega + \frac{\Delta\omega}{2}, \vec{k}_1, \vec{k}_2\right) G^*\left(\omega - \frac{\Delta\omega}{2}, \vec{k}_3, \vec{k}_4\right) \rangle_c \\ = \phi_{\omega, \vec{k}\vec{k}'}(\Delta\omega, \vec{q})(2\pi)^3 \delta(-\vec{k}_1 + \vec{k}_2 + \vec{k}_3 - \vec{k}_4). \end{aligned} \quad (2.67)$$

Three new wave vectors have been introduced in the last equation: \vec{k}, \vec{k}' and \vec{q} . They are defined by

$$\vec{k}_1 = \vec{k} + \frac{\vec{q}}{2}, \quad \vec{k}_2 = \vec{k}' + \frac{\vec{q}}{2}, \quad \vec{k}_3 = \vec{k} - \frac{\vec{q}}{2}, \quad \vec{k}_4 = \vec{k}' - \frac{\vec{q}}{2}. \quad (2.68)$$

Similar to the transform in time, there are two different scales of wave-vector, those associated with the variation of the envelope of the wave (\vec{q}), and with the variation inside the envelope described by the larger wave vector (\vec{k} and \vec{k}'). $\phi_{\omega, \vec{k}\vec{k}'}(\Delta\omega, \vec{q})$ contains all the information about the microscopic disturbance of the intensity in the medium. It represents the intensity going to direction \vec{k} coming from the direction \vec{k}' . The Bethe-Salpeter equation [equation (2.61)] was written in the frequency and space domain, as was done for the Dyson equation [equations (2.41) and (2.42)]. Writing it in the Fourier domain (in space) is easy and can be done in the same way (multiplication of the irreducible vertex with the Green's function) when using the matrix notation.

The wave vector \vec{k}' is linked to the source of the intensity, the sum over all \vec{k}' of $\phi_{\omega, \vec{k}\vec{k}'}$ gives the intensity going in the direction \vec{k} . The intensity in the medium is then:

$$\phi_{\omega, \vec{k}}(\Delta\omega, \vec{q}) = \sum_{\vec{k}'} \phi_{\omega, \vec{k}\vec{k}'}(\Delta\omega, \vec{q}) \quad (2.69)$$

2.5.2 Transport equations [14]

The intensity defined in equation (2.69) is the transported quantity measured during an experiment; transport equations remain to be discussed. By combining the Bethe-Salpeter

equation [equation (2.61)] in Fourier domain and the Green's function [equation (2.43)] obtained from the Dyson equation, a new equation for $\phi_{\omega, \vec{k}}$ can be obtained:

$$\begin{aligned} & \left(i\Delta\omega \frac{\omega}{c_0^2} - i\vec{k} \cdot \vec{q} + \Delta\Sigma_{\omega, \vec{k}}(\Delta\omega, \vec{q}) \right) \phi_{\omega, \vec{k}}(\Delta\omega, \vec{q}) \\ & = \Delta G_{\omega, \vec{k}}(\Delta\omega, \vec{q}) \left[1 + \sum_{\vec{k}'} U_{\omega, \vec{k}\vec{k}'}(\Delta\omega, \vec{q}) \phi_{\omega, \vec{k}'}(\Delta\omega, \vec{q}) \right]. \end{aligned} \quad (2.70)$$

In this equation, several different quantities have been introduced:

$$\Delta\Sigma_{\omega, \vec{k}}(\Delta\omega, \vec{q}) = \frac{1}{2i} \left[\Sigma \left(\omega + \frac{\Delta\omega}{2}, \vec{k} + \frac{\vec{q}}{2} \right) - \Sigma \left(\omega - \frac{\Delta\omega}{2}, \vec{k} - \frac{\vec{q}}{2} \right) \right], \quad (2.71)$$

$$\Delta G_{\omega, \vec{k}}(\Delta\omega, \vec{q}) = \frac{1}{2i} \left[G \left(\omega + \frac{\Delta\omega}{2}, \vec{k} + \frac{\vec{q}}{2} \right) - G \left(\omega - \frac{\Delta\omega}{2}, \vec{k} - \frac{\vec{q}}{2} \right) \right] \quad (2.72)$$

and $U_{\omega, \vec{k}\vec{k}'}(\Delta\omega, \vec{q})$, which is the Fourier transform of the irreducible vertex. It represents the part of the energy arriving from the direction \vec{k}' scattered in the direction \vec{k} by a scatterer. Equation (2.70) can be seen as a transport equation: the $i\Delta\omega$ term can be seen as the result of taking a time derivative, while the second term involving $i\vec{q}$ looks like a gradient (space-derivative). The term containing the self-energy is a loss term, *i.e.*, the energy scattered away from the direction \vec{k} . On the right-hand side, the first term is a source term and the term containing the irreducible vertex represents the gain of energy due to the wave scattered from all the directions \vec{k}' (using the sum over \vec{k}') to the direction \vec{k} . Finally, in time and space coordinates, we can write equation (2.70) as:

$$\left(\frac{\partial}{\partial t} + \vec{v} \cdot \vec{\nabla} + \text{losses}\right) I_{\vec{v}}(\vec{r}, t) = \text{source} + \text{scattering}. \quad (2.73)$$

Equation (2.73) has the same form as the transport equation of a particle of velocity \vec{v} .

In order to go further, more information is needed about the self-energy and the irreducible vertex. We have seen in the Born approximation (section 2.3.5) that the T-matrix can be expressed in terms of the scattering cross-section of the scatterer. In the context of the ladder approximation, in which only the uncrossed paths are kept [c.f. sketch b) in Figure 2.7], the self-energy can be expressed using the forward scattering of a single scatterer, and the density of scatterers n . The expression of the irreducible vertex follows the one of the self-energy. In the context of the ladder approximation:

$$\Sigma(\omega, \vec{k}) = n\tilde{T}(\omega, \vec{k}, \vec{k}) \quad (2.74)$$

and

$$U_{\omega, \vec{k}\vec{k}'}(\Delta\omega, \vec{q}) = n\tilde{T}(\omega, \vec{k}, \vec{k}')\tilde{T}^*(\omega, \vec{k}, \vec{k}'). \quad (2.75)$$

\tilde{T} has been defined in equation (2.38) and n is the density of scatterers. With these formulas, equation (2.73) can be written in a more physical way (using the link between scattering cross section, scattering mean free path, and T-matrix):

$$\left(\frac{1}{v_p} \frac{\partial}{\partial t} + \hat{u} \cdot \vec{\nabla}\right) I_{\hat{u}}(\vec{r}, t) = \frac{I_{\hat{u}}(\vec{r}, t)}{l_s} + n \int d\Omega_{\hat{u}'} \frac{d\sigma}{d\Omega_{\hat{u}'}}(\hat{u}' \rightarrow \hat{u}) I_{\hat{u}'}(\vec{r}, t) \quad (2.76)$$

The equation (2.76) is called the Equation of Radiative Transfer (ERT). \hat{u} is a unit vector representing the direction of propagation ($\hat{u} = \vec{k}/\|\vec{k}\|$), v_p is the phase velocity of the effective medium and $I_{\hat{u}}(\vec{r}, t)$ is the average local energy travelling in the direction \hat{u} . Here, we can explain each term of this equation. The left-hand side represents the temporal and spatial

variation of the intensity. The first term of the right-hand side is a loss term: the energy which is taken away from the propagation direction due to scattering. The characteristic decay length of the intensity is l_s , which is consistent with the decay length of the amplitude $2l_s$ [equation(2.49)]. The last term of the ERT represents the gain of energy from all the directions to the direction \hat{u} , this gain in energy depending on the differential scattering cross section which makes the link between the energy coming from one direction (\hat{u}') and the energy scattering to another direction (\hat{u}).

2.5.3 Diffusion approximation [13]

It is possible to retrieve a diffusion equation for local energy density $W(\vec{r}, t)$ starting from the ERT. First we need to define two new quantities, the local energy density and the local current density vector $\vec{J}(\vec{r}, t)$:

$$W(\vec{r}, t) = \frac{1}{v_p} \int_{4\pi} I_{\hat{u}}(\vec{r}, t) d\Omega_{\hat{u}}, \quad (2.77)$$

$$\vec{J}(\vec{r}, t) = \int_{4\pi} I_{\hat{u}}(\vec{r}, t) \hat{u} d\Omega_{\hat{u}}. \quad (2.78)$$

With this definition of the local current density, $\vec{J}(\vec{r}, t) \cdot \hat{u} dS$ is the flux of energy going through the surface dS with a normal vector \hat{u} .

After a great number of scattering events, the intensity $I_{\hat{u}}(\vec{r}, t)$ is going to be more and more isotropic. In the extreme case, if the distribution were completely isotropic, $I_{\hat{u}}(\vec{r}, t)$ would be independent of \hat{u} , and $\vec{J}(\vec{r}, t) = 0$. If we assume that the distribution is almost isotropic, the local

energy $I_{\hat{u}}(\vec{r}, t)$ can be written as the sum of the local density and the local current (the second term representing the difference from a perfect isotropic distribution):

$$I_{\hat{u}}(\vec{r}, t) = \frac{v_p}{4\pi} W(\vec{r}, t) + \frac{3}{4\pi} \vec{J}(\vec{r}, t) \cdot \hat{u} \quad (2.79)$$

The factors in front of $W(\vec{r}, t)$ and $\vec{J}(\vec{r}, t)$ in equation (2.79) come from their definition [equation (2.77) and (2.78)]. By inserting equation (2.79) into equation (2.76), then integrating the equation over all the solid angles, and adding a point source at $\vec{r} = 0$ and $t = 0$, equation (2.80) can be obtained. The ERT can also be integrated over all possible solid angles after it has been multiplied by \vec{u} . Equation (2.81) is the result of this operation.

$$\vec{\nabla} \cdot \vec{J}(\vec{r}, t) + \frac{\partial W(\vec{r}, t)}{\partial t} = \delta(\vec{r})\delta(t) \quad (2.80)$$

$$\vec{J}(\vec{r}, t) = -\frac{v_E l^*}{3} \vec{\nabla} W(\vec{r}, t) \quad (2.81)$$

Two new quantities have been introduced in equation (2.81): v_E the transport energy velocity and l^* the transport mean free path. In the general case, the transport velocity is different from the phase velocity or the group velocity, in particular in the case of media with resonances. This velocity is defined as the ratio of the current vector and the local energy density at a given frequency: $v_E = J(\omega)/W(\omega)$. In the case of a resonant scatterer, some energy can be “trapped” for a long time (dwell time) in the resonator which will modify the local energy density and slow down the transport. It explains why the transport energy velocity is different in this situation to the group velocity in the medium [2,14,15,16].

The transport mean free path is defined as $l^* = l_s / (1 - \langle \cos\theta \rangle)$. If $\langle \cos\theta \rangle$, the average cosine of the scattering angle, is zero, the scattering is isotropic; if it is close to 1, there is a lot of forward scattering. Unlike the scattering mean free path l_s , which has a geometrical definition (average distance between two scattering events), the transport mean free path cannot be directly associated with the geometry of the medium; it represents the distance for the wave direction to become randomized.

By combining equations (2.80) and (2.81), we can obtain a new equation for the local energy density (proportional to the intensity) $W(\vec{r}, t)$:

$$\frac{\partial W(\vec{r}, t)}{\partial t} - \frac{v_E l^*}{3} \vec{\nabla}^2 W(\vec{r}, t) = \delta(\vec{r}) \delta(t), \quad (2.82)$$

which is the diffusion equation. We have now shown that the transport of the wave intensity in a multiple scattering medium can be described by diffusive behaviour. In particular, this result will be used to explain some of the results obtained in the sample made of aluminum beads in a liquid, in chapter 0 of this thesis. The diffusion coefficient is defined as:

$$D = \frac{v_E l^*}{3}. \quad (2.83)$$

The number 3 appearing in the definition of the diffusion coefficient comes from the dimension of the medium, which is considered here to be three dimensional. The solution of equation (2.82) is well known in free space [17]:

$$W(\vec{r}, t) = \frac{1}{(4\pi Dt)^{3/2}} \exp\left(-\frac{r^2}{4Dt}\right). \quad (2.84)$$

The diffusion approximation has been used previously to explain experimental data, for example in ultrasonic experiments reported by Page et al. [1], which were performed in samples made of glass beads in water. Equation (2.84) gives the energy density in free-space, to which boundary conditions have to be added to allow comparison with experimental data. These conditions will be explained in the chapter 4, along with an explanation of the model that has been developed to describe the transport of the energy in the sample.

2.6 Renormalized diffusion and Anderson Localization

In order to obtain the ERT [equation (2.76)] and the diffusion equation [equation (2.84)], the ladder approximation had to be made (section 2.5.2), meaning that each scattering event was assumed to be independent. When the disorder is “too strong”, this approximation does not hold anymore and the diffusion approximation is not valid. A “too strong” disorder will be defined later in this chapter [equation (2.88)]. When the disorder is getting too strong, the wave transport inside the sample slows down, leading to sub-diffusive transport or even localization. In the case of sub-diffusion, the average transport of the energy is slower than in the case of diffusive transport. When Anderson Localisation is observed the energy transport will stop and stay in a volume characterized by the localisation length ξ . The concept of Anderson localization was first proposed in the case of spin diffusion by Anderson [10], and has been extended since to classical waves [18,19]. In the localized regime, the interference between different paths has to be taken into account [sketch c) in Figure 2.7], unlike what has been done in section 2.5. The scaling theory of localization [20,21] shows that as soon as some disorder exists localization will occur in a 1D or a 2D sample, but in the case of a 3D sample, there is a transition between the

diffusive regime and localization [22]. In the case of acoustic waves this transition could be seen, for example, as a function of frequency.

2.6.1 Renormalized diffusion and self-consistent theory

In 1980, a diagrammatic theory of localization was proposed by Vollhardt and Wölfle [23,24,25], and was called the “self-consistent theory” (SCT). Soon thereafter [26], this approach was also shown to lead to the same scaling relations proposed in the scaling theory of localization [22]. This new self-consistent formulation took into account the most-crossed scattering diagrams that account for interferences between the pair of Green’s functions constituting the intensity. The localization of waves inside a sample is associated with a renormalization of the diffusion coefficient D , and in theory, for an infinite sample, this coefficient goes to zero. In the case of a finite sample, as the waves can leak out of the sample, D cannot go to zero and a new development of the SCT, taking into account boundary conditions, was proposed [27,28,29]. The SCT predicted that D is reduced by interference effects, such as can occur by the presence of “loop” paths (Figure 2.8)

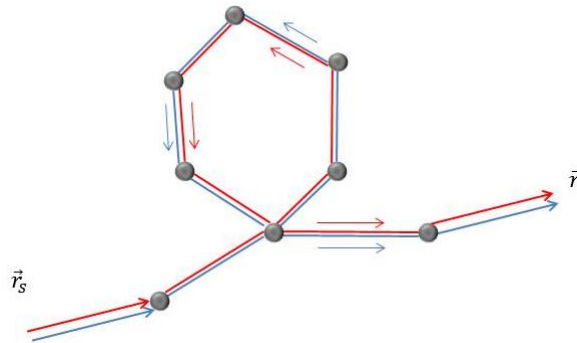


Figure 2.8: Loop path participating in the reduction of the diffusion coefficient in the Self-Consistent theory

As we have seen in the Bethe-Salpeter equation [equation (2.61)], the Intensity Green's function depends on the irreducible vertex \mathbf{U} . In the case of the ladder approximation, the transport was described as a diffusive process, characterized by the Boltzmann diffusion coefficient D_B . To go beyond the ladder approximation, we need to consider other types of paths in the vertex \mathbf{U} . The effect of these new paths is a reduction of the diffusion coefficient D , which will modify the intensity Green's function. These two quantities have to be calculated simultaneously, hence the name "self-consistent" theory. An estimation of the effect of the renormalisation of D can be done in terms of a correction δD to the Boltzmann diffusion coefficient D_B defined by equation (2.83) [8]:

$$D = D_B - \delta D, \quad (2.85)$$

where

$$\delta D \cong \frac{1}{\pi} \frac{v_E}{k^{d-1}} \begin{cases} L - l & 1\text{D} \\ \ln(L/l) & 2\text{D} \\ 1/l - 1/L & 3\text{D} \end{cases} \quad (2.86)$$

In equation (2.86), it has been assumed that the scattering is isotropic ($l = l^* = l_s$), the characteristic length of the sample is L , and d is the system dimension. These equations show in 1D and 2D that the correction δD diverges as $L \rightarrow \infty$, implying that localization will always occur if the sample is big enough. In 1D and 2D, the critical system size at which localization occurs can be estimated from the condition for localization: $D = 0$ (the absence of diffusion). This critical system size is the localization length, ξ . Setting $D = 0$ and $L = \xi$ in equation (2.86) and using the definition of D_B , knowing that the 3 in equation (2.83) comes from the system dimension d , enables the following estimates for the localization length to be obtained:

$$\xi = \begin{cases} (1 + \pi)l & 1\text{D} \\ l \exp(\pi kl/2) & 2\text{D} \\ (1/l - \pi k^2 l/3)^{-1} & 3\text{D} \end{cases} \quad (2.87)$$

For systems of dimension 1 or 2, ξ is always defined (always positive) but in the case of dimension 3 a specific relation has to exist between k and l in order for localization to occur. From equation (2.87), ξ can only be positive and finite when the condition

$$kl < \sqrt{\frac{\pi}{3}} \approx 1. \quad (2.88)$$

is satisfied. This is the Ioffe-Regel criterion [30]. The product kl is a measure of the disorder in a medium. If this product is smaller than one, the disorder is “strong enough” for localization to happen.

2.6.2 Position-dependent diffusion coefficient

The SCT was initially developed for either infinite media or finite samples with perfectly reflecting boundaries. However, for the case a finite medium with open boundaries, which is the usual case for classical waves, the waves can leak out of the sample and the renormalisation of the diffusion coefficient is no longer uniform. In the bulk of the sample, the renormalisation will be stronger than on the edge. The renormalisation of D is due to the “probability” of a given path returning to the same spot. This “return probability” is higher in the bulk of a sample than on the edge; indeed, on the edge of a sample, a “loop” can be cut by the surface, reducing the return probability [29,31].

The diffusion equation (2.82) can be rewritten to account for a position and frequency dependent diffusion coefficient:

$$[-i\Omega - \vec{\nabla} \cdot D(\vec{r}, \Omega) \vec{\nabla}] C(\vec{r}, \vec{r}', \Omega) = \delta(\vec{r} - \vec{r}'). \quad (2.89)$$

Equation (2.89) is written in the Fourier domain to simplify the convolution product $[\vec{\nabla} \cdot D(\vec{r}, t) \vec{\nabla} \otimes] C(\vec{r}, \vec{r}', t)$ that occurs in the time domain. $C(\vec{r}, \vec{r}', \Omega)$ is the intensity Green's function for a source at a position \vec{r}' . $D(\vec{r}, \Omega)$ is determined by the self-consistent condition:

$$\frac{1}{D(\vec{r}, \Omega)} = \frac{1}{D_B} + \frac{12\pi}{k^2 l} C(\vec{r}, \vec{r}, \Omega). \quad (2.90)$$

In this last equation $C(\vec{r}, \vec{r}, \Omega)$ (with two identical position variables) represents the return probability: the higher it is, the more renormalized is the diffusion coefficient. With the two last equations, we also need to define boundary conditions. This will be done in the chapter 4 at the same time as a more detailed explanation on how to solve the SCT is presented. The SCT, including the boundary conditions, with a position-dependent diffusion coefficient has been used successfully to interpret and to fit the experimental results in a sample made of brazed aluminum beads [3].

Chapter 3

Resonances of aluminum beads

3.1 Introduction

Everything that has been discussed until now supposes that waves can actually travel through the medium. It is not necessary the case for all samples at all frequencies. For a wave to couple from the exterior medium (usually water) to the sample and for the waves to exist inside the medium, the density of states needs to be different from zero at the given working frequency. For acoustic waves, the density of states is a measurement of the number of vibrational modes (phonons) per frequency per unit volume in a given sample. Many of the samples studied in this thesis are made of aluminum beads, so we have to consider the resonances (modes) of a single bead, as they play an important role in influencing the transport through a multi-bead sample by enabling a mechanism for ultrasonic transport through a network of touching beads [3,32,33].

Beads (as all finite size objects) exhibit mechanical resonant frequencies depending on their size and shape. These frequencies characterize the natural vibration of a given object. The resonant frequencies of an aluminum sphere can be determined quite easily due to the high symmetry of the object and the isotropy of the material: the values of the natural frequency depend only on the radius of the sphere and on the two velocities of aluminum (velocity of compressional waves and velocity of shear waves). The natural frequencies of a given sphere are important as, in a sample made of several beads, these frequencies give rise to the pass bands (frequencies for which the density of states in the sample is different than zero), and therefore determine the transmission profile of a given sample [32].

In this chapter, I present analytic calculations leading to the determination of the resonance frequencies of an aluminum bead. These theoretical predictions are compared with experimental results in order to determine the mechanical properties of the high purity aluminum from which

the beads were made. This information is needed to accurately model the experimental data in chapters 4 and 5. Simulations were also performed to be able to determine a complete list of resonance frequencies in the relevant frequency band, including some resonances that could not be excited with the experiment described in this chapter. These characteristic frequencies help in understanding the frequency dependence of the density of states of samples made of several of these aluminum beads. Another set of simulations is described to observe the leakage of energy from a bead to a fluid in which the bead is immersed. These simulations enabled a characteristic dwell time to be obtained, which helps with understanding the long-time behaviour in the experiment described in chapter 4. Overall this chapter gives important information about the acoustic properties of aluminum beads.

3.2 Natural frequencies of a sphere [34]

The natural frequencies of an object are found by solving the wave equation inside this object and by applying the right boundary conditions. In this situation, the boundary condition is that there is no stress on the surface, so the natural frequencies are obtained when the object is resonating in vacuum. If a liquid were surrounding the object, the resonant frequency might be slightly shifted due to the change in the boundary condition. The liquid applies a load on the object.

To solve this problem, the velocity \vec{v} of displacement of the particle (particle velocity) due to an elastic wave is needed and can be written in terms of two potentials. The relationship between \vec{v} and these potentials is

$$\vec{v} = \vec{\nabla}\phi + \vec{\nabla} \times \vec{\psi}. \quad (3.1)$$

In this equation, ϕ is a scalar potential, which leads to the compressional wave (velocity v_l) in the object, and $\vec{\Psi}$ is vector potential leading to the shear waves (velocity v_s) inside the object. A wave equation can be defined for each of these potentials:

$$\vec{\nabla}^2 \phi + \left(\frac{\omega}{v_l}\right)^2 \phi = 0 \quad (3.2)$$

and

$$\vec{\nabla}^2 \vec{\Psi} + \left(\frac{\omega}{v_s}\right)^2 \vec{\Psi} = \vec{0}. \quad (3.3)$$

In the case of a sphere, equations (3.2) and (3.3) can be solved using separation of variables.

The solutions are:

$$\phi_{mn}(r, \theta, \varphi) = z_n \left(\frac{\omega r}{v_l}\right) P_n^{|m|}(\cos\theta) e^{im\varphi} \quad (3.4)$$

and

$$\Psi_{mn}(r, \theta, \varphi) = z_n \left(\frac{\omega r}{v_s}\right) P_n^{|m|}(\cos\theta) e^{im\varphi}, \quad (3.5)$$

with:

$$\vec{v}_{mn} = \vec{\nabla} \times \vec{r} \Psi_{mn}. \quad (3.6)$$

In the equations (3.4) and (3.5), z_n represents the spherical Bessel function of order n , of the first or second kind. $P_n^{|m|}$ is the associated Legendre polynomial, m and n are integers and $-n \leq m \leq n$: there are $2n + 1$ values of m for a given value of n . The different values of m do not lead to new resonances but correspond to the degree of degeneracy of a given resonance. The solution given by equation (3.6) is such as $\vec{\nabla} \cdot \vec{\Psi} = 0$, a condition that is identical to the Coulomb gauge in electromagnetism.

As stated above, the natural frequencies of the sphere are found when no radial stress is applied to the surface of the sphere resonating in vacuum. This boundary condition can be written:

$$\mathbf{T} \cdot \vec{r} = \vec{0}. \quad (3.7)$$

where \mathbf{T} is the stress tensor, which is symmetric: and can be written in the spherical coordinate as

$$\mathbf{T} = \begin{bmatrix} T_{rr} & T_{r\theta} & T_{r\varphi} \\ T_{r\theta} & T_{\theta\theta} & T_{\theta\varphi} \\ T_{r\varphi} & T_{\theta\varphi} & T_{\varphi\varphi} \end{bmatrix}. \quad (3.8)$$

With the definition of the stress tensor, and because there is only one non-zero component in the vector $\mathbf{T} \cdot \vec{r}$, the condition represented by equation (3.7) can be reduced to :

$$T_{rr} + T_{r\theta} + T_{r\varphi} = 0. \quad (3.9)$$

The last equation can be rewritten as a function of the displacement inside the sphere, or for a harmonic regime, as a function of the particle velocity. The expressions for each term of equation (3.9) are:

$$T_{rr} = \lambda \left(\frac{\partial u_r}{\partial r} + 2 \frac{u_r}{r} + \frac{1}{r} \frac{\partial u_\theta}{\partial \theta} + \frac{\cot(\theta)}{r} u_\theta + \frac{1}{r \sin(\theta)} \frac{\partial u_\varphi}{\partial \varphi} \right) + 2\mu \frac{\partial u_r}{\partial r}, \quad (3.10)$$

$$T_{r\theta} = \mu \left(\frac{1}{r} \frac{\partial u_r}{\partial \theta} + \frac{\partial u_\theta}{\partial r} - \frac{u_\theta}{r} \right) \quad (3.11)$$

and

$$T_{r\varphi} = \mu \left(\frac{1}{r \sin(\theta)} \frac{\partial u_r}{\partial \varphi} + \frac{\partial u_\varphi}{\partial r} - \frac{u_\varphi}{r} \right). \quad (3.12)$$

λ and μ are the Lamé parameters, and the displacement vector is defined as

$$\vec{u} = u_r \hat{r} + u_\theta \hat{\theta} + u_\varphi \hat{\phi}. \quad (3.13)$$

By solving equations (3.2) and (3.3) using the conditions defined with equations (3.4) to (3.12), the natural resonant frequencies of a sphere can be obtained. In the following sections, three different modes are analysed in detail and their frequencies calculated.

3.2.1 First “breathing” mode

A breathing mode is obtained when only the compressional part of the wave acts on the bead.

In this case, equation (3.1) becomes:

$$\vec{v} = \vec{\nabla}\phi. \quad (3.14)$$

To obtain the first “breathing” mode, n and m are fixed at zero, so equation (3.4) becomes:

$$\phi_{00}(r, \theta, \varphi) = j_0\left(\frac{\omega r}{v_l}\right). \quad (3.15)$$

j_0 represents the spherical Bessel function of the first kind ($P_0^0 = 1$). In this situation, the Bessel function of the second kind cannot be used as the field needs to be finite in the centre of the bead⁴. As the displacement is purely radial, the only component is along \hat{r} and there is only a dependence on r . Then the boundary condition becomes:

⁴ Bessel functions of the second kind diverge at 0.

$$\begin{aligned}
& (\lambda + 2\mu) \frac{\partial u_r}{\partial r} + 2\lambda \frac{u_r}{r} \\
&= \frac{1}{i\omega} \left[(\lambda + 2\mu) \frac{\partial v_r}{\partial r} + 2\lambda \frac{v_r}{r} \right] \\
&= \frac{1}{i\omega} \left[(\lambda + 2\mu) \frac{\partial^2}{\partial r^2} j_0 \left(\frac{\omega r}{v_l} \right) + \frac{2\lambda}{r} \frac{\partial}{\partial r} j_0 \left(\frac{\omega r}{v_l} \right) \right] \\
&= 0.
\end{aligned} \tag{3.16}$$

By substituting the expression for the Bessel function ($j_0(z) = \sin(z)/z$) in equation (3.16), the boundary condition becomes:

$$\tan \left(\frac{\omega a}{v_l} \right) = \frac{\omega a / v_l}{1 - \frac{(\lambda + 2\mu)}{4\mu} \left(\frac{\omega a}{v_l} \right)^2}, \tag{3.17}$$

with a being the radius of the sphere. The roots of equation (3.17) give the values of the resonant frequencies, but the values of the Lamé parameters are needed to calculate the resonance frequencies.

3.2.2 Pure shear modes

The simplest pure shear mode is obtained for $n = 1$ and $m = 0$ [the velocity is equal to zero for $n = 0$ due to the definition of Ψ_{mn} in equation (3.5) and the condition given by equation (3.6)]. In this situation, the velocity is:

$$\vec{v}_{01} = \sin(\theta) j_1 \left(\frac{\omega r}{v_s} \right) \hat{\phi}. \tag{3.18}$$

By using the expression for the Bessel function in equation (3.18) [$j_1(z) = \sin(z)/z^2 - \cos(z)/z$] and applying the boundary condition [equation (3.9)], the resonant frequencies can be found from:

$$\tan\left(\frac{\omega a}{v_s}\right) = \frac{\omega a/v_s}{1 - \frac{1}{3}\left(\frac{\omega a}{v_s}\right)^2}. \quad (3.19)$$

The first root gives

$$\frac{\omega a}{v_s} = 5.76. \quad (3.20)$$

The value of the shear velocity of the aluminum is necessary to calculate the value of the resonant frequency.

The lowest resonant frequency of the sphere is another shear mode, it is obtained for $n = 2$ and $m = 0$. The frequency relationship is a little more complicated to derive due to the expression of the Bessel function $j_2(z)$. The frequency of this resonance is defined by:

$$\frac{\omega a}{v_s} = 2.50. \quad (3.21)$$

3.2.3 Mixed mode

A third type of mode can be defined for a bead: the mixed modes. These modes use both the scalar potential ϕ and the vector potential $\vec{\Psi}$. The frequency relationship is much more complicated to obtain. The frequency of the first of these modes is given by:

$$\frac{\omega a}{v_s} = 2.64 \quad (3.22)$$

for aluminum, which has a Poisson's ratio [$\nu = \lambda/2(\lambda + \mu)$] of 0.345.

3.3 Experimental determination of the resonant frequencies

I performed an experiment to measure the resonant frequency values of the aluminum beads that were used for the fabrication of the samples described in chapters 0 and 0 of this thesis. By comparison with the theoretical predictions, these resonant frequencies of single beads were also used to determine the values of the mechanical properties of the aluminum.

3.3.1 Experimental setup

This experiment was performed on a single bead squeezed between two transducers in a vacuum chamber (Figure 3.1). One of the two transducers emitted a short pulse while the second transducer received the signal going through the beads. The emitted pulse, called "Gauss2", is the multiplication of a cosine wave by a Gaussian envelope so that the resulting pulse contains two main oscillations (Figure 3.2). The experiment had to be performed in a vacuum chamber to suppress all possibilities for a signal to travel between the two transducers without going through the bead. During the experiment, the pressure inside the vacuum chamber was around 20 Pa. The bead used in this experiment has a radius of 2.065 ± 0.005 mm and a density of $\rho = 2710 \pm 20$ kg/m³.

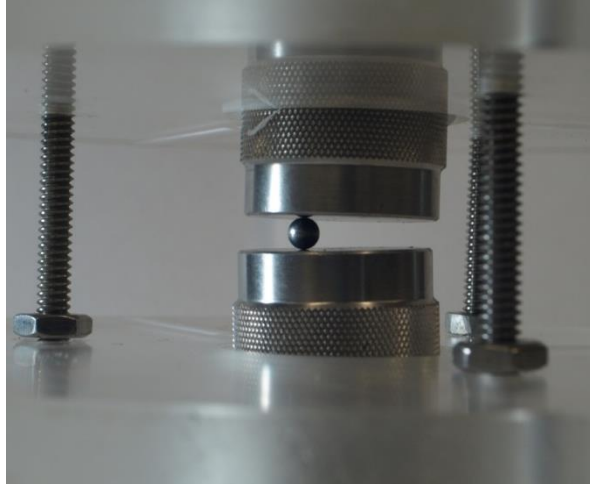


Figure 3.1: Picture of the experimental setup. A bead was placed between two transducers.

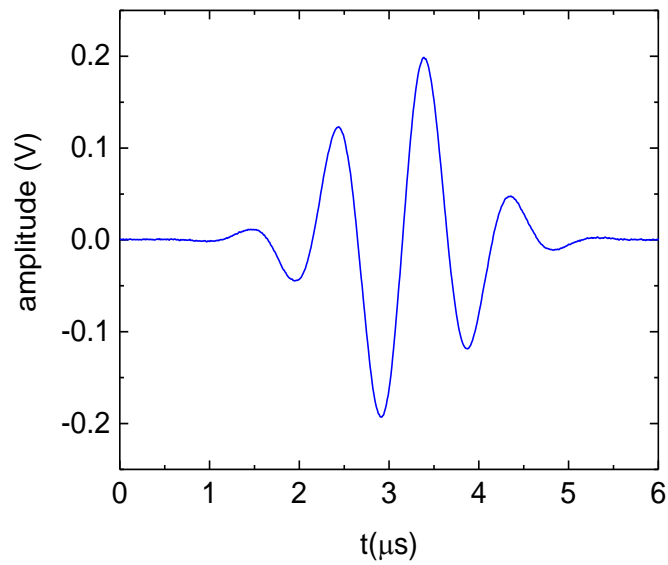


Figure 3.2: Pulse "Gauss2" with a central frequency of 1 MHz

The recorded signal lasted for several hundreds of microseconds (Figure 3.3) and its frequency content contained the resonant frequencies of the bead, because the long-time reverberation inside the bead happened only for these frequencies. It was possible to observe

signals at such long times because there were only two contact points between the bead and the transducers, so there was no efficient way for the waves to couple otherwise to an outside medium.

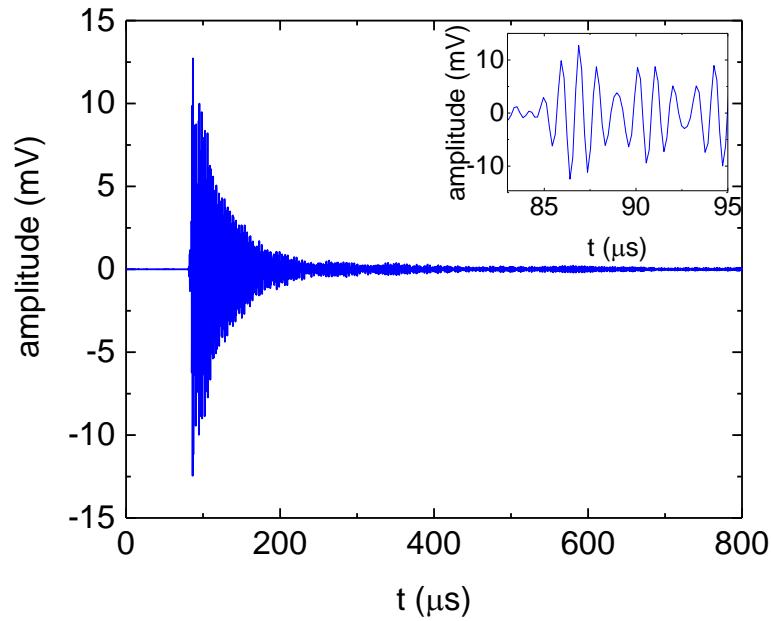


Figure 3.3: Recorded signal through a single bead at 1 MHz. The inset is zoomed in to show the phase variation of the signal.

3.3.2 Analysis and results

The resonant frequencies of the beads were determined from the Fourier transform of the received signal. An analysis similar to the one performed by Kurt Hildebrand in his M.Sc. thesis [35] or by Eric Lee in his Ph.D. thesis [32] was done. In order to improve the frequency resolution of the peaks in the Fourier transform, the time signal was multiplied by a Blackman-Harris window. The peaks visible on the Fourier transform are the resonant frequencies of the

bead (Figure 3.4). The two transducers were longitudinal transducers, so the shear modes were not excited. Therefore the only visible modes are expected to be the breathing and the mixed modes.

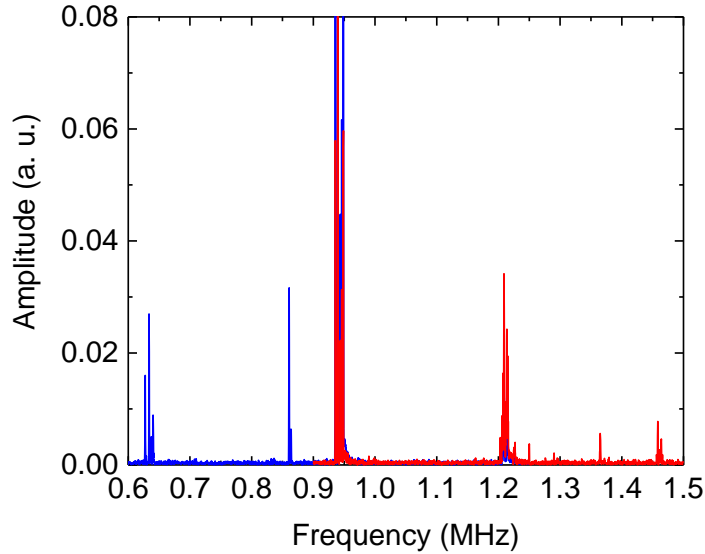


Figure 3.4: Fourier transform of a signal going through a single bead. Two acquisitions at two different frequencies have been done to cover a larger frequency band (Blue: 1 MHz, Red: 1.3 MHz).

The values of the resonant frequencies of the bead can be determined from Figure 3.4. Several of these peaks display multiple peaks, some of the degeneracy having been lifted. This can either be due to the bead which might not be perfectly spherical, or to the transducers that might deform the bead slightly. The frequencies are:

Frequency (MHz)	# of peaks
0.634 ± 0.006	4
0.860 ± 0.003	2
0.942 ± 0.007	6
1.210 ± 0.007	5
1.365 ± 0.001	1
1.460 ± 0.005	5

Table 3.1: Experimental values of the resonant frequencies (average) of a single bead

The experimental values of the frequencies and the theoretical relationships for the resonant frequencies derived in section 3.2 can be used to determine the mechanical properties of the aluminum. The lowest frequency that was measured experimentally is the first mixed mode, so this frequency has to obey equation (3.22). With a value of 0.634 MHz, the shear velocity is 3.12 ± 0.03 mm/ μ s. Since the second Lamé parameter μ depends only on the shear velocity and the density, its value can be calculated with:

$$v_s = \sqrt{\frac{\mu}{\rho}}. \quad (3.23)$$

The value for the second Lamé parameter is $\mu = 26.3 \pm 0.5$ GPa.

The second useful frequency is the first breathing mode allowing the determination of the longitudinal velocity of the aluminum. The value of this frequency is 1.365 MHz, leading to a value of the velocity of 6.40 ± 0.05 mm/ μ s, using equation (3.17). The first Lamé parameter is obtained from:

$$v_l = \sqrt{\frac{\lambda + 2\mu}{\rho}}. \quad (3.24)$$

and gives $\lambda = 58 \pm 1$ GPa.

The theoretical expression for the resonance frequencies and the experimental measurements allow quite accurate calculations to be made of the mechanical properties of the aluminum alloy used in the beads. These beads are the main constituent of the different samples described in chapters 0 and 0 of this thesis.

3.4 Simulation of the resonant frequency

The commercial software Comsol⁵ was used to simulate the resonances of a bead and hence to determine the resonant frequencies and visualize the associated deformations, leading to additional information on the resonances and enabling the mechanical parameters determined in the previous section to be confirmed. Comsol is a finite-element modelling software used to simulate many types of physics problems. The elastic waves can be simulated using the “Solid-Mechanics” module. The mode “Eigenfrequency” of Comsol is made to calculate the natural frequencies of an object. This simulation is a way to verify that the frequencies that have been chosen to obtain the mechanical properties are the right frequencies (the first mixed mode and the first breathing mode).

To perform the simulation, the geometry of the object was defined (sphere) as well as the mechanical properties of the material. In this module three properties are needed, the density ρ , the Young’s modulus E and Poisson’s ratio ν . Young’s modulus and Poisson’s ratio can be calculated from the Lamé parameters or from the two velocities of sound in aluminum [36]. The eigenfrequencies of an object depend on the boundary conditions, which have to be defined as a free boundary in order to obtain the natural frequencies of the object. Thus, in these simulations, there was no load on the surface of the bead. The natural frequencies of an aluminum bead with a radius of 2.065 mm are:

⁵ www.comsol.com

Frequency (MHz)	Degeneracy	Type
0.601	5	Shear
0.637	5	Mixed
0.869	3	Mixed
0.928	7	Shear
0.950	7	Mixed
1.219	9	Mixed
1.223	9	Shear
1.231	5	Mixed
1.365	1	Breathing
1.384	3	Shear
1.471	11	Mixed

Table 3.2: Resonant frequencies obtained from Comsol with their degeneracy and the type of resonances.

The Comsol results match well the theoretical and experimental values obtained in the previous sections. The two frequencies used to obtain the mechanical properties are recovered as well as the two shear modes described by equation (3.20) ($f = 1.384$ MHz) and equation (3.21) ($f = 0.601$ MHz).

Comsol can also be used to simulate the resonant frequencies of a bead surrounded by a liquid. For the results reported in chapter 4, the aluminum beads are surrounded by the liquid hexamethyldisiloxane, and it is relevant for interpreting these results to see if surrounding a bead by this liquid shifts significantly the resonant frequencies. In order to perform this different simulation, a sphere of liquid was added around the bead (the radius of this new sphere was 5 mm) to simulate the load of the liquid on the bead. For the sake of the simulation, attenuation was added to the liquid so that edge effects on the outside of the liquid layer were negligible. This simulation shows that the surrounding liquid has almost no effect on the resonant frequencies, which are very similar to those of the bare beads (see Table 3.3 compared with Table 3.2). The main difference between a bead resonating in air or in a liquid is the amplitude of the displacements due to the resonances.

Frequency (MHz)	Degeneracy
0.601	5
0.637	5
0.868	3
0.929	7
0.951	7
1.220	9
1.225	9
1.230	5
1.347	1
1.386	3
1.473	11

Table 3.3: Resonant frequencies, with their degeneracy, of a bead surrounded by hexamethyldisiloxane (see section 4.2.3) obtained from Comsol.

With Comsol, it is also possible to display the displacement field patterns for these modes. Figure 3.5 to Figure 3.8 are the representation of the four modes discussed in the section 3.2. The scales on the different figures are in arbitrary displacement units, but the units are the same for all these figures so that the scales can be reliably compared.

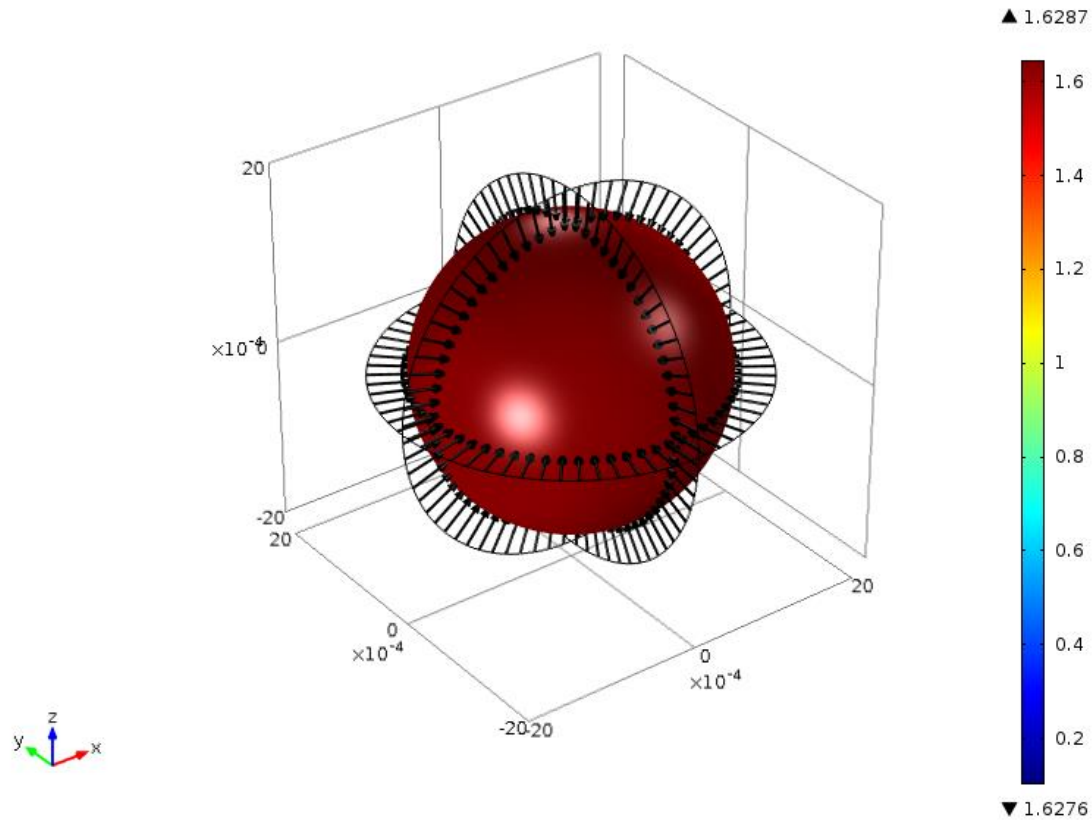


Figure 3.5: Simulation of the first breathing mode obtained with Comsol at 1.37 MHz. The color of the sphere represents the amplitude of the displacement and the arrows indicate the direction. For this mode, the displacement is purely radial.

The picture in Figure 3.5 shows the deformation of the beads for the breathing mode. The deformation is purely radial, so that the sphere simply gets bigger or smaller, depending on the time at which the displacement is recorded.

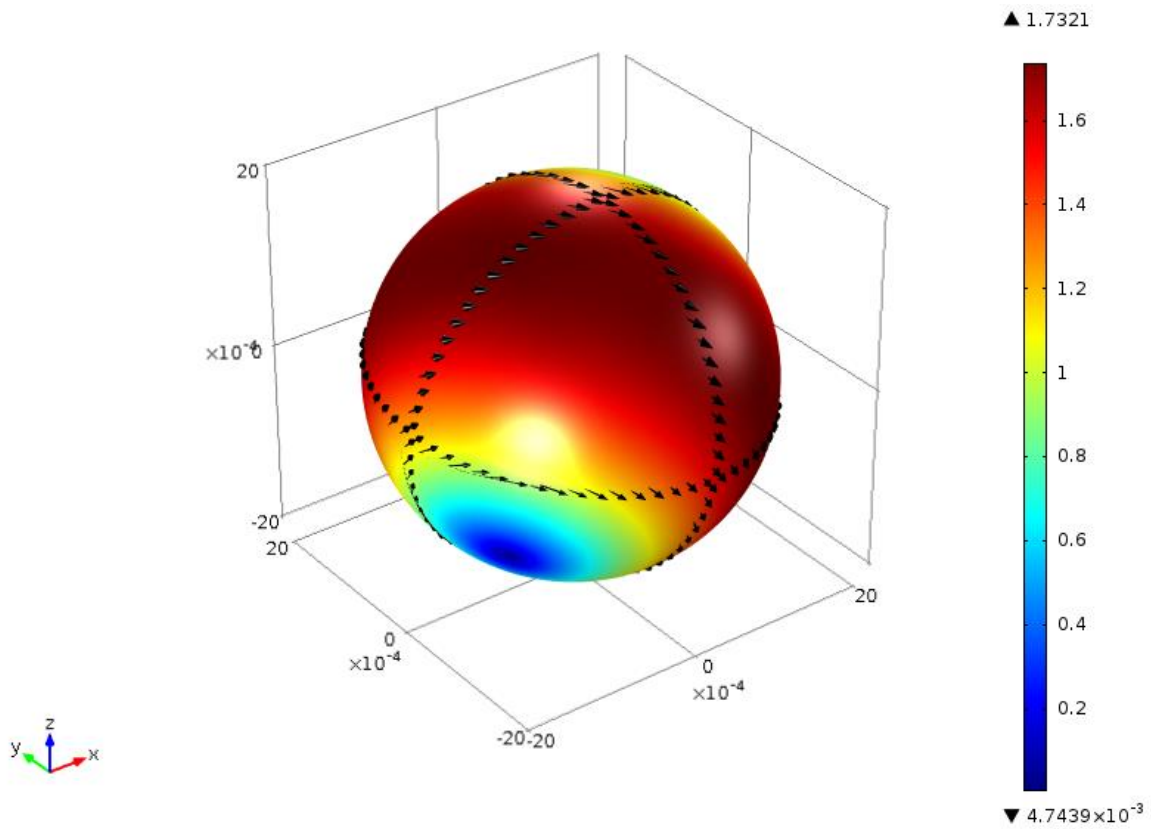


Figure 3.6: Simulation of the $n=1$ torsional mode obtained with Comsol at 1.38 MHz. The color of the sphere represents the amplitude of the displacement and the arrows indicate the direction. For this mode, the displacement is along the surface of the sphere.

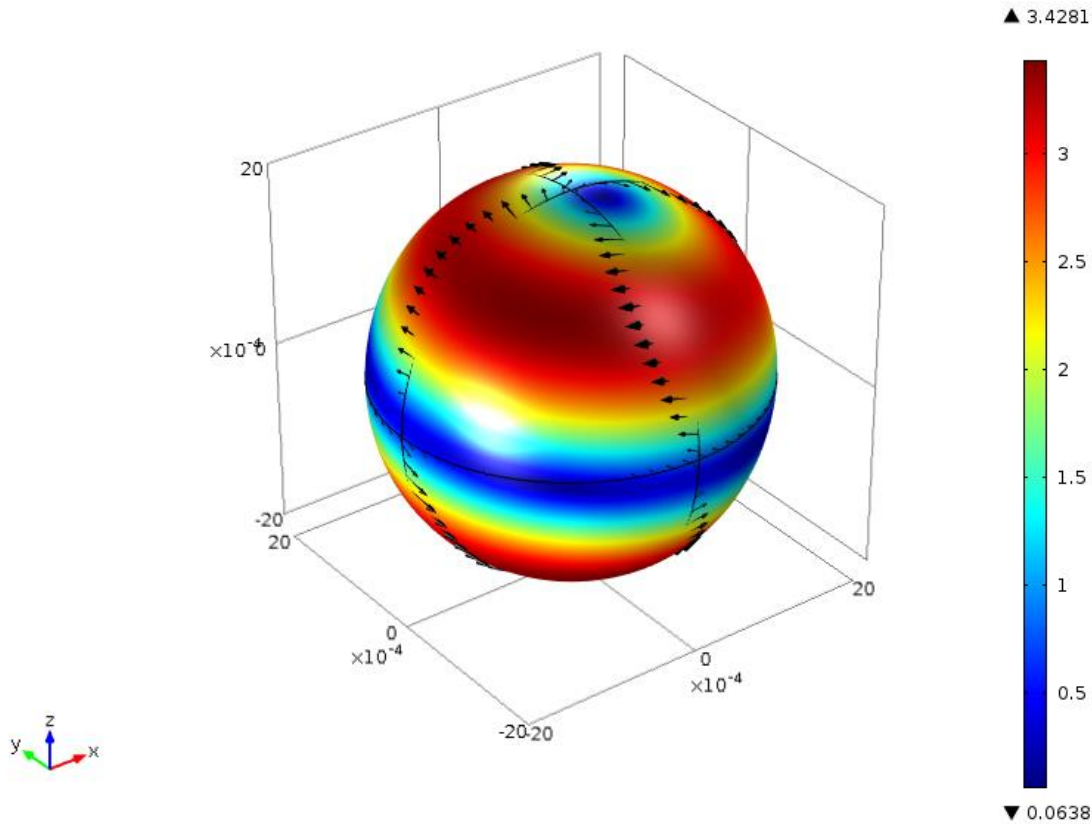


Figure 3.7: Simulation of the $n=2$ torsional mode obtained with Comsol at 0.60 MHz. This is the lowest resonant frequency for an aluminum bead. The color of the sphere represents the amplitude of the displacement and the arrows indicate the direction. For this mode the displacement is along the surface of the sphere.

Figure 3.6 and Figure 3.7 show two torsional modes that cannot be excited with compressional transducers. The displacement field is entirely along the surface of the sphere, and there is no change in volume. The number of nodes, *i.e.*, the number of bands along the surface of the beads for which the displacement is null, depends on the index n of the mode.

Figure 3.8 represents the lowest frequency mixed mode. The bead is deformed along two axes; there is an elongation along one of the axes and a compression along the second axis. The arrows representing the total displacement are not in the plane of the surface of the beads as in Figure 3.6 and Figure 3.7, and not all of them are pointing toward the centre of the sphere as in

Figure 3.5; consequently it is necessary to take into account both the shear and the compressional waves to describe this mode, which is why it is called a mixed mode.

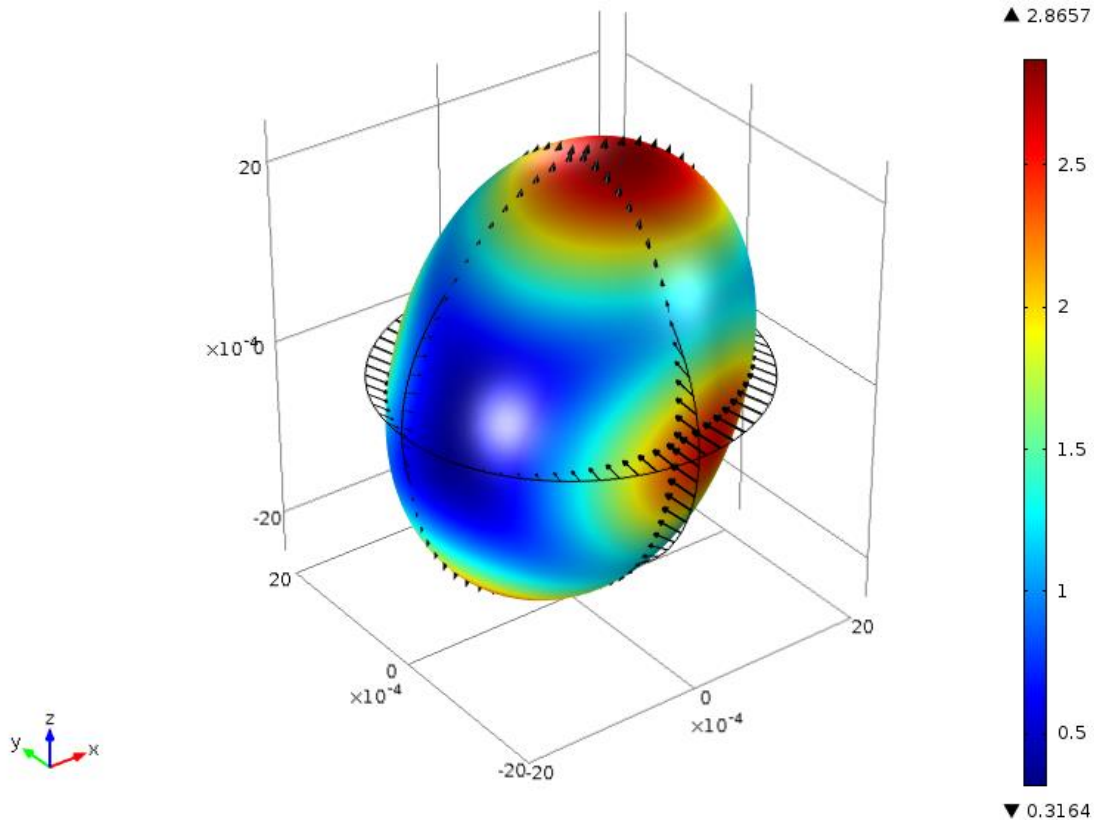


Figure 3.8: Simulation of the lowest frequency mixed mode obtained with Comsol at 0.64 MHz. The color of the sphere represents the amplitude of the displacement and the arrows indicate the direction.

3.5 Dwell time of aluminum beads

One of the consequences of the presence of sharp resonances in the beads is the long dwell time of ultrasound in the aluminum beads: energy entering the beads takes a long time to leave the beads. Simulation of an immobile 4-mm-diameter aluminum bead in a liquid (silicone oil of low viscosity) being excited by a short acoustic pulse was performed using the simulation

software Simsonic⁶ [37]. Simsonic uses the Finite-Difference Time-Domain (FDTD) technique to model the wave equation. The emitted signal was short (around 1 μs , see Figure 3.9) but the simulation was run for thirty times longer in order to evaluate the decay⁷ of the energy inside the bead.

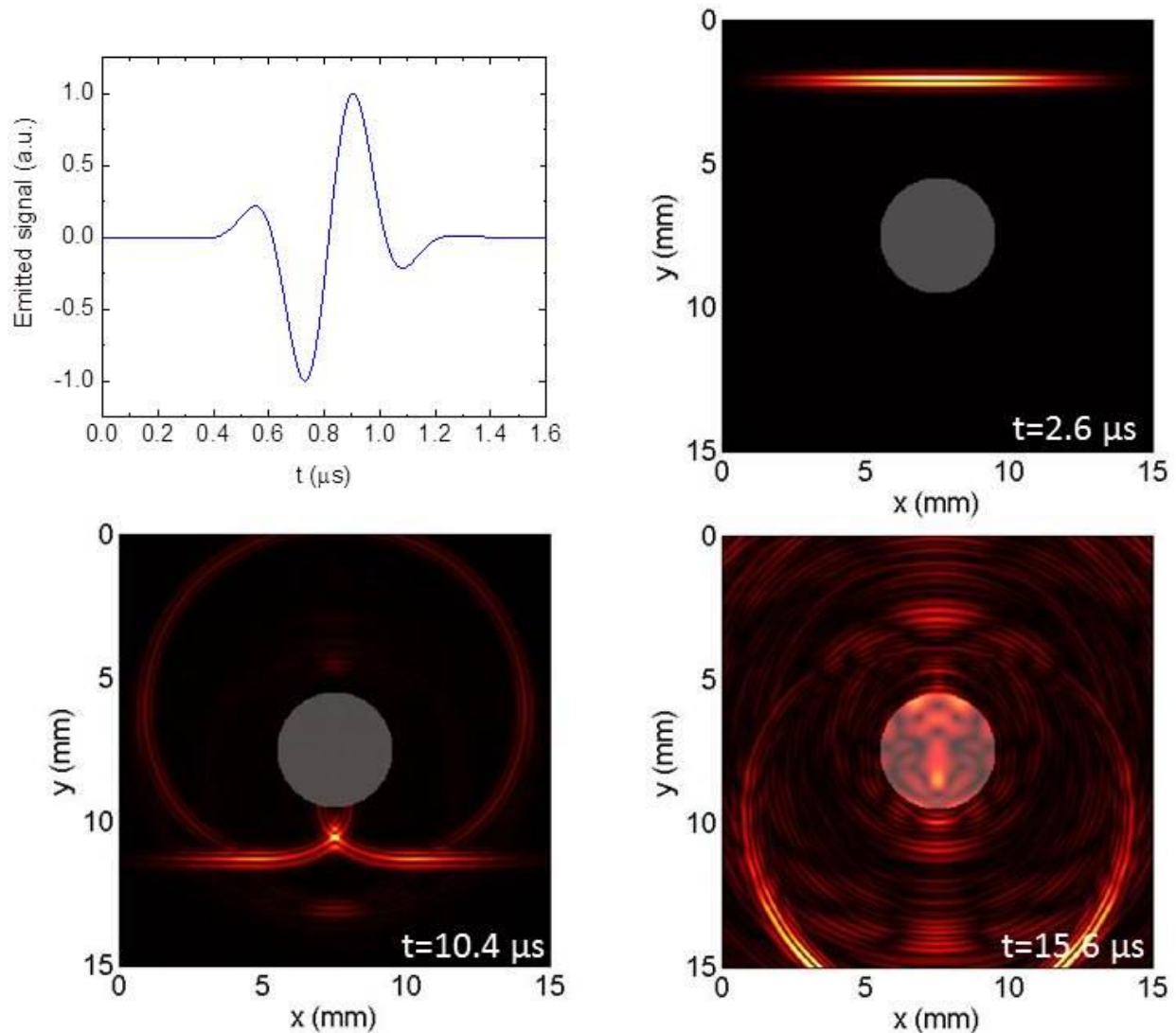


Figure 3.9: Top Left: Normalized emitted signal in the liquid. Other three pictures: amplitude of the particle velocity at three different times. The color scale is adjusted for each image. Top right: $t = 2.6 \mu\text{s}$, $max = 20.2$, bottom left: $t = 10.4 \mu\text{s}$, $max = 23.0$ and bottom right: $t = 15.6 \mu\text{s}$, $max = 0.9$.

⁶ www.simsonic.fr

⁷ Simsonic does not take into account any absorption, the decay is purely due to the leakage of energy to the outside medium.

In Figure 3.9, the amplitude of the particle velocity field at three different times during the simulation is displayed. The first case ($t = 2.6 \mu\text{s}$) corresponds to a time before the wave reaches the bead; it allows us to see the incident pulse sent towards the bead. The second image ($t = 10.4 \mu\text{s}$) shows the field just after the incident pulse went around the bead. The maximum value on the image is higher than the maximum value of the first image due to the constructive interference of the waves which have gone around the bead (bright spot just behind the bead). The third image ($t = 15.6 \mu\text{s}$) corresponds to a time for which the incident pulse is beyond the calculation area, which explains the low value for the maximum amplitude of the field. In this image, the field inside the bead is visible, as well as the field in the liquid radiated from the bead.

The three velocity fields (along \vec{x} , \vec{y} and \vec{z}) as well as the six independent components of the stress tensor inside the beads are calculated by Simsonic, allowing the total energy inside the bead to be calculated. The total energy is the sum of the potential energy (E_p) and the kinetic energy (E_k) [12]:

$$E_k(\vec{x}, t) = \frac{1}{2} \rho v_i^2(\vec{x}, t) \quad (3.25)$$

and

$$E_p(\vec{x}, t) = \frac{1}{2} c_{\alpha\beta} S_\alpha(\vec{x}, t) S_\beta(\vec{x}, t). \quad (3.26)$$

In equations (3.25) and (3.26), ρ is the density of aluminum, $c_{\alpha\beta}$ are the components of the stiffness tensor and S_α are the components of the strain tensor. The Einstein summation convention and the Voigt notation have been used (see Appendices 8.1 and 8.2). The strain tensor can be obtained from the recorded stress tensor (T_β) using the compliance coefficients ($s_{\alpha\beta}$):

$$S_{\alpha} = s_{\alpha\beta}T_{\beta}. \quad (3.27)$$

The compliance coefficients and the stiffness coefficients are linked:

$$s_{\alpha\beta}c_{\beta\gamma} = \delta_{\alpha\gamma}. \quad (3.28)$$

$\delta_{\alpha\gamma}$ is the Kronecker delta (the two tensors are inverses of each other). Thanks to these different formulas, the energy was calculated at any position inside the bead. By summing over all positions in the bead, the total energy inside the bead was obtained as a function of time.

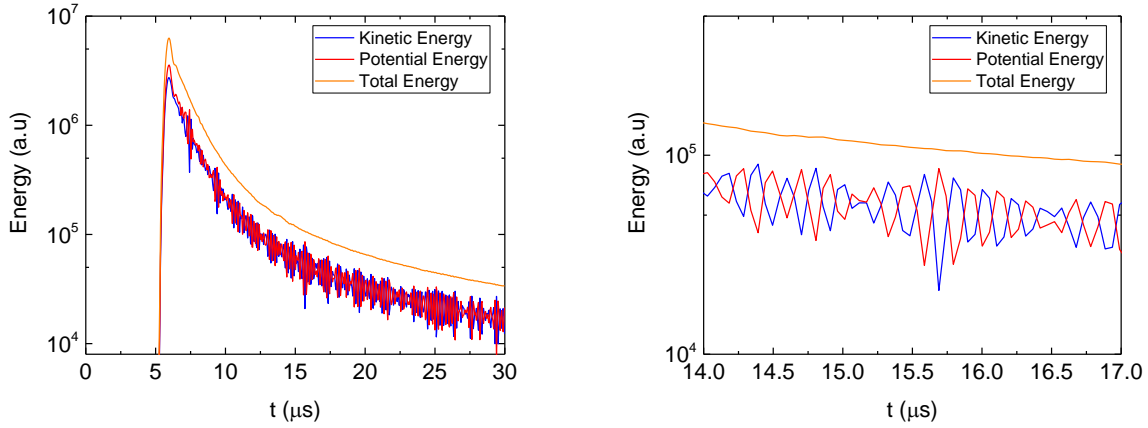


Figure 3.10: Evolution of the energy with time inside the bead; the two figures represent the same data obtained with Simsonic. On the left, it is shown that after 30 μs the energy inside the beads is still several orders of magnitude above zero. The figure on the right shows that the variation of kinetic and potential energies compensates each other to give a total energy decaying at all times.

Even though the incident pulse was only 1 μs long, energy was still observed inside the beads more than 20 μs after the pulse was incident on the bead. Of course the decay of energy with time depended on the impedance of the outside fluid: the closer the impedance of the fluid is to the impedance of aluminum, the faster the decay occurs. A characteristic decay time (dwell time) can be obtained by calculating the average time of the energy as a function of time, $E(t)$. The decay time $\langle\tau\rangle$ is obtained from:

$$\langle \tau \rangle = \frac{\int tE(t)dt}{\int E(t)dt}. \quad (3.29)$$

Using Figure 3.10, the dwell time obtained is $\langle \tau \rangle = 5 \mu\text{s}$. This value of the decay time is a minimum possible value due to the slow decay of energy with time and the maximum time calculated in the simulation. Another simulation was performed, with a second bead behind the first one. The idea of this second simulation is to look at the influence of the beads on each other.

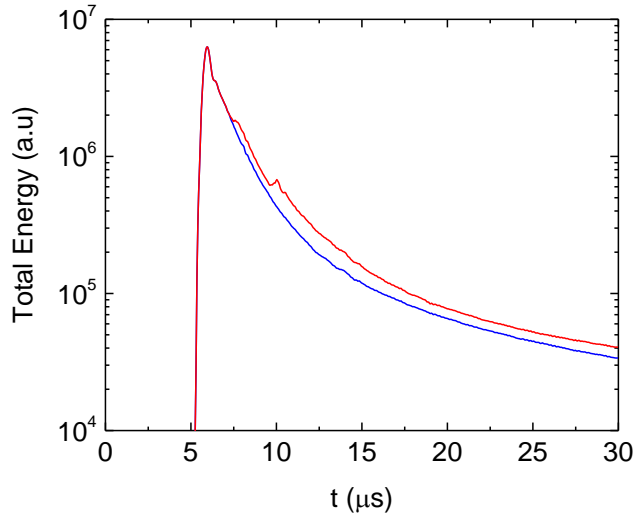


Figure 3.11: Total Energy in a bead as a function of time: blue, one bead in the system, red, a second bead is placed behind the first one. The energy represented is the energy of the first bead.

Figure 3.11 shows that the energy in a bead when there is a second bead 1 mm behind it⁸, is higher at long times. Some of the energy hitting the second bead is reflected back to the first bead, leading to an increase of the energy of the first bead. The two beads can exchange energy between each other leading to a higher energy at long times. This phenomenon of exchange of

⁸ The first bead was at the same as for the results shown in Figure 3.10, a second bead was placed behind the first with respect to the direction of the incident plane wave.

energy between the beads, observed with only two beads, will be amplified when the number of beads is increased and can lead to the observation of very long signals going through a sample, increasing the characteristic decay time calculated in the previous section. For example, in the sample made of aluminum beads in a liquid, signal can be observed going out of the sample up to 600 μs after the sound has entered the sample, even though the incident pulse was only 4 μs long.

3.6 Density of states and pass-band

In a sample made of several beads, either in simple contact or brazed together, the resonances of individual beads lead to the vibrational modes (phonons) of the sample. In the samples composed of several beads, the degeneracy of the resonances is lifted and the coupling between the beads can shift and broaden the resonant frequencies due to the different stiffness experienced by the beads. The density of states varies with frequency and, for an elastic wave to propagate in a given sample, the frequency of this wave has to be one for which the density of states is non-zero.

A finite sample of coupled beads have some frequency bands with a high density of states, leading to a good coupling of the wave from the outside to the inside of the sample and a good transmission through the sample, and some frequency bands with a low density of states leading to a poor coupling into the sample and a low transmission (see Figure 3.12 for an example) [3,32,38]. The effects of the number of beads and of the strength of the links between beads on the density of states, hence, on the transmission, have been previously studied [32]. The frequency bands with a low density of states are crucial in the observation of Anderson localization, as localization is easier to observe at the upper edge of these pass bands [5,7,39].

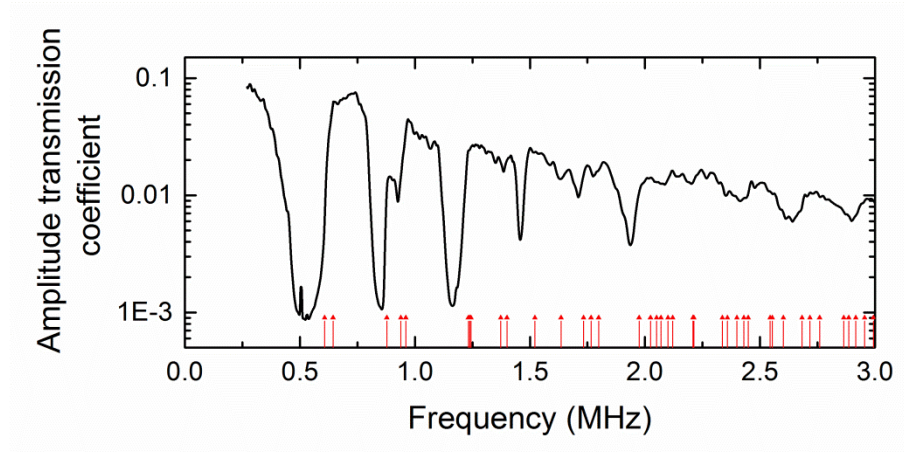


Figure 3.12: Example of the frequency transmission coefficient in a sample made of brazed aluminum beads (diameter 4.11 ± 0.03 mm) for a sample with a thickness of 14.5 mm. The red arrows represent the resonance frequencies of a single bead [3]. Figure shown with kind permission from Springer Nature.

In the experiment discussed in this thesis, the same behaviour of the transmission will be observed, *i.e.*, at some frequencies, there is a transmission through the sample, while at other frequencies, there is no transmission through the network of beads (chapters 4 and 5).

3.7 Conclusion

The resonant frequencies of aluminum beads allow us to understand the transmission in a more complex sample as the pass bands will be determined formed from the resonances of the individual beads. Moreover, I was able to measure the mechanical properties of the aluminum via a simple experiment. These properties are summarized in the following table.

Density(kg/m ³)	2710±10
Longitudinal wave velocity (m/s)	6400±50
Shear wave velocity (m/s)	3120±30
First Lamé parameter (GPa)	58±1
Second Lamé parameter (GPa)	26.3±0.5
Young's Modulus(GPa)	70±4
Poisson's ratio	0.34±0.01

Table 3.4: Measured mechanical properties of the aluminum beads used in different samples of this thesis. The values of the velocities and density are very close to the literature values in reference [40] [$\rho = 2700 \text{ kg/m}^3$, $v_l = 6380 \text{ m/s}$ and $v_s = 3120 \text{ m/s}$]

Chapter 4

Anomalous wave transport in a biphasic disordered medium

4.1 Introduction

Samples made of beads are good candidates to study the properties of multiply scattered ultrasound in 3D media. In the past, different experiments have been performed on many different samples. Samples made of glass beads in water have been studied and were used to demonstrate that the propagation of ultrasound in strongly scattered media can be described by the diffusion approximation [1]. Experiments have also been performed on samples made of aluminum beads. In particular, the first evidence of Anderson Localization of classical waves in 3D was demonstrated with a sample made of brazed 4-mm-diameter aluminum beads in vacuum [3]. Aluminum bead samples have a huge advantage compared to the samples made of glass beads, as the dissipation (loss of energy via heating) is lower in aluminum. These types of sample have been studied extensively to look at different properties of waves in a strongly scattering medium, such as recurrent scattering [6], coherent back-scattering which enabled the study of a complete mobility gap [7], or long range and infinite range correlations in the strong scattering regime [5]. Recurrent scattering describes the presence of closed multiply scattered paths in the medium; these paths increase the return probability of the waves. This return probability is a key quantity in the self-consistent theory of localization [equations (2.89) and (2.90)]. The mobility gap is the frequency range for which localization occurs. It was studied with back-scattered signals, which are the waves that leave the sample on the same side in which they entered (i.e., they are scattered backwards) after being multiply scattered inside the sample. The long-range correlations of the fluctuations of the field in a disordered sample depend on the nature of the transport, *i.e.*, on whether it is diffusive or localized. For strong disorder, these correlations are enhanced close to the mobility edge, which is the frequency at which the transition to localization occurs. There are several different types of long-range correlations, one

of which (called C_0) is actually of infinite extent and depends on the fluctuations of the local density of states at the points where the waves either enter or leave the medium.

All these experiments were performed on evacuated samples made of brazed aluminum beads. The ultrasonic waves were therefore able to travel only through the beads. Another experiment, in which one sample was filled with ethanol, was also performed by Kurt Hildebrand [41]. The idea of this new experiment was to reduce the contrast between the aluminum beads and the matrix of the sample (vacuum vs. ethanol) and consequently to change the local density of states of the sample, thereby affecting the infinite range C_0 correlations. Instead of achieving this goal in a clear way, this experiment produced results which were not completely understood: the characteristics of the ballistic signal suggested diffusive behaviour ($kl_s \gg 1$) [30], but the long-time coda was not consistent with diffusive transport. A possible explanation of the transport in the sample filled with ethanol is the presence of two different pathways through the sample, one through the liquid and one through the solid constituents. Such behaviour has been observed at low frequencies in porous samples, such as bones [42,43] or sintered glass bead systems [44], but it has never been observed in samples in which both components are multiply scattered. The low frequency propagation in porous media is usually interpreted by using a homogenization model such as Biot's theory [45,46]. In this model, the properties of the homogeneous medium are the average properties of the two constituents of the porous medium and lead to two distinguishable travelling wave pulses (ballistic pulses with different arrival times). Biot's theory has also been used to quantify properties of porous food materials (bread), in particular in the measurement of the tortuosity of the fluid phase [47]. The two components that were postulated to travel through the sample of brazed aluminum beads filled with ethanol are not separable as their codas are mixed together.

In this chapter, I will describe an experiment that has been designed to understand the results obtained in the ethanol-filled sample [41], and more particularly to examine the possibility of two coupled multiply scattered components of the total wave field travelling in the sample. A new sample made of loose beads surrounded by ethanol was designed, very similar to the sample made of loose glass beads in water [1]. The main difference, apart from the size of the beads and the system, is the absorption, which is much lower in ethanol and aluminum compared to water and low-quality soda-lime glass, respectively. In this new experiment, we expected to observe similar results as in the glass beads sample, but for a longer range of propagation times thanks to the small absorption.

In the experiments of aluminum beads in a liquid made by Kurt Hildebrand [41], the hypothesis was that two wave components exist including one propagating through the solid network of brazed beads. This component might vanish in the case of loose beads, as there are no solid connections between the different scatterers. However, I will show in this chapter that the transport observed in the sample composed of loose beads is similar in many ways to the sample made of brazed beads, indicating that, despite the lack of solid “necks” between the beads, the contact between them is sufficient to allow waves to travel through the network of touching beads, and allowing me to undertake a comprehensive study of the unusual multiply scattering transport phenomenon exhibited by these two systems.

In summary, in these samples made of two low-loss materials (aluminum beads surrounded by ethanol), the transport seems to be described by two travelling components. I will present in this chapter experimental results showing this two-component behaviour and a model that I developed, using two multiply scattered travelling components, describing the total propagation

in the sample. I will also present numerical calculations that I performed to confirm the essential idea on which the model is based.

4.2 Sample description and fabrication

As mentioned in section 4.1, the samples investigated in this chapter were made of loose aluminum beads surrounded by liquid. During the fabrication of the sample, I encountered two main issues that required special attention (or special care): (i) because of gravity, the sample had a tendency to sag, which should be absolutely avoided, and (ii) I had to make sure that the beads were as disordered as possible in order to minimize the tendency for the beads to create a hexagonal pattern, as in a crystal. The final sample was a disk of dimensions 12.7-mm thick and 180 mm in diameter. These dimensions were chosen to make the diameter of the sample much larger than the thickness, in order to be able to consider the sample as an infinite slab.

4.2.1 Aluminum beads

Aluminum is a very convenient material in which to perform sound experiments as the dissipation (loss of energy in heat) is very low. The aluminum beads used to make the sample are slightly polydisperse to help attain a well disordered medium. The diameter of each bead was measured by photographing a single layer of the beads (Figure 4.1), and then using an image analysis technique using the software ImageJ [48]. The mean diameter obtained on the 8143 available beads was 3.86 mm with a standard deviation of 0.17 mm. As the distribution of diameters was not uniform, we can obtain more information by looking at the nine deciles of the distribution (Table 4.1).

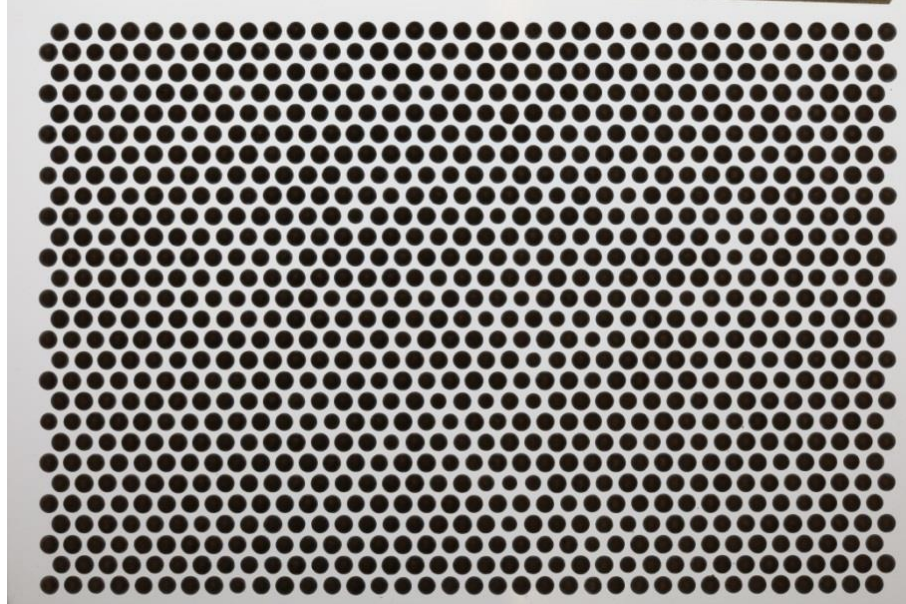


Figure 4.1: Picture of 1008 beads used to measure the diameters of the beads (9 pictures were used). Beads were placed on a clear plastic plate with little holes in it and a light was put behind the plate.

Decile	1 st	2 nd	3 rd	4 th	5 th	6 th	7 th	8 th	9 th
Diameter (mm)	3.66	3.74	3.79	3.84	3.89	3.93	3.98	4.02	4.05

Table 4.1: The 9 deciles of the bead diameter distribution. The smallest bead has a diameter of 3.08 mm and the biggest diameter is 4.21 mm.

In Table 4.1, we can see that there are more beads with bigger diameters than the mean so that the distribution is not symmetric with respect to the mean value (Figure 4.2).

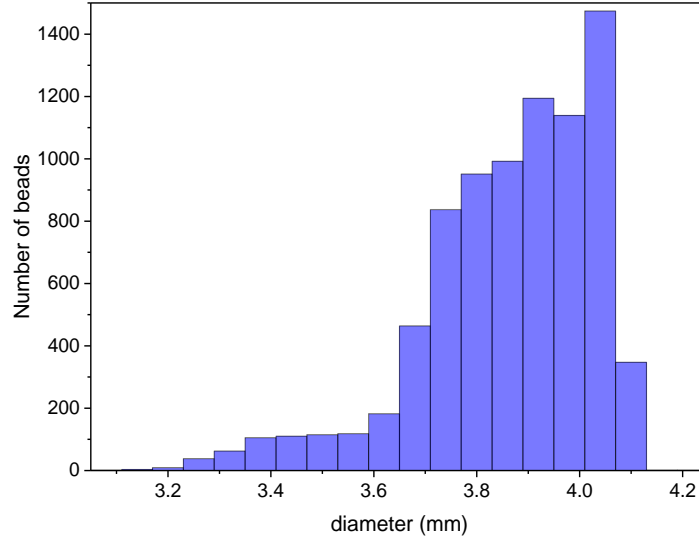


Figure 4.2: Distribution of the diameter of the beads used in the sample (data for 8143 beads)

4.2.2 Liquid surrounding the beads

Two different liquids have been used for the experiments; both have been chosen for their low viscosity, leading, according to the Navier-Stokes equation, to a low dissipation of pressure waves: ethanol (C_2H_6O) and hexamethyldisiloxane ($C_6H_{18}OSi_2$). The hexamethyldisiloxane is a low viscosity silicone oil, of kinematic viscosity around 0.65 cSt (for comparison, the kinematic viscosity of water is 1 cSt).

The second criterion for choosing the liquid was the thermodynamic properties. As the sample was made of loose beads and because I wanted to have the walls surrounding the sample to be as thin as possible, the sample could sag quite easily. The best solution to avoid the sagging of beads was to decrease the pressure inside the sample: the outside medium (air or water during the experiments) pushed on the sample and this helps to hold the beads in a slab shape. The under-pressure imposed on the sample has two consequences for the liquid. As

stated by Henry's law, the concentration of gas dissolved in a liquid is proportional to the pressure applied on the liquid. As a consequence, when the pressure was reduced below atmospheric pressure, some of the air that was initially dissolved will get out of the liquid. This air created bubbles inside the sample that remained trapped between the beads. The second issue arising from the under-pressure inside the sample was the evaporation of the liquid if the pressure inside the sample was getting close to or below the vapour pressure. The silicone oil and ethanol had similar vapour pressure (5.62×10^3 Pa for the oil and 5.95×10^3 Pa for the ethanol). These two values of pressure are well below the pressure imposed inside the sample which was around 80% of atmospheric pressure (8×10^4 Pa). Therefore, both liquids were satisfactory in terms of the evaporation issue. However, even though predictions about the first issue cannot be made since the Henry constant of hexamethyldisiloxane is not known, I observed experimentally that ethanol is able to trap much more air inside the sample than silicone oil. If a beaker filled with ethanol was placed in a vacuum chamber, I saw the liquid "boiling" when the pressure was decreased. In the case of a beaker of silicone oil, no bubbles leaving the silicone oil was observed when the pressure was decreased. Similarly, when the aluminum-in-liquid sample was sealed and the under-pressures applied, bubbles trapped between the beads appeared after a few hours (time for the sample to reach equilibrium) when the liquid was ethanol. In contrast, there were no bubbles in the case of the silicone oil, which made this liquid easier to use in my experiments.

4.2.3 How the sample is made

The slab of aluminum beads in the silicone oil needed to be sealed to prevent the oil from getting out or the water in the water tank from going in. The sample was put inside a food saver bag, using a commercial vacuum sealer (Foodsaver 2000 series). A circular shape was given to

the bag with the sealer and to ensure the sample keeps the shape of a disk, a ring was added inside the bag. This ring was 12.7-mm-thick and had an inner diameter of 180 mm (outer diameter 200 mm).

Once the ring was inside the plastic bag, it was sealed all around the ring except for a segment of two centimeters. A funnel was introduced inside the hole to pour the aluminum beads inside the bag. Pouring the beads was much faster than putting them one by one, and made it easier to obtain random positions of the beads. The two sides of the sample were held by plastic plates to avoid the sagging of the beads. Next, the last segment of the bag was closed with the vacuum sealer.



Figure 4.3: Picture of the sample. At the top of the picture there is the tube used to flow the liquid between the beads and to control the pressure in the sample.

The last step of the fabrication was to put the liquid inside the sample. A tube was inserted inside the plastic and the bag was sealed around it. This tube was then used to evacuate the sample and to suck the liquid in the slab, between the beads. A pressure gauge was installed at the end of tube, so it was possible to monitor the pressure inside the sample during the experiments. The tube was linked to a ballast, so that the pressure inside the sample could be adjusted if the pressure increased during the experiment. The pressure inside the sample was kept at 80% of atmospheric pressure.

The experiments were done in transmission. To ensure that the signal recorded on the acquisition side of the sample had travelled through it, and not around it, a plastic frame wrapped in Teflon tape (40 cm in length) was added around the sample. Teflon tape is commonly used in the lab as it is a good reflector and therefore prevents the ultrasound from going inside the frame and through to the other side of the sample.

The acoustical properties of the aluminum, ethanol and hexamethyldisiloxane are summarized in Table 4.2. The density of silicone oil is the one provided by the manufacturer (Aldrich 2053389-500ml), the sound velocity was measured using a reflection setup.

	Aluminum	Ethanol	hexamethyldisiloxane
Density (kg/m ³)	2710±20	789	764
Longitudinal velocity(m/s)	6400±50	1150	894±4
Shear velocity (m/s)	3120±30		

Table 4.2: Acoustic properties of the different constituents of the sample

4.3 General experimental setup

4.3.1 Transverse confinement setup

All the experiments performed on the sample made of aluminum beads in a fluid were done in a water tank as in previous studies [1,3,5,7,39,41,49]. A focusing immersion transducer and a sub-wavelength hydrophone were used. The transducer and the hydrophone were on opposite sides of the sample as shown in Figure 2.2, so that the transmitted signal through the sample could be measured. To ensure that only the signal going through the sample was measured, a cone-shaped aperture (see Figure 2.2) and a baffle, installed in front of the sample, were used. These two elements were made to prevent signals going around the sample. The aperture allowed a well-defined point-like source to be obtained on the input side of the sample.

Usually, the amplitude of the signal going through the sample was weak, so for each acquisition, I needed to average the detected signal obtained from many repetitions of the input pulse to reduce the random noise fluctuations of the signal, such as electronic noise. To obtain one signal, I usually averaged 4000 different signals acquired one after the other. To do these repeated acquisitions, I made sure that, from one signal to the next, there was no cross-talk: when a pulse was emitted, no energy from the previous signal should remain in the sample. Between each emission of ultrasonic wave in the sample, there was a delay, which was usually around 8 ms. As a comparison, the length of the emitted pulse (see section 4.3.2.1) for the 1 MHz transducer was around 4 μ s.

For this experiment, it is interesting to measure the spreading of the energy in the sample with propagation time. To have information about the spreading from the point source, the field

needs to be measured at different detection positions, defined as ρ in Figure 2.2⁹. To get the best spatial resolution with our experimental setup, the field should be detected near the surface of the sample. To obtain enough data about the evolution of the ultrasonic energy with position and time, the signal was usually detected at 13 different positions with four different values of ρ (15, 20 and 25 mm from the on-axis position $\rho = 0$, see Figure 4.4), by moving the hydrophone parallel to the surface of the sample. For a given distance ρ , the different signals were averaged as the information obtained is statistically equivalent (the important parameter is the distance from the source, not the direction).

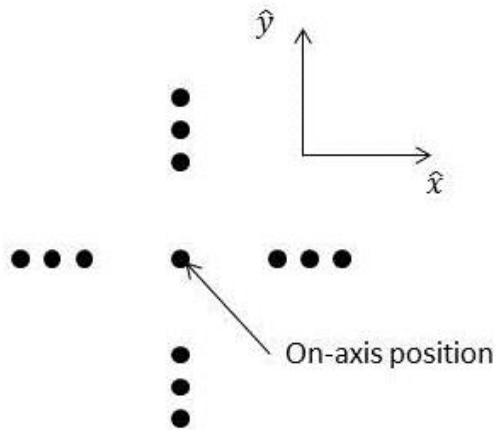


Figure 4.4: Position of the 13 acquisitions on the output side of the sample for each source position. The on-axis position is in front of the source, which is on the other side of the sample. The distances between the on-axis position and the other points are 15, 20 and 25 mm.

The measurement was repeated for many sample positions relative to the source - usually 3025 positions (a grid of 55x55 positions of the sample). Between each position the sample was moved by a distance of at least $\lambda/2$, so two adjacent positions correspond to essentially independent point sources. The acquisitions over the different positions of the sample (for a

⁹ In this chapter, ρ is the transverse distance of the transverse confinement experiments.

given value of ρ) were also averaged. This operation allowed the data to be averaged over the disorder of the sample, and also helped to obtain a better signal-to-noise ratio.

In the next section, a description of the equipment used for this experiment is presented.

4.3.2 Electronics

The entire acquisition setup is represented in Figure 4.5 and will be fully described in the following paragraphs.

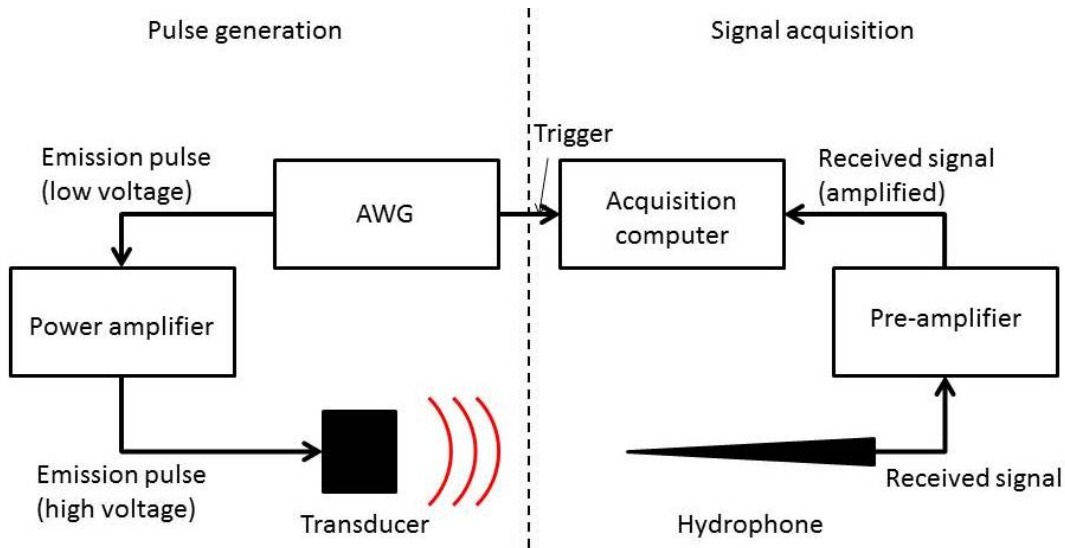


Figure 4.5: Block diagram of the electronic equipment used for transverse confinement experiments. The sample is placed between the transducer and the hydrophone, immersed in a water tank. Sample and hydrophone positions are controlled by multi-axis translation stages with step motor controllers, not represented here.

4.3.2.1 Arbitrary wave generator (AWG)

The signal generation was done using an Agilent 33220A arbitrary wave generator (AWG). This device can create any kind of electronic signal with a frequency up to 10 MHz. In the laboratory, a broadband pulse called “Gauss2” has been defined. This pulse is roughly two periods of a cosine wave multiplied by a Gaussian envelope (see Figure 4.6). The central

frequency of the pulse is chosen according to the central frequency of the transducers. Finally, for the transverse confinement experiment, the burst mode of the AWG was selected, with a controlled delay between each emission of the pulse. The AWG was also used to trigger the acquisition computer, *i.e.*, a signal was sent to the oscilloscope card of the computer each time a pulse was emitted, so it knew when to start recording the received signal.

The AWG is able to generate signals from 10 mVpp up to 10 Vpp (Volts peak-to-peak). The amplitude of the emitted signal during an experiment depends on the power amplifier used to send the signal to the transducer. A typical value used is 400 mVpp.

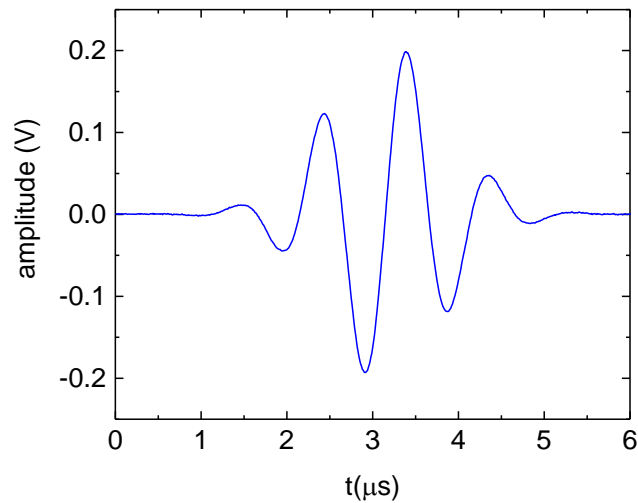


Figure 4.6: Example of a "Gauss2" signal at 1MHz.

4.3.2.2 Power amplifier

The power amplifier is used to amplify the signal generated by the AWG to a higher voltage in order to excite the transducer with a larger signal and therefore to obtain a larger amplitude of the ultrasonic wave. This amplification is often necessary to be able to detect the signal that has travelled through a scattering medium. The power amplifier used for these experiments was the

Electronics & Innovation 2200L (E&I 2200L). It is a linear continuous amplifier, which means that it amplifies all of the time as soon as it is turned on, and therefore does not need any trigger. The range of working frequencies is 10 kHz to 12 MHz, the gain is fixed at 53 dB with a maximum output voltage of 400 Vpp. With the typical input amplitude of 400 mVpp, the output signal has an amplitude around 200 Vpp.

4.3.2.3 Transducers

In these experiments, the transducers used are piezoelectric transducers made by Olympus (formerly Panametrics). More specifically, I used focusing transducers to obtain a focal spot at a given distance from the transducer. This focal spot is elongated along the distance of propagation as shown in Figure 4.7.

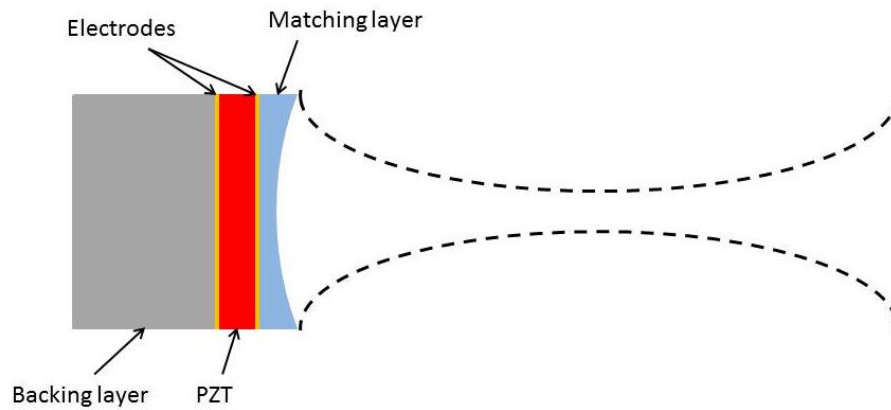


Figure 4.7: Schematic diagram of a piezoelectric focusing transducer used in the transverse confinement experiments.

In Figure 4.7, the transducer is made from PZT, an acronym for “Lead-Zirconate-Titanate”, which is a piezoelectric ceramic. The PZT layer deforms when a voltage is applied between the two electrodes, creating an elastic wave. For this transducer, the matching layer has two purposes: it helps the transmission of the wave to the outside medium as its impedance is between the impedance of the PZT and the impedance of water, and the curvature of this layer

determines the focal length of the transducer. The backing layer is used to attenuate waves that are going toward the back of the transducer and provide an impedance matched load that serves to broaden the bandwidth and reduce ringing of the transducer.

More generally, the transducers used in the laboratory have a diameter ranging from 0.25 inch to 2 inches, and, if the matching layer is not flat, a focal length of 2 to 12 inches, depending on the curvature of the lens and the frequency.

4.3.2.4 Hydrophone

As was just discussed in section 4.3.2.3, a piezoelectric material can be used in emission, as it deforms, creating an acoustic wave when a voltage is applied to it. Conversely, this material, when deformed, creates a voltage, and as a consequence can also be used in reception. The hydrophone that is used as a receiver to detect the signal is also made of a piezoelectric ceramic, but the ceramic is much smaller than in the transducers.

The receiver used in my experiments was the ONDA HNC-0400 needle hydrophone. Its diameter is 400 μm , which is smaller than the wavelength of an acoustic wave in water at the frequencies used in these experiments (e.g., 1.5 mm at 1 MHz). For this reason, in all the experiments, this hydrophone is considered as a point receiver. According to the manufacturer, the angular aperture at -6 dB is 60° , and the bandwidth is from 1 MHz to 10 MHz. This bandwidth being defined at -6 dB below the maximum sensitivity, signals at a lower frequencies can still be recorded, making the use of this hydrophone for experiments at frequencies as low as 500 kHz possible.

During experiments, the hydrophone had to be placed as close as possible to the sample so it detects signals directly coming from a small spot on the sample surface. If it were farther away from the surface (more than a wavelength), the signal would propagate further through the water outside of the sample. In this non-ideal situation, signals recorded would not come from only a specific point on the sample surface, and some of the advantages of having such a small detector will be lost. The signal detected would then be an average of the waves coming from a larger spot on the surface of the sample, and the spatial resolution would be degraded.

4.3.2.5 Pre-amplifier

The pre-amplifier was used to amplify the signal coming from the hydrophone, in reception. The purpose is the same as a power amplifier, but for much smaller signals. Contrary to the power amplifier used to obtain a high voltage (and high power signal), the pre-amplifier is used to amplify very small signals (μV to mV) to a signal of hundreds of millivolts. The signals going in and out of this device are quite small, so the amplification should not add too much noise. The amplification of the hydrophone signal increases the dynamic range of the data measured on the receiving computer.

A typical pre-amplifier used in the laboratory is the Ritec Broadband receiver BR-640A. This receiver is able to amplify by as much as 64 dB, with a 1 dB step, and has a maximum output Voltage of 1 Vpp. The bandwidth of this receiver goes from 100 kHz to 50 MHz, so it can be used for all the experiments described in this section.

4.3.2.6 Receiving oscilloscope and computer

Two very different integrated oscilloscopes and computers have been used for these experiments to record the transduced and amplified ultrasonic signals. Despite the fact that they are different, their key characteristics are very similar. The first oscilloscope computer used was a computer-based oscilloscope from Tektronix (TDS5052), which has all the features of an oscilloscope but runs a Windows OS. The oscilloscope features are very convenient, as it is easy to visualize the signal and modify the recording parameters (such as the time scale, the voltage scale...). The Windows OS is useful not only for saving the waveforms to disk but also for controlling other apparatus such as the motor controller used to move the hydrophone or the sample. The second system used to record the signal is a computer with a PCI oscilloscope card (Octopus 8227 from GaGe), acting as a signal receiver.

The main characteristics needed for these recording systems were the sampling frequency, (typically 25 MHz), the number of digitizing bits, which is 16 after averaging (without averaging, the number of bits is 8), and the number of averages that can be done for a given acquisition. For these experiments, the typical number of averages was several thousands (most often 4000). The system using the PCI card is faster to perform the averaging.

4.3.3 Plane wave experiment

A second type of experiment done with the sample of aluminum beads in a liquid was plane wave experiments. Such experiments gave a better access to information about the ballistic signal going through the sample.

The setup was very similar to the one described previously. I just needed to replace the focusing transducer and the hydrophone by two plane transducers (with a flat matching layer). The first transducer was used to generate the signal (still a Gauss2 signal, as described in 4.3.2.1). The second transducer was used as a receiver. These transducers are larger than the wavelength (the diameter is typically 1 inch), so the measured field was averaged over a larger area. Moreover, the transducers were not close to the sample, so the incident beam propagated in water and insonified an area of the sample larger than the size of the transducer; similarly the detecting transducer collected signals from a comparably sized area of the sample, which increased the averaging over the disorder of the sample. This experiment was done for different sample positions to average over the position disorder of the beads comprising the sample.

The signals obtained from this experiment combined with a reference experiment (no sample between the two transducers) gave access to important information about the sample, such as the phase velocity and the attenuation, allowing the wave number inside the sample and the scattering mean free path to be measured (section 4.4.1).

4.4 Results

4.4.1 Ballistic Measurement

The plane wave experiments were used to measure the ballistic signal, *i.e.*, the coherent signal going directly through the sample, without being scattered away from the forward direction. The time delay of the wave oscillations or the phase shift of the Fourier transform of this signal for a sample of known thickness gave the phase velocity in the sample. The phase shift is the difference of phase between the signal going through the sample and a reference

signal. The reference signal was a signal acquired in the exact same condition as the experiment, but without the sample between the two transducers. Thus, the phase shift $\Delta\varphi$ is given by $\Delta\varphi = \text{Re}(k_s - k_w)L$, with k_s the wave number in the sample, k_w the wave number in water and L the thickness of the sample. The velocity in the sample v_s was obtained as a function of the velocity in water v_w and the angular frequency ω from

$$v_s = \frac{\omega}{k_s} = \frac{\omega L v_w}{v_w \Delta\varphi + \omega L}. \quad (4.1)$$

The amplitude of the ballistic signal with respect to the amplitude of the reference is related to the value of the attenuation in the sample. The amplitude, A , of a wave after travelling through a sample of thickness L can be written:

$$A = A_0 e^{-\alpha L/2}, \quad (4.2)$$

with A_0 the amplitude of the wave entering the sample and α the attenuation coefficient. If the attenuation is only due to scattering (the amplitude of the wave is reduced only because part of the energy is scattered in other directions) and not due to absorption (loss of energy), the attenuation and the scattering mean free path, l_s , are directly linked. As explained in the second chapter of this thesis [8]:

$$\alpha = \frac{1}{l_s}. \quad (4.3)$$

The plane wave experiment was performed with four different pairs of transducers at four different central frequencies in order to cover the widest possible frequency range.

	Central frequency (MHz)	Useful Bandwidth (MHz)	Diameter (in)
Transducers 1	0.25	0.2 - 0.3	1.5
Transducers 2	0.5	0.3 - 0.7	1
Transducers 3	1	0.7 - 1.3	1
Transducers 4	2.25	1.4 - 2.5	1

Table 4.3: Characteristics of the plane wave transducers.

The signals obtained from one experiment are averaged over the different positions of the sample to estimate the coherent signal going through the sample (see Figure 4.8).

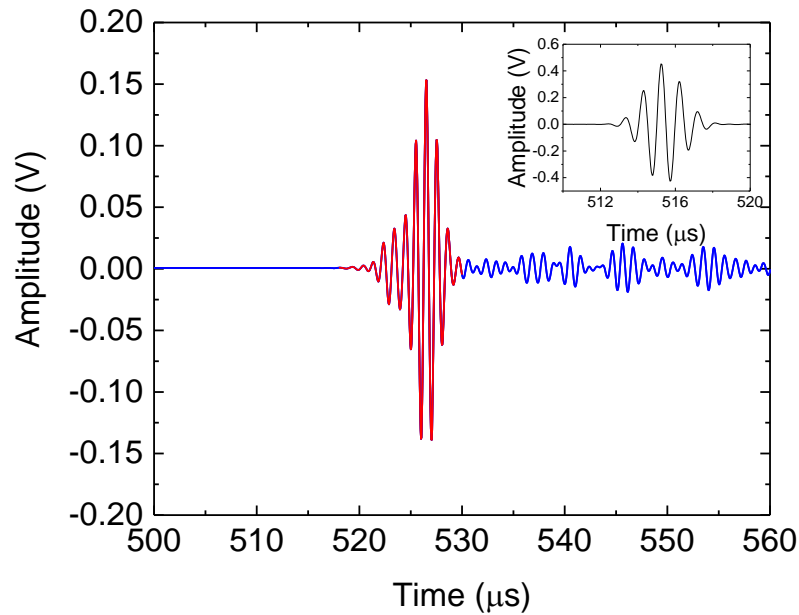


Figure 4.8: Coherent plane wave signal going through the sample at 1 MHz. (Red: ballistic signal, blue: average signal for the entire transmitted pulse, Inset: reference signal). The time zero corresponds to the emission time.

The inset of Figure 4.8 shows the emitted pulse. The effect of multiple scattering is here clearly visible: the signal is spread over a much longer time, and the initial shape is not conserved due likely to imperfect cancellation of the scattered signals and possible dispersion effects. Because I was not able to clearly distinguish the possible contribution of imperfectly cancelled scattered signals at later times in the pulse, I have focused my analysis of the ballistic

signal on the first few oscillations. This part of the signal is indicated in Figure 4.8. The Fourier transform of this signal was calculated and was compared with the Fourier transform of the reference signal to obtain the phase shift and the amplitude of the transmission. The analysis of this ballistic signal gave reliable information on the overall behaviour of the phase velocity and attenuation with frequency, but may underestimate the effects of resonances that can cause pulse broadening due to dispersive effects [50].

The analysis of the ballistic signal to obtain the phase velocity and the attenuation was performed on the four different experiments done at different frequencies. Phase velocity and attenuation calculated from plane wave experimental data for a sample of aluminum beads in hexamethyldisiloxane are shown in Figure 4.9 and Figure 4.10.

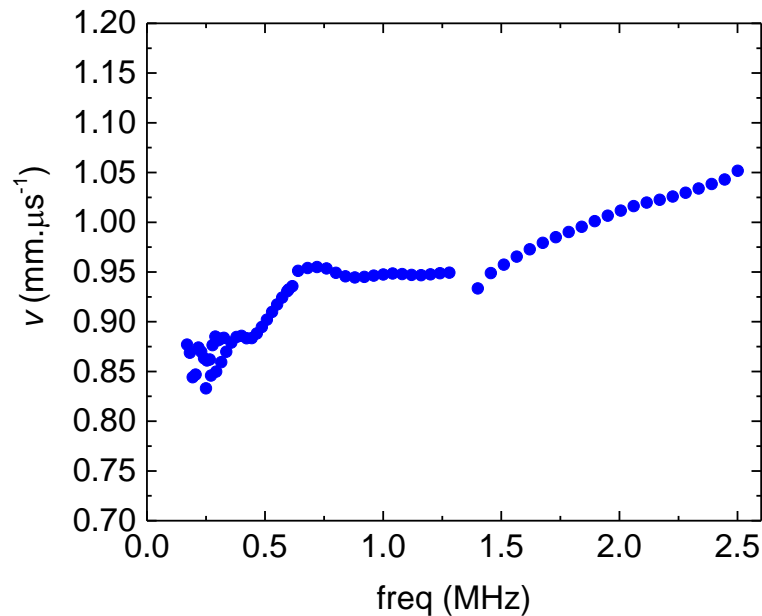


Figure 4.9: Phase velocity of ultrasonic waves propagating in the sample of aluminum beads in liquid obtained from the ballistic signal recorded during plane wave experiments.

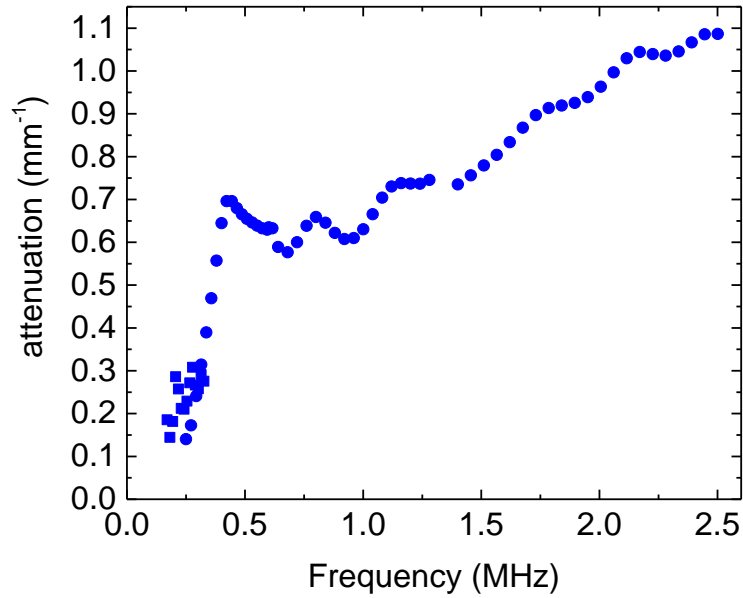


Figure 4.10: The attenuation coefficient obtained from the same set of data as was used to determine the phase velocity in Figure 4.9.

The wave number, k , and the scattering mean free path can be calculated from the phase velocity and the attenuation. These quantities allow me to calculate kl_s , a dimensionless number characterizing the scattering strength in the sample. According to the Ioffe-Regel criterion, if kl_s is sufficiently large compare to 1, the behaviour of the wave transport by multiply scattered waves inside the sample can be approximated by the diffusion approximation, whereas if $kl_s \lesssim 1$, the waves may become localized [8,30].

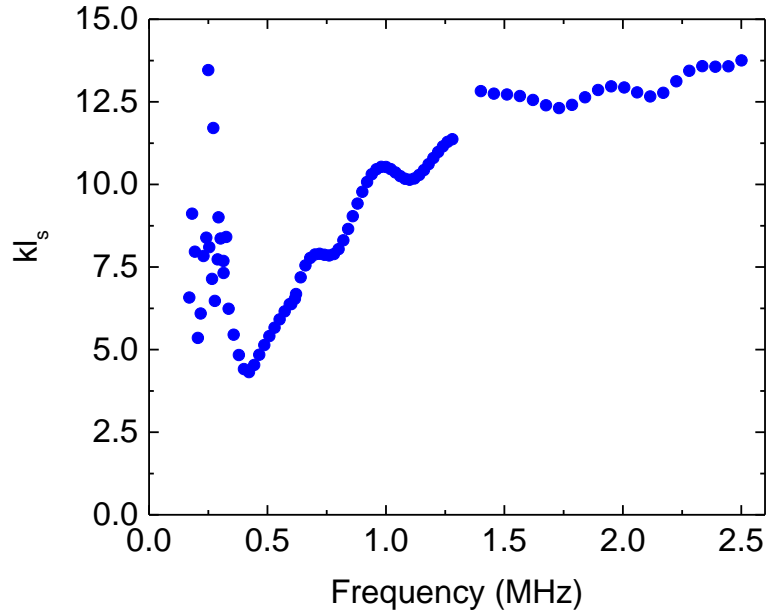


Figure 4.11: Frequency dependence of kl_s obtained from the ballistic signal. kl_s is calculated from the phase velocity and attenuation shown in Figure 4.9 and Figure 4.10.

The graph in Figure 4.11 shows that the value of kl_s varies with the frequency from less than 5 to more than 10. These values show that the wave transport in the sample, according to the ballistic signal, is not expected to be localized.

4.4.2 Transverse confinement experiment

Transverse confinement experiments were performed using three different transducers at three different central frequencies 0.5, 1 and 2.25 MHz, but I focused my attention more especially on the data obtained with the 1 MHz transducer, which is of better quality. This transducer indeed allows data to be recorded from 0.5 to 1.5 MHz with a high signal-to-noise ratio, and, as we will see in the section 4.4.2.3, there are many interesting features inside this frequency range. Additionally, the experiments were easier to perform at 1 MHz compared to

0.5 MHz. Indeed, for the lower frequency experiments, the data were more influenced by reflections from the edge of the water tank that affect the signal after a given time (typically around 300 μs after the start of the real signal going through the sample), making impossible the extraction and analysis of long time signals necessary to fully characterize the scattering behaviour of waves propagating in the sample.

4.4.2.1 Frequency filtering

To study the frequency dependence of the transport by multiply scattered waves through the sample, the first step of the analysis was to filter the data around each frequency of interest. To do so, the Fourier transform of the time signal was multiplied by a Gaussian,

$$\exp\left(-\frac{(f - f_c)^2}{2\sigma^2}\right), \quad (4.4)$$

centered on the central frequency, f_c , with a given bandwidth, σ . Finding the best value of the bandwidth was challenging: if the bandwidth was too large, the filtering process was not very efficient as many frequencies remained in the signal, but if the bandwidth was too narrow, the broadening of the time signal induced by the filtering process was too large in time and jeopardizes the analysis of the time-dependent signal. In the recorded time signal, each frequency did not have the same amplitude; those differences in amplitude can affect the central frequency of the filtered signal (Figure 4.12).

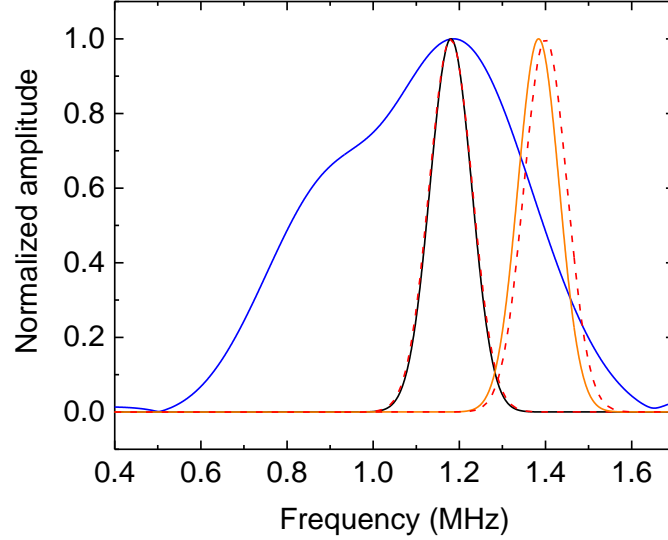


Figure 4.12: Effect of the filtering on the Fourier transform of a wave (blue). Two different Gaussian filters ($f_c = 1.18$ MHz or $f_c = 1.40$ MHz) are applied to the original wave (dashed red lines). The result of the first filter (black) is centred at 1.18 MHz, the result of the second filter (orange) is centred at 1.38 MHz. The bandwidth of both filters is 50 kHz. For this figure, the signal going only through water is used (no multiple scattering).

Once a filter had been successfully defined, it was applied to the data obtained from the transverse confinement experiments. As explained in section 4.3, signal was acquired at four different distances from the on-axis position, and because of the strong scattering inside the sample, all signals had a very long coda (Figure 4.13). The long coda made the choice of the right bandwidth even more critical in this situation, since if the bandwidth was too narrow, the filtering process could smear out the time-dependent coda, which was necessary to access the scattering behaviour, whereas if the bandwidth was too wide, possible variations with frequency could be blurred.

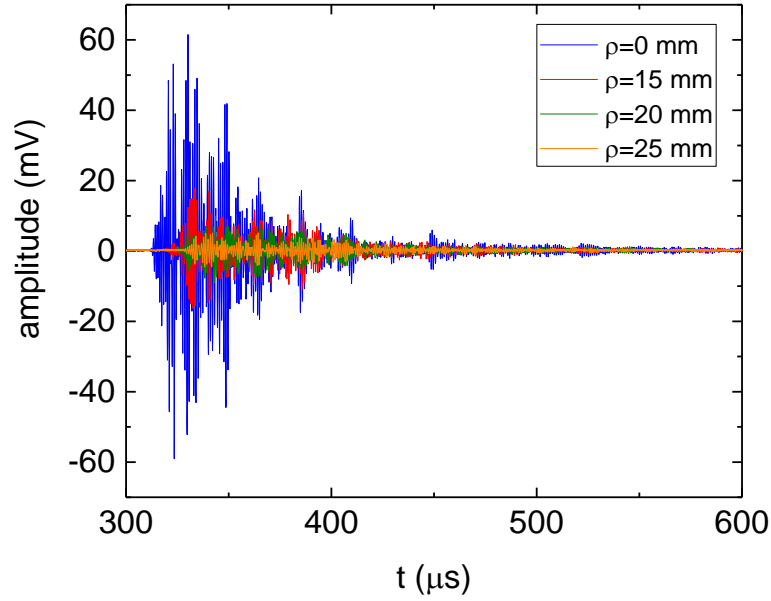


Figure 4.13: Example of four different signals obtained during a transverse confinement experiment on the sample of aluminum beads in liquid, filtered at 1.00 MHz with a bandwidth of 25 kHz.

4.4.2.2 Transverse width

From the transverse confinement experiments, the time-dependent transverse width of the acoustic beam propagating inside the sample was calculated [3,51], and used to characterize the transport behaviour inside the sample. We suppose that the intensity at a distance ρ away from the on-axis position is:

$$I(\rho, t) = I(0, t) e^{-\frac{\rho^2}{w^2(t)}}. \quad (4.5)$$

If the wave transport in the sample were perfectly diffusive, the width $w(t)$ would be:

$$w(t) = \sqrt{4Dt}, \quad (4.6)$$

for all distances ρ . D is the diffusion coefficient, characterizing the transport. In the general situation, we can define the transverse width by inverting equation (4.5):

$$w^2(t) = -\frac{\rho^2}{\ln\left(\frac{I(\rho, t)}{I(0, t)}\right)}. \quad (4.7)$$

The transverse width can be used to discriminate between different types of transport behaviour. If the width squared increases linearly with time, the transport is diffusive. In the opposite case, when the width squared saturates after a given time, it is a sign of localization. Between these two situations, when the width squared increases more slowly than a linear function, the transport is sub-diffusive.

To calculate the transverse width of the acoustic beam, the average intensity of the acoustic wave for each value of ρ needs to be calculated. The intensities obtained for each position of the sample, for a given distance (ρ) from the on-axis position, are averaged in order to average over the disorder of the sample, since it is the ensemble averaged intensity that is most physically meaningful (results from a specific point in the sample reflect the complex interference pattern of waves scattered from a huge number of beads in the sample, and therefore depend on sample-specific details of the microstructure that are not useful for characterizing general transport properties). A Hilbert transform is used to obtain the envelope of the signal, which is squared to obtain the intensity. For a typical experiment, the acquisition was done at 3025 positions of the sample, and for each position of the sample, four acquisitions were obtained for each non-zero value of ρ but only one acquisition for the on-axis position. At the end, the intensities obtained for each off-axis position were the results of more than 12,000 averages (3025 \times 4 acquisitions for a given value of ρ).

The error bars of the intensities are represented by the error of the mean. It was assumed that the 3025 source positions are independent of each other. The error bars for the width squared were calculated using the propagation of errors using the uncertainties of the intensities.

4.4.2.3 Results

a) 375 kHz

We can start to look at the intensity and the width squared at 375 kHz (Figure 4.14 and Figure 4.15), which is below the first resonance of the aluminum beads (see chapter 3). In these figures, and all subsequent graphs showing the intensity and the width squared, the zero of time corresponds to the time when the incident pulse entered the sample.

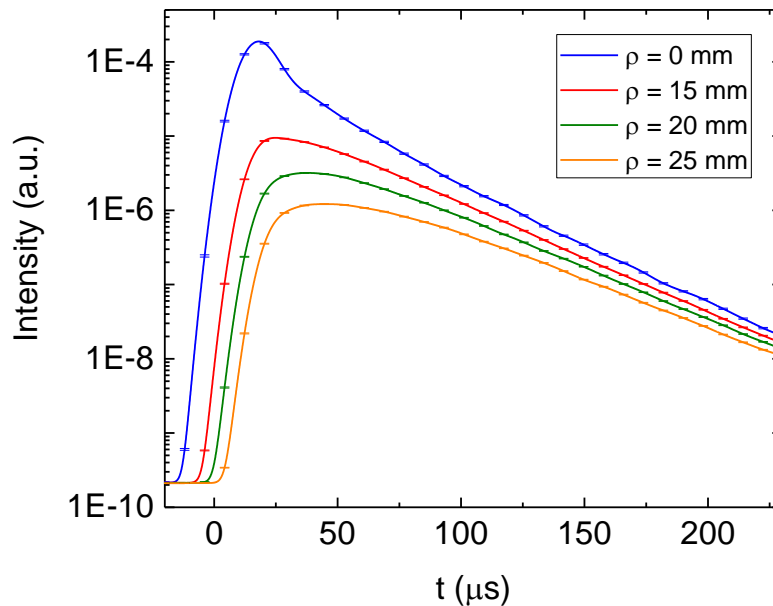


Figure 4.14: Intensities measured at 375 kHz (bandwidth of the filter: 25 kHz)

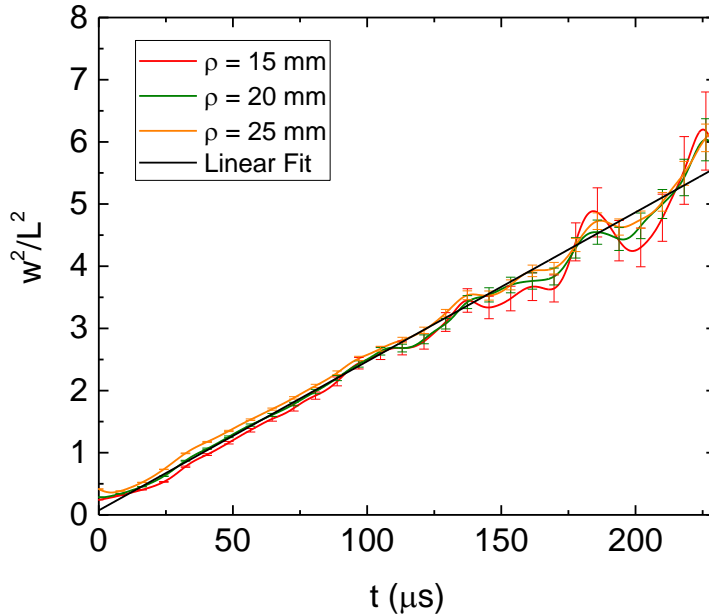


Figure 4.15: Normalized width squared at 375 kHz. The black curve is a linear fit of the average of the three curves (equation of the fit: $y = 0.024t + 0.073$, R-square = 0.988)

The width squared of the acoustic beam varies linearly with time as shown in Figure 4.15, which means that at a frequency below the first resonance of the aluminum beads the transport inside the sample is diffusive. This transport corresponds to a wave travelling mainly through the fluid scattering off the beads. From the equation of the linear fit, the value of the diffusion coefficient D is obtained [equation (4.6)]. For this example, the diffusion coefficient is: $D = 0.967 \pm 0.002 \text{ mm}^2/\mu\text{s}$.

b) 1000 kHz

The next step is to look at the results obtained at a frequency above the first resonances of the beads. For these frequencies, the behaviour of the intensity and of the width squared is very unusual (Figure 4.16 and Figure 4.17) and can be explained, as we will discuss later, by wave transport happening both in the fluid and in the network of touching beads at the same time.

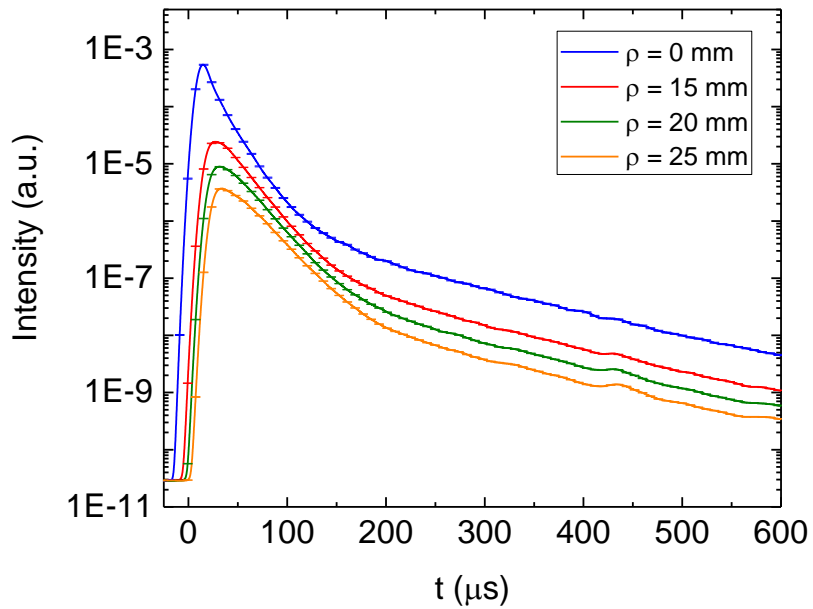


Figure 4.16: Intensities measured at 1000 kHz (bandwidth of the filter: 25 kHz)

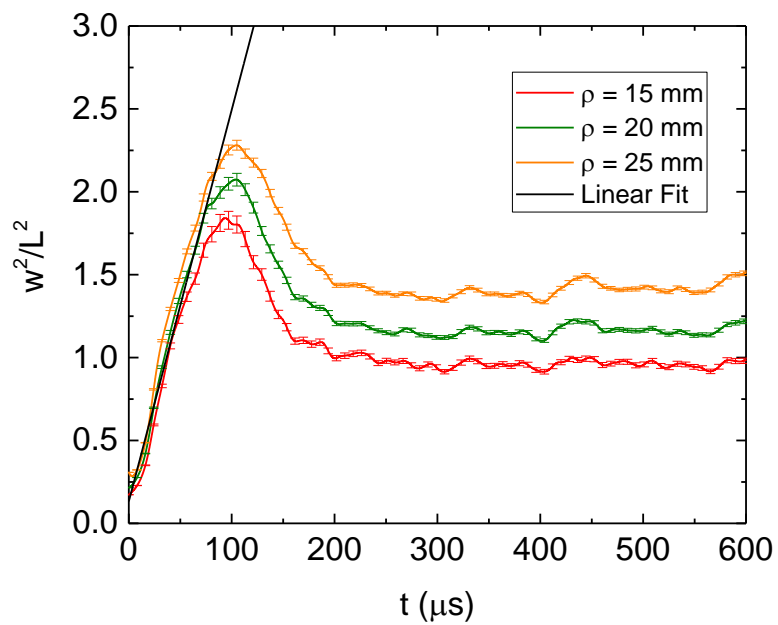


Figure 4.17: Normalized width squared at 1000 kHz. The black curve is a linear fit of the average of the three curves for the first 80 μs (equation of the fit: $y = 0.024t + 0.13$, R-square = 0.985)

According to its definition, the width is expected to always grow monotonically, and in the case of localization, to saturate. In Figure 4.17, the width goes through a maximum at 120 μs , and then decreases to reach a plateau, which may be either constant or slightly increases at long times. In the intensity profiles (Figure 4.16), this maximum in the width squared corresponds to a change of slope at intermediate times (200 μs). The definition of the width squared supposed a Gaussian shape for the intensity. But, in this sample composed of aluminum beads inside a fluid, the transport might be decomposed into two coupled multiply scattered propagations. These two components might be travelling together through the sample (Figure 4.18): one through the liquid scattering off the beads and the second through the solid network of beads using the coupling between the different beads. These two different mechanisms of transport have different characteristic times, and the first component dominates the short-time signal while the second component, using the beads, dominates the long times. We will see in section 4.6 that this hypothesis explains this unusual shape of the width squared.

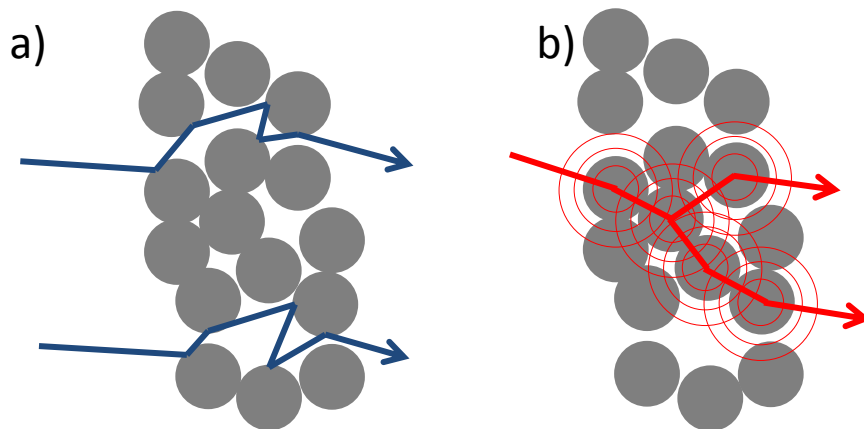


Figure 4.18: Schematic diagram illustrating a two-component mechanism for wave transport through the sample: a) waves travelling through the liquid scattering off the beads, b) waves travelling through the solid network of beads using resonances.

c) 800 kHz

We know from previous work [3] that a solid network of beads has some frequency band gaps, *i.e.*, some frequencies for which the sound could not travel through the sample if it were infinitely thick. Figure 3.12 shows, for example, the transmission inside a sample made of brazed aluminum beads in vacuum. The transmission profile exhibits several dips, or band gaps, which are expected to be very similar in the sample of touching beads surrounded by a liquid, as the resonance frequencies are almost identical (see section 3.4). The first band gap, around 500 kHz, has been discussed in section 4.4.2.3 a). The two next band gaps, around 800 kHz and 1.2 MHz, are due to the absence of modes (no resonances) of the network of beads, so wave transport is strongly attenuated at these frequencies inside the network of beads surrounded by liquid.

In the current sample made of loose beads surrounded by a liquid, the transport cannot be blocked as the network of beads was not the only propagation medium: the wave could always use the liquid as a medium of propagation. At 800 kHz, we observe a similar behaviour as at 375 kHz (Figure 4.14 and Figure 4.15).

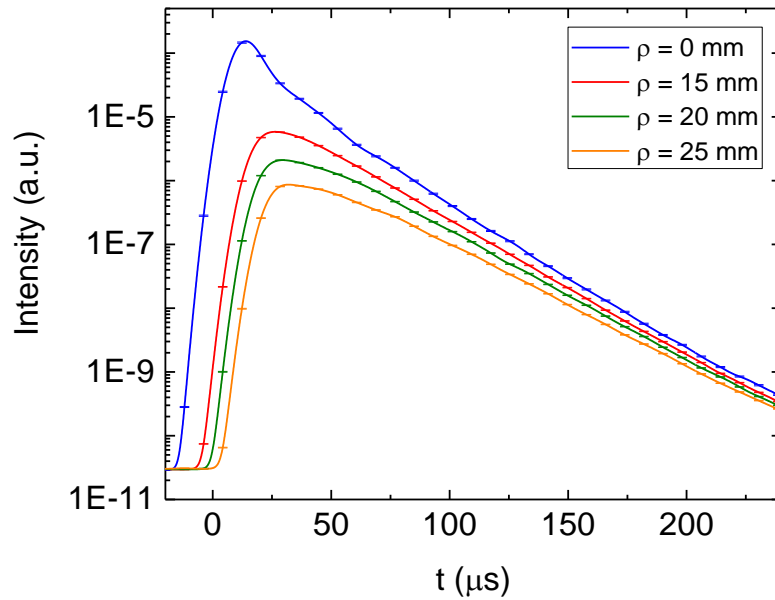


Figure 4.19: Intensities measured at 800 kHz (bandwidth of the filter: 25 kHz)

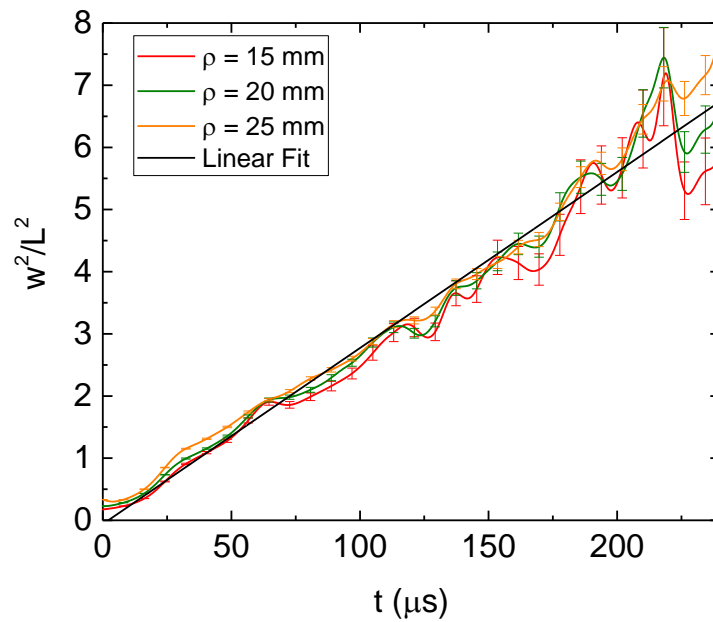


Figure 4.20: Normalized width squared at 800 kHz. The black curve is a linear fit of the average of the three curves (equation of the fit: $y = 0.028t - 0.06$, R-square = 0.982)

At 800 kHz, the transport inside the sample is diffusive ($D = 1.141 \pm 0.003 \text{ mm}^2/\mu\text{s}$). At this frequency, a transport component going through the solid network is blocked and only a component using the liquid as a transport medium can be seen. This observation confirms that the behaviour observed at 1000 kHz (Figure 4.17) is due to the coexistence of two components travelling through the sample, one using the liquid and one using the network of beads.

At short times the width squared shown in Figure 4.17 describes transport dominated by a fast-diffusive component travelling through the liquid and scattering off the beads, which is the component that we can see by itself in Figure 4.20. At long times in Figure 4.17 the transport is dominated by propagation through the network of touching beads. The maximum of the width around $120 \mu\text{s}$ corresponds to the transition between the two transport mechanisms, *i.e.*, a change in the component that dominates the transport through the sample.

4.5 Analysis

As was discussed in section 4.4, the transport in the sample can be described as the transport of two coupled components inside the sample. The first component appears to have diffusive behaviour but the transport properties of the second component are more complicated to ascertain.

Indeed, the behaviour of the first component is determined both by experimental data (Figure 4.15 and Figure 4.20) and is consistent with previous results obtained in a sample made of glass beads in water [1]. The second component, on the other hand, can have *a priori* different possible natures. It can be diffusive, with a smaller diffusion coefficient than the one of the first component, but can also be a renormalized propagation, either sub-diffusive or localized. In order to characterize the properties of the second component, two different theoretical models

have been solved numerically and compared with the experimental data. In section 4.5.1, I will start by describing calculations using a model in which both components are diffusive, as this is the simpler case. Then in section 4.5.2, I will discuss the numerical solutions of a model that I developed, in collaboration with Sergey Skipetrov, in which one of the components propagates diffusively and is coupled with a renormalized component in which the transport is influenced by interference effects described using the self-consistent theory of localization.

4.5.1 Two coupled diffusive modes of transport

For the case of two coupled diffusive components, Finite Difference Time Domain (FDTD) simulations have been implemented to observe the behaviour of such a system. The first step was to write down the equations to model the transport of energy:

$$\frac{\partial E_1(\vec{r}, \vec{r}', t)}{\partial t} - D_1 \nabla^2 E_1(\vec{r}, \vec{r}', t) = c_{21} E_2(\vec{r}, \vec{r}', t) - c_{12} E_1(\vec{r}, \vec{r}', t) \quad (4.8)$$

and

$$\frac{\partial E_2(\vec{r}, \vec{r}', t)}{\partial t} - D_2 \nabla^2 E_2(\vec{r}, \vec{r}', t) = \delta(\vec{r} - \vec{r}', t) + c_{12} E_1(\vec{r}, \vec{r}', t) - c_{21} E_2(\vec{r}, \vec{r}', t). \quad (4.9)$$

In equations (4.8) and (4.9), E_1 and E_2 represent the energy density of each mode, D_1 and D_2 are the two coefficients of diffusion, and c_{12} and c_{21} represents the coupling between the two components. I assumed that the coupling might not be symmetrical, so c_{12} and c_{21} can be different. The Dirac function, $\delta(\vec{r} - \vec{r}', t)$, represents the source inside the system.

4.5.1.1 Discretization

Equations (4.8) and (4.9) have to be discretized in order to run the simulation. The FDTD simulation was run in a space cut in little cubes, the energy being calculated on all the corners of

the cubes. The position of each corner is defined with three indexes as shown in Figure 4.21, that are called l , m and n .

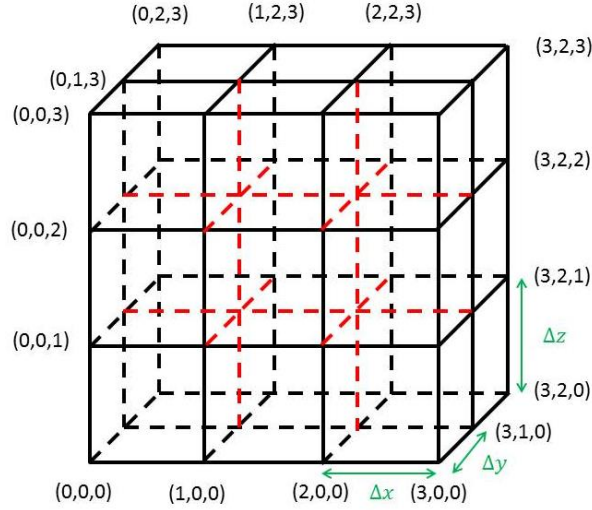


Figure 4.21: Example of the space used for the FDTD simulations. For clarity, only the points on the outside of the drawing are labelled.

As shown in Figure 4.21, three different space steps (Δx , Δy and Δz) can be defined, and for simplicity, the same discretization step was used for the three directions. The time step, Δt , also needed to be defined. The time t_i is defined as $t_i = i\Delta t$ (i : integer). Finally, the discretized energy is written:

$$E(x_l, y_m, z_n, t_i) = E_i(l, m, n). \quad (4.10)$$

The discretized derivatives needed to solve the diffusion equations were obtained using a Taylor expansion¹⁰:

¹⁰ In equations (4.11) to (4.14), the energy density in the different derivatives is the actual energy density, not the discretized one.

$$\begin{aligned}
E_i(l+1, m, n) &= E_i(l, m, n) + \Delta x \left. \frac{\partial E}{\partial x} \right|_{x=l} + \frac{\Delta x^2}{2} \left. \frac{\partial^2 E}{\partial x^2} \right|_{x=l} + \frac{\Delta x^3}{6} \left. \frac{\partial^3 E}{\partial x^3} \right|_{x=l} \\
&+ O(\Delta x^4).
\end{aligned} \tag{4.11}$$

Using the same formula for $l-1$ instead of $l+1$, we can write the second derivative in space needed in equations (4.8) and (4.9):

$$\frac{E_i(l+1, m, n) + E_i(l-1, m, n) - 2E_i(l, m, n)}{\Delta x^2} = \left. \frac{\partial^2 E}{\partial x^2} \right|_{x=l} + O(\Delta x^2). \tag{4.12}$$

Likewise, the time derivative can be obtained:

$$\frac{E_{i+1}(l, m, n) - E_i(l, m, n)}{\Delta t} = \left. \frac{\partial E}{\partial t} \right|_{t=i} + O(\Delta t). \tag{4.13}$$

By combining equations (4.12) and (4.13), and taking the space derivatives in all three directions, assuming the same step, Δx , for all directions:

$$\begin{aligned}
\frac{\partial E}{\partial t} - D\nabla^2 E &= \frac{\partial E}{\partial t} - D \left(\frac{\partial^2 E}{\partial x^2} + \frac{\partial^2 E}{\partial y^2} + \frac{\partial^2 E}{\partial z^2} \right) = 0 \\
&= \frac{E_{i+1}(l, m, n) - E_i(l, m, n)}{\Delta t} \\
&\quad - \frac{D}{\Delta x^2} (E_i(l+1, m, n) + E_i(l-1, m, n) + E_i(l, m+1, n) \\
&\quad + E_i(l, m-1, n) + E_i(l, m, n+1) + E_i(l, m, n-1) \\
&\quad - 6E_i(l, m, n)) + O(\Delta t) + O(\Delta x^2).
\end{aligned} \tag{4.14}$$

The steps in time and space cannot be chosen independently. They are linked by the CFL (Courant-Friedrichs-Lewy) condition, helping the convergence of the simulation by cancelling

out the two O terms in equation (4.14). In the case of the 3D diffusion equation, I have found that the relation

$$\Delta t = \frac{(\Delta x)^2}{12D} \quad (4.15)$$

linking Δt and Δx is valid. Also, I have shown that the simulation results match well the theoretical results in the case of solving the diffusion equation in an infinite medium. The simulation is done in time steps so equation (4.14) needs to be rewritten to express the energy at time $(i + 1)\Delta t$ as a function of the energy at time $i\Delta t$:

$$\begin{aligned} E_{i+1}(l, m, n) = & E_i(l, m, n) \\ & + \frac{\Delta t D}{\Delta x^2} (E_i(l + 1, m, n) + E_i(l - 1, m, n) + E_i(l, m + 1, n) \\ & + E_i(l, m - 1, n) + E_i(l, m, n + 1) + E_i(l, m, n - 1) \\ & - 6E_i(l, m, n)). \end{aligned} \quad (4.16)$$

The equation (4.16) is only valid for the bulk of a sample, so that the boundary conditions also need to be defined. A reflection coefficient, R , is defined to take into account the fact that at the boundary some of the energy is reflected back into the sample. To describe the reflected energy, I put on the other side of the boundary a virtual source of amplitude $R \times E$, E being the amplitude of the energy density close to the boundary inside the sample. This virtual source simulated the reflected part of the energy density inside the sample. On the edge of the sample, equation (4.16) becomes:

$$\begin{aligned}
E_{i+1}(L, m, n) &= E_i(L, m, n) \\
&+ \frac{\Delta t D}{\Delta x^2} (RE_i(L, m, n) + E_i(L - 1, m, n) + E_i(L, m + 1, n) \\
&+ E_i(L, m - 1, n) + E_i(L, m, n + 1) + E_i(L, m, n - 1) \\
&- 6E_i(L, m, n)).
\end{aligned} \tag{4.17}$$

In equation (4.17), L represents a position on the edge of the sample. Equations (4.16) and (4.17) are written in the case of single diffusive component. The next step was to rewrite these equations for the case of two coupled components [equations (4.18) and (4.19)].

4.5.1.2 Two coupled equations: numerical equations

In the case of the two coupled diffusion equations, equation (4.16) can be used for both components with the addition in both cases of the coupling term between the components:

$$\begin{aligned}
E_{i+1}^1(l, m, n) &= E_i^1(l, m, n) \\
&+ \frac{\Delta t D}{\Delta x^2} (E_i^1(l + 1, m, n) + E_i^1(l - 1, m, n) + E_i^1(l, m + 1, n) \\
&+ E_i^1(l, m - 1, n) + E_i^1(l, m, n + 1) + E_i^1(l, m, n - 1) \\
&- 6E_i^1(l, m, n)) + c_{21}\Delta t E_i^2(l, m, n) - c_{12}\Delta t E_i^1(l, m, n)
\end{aligned} \tag{4.18}$$

and

$$\begin{aligned}
E_{i+1}^2(l, m, n) = & E_i^2(l, m, n) \\
& + \frac{\Delta t D}{\Delta x^2} \left(E_i^2(l+1, m, n) + E_i^2(l-1, m, n) + E_i^2(l, m+1, n) \right. \\
& + E_i^2(l, m-1, n) + E_i^2(l, m, n+1) + E_i^2(l, m, n-1) \\
& \left. - 6E_i^2(l, m, n) \right) - c_{21} \Delta t E_i^2(l, m, n) + c_{12} \Delta t E_i^1(l, m, n).
\end{aligned} \tag{4.19}$$

Equations (4.18) and (4.19) were then used to calculate the value of each energy at every point in space for every time, for a given point source. The space being defined as a rectangular parallelepiped with two squared faces, the source was set in the centre of one of these faces. The third dimension was smaller than the size of the square to be as close as possible to a slab geometry. Even though energies were calculated in the full volume, only the values on the opposite square face were recorded.

4.5.1.3 Results

As an output of the simulations, I had the value of the energy for both components for all the times and positions on the output face of the simulated volume. The same analysis as for the experimental data was performed: the width squared of the intensity beams was calculated for $\rho = 15$ mm (Figure 4.22). Here, the intensity is the sum of the two components.

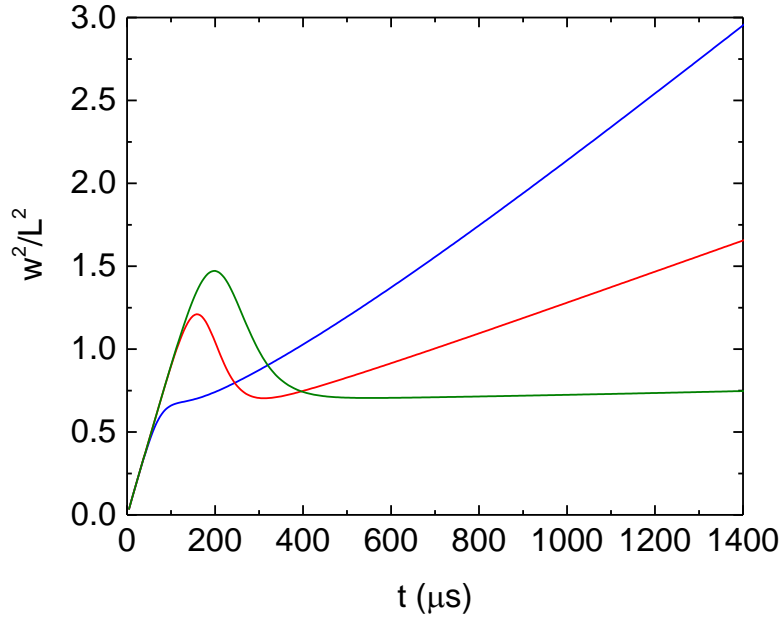


Figure 4.22: Width squared obtained for three different sets of parameters (described in Table 4.4) obtained from the coupled diffusion simulations

Parameter	Green	Red	Blue
$D_1 \left(\frac{mm^2}{\mu s} \right)$	0.01	0.1	0.1
$D_2 \left(\frac{mm^2}{\mu s} \right)$	1	1	1
$c_{12} \left(\frac{1}{\mu s} \right)$	0.001	0.01	0.01
$c_{21} \left(\frac{1}{\mu s} \right)$	0.001	0.0001	0.01

Table 4.4: Parameters of the coupled diffusion simulations

Data from the simulations (Figure 4.22) and from experiments (Figure 4.17) are compared to see if there is any correspondence or similar behaviour. The first main feature of the simulation results is the maximum appearing in the width squared which corresponds to the time when the slow component starts to dominate the overall intensities. Indeed, as the second component is

slower, it takes more time to build up, but the decay at long times is also slower. Consequently, the slow component has a larger amplitude than the fast component after a given time.

The value of D_2 determines the initial slope of the width squared, and the value of D_1 the long time slope, which is also affected by the value of the coupling coefficients. The transition between which component dominates the overall intensities can either lead to the presence of a maximum in the width (red and green, Figure 4.22) or a gradual transition without any maximum (blue, Figure 4.22). For the red curve (Figure 4.22), the time for the transition to occur is around $150 \mu\text{s}$ (time of the maximum of the width squared) which is comparable to the transition time observed in the experiment ($120 \mu\text{s}$) in Figure 4.17. But in order to obtain this similar crossover time, we need to set D_1 not too different from D_2 , leading to an appreciable long time slope, which is not observed experimentally. Another feature observed on the experimental data is plateau behaviour at long times, with the width squared being essentially constant (at least within the experimental uncertainty imposed by the time-dependent fluctuations). To recover this plateau at long times with the simulation, D_1 has to be very small compare to D_2 , as the long-time slope of the width squared depends on the value of D_1 . The parameters used to obtain the green curve in Figure 4.22 correspond to this description. Here the long-time behaviour is almost a plateau, but to obtain such a result, the two components are very different, the transition happens at a longer time ($\sim 250 \mu\text{s}$) and the ratio between the height of the maximum and the position of the plateau is large (2 compared to 1.5 for the experimental data). The last thing to compare is the value of normalized width squared at long times. On the simulation (green curve) the value is approximately 0.75 compared to 1.5 for the experimental data. A value smaller than one for the normalized width squared means that the lateral extent of the intensity beam is smaller than the thickness of the sample, which does not correspond to the experimental

observations. It is therefore impossible to find parameters that can be satisfying enough to recover all the features visible on the experimental width-squared. This strongly suggests that the model of two coupled diffusive transports is not representative of the behaviour of wave transport in a sample of loose aluminum beads in a low-attenuation fluid.

4.5.2 Coupled diffusive and slow renormalized transport

As mentioned in the introduction of section 4.5, and considering that the model of two coupled diffusive transports is not satisfactory, a possible explanation to the observed behaviour is for the second component to be sub-diffusive or localized, or in other words, renormalized. The fact that the transport in a sample made of brazed aluminum beads in vacuum is renormalized [3] is also leading us in this direction. The description of the model using a second component for which the transport is renormalized starts with a set of two equations, like equations (4.8) and (4.9) for the two coupled diffusive transport case, with the addition of a third equation describing the renormalization of the diffusion coefficient for the second component. Equations (4.20) and (4.22) are from the self-consistent theory (SCT) of localization (see section 2.6) [52], while equation (4.21) is an equation similar to (4.8) and describes diffusive transport.

$$[-i\Omega - \nabla_r \cdot D_1(\vec{r}, \Omega) \nabla_r] C_1(\vec{r}, \vec{r}', \Omega) = \delta(\vec{r} - \vec{r}') + \theta [C_2(\vec{r}, \vec{r}', \Omega) - C_1(\vec{r}, \vec{r}', \Omega)] \quad (4.20)$$

and
$$[-i\Omega - D_2 \nabla^2] C_2(\vec{r}, \vec{r}', \Omega) = \theta [C_1(\vec{r}, \vec{r}', \Omega) - C_2(\vec{r}, \vec{r}', \Omega)] \quad (4.21)$$

with
$$\frac{1}{D_1(\vec{r}, \Omega)} = \frac{1}{D_{B1}} + \frac{12\pi}{k_1^2 l_{B1}^*} C_1(\vec{r}, \vec{r}, \Omega). \quad (4.22)$$

In equations (4.20) to (4.22), C_1 and C_2 are the intensities of each component, Ω is the conjugate variable of time (in s^{-1}) and θ is the coupling between the two components, *i.e.*, a transfer rate (in s^{-1}).

4.5.2.1 Solving the SCT for a slab geometry

Before solving the full system of equations (4.20) to (4.22), I will explain the method used to solve numerically the SCT by itself [53]. These calculations correspond to the analysis performed for the samples of brazed beads in vacuum in which Anderson Localization has been observed [3,4,5,6,7]. The system of equations to solve is basically similar to equations (4.20) and (4.22) without the coupling term:

$$[-i\Omega - \nabla_r \cdot D(\vec{r}, \Omega) \nabla_r] C(\vec{r}, \vec{r}', \Omega) = \delta(\vec{r} - \vec{r}') \quad (4.23)$$

and

$$\frac{1}{D(\vec{r}, \Omega)} = \frac{1}{D_B} + \frac{12\pi}{k^2 l_B^*} C(\vec{r}, \vec{r}, \Omega). \quad (4.24)$$

a) Slab geometry

All the experiments were performed on samples with a slab geometry, which was assumed to be infinite in the x and y directions (long dimensions of the slab). The Cartesian coordinate system in these samples can be redefined using a cylindrical system of coordinates: \vec{r} is defined as (ρ, z) with ρ the position in the $x - y$ plane and z the depth in the sample.

In this geometry, the intensities do not depend on the specific (x, y) coordinates of the observation point, but only on the distance ρ from the source and z . The intensity $C_1(\vec{r}, \vec{r}', \Omega)$ which depends on both \vec{r} and \vec{r}' can then be written as $C_1(\rho - \rho', z, z', \Omega)$.

It is easier to solve equations (4.23) and (4.24) in Fourier space. The Fourier transform in the $x - y$ plane is defined by [31]:

$$C(\vec{r}, \vec{r}', \Omega) = \int_0^\infty \frac{d^2 \vec{q}_\perp}{(2\pi)^2} C(q_\perp, z, z', \Omega) \exp(-i\vec{q}_\perp \cdot (\vec{\rho} - \vec{\rho}')). \quad (4.25)$$

In Fourier space, equations (4.23) and (4.24) become:

$$\left\{ -i\Omega + D(z, \Omega)q_\perp^2 - \frac{\partial}{\partial z} \left(D(z, \Omega) \frac{\partial}{\partial z} \right) \right\} C(q_\perp, z, z', \Omega) = \delta(z - z') \quad (4.26)$$

and

$$\frac{1}{D(z, \Omega)} = \frac{1}{D_B} + \frac{6}{k^2 l_B^*} \int_0^{q_\perp^{\max}} dq_\perp q_\perp C(q_\perp, z, z, \Omega). \quad (4.27)$$

In equation (4.27), a cut-off q_\perp^{\max} has to be introduced in the integral to avoid its divergence.

This cut-off is proportional to the inverse of the transport mean free path:

$$q_\perp^{\max} = \frac{\mu}{l_B^*}. \quad (4.28)$$

The value of μ , the proportionality constant of the cut-off, defines the value of the mobility edge: *i.e.*, the value of kl_s for which the system becomes localized [section 4.5.2.2 c)ii)].

b) Boundary conditions

The medium that is being described is finite, which means that boundary conditions have to be defined. In the slab geometry, there are two boundaries: a plane at $z = 0$ and a plane at $z = L$ (L being the thickness of the slab). At each boundary, there is an average reflection coefficient, R [54], that we assume to be identical on both sides of the sample. An extrapolation length, z_0 , is used to describe the boundary condition [52]. The extrapolation length is the

distance from the surface of the sample at which the intensity extrapolates to zero. The equations used at the boundary are then:

$$C(q_{\perp}, z, z', \Omega) \pm z_0 \frac{D(z, \Omega)}{D_B} \frac{\partial}{\partial z} C(q_{\perp}, z, z', \Omega) = 0. \quad (4.29)$$

The equation with the minus sign is used at $z = 0$ and the one with the plus sign at $z = L$.

The extrapolation length is defined as:

$$z_0 = \frac{2}{3} l_B^* \frac{1 + R}{1 - R}. \quad (4.30)$$

c) Transmission

There are two distinct steps to perform to solve the SCT. First, the diffusion coefficient needs to be calculated for every value of z and Ω . Then, once the diffusion coefficient is known for every position and frequency, the transmission through the sample is calculated.

Equations (4.26), (4.27) and (4.29) are used to find the value of the renormalized diffusion coefficient, $D(z, \Omega)$. Once the diffusion coefficient is known, equation (4.26) is solved one last time to obtain the transmission through the sample. In this last calculation, the source position z' is chosen to be at the same position as during an actual experiment, which is $z' = l_B^*$ inside the sample. This distance is the necessary distance for the direction of an incident pulse to be randomized. To obtain the transmission, the intensity is calculated at the output side of the sample at $z = L$ in equation (4.26). For the first step of the calculation [determination of $D(z, \Omega)$], equation (4.26) is solved for all possible source positions z' along the thickness of the

sample to obtain the return probability everywhere in the sample. Once the diffusion coefficient $D(z, \Omega)$ is known, solving a second time equation (4.23) leads to equation (4.31):

$$\left\{ -i\Omega + D(z, \Omega)q_{\perp}^2 - \frac{\partial}{\partial z} \left(D(z, \Omega) \frac{\partial}{\partial z} \right) \right\} C(q_{\perp}, z, z' = l_B^*, \Omega) = \delta(z - [z' = l_B^*]). \quad (4.31)$$

Equation (4.31) describes the intensity at the position z for a source located at l_B^* inside the sample. Finally, the transmitted flux through the sample is [1]:

$$T(q_{\perp}, \Omega) = -D(z, \Omega) \frac{\partial C(q_{\perp}, z, l_B^*, \Omega)}{\partial z} \Big|_{z=L}. \quad (4.32)$$

Once the transmitted flux in Fourier space is obtained, a double inverse Fourier transform of $T(q_{\perp}, \Omega)$ is performed to get back in real space, both in position and time:

$$T(\vec{\rho}, t) = \int_{-\infty}^{+\infty} \frac{d\Omega}{2\pi} e^{-i\Omega t} \int \frac{d^2 q_{\perp}}{(2\pi)^2} e^{-i\vec{q}_{\perp} \cdot \vec{\rho}} T(q_{\perp}, \Omega). \quad (4.33)$$

The integral over Ω is difficult to evaluate as $T(q_{\perp}, \Omega)$ is a slowly decaying oscillatory function of Ω . The numerical integration would require a fine step in Ω over a large range to be accurate. To solve this issue, the integration is performed in the complex plane. It is known that the function $T(q_{\perp}, \Omega)$ has poles only on the negative part of the imaginary axis [29]. The residue theorem [equation (4.34)] is used to solve the integral over Ω of equation (4.33). The residue theorem states:

$$\oint_{\gamma} f(Z) dZ = 2\pi i \sum_k \text{Res}(f, a_k). \quad (4.34)$$

In the residue theorem, γ is a closed contour of integration in the complex plane, $\text{Res}(f, a_k)$ is the residue of the function at the point a_k (a pole of the function f) inside the integration contour and Z is a complex number on the contour γ . The main consequence of this theorem is that the integration contour γ on which the integration is done can be any contour that includes all the poles.

The original integration path of equation (4.33) is represented by the red line in Figure 4.23, along the real axis of Ω . It is possible to add to this path the blue semi-circle defined with a radius $R \rightarrow \infty$. As $T(q_{\perp}, \Omega) \rightarrow 0$ when $|\Omega| \rightarrow \infty$, the addition of the path on the integration contour does not change the value of the integral. This new path of integration is closed and includes all the poles of $T(q_{\perp}, \Omega)$. According to the Residue theorem, the result of the integral is the same if it is performed on another path which also encloses all the poles. A new path is defined, composed of the two green lines which are at a small distance ε from the imaginary axis, plus the part of the red line and blue line joining them.

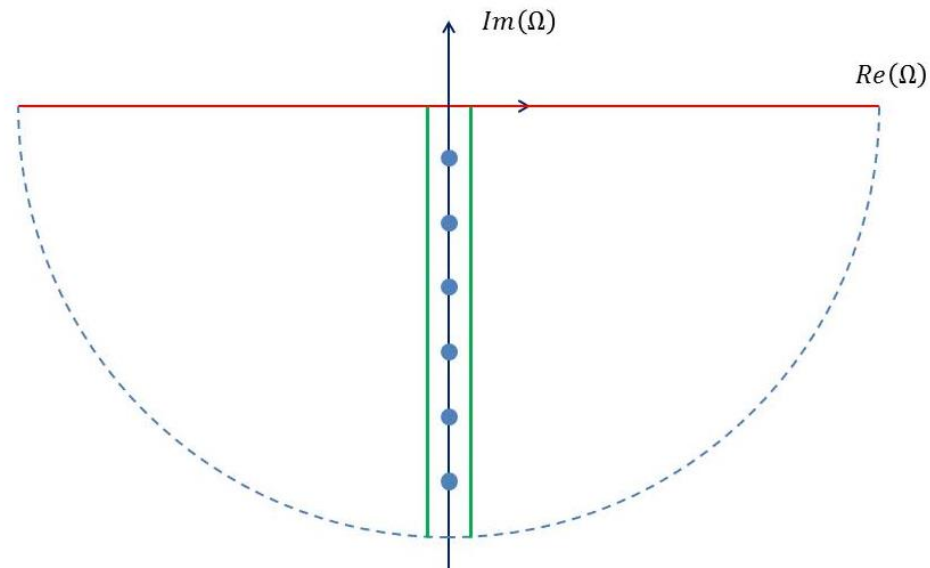


Figure 4.23: $T(q_{\perp}, \Omega)$ represented in the complex plane of Ω . The blue dots represent the poles of the function.

The new path of integration is composed of two lines parallel and as close as possible to the imaginary axis and two little segments along the real axis, and equation (4.33) becomes:

$$\begin{aligned}
T(\vec{\rho}, t) &= \int_{-\infty}^{+\infty} \frac{d\Omega}{2\pi} e^{-i\Omega t} \int \frac{d^2 q_{\perp}}{(2\pi)^2} e^{-i\vec{q}_{\perp} \cdot \vec{\rho}} T(q_{\perp}, \Omega) \\
&= -i \lim_{\varepsilon \rightarrow 0} \int_0^{+\infty} \frac{d\alpha}{2\pi} e^{-\alpha t} \int \frac{d^2 q_{\perp}}{(2\pi)^2} e^{-i\vec{q}_{\perp} \cdot \vec{\rho}} (T(q_{\perp}, \Omega = -i\alpha + \varepsilon) \\
&\quad - T(q_{\perp}, \Omega = -i\alpha - \varepsilon)),
\end{aligned} \tag{4.35}$$

where α represents the negative imaginary part of the complex Ω . This has the effect of changing the inverse Fourier transform in time of equation (4.33) to an inverse Laplace transform [equation (4.35)] in time. Now, we need to calculate $T(q_{\perp}, \alpha)$. The calculation is done only for positive values of α as all the poles of $T(q_{\perp}, \alpha)$ are in the bottom half of the plane [$\text{Im}(\Omega) = -\alpha$]. The $\exp(-\alpha t)$ term in the Laplace transform decays rapidly, so the integral in equation (4.35) is easier to perform numerically than the integral in equation (4.33).

d) What does $T(q_{\perp}, \alpha)$ look like?

A rapid calculation can be done to have an idea of what $T(q_{\perp}, \alpha)$ looks like in the case of perfectly diffusive behaviour ($D = D_B$) and to explain the position of the poles. For a slab, the exact solution for the time and position dependent transmission is [1,17]:

$$T(\rho, t) = \frac{\exp\left(-\frac{\rho^2}{4Dt}\right)}{2\pi Dt} \sum_{m=1}^{\infty} \exp(-D\alpha_m^2 t) f_m(z, z'), \tag{4.36}$$

where the α_m are the positive solutions of the transcendental equation:

$$\tan(\alpha L) = \frac{2\alpha z_0}{(\alpha z_0)^2 - 1}. \quad (4.37)$$

We can obtain an expression for $T(q_{\perp}, \alpha)$ in the perfect diffusive case by taking its Fourier transform in space and its Laplace transform in time:

$$\begin{aligned} T(q_{\perp}, \alpha) &\propto \frac{1}{\sqrt{\alpha}} \otimes \sum_{m=1}^{\infty} \left(\frac{1}{\alpha + D(q_{\perp}^2 + \alpha_m^2)} \right) f_m(z, z') \\ &= \frac{1}{\sqrt{\alpha}} \otimes \sum_{m=1}^{\infty} \left(\frac{1}{\alpha + Dq_{\perp}^2 + \frac{(L + 2z_0)^2 \alpha_m^2}{\pi^2 \tau_D}} \right) f_m(z, z'). \end{aligned} \quad (4.38)$$

In equation (4.38), the diffusion time τ_D has been introduced and represents the characteristic time for the waves to go through a sample of thickness L , with given boundary conditions (characterized in terms of z_0):

$$\tau_D = \frac{(L + 2z_0)^2}{\pi^2 D}. \quad (4.39)$$

By inspection of equation (4.38), we can retrieve the poles that were introduced with the Residue theorem. The location of each pole depends on the value of τ_D and is defined by [29]:

$$\alpha \tau_D + q^2 D \tau_D = \frac{(L + 2z_0)^2}{\pi^2} \alpha_m^2 \quad (4.40)$$

Figure 4.24 shows an example of $T(q_{\perp}, \alpha)$ as a function of $\alpha \tau_D$ in the case $T(q = 0, \alpha)$.

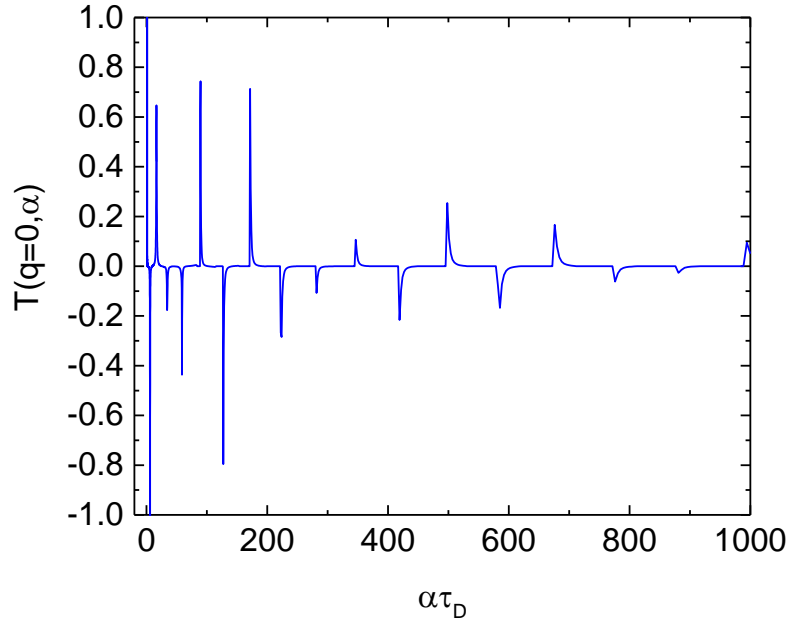


Figure 4.24: $T(q = 0, \alpha)$ for almost diffusive transport. A small imaginary part is added to α to be just off the imaginary axis corresponding to a green line of Figure 4.23, to avoid being exactly at the poles of the function.

As shown in Figure 4.24, $T(q = 0, \alpha)$ is a function made of a lot of very sharp peaks in the case of diffusive transport. These peaks are known as the diffusion poles [29]. When the transport becomes sub-diffusive or localized, the peaks widen and are slightly shifted toward smaller α .

Because it is impossible to have a good discretization of sharp peaks in numerical calculations, having very sharp peaks is an issue for the numerical solutions of the system of equations (4.20) to (4.22). Therefore, to model the transport behaviour, equation (4.21), representing purely diffusive transport, was replaced by equations for renormalized transport very far from localization (sub-diffusive) (see section 4.5.2.3 for the definition of far from localization). As a consequence, I ended up with equations describing two renormalized

transports to model the behaviour in the biphasic sample; they will be discussed in section 4.5.2.3.

4.5.2.2 Solving the SCT numerically [55,53]

a) Dimensionless variables

To solve equations (4.26) and (4.27) numerically, it is easier to solve these equations with dimensionless variables, so the first step is to transform these two equations into dimensionless equations. For each variable of the equations, dimensionless variables are defined:

$$\tilde{z} = z/L, u = (q_{\perp}L)^2, \tilde{\Omega} = \Omega L^2/D_B, \tilde{C} = -i\Omega L \times C, d = D/(-iD_B\tilde{\Omega}).$$

Then, equations (4.26) and (4.27) become:

$$[1 + ud(\tilde{z}, \tilde{\Omega})]\tilde{C}(u, \tilde{z}, \tilde{z}', \tilde{\Omega}) - \frac{\partial}{\partial \tilde{z}} \left[d(\tilde{z}, \tilde{\Omega}) \frac{\partial}{\partial \tilde{z}} \tilde{C}(u, \tilde{z}, \tilde{z}', \tilde{\Omega}) \right] = \delta(\tilde{z} - \tilde{z}') \quad (4.41)$$

and

$$\frac{1}{d(\tilde{z}, \tilde{\Omega})} = -i\tilde{\Omega} + \frac{3}{(kl_B^*)^2} \frac{l_B^*}{L} \int_0^{u_{\max}} \tilde{C}(u, \tilde{z}, \tilde{z}', \tilde{\Omega}) du. \quad (4.42)$$

The Boltzmann diffusion coefficient D_B use in the definition of the dimensionless variables is a fitting parameter for the time scale through the diffusion time τ_D [equation (4.39)].

b) Discretization

The equations (4.41) and (4.42) need to be discretized to solve them numerically. The discretization has to be done for several of the dimensionless variables, the thickness (variable z), the transverse dimension (variable u) and frequency (variable Ω). We can define:

$$z_n = (n - 1)\Delta z \text{ with } \Delta z = \frac{1}{N - 1} \quad (4.43)$$

$$u_\nu = (\nu - 1)\Delta u \text{ with } \Delta u = \frac{1}{M - 1} \quad (4.44)$$

From the discretized variables, the diffusion coefficient d and the intensity \tilde{C} can also be defined for the numerical calculations: $d(z_n, \tilde{\Omega}) = d_n(\Omega)$ and $\tilde{C}(u, z_n, z_m, \tilde{\Omega}) = C_{nm}(u_\nu, \Omega)$ ¹¹.

For each value of Ω , the equation to solve is:

$$\begin{aligned} C_{nm}(u_\nu, \Omega) & [(\Delta z)^2(1 + u_\nu d_n(\Omega)) + 2d_n(\Omega)] \\ & - C_{(n+1)m}(u_\nu, \Omega) \left[d_n(\Omega) + \frac{\Delta z}{2} d'_n(\Omega) \right] \\ & - C_{(n-1)m}(u_\nu, \Omega) \left[d_n(\Omega) - \frac{\Delta z}{2} d'_n(\Omega) \right] = \Delta z \delta_{nm}. \end{aligned} \quad (4.45)$$

d'_n is the derivative of the diffusion coefficient with respect to the position: $d'_n = (d_{n+1} - d_{n-1})/2\Delta z$.

Equation (4.45) can also be written as:

$$a_n C_{nm}(u_\nu, \Omega) + b_n C_{(n+1)m}(u_\nu, \Omega) + c_n C_{(n-1)m}(u_\nu, \Omega) = \Delta z \delta_{nm}. \quad (4.46)$$

This equation can be seen as a multiplication of tridiagonal matrix \mathbf{M} [$\mathbf{M}(n, n) = a_n$, $\mathbf{M}(n, n + 1) = b_n$ and $\mathbf{M}(n, n - 1) = c_n$] with the matrix \mathbf{C} [$\mathbf{C}(n, m) = C_{nm}$]. We can solve for \mathbf{C} by inverting the matrix \mathbf{M} . The diffusion coefficient is calculated using the discretized version of equation (4.42) (C_{mm} represents the return probability):

¹¹ In the discretized equations, the tilde of the dimensionless variables is omitted to reduce the complexity of the notation.

$$\frac{1}{d_m(\Omega)} = -i\Omega + \frac{3}{(kl_B^*)^2} \frac{l_B^*}{L} \Delta u \left\{ \sum_{v=1}^M C_{mm}(u_v, \Omega) - \frac{1}{2} (C_{mm}(u_1, \Omega) + C_{mm}(u_M, \Omega)) \right\}. \quad (4.47)$$

The transmission is obtained using equation (4.32) and can be expressed with the dimensionless and discretized variables [using a discretized version of the boundary condition defined in equation (4.29)]:

$$\begin{aligned} T(q_{\perp}, \Omega) &= -D(z, \Omega) \frac{\partial C(q_{\perp}, z, l_B^*, \Omega)}{\partial z} \Big|_{z=L} \\ &= \frac{D_B C(q_{\perp}, z, l_B^*, \Omega)}{z_0} \Big|_{z=L} \\ &= -\frac{C_{Nm'}(u_v, \Omega)}{i\tilde{\Omega}\tilde{z}_0}. \end{aligned} \quad (4.48)$$

In the last line of the equation (4.48), $C_{Nm'}(u_v, \Omega)$ represents the energy density at the position N (i.e., $z = L$) for a source at the position m' ($z' = l_B^*$).

c) How to solve the system of equations

i) *Numerical technique*

There are two steps to solve this system of equations. First, the value of the diffusion coefficient needs to be found, and then, the transmission through the sample can be calculated. The calculation of the diffusion coefficient is done by iteration: it starts by assuming the

diffusion coefficient to be equal to the Boltzmann diffusion coefficient D_B^{12} , and then it calculates the return probability for each source position z' , and finally from this return probability, a new value of the diffusion coefficient using equation (4.42) is obtained. This operation is repeated until no more modification of $D(z, \Omega)$ is happening within a specified convergence criterion: the maximum percentage difference allowed for D is 10^{-5} from one iteration step to the next one.

Once the final values of $D(z, \Omega)$ are obtained, the transmission is calculated when the source is at the right position (l_B^* inside the sample) and when the observation is done at the position L (thickness of the sample).

ii) Parameters

The parameters to solve the SCT can be separated into two categories, the physical parameters of the sample and the parameters characterizing the discretization of the system.

Parameters of the sample:

- L : thickness of the sample
- R : mean reflection coefficient
- l_s : scattering mean free path
- l_B^* : transport mean free path
- kl_s : wave number times scattering mean free path
- kl_c : value of kl_s at the mobility edge (adjustable parameter)

¹² In order to reduce the calculation time, the diffusion coefficient is assumed to be equal to the Boltzmann diffusion coefficient at the beginning of the iteration, for the first value of Ω . For the next value of Ω , the first guess for the diffusion coefficient is the diffusion coefficient obtained at the end of the iteration for the previous Ω . The results for the diffusion coefficient are quite close from one value of Ω to the next one.

Numerical parameters

- $\alpha_{\min}, \alpha_{\max}$: range of value of α (Laplace transform variable corresponding to frequency)
- $n_{\text{alpha}}, n_z, n_u$: number of points used for α, L and u_{\max}
- $n_{\text{iter}}, \varepsilon_0$: maximum number of iterations and convergence criterion

From these parameters, we can determine the ratio of the thickness L over the localization length ξ (see the supplementary material of [7]):

$$\frac{L}{\xi} = \frac{Ll_B^*(kl_c)^2(1 - \chi^4)}{6\chi^2l_s^2} \text{ with } \chi = \frac{kl_s}{kl_c} \quad (4.49)$$

When the value of L/ξ given by this expression is positive, the transport is localized, if it is negative, by this convention, the transport is sub-diffusive ($kl_s > kl_c$).

Most of the parameters can be determined experimentally for a given sample. From the ballistic measurement, l_s , the phase velocity, and kl_s ($k = \omega/v_p$) can be accessed. The reflection coefficient is calculated from the phase velocity and the density [54]. In the end, there are only three parameters l_B^* , kl_c and D_B that need to be determined by comparing model predictions with experimental data for the time of flight profiles and the width squared.

iii) Definition of q_{\max}

The cut-off value for the integration over q [equation (4.27)] is defined as $q_{\max} = \mu/l_B^*$, with μ close to one. In the model, we define:

$$\mu = \frac{1}{3}(kl_c)^2 \left(\frac{l_B^*}{l_s} \right)^2 \quad (4.50)$$

This definition of u_{\max} ensures that the mobility edge is occurring for $kl_s = kl_c$.

4.5.2.3 Two coupled components

For the system made of aluminum beads in a liquid, the next step is to describe how to make quantitative calculations of model predictions for the coupled propagation of a diffusive mode and a renormalized mode. As seen with equation (4.38) and with Figure 4.24, the Laplace transform of the expression describing diffusive transmission is made of very sharp Dirac peaks, which makes numerical calculations problematic. To go around this issue, it was decided to use two renormalized diffusion coefficients with one of them being calculated at a large negative value of L/ξ . For example, when kl_s is 3 to 5 times bigger than kl_c , L/ξ will be smaller than -50, which is small enough to obtain almost perfectly diffusive behaviour.

The system of equations to solve is:

$$\begin{aligned} \left\{ -i\Omega + D_1(z, \Omega)q_{\perp}^2 - \frac{\partial}{\partial z} \left(D_1(z, \Omega) \frac{\partial}{\partial z} \right) \right\} C_1(q_{\perp}, z, z', \Omega) \\ = \delta(z - z') + \theta [C_2(q_{\perp}, z, z', \Omega) - C_1(q_{\perp}, z, z', \Omega)], \end{aligned} \quad (4.51)$$

$$\begin{aligned} \left\{ -i\Omega + D_2(z, \Omega)q_{\perp}^2 - \frac{\partial}{\partial z} \left(D_2(z, \Omega) \frac{\partial}{\partial z} \right) \right\} C_2(q_{\perp}, z, z', \Omega) \\ = \theta [C_1(q_{\perp}, z, z', \Omega) - C_2(q_{\perp}, z, z', \Omega)], \end{aligned} \quad (4.52)$$

and

$$\frac{1}{D_1(z, \Omega)} = \frac{1}{D_{B1}} + \frac{6}{k_1^2 l_{B1}^*} \int_0^{q_{\perp}^{\max}} dq_{\perp} q_{\perp} C_1(q_{\perp}, z, z, \Omega). \quad (4.53)$$

The diffusion coefficient of the diffusive component, $D_2(z, \Omega)$, is calculated without any coupling between the two components, using the system of equations (4.26) and (4.27). Once this diffusion coefficient is obtained, it is used in the new system of equations (4.51) to (4.53), without any further renormalization. D_2 obtained from the SCT with $L/\xi < -50$ is very close to

the diffusion coefficient of a perfectly diffusive transport. The use of this diffusion coefficient, without its renormalization in the system of equations (4.51) to (4.53) allows me to have a model as close as possible to the original model I wanted, using a perfectly diffusive transport [equations (4.20) to (4.22)]. Consequently, in this new model [equations (4.51) to (4.53)], only one of the two diffusion coefficients is calculated [equation (4.53)]. As has been discussed earlier [section 4.5.2.2 c)i)], two steps are needed to solve the SCT equations. First, the diffusion coefficient is calculated, followed by the actual transmission through the sample.

The calculation of the diffusion coefficient is made using a Dirac source $[\delta(z - z')]$ at every position z in the sample. Once the diffusion coefficient is known for all z and Ω , a point source is used on the input side of the sample (at a distance l_B^* inside the sample), and the transmission is calculated on the other side of the sample:

$$\begin{aligned} & \left\{ -i\Omega + D_1(z, \Omega)q_{\perp}^2 - \frac{\partial}{\partial z} \left(D_1(z, \Omega) \frac{\partial}{\partial z} \right) \Big|_{z=L} \right\} C_1(q_{\perp}, z = L, z' = l_{B1}^*, \Omega) \\ & = \beta \delta(z - z') \\ & + \theta [C_2(q_{\perp}, z = L, z' = l_{B1}^*, \Omega) - C_1(q_{\perp}, z = L, z' = l_{B1}^*, \Omega)] \end{aligned} \quad (4.54)$$

and

$$\begin{aligned} & \left\{ -i\Omega + D_2(z, \Omega)q_{\perp}^2 - \frac{\partial}{\partial z} \left(D_2(z, \Omega) \frac{\partial}{\partial z} \right) \Big|_{z=L} \right\} C_2(q_{\perp}, z = L, z' = l_{B1}^*, \Omega) \\ & = (1 - \beta) \delta(z - z') \\ & + \theta [C_1(q_{\perp}, z = L, z' = l_{B1}^*, \Omega) - C_2(q_{\perp}, z = L, z' = l_{B1}^*, \Omega)]. \end{aligned} \quad (4.55)$$

Here, the source is shared between the two components to reflect the amount of energy entering the sample in the liquid or the solid phase (β represents the distribution of the source between the two components). Of course, to solve the system of equations (4.51) to (4.53) [or

(4.54) and (4.55)], boundary conditions are needed. They are identical to the one described in equation (4.29) for each component.

a) Dimensionless variables

For simplicity, these equations are solved with dimensionless variables. For each variable of the equations, a dimensionless variable is defined:

$$\begin{aligned} \tilde{z} &= z/L, & u &= (q_{\perp}L)^2, & \tilde{\Omega} &= \Omega L^2/D_{B1}, & \tilde{C}_1 &= -i\Omega L \times C_1, & \tilde{C}_2 &= -i\Omega L \times C_2, \\ d_1 &= D_1/(-iD_{B1}\tilde{\Omega}), & d_2 &= D_2/(-iD_{B1}\tilde{\Omega}), & \tilde{\theta} &= \theta L^2/D_{B1}. \end{aligned}$$

Using dimensionless variables, equations (4.51) to (4.53) become:

$$\begin{aligned} &\left\{1 + d_1(\tilde{z}, \tilde{\Omega})u - \frac{\partial}{\partial \tilde{z}}\left(d_1(\tilde{z}, \tilde{\Omega})\frac{\partial}{\partial \tilde{z}}\right)\right\}\tilde{C}_1(u, \tilde{z}, \tilde{z}', \tilde{\Omega}) \\ &= \delta(\tilde{z} - \tilde{z}') + i\frac{\tilde{\theta}}{\tilde{\Omega}}\left(\tilde{C}_2(u, \tilde{z}, \tilde{z}', \tilde{\Omega}) - \tilde{C}_1(u, \tilde{z}, \tilde{z}', \tilde{\Omega})\right), \end{aligned} \quad (4.56)$$

$$\begin{aligned} &\left\{1 + d_2(\tilde{z}, \tilde{\Omega})u - \frac{\partial}{\partial \tilde{z}}\left(d_2(\tilde{z}, \tilde{\Omega})\frac{\partial}{\partial \tilde{z}}\right)\right\}\tilde{C}_2(u, \tilde{z}, \tilde{z}', \tilde{\Omega}) \\ &= i\frac{\tilde{\theta}}{\tilde{\Omega}}\left(\tilde{C}_1(u, \tilde{z}, \tilde{z}', \tilde{\Omega}) - \tilde{C}_2(u, \tilde{z}, \tilde{z}', \tilde{\Omega})\right), \end{aligned} \quad (4.57)$$

and

$$\frac{1}{d_1(\tilde{z}, \tilde{\Omega})} = -i\tilde{\Omega} + \frac{3}{(k_1 l_{B1}^*)^2} \frac{l_{B1}^*}{L} \int_0^{u_{\max}} du \tilde{C}_1(u, \tilde{z}, \tilde{z}, \tilde{\Omega}) \quad (4.58)$$

The boundary conditions can also be written with dimensionless variables. For each of the components, equation (4.29) becomes:

$$\widetilde{C}_1(u, \tilde{z}, \tilde{z}', \tilde{\Omega}) \mp i\tilde{z}_{01}\tilde{\Omega}d_1(\tilde{z}, \tilde{\Omega}) \frac{\partial}{\partial \tilde{z}} \widetilde{C}_1(u, \tilde{z}, \tilde{z}', \tilde{\Omega}) = 0 \quad (4.59)$$

and

$$\widetilde{C}_2(u, \tilde{z}, \tilde{z}', \tilde{\Omega}) \mp i\tilde{z}_{02}\tilde{\Omega}d_2(\tilde{z}, \tilde{\Omega}) \frac{D_{B1}}{D_{B2}} \frac{\partial}{\partial \tilde{z}} \widetilde{C}_2(u, \tilde{z}, \tilde{z}', \tilde{\Omega}) = 0 \quad (4.60)$$

The dimensionless variables have been defined using D_{B1} , and this choice leads to the ratio D_{B1}/D_{B2} in equation (4.60), which is a parameter of the calculations that has to be determined by comparison with the experimental data. The value of D_{B2} is known experimentally, since $1/4D_{B2}$ corresponds to the initial slope of the dynamic transverse width squared of the intensity beam (Figure 4.17).

b) Discretization

The discretization of the equations (4.56) to (4.60) is done the same way as explained in section 4.5.2.2 b). Equations (4.56) and (4.57) (with the boundary conditions) can be reduced to the multiplication of a tridiagonal matrix with $C_{1,nm}$ (or $C_{2,nm}$) equal to the right-hand side of the equations.

The last step of the calculation, the actual calculation of the transmission, is different with the two coupled components compared to a single component SCT. If $C_{1,sm}(u_\nu, \Omega)$ represents the value of $C_1(q_\perp, z, z', \Omega)$ with the source position defined as $z' = l_B^*$ (s is the position index of the source), equations (4.54) and (4.55) become:

$$AC_{1,sm}(u_\nu, \Omega) = \beta\delta_{sm} + \theta[C_{2,sm}(u_\nu, \Omega) - C_{1,sm}(u_\nu, \Omega)] \quad (4.61)$$

and

$$BC_{2,sm}(u_\nu, \Omega) = (1 - \beta)\delta_{sm} + \theta[C_{1,sm}(u_\nu, \Omega) - C_{2,sm}(u_\nu, \Omega)]. \quad (4.62)$$

$C_{1,sm}(u_\nu, \Omega)$ in equations (4.61) and (4.62) is actually a vector, not a matrix, as only one of the indices varies, the index of the source s being fixed. \mathbf{A} and \mathbf{B} are tri-diagonal matrices defined in a similar manner to the matrix \mathbf{M} of section 4.5.2.2 b) defined from the equation (4.46). The two last equations [(4.61) and (4.62)] can be inverted to obtain the results shown in equations (4.63) and (4.64):

$$C_{1,sm} = \left(\mathbf{A}' - \theta^2 \mathbf{B}'^{-1} \right)^{-1} (\beta \delta_{sm} + \theta \mathbf{B}'^{-1} (1 - \beta) \delta_{sm}) \quad (4.63)$$

and

$$C_{2,sm} = \left(\mathbf{B}' - \theta^2 \mathbf{A}'^{-1} \right)^{-1} ((1 - \beta) \delta_{sm} + \theta \mathbf{A}'^{-1} \beta \delta_{sm}). \quad (4.64)$$

Two new matrices have been defined to write (4.63) and (4.64): $\mathbf{A}' = \mathbf{A} + \theta \mathbf{I}$ (and similarly $\mathbf{B}' = \mathbf{B} + \theta \mathbf{I}$), \mathbf{I} being the identity matrix. In order to simplify the calculation of this last step, the small θ^2 term can be neglected:

$$C_{1,sm} = \mathbf{A}'^{-1} (\beta \delta_{sm} + \theta \mathbf{B}'^{-1} (1 - \beta) \delta_{sm}) \quad (4.65)$$

and

$$C_{2,sm} = \mathbf{B}'^{-1} ((1 - \beta) \delta_{sm} + \theta \mathbf{A}'^{-1} \beta \delta_{sm}). \quad (4.66)$$

This simplification can be checked once the calculation is done: θ^2 needs to be negligible compared to all the diagonal elements of \mathbf{A}' and \mathbf{B}' .

c) Computational technique

As explained in the section 4.5.2.2 c), an iterative procedure is needed to solve the SCT: the diffusion equation is solved first to calculate the return probability and with this probability, the diffusion coefficient is recalculated. This process is then repeated iteratively, using the recalculated diffusion coefficient in the diffusion equation to obtain an improved calculation of

the return probability, and so on until the solution converges. The same technique is used for the calculations with the two coupled components. Also, for each of the two components a set of parameters similar to the one explained in part 4.5.2.2 c) has to be defined.

The main difference between the computational approach explained in section 4.5.2.2 c)i) and the case with the two coupled components is the first “guess” of the diffusion coefficient of the renormalized component. Instead of setting the initial parameter at the beginning of the iteration to be the Boltzmann diffusion coefficient, the starting values of the diffusion coefficient are obtained from an uncoupled calculation ($\theta = 0$) with all other parameters being the same. It is assumed that the coupling of the two components only adds a correction factor to the classic calculation, so that with this alternative approach more rapid convergence can be achieved.

The overall idea for the iterative process is very similar to the one described previously [section 4.5.2.2 c)i)]. \widetilde{C}_1 [equation (4.56)] and \widetilde{C}_2 [equation (4.57)] are calculated; these values are used to calculate d_1 [equation (4.58)] and the new value of d_1 is used to recalculate the two intensities. When the iteration has converged, meaning that the change in d_1 between the last two steps of the iteration is less than a predefined convergence criterion, the last step of the calculation is performed, and the transmission for a source position is calculated.

In the new calculation, there is a large number of parameters. The list of parameters can be divided into four parts: the parameters for each of the two components (identical to the list “parameters of the sample” in part 4.5.2.2 c), the numerical discretization parameters of the calculation [see the list for the classic SCT calculation, section 4.5.2.2 c)ii)] and the four parameters linking the two components:

- θ (s^{-1}): the coupling constant between the two components (transfer rate)
- D_{B1}/D_{B2} : the ratio of the two Boltzmann diffusion coefficients.
- β : distribution of the source between the two components
- γ : the ratio of the two components on the output side

4.5.2.4 Parameters of the calculation

Among the large number of parameters, some of them can be determined experimentally, such as, in particular, the parameters governing the diffusive component going through the liquid. For the second component, some of the parameters can be measured, but the other ones will be used as adjustable parameters to be determined through the comparison of the theoretical predictions to the experimental results.

a) Parameters of the diffusive component

Most of the parameters for the diffusive component can be measured using the ballistic signal shown in part 4.4.1 or are general properties of the sample. Properties of the diffusive components can be extracted from the ballistic measurement as this component dominates the signal at short times. According to the ballistic measurement, the scattering mean free path l_s ranges from 1 mm to 1.5 mm and kl_s from 5 to 10 in the frequency range of interest. The thickness of the sample is known ($L = 12.7$ mm). The velocity obtained with the ballistic data can be used to calculate the average reflection coefficient [54], using also the density of the fluid and the properties of water (the outside medium). The value obtained for the reflection coefficient is $R = 0.6$. The transport mean free path is harder to determine, we know that it is larger than the scattering mean free path so I choose $l_B^* = 2$ mm (see chapter 2). The last parameter to determine for the diffusive component is the critical value of kl , kl_c . This

component needs to be almost diffusive, so a large negative value of L/ξ is needed. For $kl_s = 5$ and $kl_c = 1$, we have $L/\xi \approx -100$, leading to an almost perfectly diffusive behaviour¹³.

b) Parameters of the renormalized component

It is more difficult to obtain parameters for the renormalized component, as the ballistic signal of this component cannot be measured for this sample since it is buried in the coda of the diffusive (and possibly also the renormalized) component. Some parameters can be estimated if we assume, since the resonant frequencies of the beads in liquid or in vacuum are almost identical, that the properties of the network of beads surrounded by a liquid are not too different from the properties of a sample made of brazed beads in vacuum. In the latter case, the wave can travel only through the beads, as no acoustic wave propagation can occur in vacuum. The parameters used to describe the component travelling through the network of beads were estimated based on fits of self-consistent theory predictions to experimental data on brazed aluminum bead samples [3,35,39]. Based on these results, the parameters used in my calculations are: $kl_s = 2.87$, $l_s = 1.0$ mm, $l_B^* = 2.0$ mm and $R = 0.667$. The remaining parameter, kl_c , cannot be determined from these results and therefore is used as a adjustable parameter of the model. It controls how strongly the second component is renormalized: the closer kl_c is to kl_s , the more renormalized is the propagation through the network of beads. In particular, if kl_c is bigger than kl_s the second component behaves as though it were localized.

c) Parameters linking the two components

Four parameters making the link between the two components [see the list in section 4.5.2.3 c)] have to be determined. θ represents the exchange rate of energy between the two

¹³ Taking into account the entire ranges of scattering mean free path and of kl_s , L/ξ goes from -50 to -400.

components, and so it is the reciprocal of a characteristic time. As has been discussed in chapter 3 with the Simsonic simulations, the decay time of energy is quite long for a single bead, a characteristic dwell time of approximately $5 \mu\text{s}$ is calculated (see chapter 2) (after the bead is hit by $1.5\text{-}\mu\text{s}$ long signal). This $5 \mu\text{s}$ represents a lower bound of the dwell time as the long-time decay is not included in this simulation. This decay time will be even larger when the number of beads is increased, as more back and forth propagation of waves, to and from neighbouring beads, will happen around a given bead. The minimum value of characteristic decay time being around $5 \mu\text{s}$ means that the maximum possible value of θ should be of the order of $0.2 \mu\text{s}^{-1}$, with a value of approximately 10 times smaller being more likely.

The ratio of the two Boltzmann diffusion coefficients can be seen as the ratio of each component's time scales, each of them being defined with their diffusion times τ_D , which are inversely proportional to their respective D_B . The two time scales cannot be hugely different as the two components overlap, *i.e.*, their time-of-flight profiles are not distinctly separated as a function of time. As a consequence, it is likely that D_{B1}/D_{B2} is between 0.1 and 10, constraining the starting value of this ratio in the calculations.

The ratio of the energy going into each component, β , can be estimated by looking at the average reflection coefficients [54] for acoustic waves in water at an interface between a medium with properties of the fast component (travelling in the liquid), and at an interface between water and a medium with properties of the slow component (travelling in the aluminum beads). An important consideration is that this interface is not flat, but follows the contours imposed by the beads; therefore the reflection of waves over a large range of effective incident angles has to be taken into account, just as for diffuse waves trying to leave the sample from inside [49,54]. The density of the liquid is $d = 760 \text{ kg/m}^3$ and the velocity is $0.894 \text{ mm}/\mu\text{s}$, leading to an average

reflection coefficient from water to the sample $R = 0.26$, using the calculations explained in reference [49]. It means that 74% of the energy can enter the sample in the liquid surrounding the beads. As a comparison, the average reflection coefficient between water and aluminum beads is $R = 0.92$ ¹⁴. The large difference between these two values of R is due to the presence of a critical angle for the waves going from water to aluminum. The sample is composed of 45 % liquid and 55 % aluminum beads, which corresponds also to the fractions of aluminum and liquid touching the surface of the sample. By weighting the quantity of energy entering the sample for each component with the surface area of solid or liquid, I estimate that 90 % of the energy entering the sample is entering in the liquid (fast component) and 10 % in the aluminum beads (slow component). Thus, the ratio of energy initially coupling into the slow component divided by the corresponding quantity for the fast component is $\beta \approx 0.1$.

The same idea is applied on the output side of the sample: the two components are summed with some weight. This weight depends on the average reflection coefficient of each component. By taking the properties of the silicone oil for the diffusive (or fast) component, the value of the average reflection coefficient is $R = 0.6$ [49]. Most of the calculation of the renormalized (or slow) component has been done with $R = 0.667$, used by Laura Cobus in her Ph.D Thesis [39] for a sample made of aluminum beads in vacuum. As these two values of R are close to each other, and the surface area of each component on the output side are approximately equal, the weight of each component should be similar. Consequently, the parameter γ introduced in section 1.5.2.3 c) should be close to 0.5.

¹⁴ This reflection coefficient is obtained from the amplitude reflection coefficient of a liquid on a solid [11] and by calculated the mean reflected flux [46].

d) Parameters of the numerical calculation

Numerical calculations are done on a discretized grid in space and time. In the context of these calculations, *i.e.*, using a slab geometry in the Fourier domain for two of the dimensions and in the Laplace domain for the time, there are three parameters to discretize: the thickness L of the sample, the conjugate variables q and α of the transverse dimension ρ and the time t .

The thickness is divided in n_z intervals of size Δz . The value of Δz needs to be smaller than all the dimensions in the numerical calculations. The smallest parameter being l_s for both components, Δz needs to be at least ten times smaller than the smaller of the two l_s . In all the simulations done, n_z has been chosen to be 301, corresponding to $l_s \approx 24\Delta z$ for $l_s = 1$ mm, the smallest of the scattering mean free path. It is important to keep n_z small as the calculation time is very dependent on this value, *via* the inversion of square matrices of size n_z . Moreover, the larger the matrices, the less accurate is the inversion.

The conjugate value of the transverse dimension, q_{\perp} , has to go from 0 to q_{\perp}^{\max} [equation (4.28)], and is divided into n_u intervals. A typical value used for n_u is 600. One can think that having a larger n_u will improve the simulation accuracy, but I have noticed that the results of the calculations for my system do not vary if the number n_u is increased.

For the Laplace transform equivalent of frequency, I need to choose the minimum value α_{\min} , the maximum value α_{\max} as well as the number of points n_{α} . In the calculation α is normalized by the diffusion time τ_D . As explained in the section 4.5.2.1 d), $T(q, \alpha)$ is a very peaked function. As alpha corresponds to a frequency, small or large alpha corresponds to long ($t > \tau_D$) or short times ($t < \tau_D$) respectively. The value of $T(q, \alpha)$ describes, therefore, the long- or short-time behaviour depending on the value of alpha. Consequently, because the first

peak of $T(q, \alpha)$ describes the long-time decay of the intensity, it is very important to have an α small enough to capture it. The peaks at large α describe the short time increase of the intensity. Usually, in these simulations, $\alpha_{\min} = 0.01$ and $\alpha_{\max} = 1000$ with $n_\alpha = 2000$. The chosen value of α_{\max} is enough to describe accurately the behaviour at short times. The spacing between each value of α is defined exponentially and not linearly to obtain a good description of all the time scales. Furthermore, a large number of α is needed to resolve accurately these sharp peaks in $T(q, \alpha)$.

4.5.2.5 Predictions of the model

Numerical calculations for different sets of parameters have been performed in order to study their effects on the transport. In the results presented in the following paragraphs many of these parameters are well enough known independently that they are always fixed. For all of them, the subscript “1” refers to the slow, renormalized component and “2” to the fast, mostly diffusive component as defined in equations (4.51) to (4.66). The fixed parameters are:

- $kl_{s1} = 2.87$
- $l_{s1} = 1 \text{ mm}$
- $l_{B1}^* = 2 \text{ mm}$
- $kl_{s2} = 5.00$
- $kl_{c2} = 1.00$
- $l_{s2} = 1 \text{ mm}$
- $l_{B2}^* = 2 \text{ mm}$
- $R_2 = 0.6$
- $L = 12.7 \text{ mm}$
- $\beta = 0.1$

The values of kl_{s2} and kl_{c2} lead to $L/\xi_2 = -103$ giving an almost perfectly diffusive mode.

The parameters that are allowed to vary are:

- kl_{c1}
- R_1
- D_{B1}/D_{B2}
- θ
- γ

The variation of kl_{c1} is used to modify the value of L/ξ_1 . By convention, we sometimes employ the term “time-of-flight profile” to describe the “intensity” profile. The calculated time-of-flight profiles $T(t, \rho)$ displayed in the following figures and used to calculate the width squared are the weighted sum of the two component intensities:

$$T(t, \rho) = \gamma T_1(t, \rho) + (1 - \gamma) T_2(t, \rho). \quad (4.67)$$

a) Comparison with the uncoupled propagation

Before presenting the results of the total intensity (sum of the two components), the intensity profile of each component obtained in the case of two coupled propagating components are compared to the profiles obtained in the case of only one component propagating in the medium [solution of the equations (4.23) and (4.24)] for the same set of parameters.

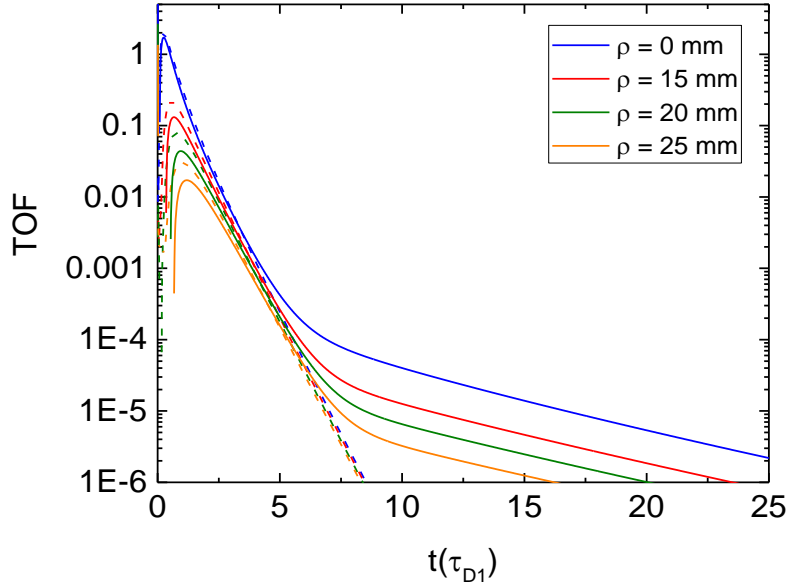


Figure 4.25: Comparison between the results of the simulation for uncoupled propagation (dashed) of the fast component and the equivalent component in the coupled case (line). The color code is the same for both cases.

In Figure 4.25, the fast-diffusive component is displayed. The time scale is normalized with the diffusion time τ_D of the slow component. All the parameters of the fast-diffusive component are defined in section 4.5.2.5, and the calculation for the coupled situation has been done with:

- $kl_{c1} = 2.85$
- $R_1 = 0.666$
- $D_{B1}/D_{B2} = 1$
- $\theta = 0.01 \mu S^{-1}$

The chosen value of kl_{c1} leads to $L/\xi_1 = -1$.

The main difference between the two situations in Figure 4.25 is observed at long-times, after $10\tau_D$. The decay of the fast component slows down dramatically when a slow component, coupled to the first one, is in the medium. The slow component is feeding the fast component *via* the coupling term θ . At short times, for the non-zero values of ρ , the maximum of the intensity is smaller when the second component is present. This reduction of the maximum is

due to the transfer of some of the energy of this component to the other component which is occurring even at such short times. This is more visible for the large values of ρ , as the path to reach the output of the sample is then longer. When ρ is zero, *i.e.*, on axis propagation, no difference is visible.

Figure 4.26 presents the intensities of the slow component with or without coupling.

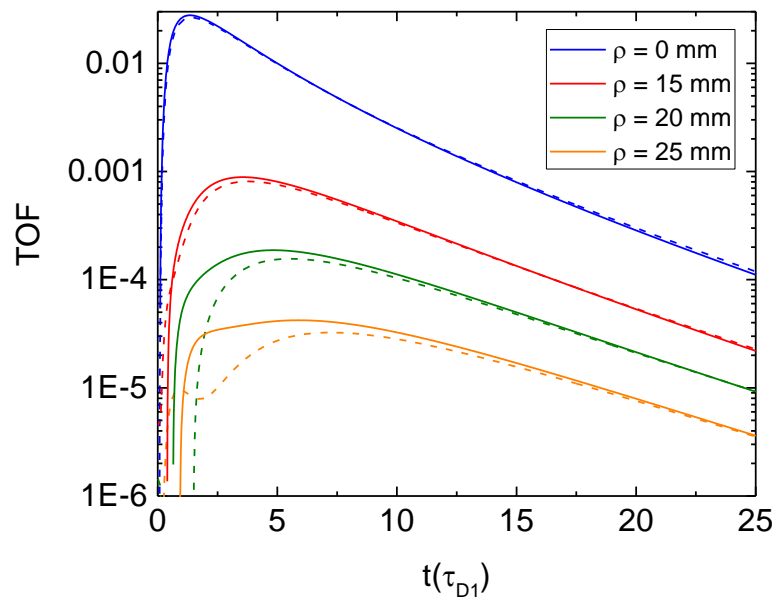


Figure 4.26: Comparison between the results of the calculation for uncoupled propagation (dashed) and the equivalent component in the coupled case (line). The color code is the same for both cases.

The parameters used to obtain Figure 4.26 are the same as the ones used to obtain Figure 4.25. Unlike the fast-diffusive-component intensity profiles in Figure 4.25, the main differences between the coupled and uncoupled cases for the slow component are observed at short times. The intensity of the slow component at short times is higher for larger ρ when there is a coupling with a fast component. This is coherent with the decrease of the maximum of intensity of the fast component at short times observed in Figure 4.25. Indeed, the loss of energy of the fast

component observed in Figure 4.25 corresponds to the gain in energy of the slow component in Figure 4.26. The change at long times in Figure 4.26 is not as dramatic as the one observed in Figure 4.25; it looks like the long times are not influenced a lot by the coupling as far as the slow component is concerned. By comparing the two figures, we can see that there is at least one order of magnitude difference between the coupled fast and slow component intensities at long times. Therefore, the fast component cannot influence the slow component as strongly as the slow component can affect the fast component at long times.

b) Time of flight profiles: comparison of slow and fast coupled components

The total intensity displayed in Figure 4.27 has been obtained for equal weight of both components ($\gamma = 0.5$); all the other parameters are the same as the ones used in section 4.5.2.5 a). In this figure, the transition between the two propagating components inside the sample can clearly be seen by the change in the decay of the total intensity, happening between 5 and $8 \tau_D$. The total intensity follows the fast component intensity until $5 \tau_D$ and the slow component intensity after $8 \tau_D$.

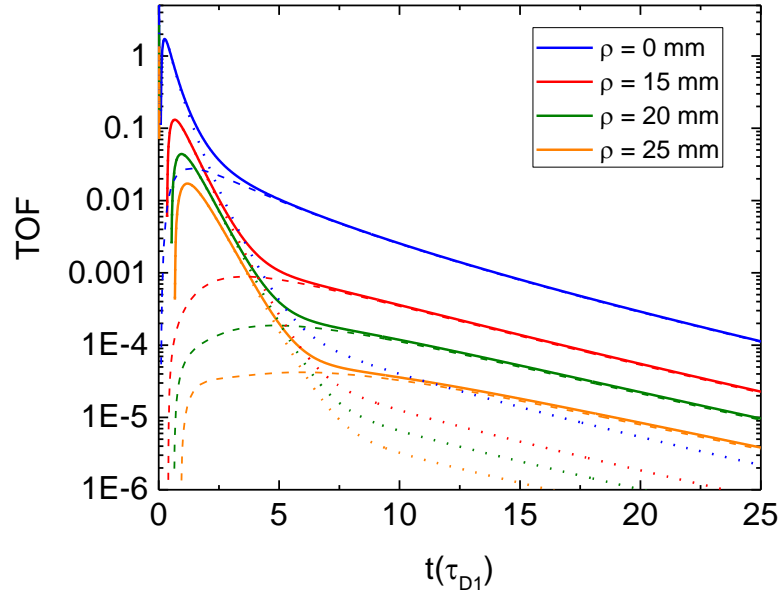


Figure 4.27: Time of flight of the two individual components (with coupling): fast diffusive component (dot) and slow renormalized component (dashed), as well as the total intensity (solid line).

In Figure 4.25, Figure 4.26 and Figure 4.27, the time axis is normalized by the diffusion time of the slow component which depends on the thickness of the sample and on the reflection coefficient [equation (4.39)]. In the following sections, the variations of the calculation results with several parameters are investigated. In order to compare some of these results, and because the value of τ_{D1} varies depending on the parameters of the calculation, in particular the reflection coefficient, an absolute time scale has to be defined. The best way to choose a time scale is to fix the value of D_{B2} by looking at the experimental value of the initial slope of the width squared, which should correspond quite closely to the diffusion coefficient of the fast mode. Here, $D_{B2} = 0.9 \text{ mm}^2/\mu\text{s}$ is chosen. If \tilde{t} is the dimensionless time normalized by τ_{D1} , the absolute time t can then be defined as [with z_{01} depending on R_1 , equation (4.30)]:

$$t = \tilde{t} \tau_{D1} = \frac{\tilde{t}(L + 2z_{01})^2}{\pi^2 D_{B1}} = \tilde{t}(L + 2z_{01})^2 \frac{D_{B2}}{D_{B1}} \frac{1}{\pi^2 D_{B2}}. \quad (4.68)$$

c) Influence of L/ξ_1

L/ξ_1 influences the renormalisation of the slow component travelling through the sample and is determined by the value of kl_{c1} . If kl_{c1} is larger than kl_{s1} , the slow component is localized and if kl_{c1} is smaller than kl_{s1} , the slow component is sub-diffusive. Figure 4.28 shows the width squared obtained for different values of L/ξ_1 . The other parameters are $R_1 = 0.666$, $D_{B1}/D_{B2} = 1$, $\theta = 0.01 \mu\text{s}^{-1}$ and $\gamma = 0.5$.

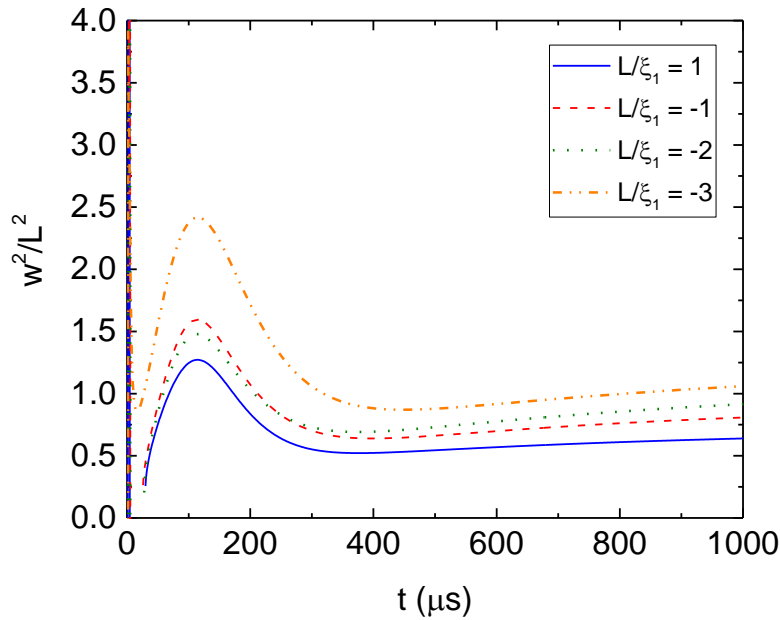


Figure 4.28: Width squared for four different values of L/ξ_1 . The width squared is calculated for $\rho = 15$ mm.

L/ξ_1 influences the overall magnitude of the width squared, both the height of the maximum and its long-time value: the more negative is L/ξ_1 , the higher is the magnitude and the steeper is

the long-time slope of the width squared. The overall transition time between the two components (which component dominates at a given time), determined by the width of the peak, is not strongly influenced by this parameter.

d) Influence of R_1

The value of the reflection coefficient of the slow component changes the decay rate of this component: the larger R_1 is, the longer it takes for the energy to get out of the sample. R_1 is used in the calculation of the diffusion time for this reason. The parameters used to obtain Figure 4.29 are the same as in the previous section (section 4.5.2.5) with $L/\xi_1 = -1$.

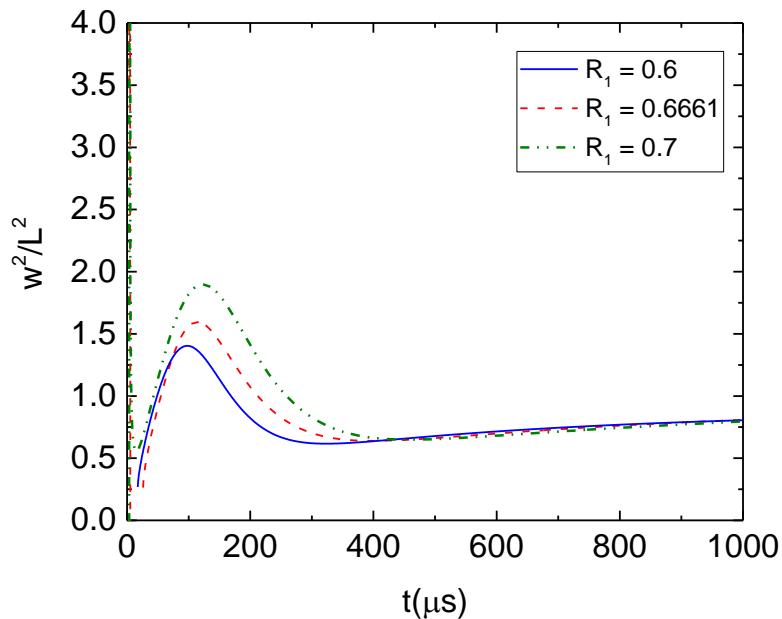


Figure 4.29: Width squared for three different values of R_1 . The width squared is calculated for $\rho = 15$ mm.

The main influences of R_1 on the decay rate of the slow component are to change the transition time between the two components and the maximum value of the width squared. The

larger R_1 is, the longer it takes for the transition to occur, and the higher is the maximum value of the width. The long-time value of the width does not change significantly with R_1 .

e) Influence of θ

The value of the coupling constant θ affects the exchange rate of energy between the two components. The parameters used to obtain Figure 4.30 are the same as in the section 4.5.2.5 c) with $L/\xi_1 = -1$.

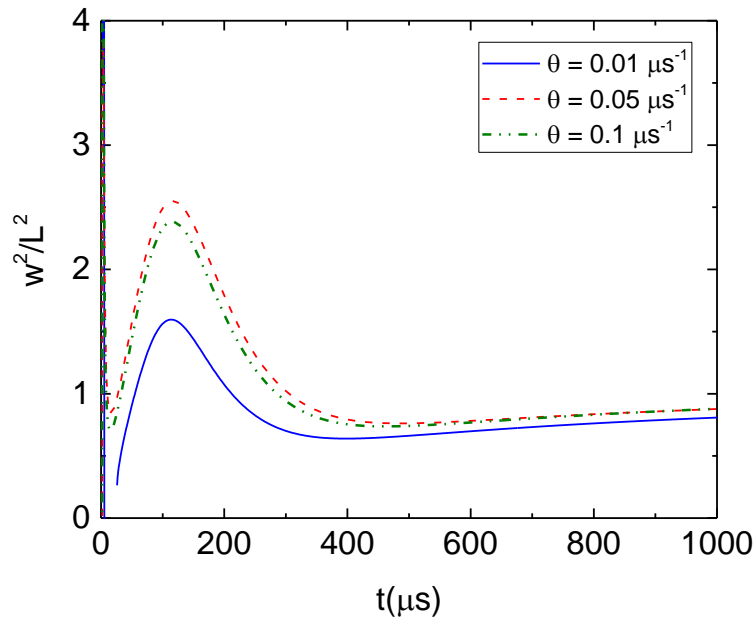


Figure 4.30: Width squared for three different values of θ . The width squared is calculated for $\rho = 15$ mm.

The value of the coupling constant does not have a strong influence on the long-time value of the width squared, but influences the value of the maximum, at least from 0.01 to $0.05 \mu\text{s}^{-1}$. For θ greater than $0.05 \mu\text{s}^{-1}$, the maximum of the width squared does not vary significantly compared to the variation with θ going from 0.01 to $0.05 \mu\text{s}^{-1}$. The fact that the maximum

value of the width squared can change without significantly affecting its long-time behaviour allows control of the ratio between the maximum and the long-time values.

f) Influence of γ

The weighting of the two components on the output side influences the predominance of a component compared to the other, and consequently, influences the transition time between the two components. It does not change however the long-time behaviour. The parameters used to show this effect in Figure 4.31 are $R_1 = 0.666$, $D_{B1}/D_{B2} = 1$, $\theta = 0.01 \mu\text{s}^{-1}$ and $L/\xi_1 = -3$.

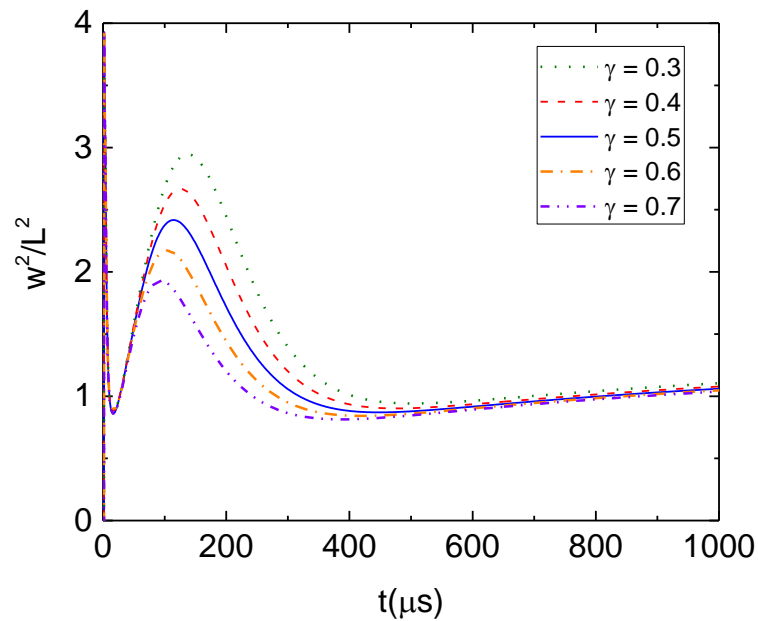


Figure 4.31: Width squared for three different values of γ . The width squared is calculated for $\rho = 15$ mm.

According to Figure 4.31, the weighting constant between the two components does not change the behaviour once the transition between the two components has occurred, but it has an effect on the transition; the smaller γ is, the higher is the maximum of the width squared.

g) Conclusions on the influence of adjustable parameters on the width squared

The influence of the different adjustable parameters has been discussed. However, a demonstration of the effect of varying the ratio of Boltzmann diffusion coefficients has been deliberately omitted since I found that for any value of this ratio different to 1, the time scales at which the two components evolve was too different, leading to a shape of the width squared far from the experimental observations.

By looking at the different parameters, we have seen that the long-time value of the width squared is influenced by L/ξ_1 . The coupling constant θ , the weighting factor γ and the reflection coefficient R_1 on the other hand have an effect on the value of the maximum. The two latter parameters (reflection coefficient R_1 and the weighting factor γ) also influence the duration of the transition (width of the peak of the width squared).

4.6 Comparison between experimental results and simulations

Three frequencies have been selected to perform the comparison between the experimental results and simulations, one per pass band of the component travelling through the network of beads (slow component) that can be seen in Figure 3.12. These three frequencies are 625 kHz, 1000 kHz and 1225 kHz and the filtering was performed with a bandwidth of 25 kHz. For each of these three frequencies, the behaviour of the width squared as a function of time is representative of the behaviour in the corresponding pass band. Figure 4.32 shows that the behaviour from one pass band to the next is different.

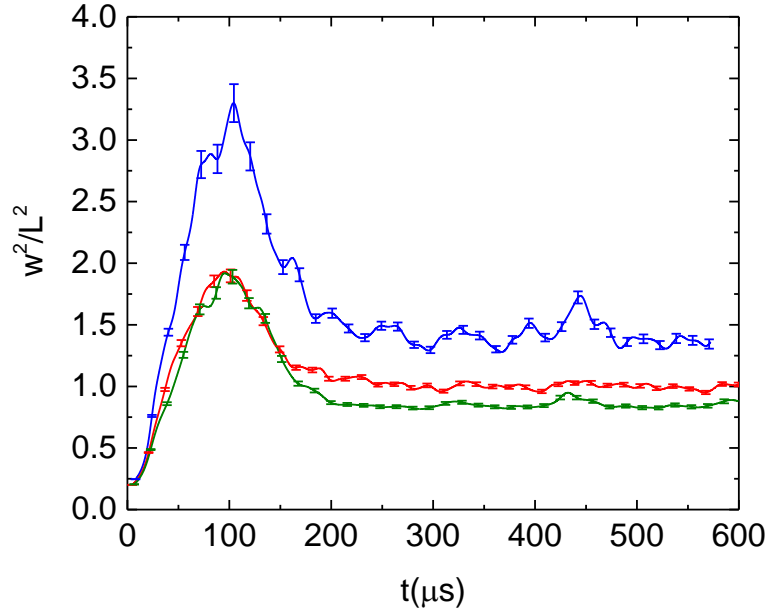


Figure 4.32: Width squared for $\rho = 15$ mm at three different frequencies: 650 kHz (blue line), 1000 kHz (red line) and 1225 kHz (green line).

The width squared at 650 kHz observed in Figure 4.32 has a steeper slope at short times and its maximum is higher than for the two other frequencies. At long times, the value of the width-squared also remains higher. The two other frequencies, 1000 kHz and 1225 kHz differ only by the value of the width squared at long times: at 1000 kHz its plateau remains a little higher than at 1225 kHz. The steeper slope of the 650-kHz curve means that the diffusion coefficient of the fast-diffusive component D_{B2} is larger at this frequency than for the two other ones.

4.6.1 650 kHz

The best match at this frequency has been obtained for a simulation with $R_1 = 0.666$, $D_{B1}/D_{B2} = 1$, $\theta = 0.01 \mu s^{-1}$, $\gamma = 1/6$ and $L/\xi_1 = -5$. The best time scale was obtained for $D_{B2} = 1.5 \text{ mm}^2/\mu s$. The results are shown in Figure 4.33.

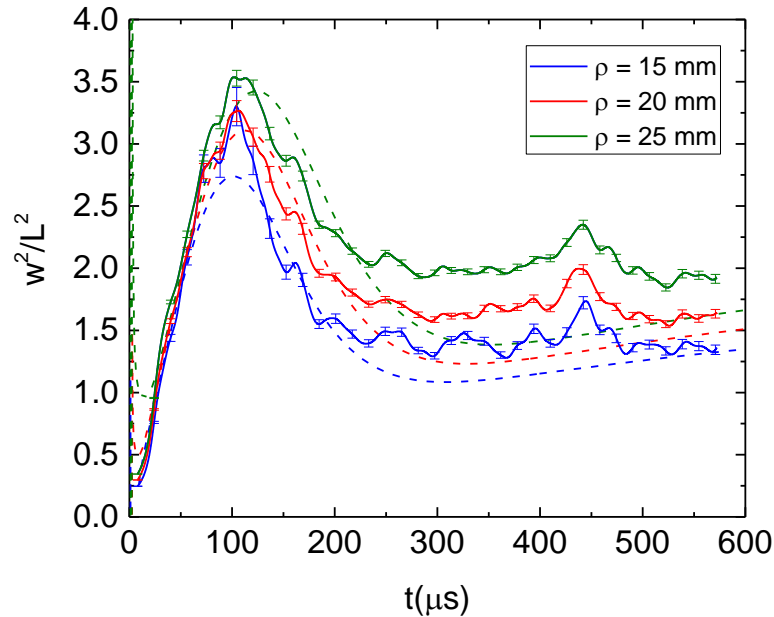


Figure 4.33: Comparison of the experimental values (solid line) of the width squared at 650 kHz with the theoretical predictions (dashed line) for three different values of ρ . The colors have the same meaning for experiment and theory.

Figure 4.33 shows that there is a good agreement between the experimental data and the theory results for the initial slope, the value of the maximum and the decay of the width after the maximum. The slope of the long-time behaviour of the width squared is reproduced but not its absolute value. In particular, the spacing between the different curves is very small for the theoretical predictions compared to what is observed experimentally. The difference in the spacing between the three experimental curves (or the three theory curves), *i.e.*, the difference between values of the width squared for different ρ at the same time is influenced by the time at which the transition occurs for each value of ρ , which depends on several parameters of both components such as l_B^* . As a consequence, the fact that a difference between the experiment and theory is observed for the separation of the width-squared values at long times is at least partly due to a different transition time in the experiment and the theoretical prediction. To visualize the transition times, the experimental and theoretical results for the intensity can be plotted

(Figure 4.34). It is visible on this figure that the change of slope occurs later for the theory prediction, which means that the transition time is larger than in the experiment.

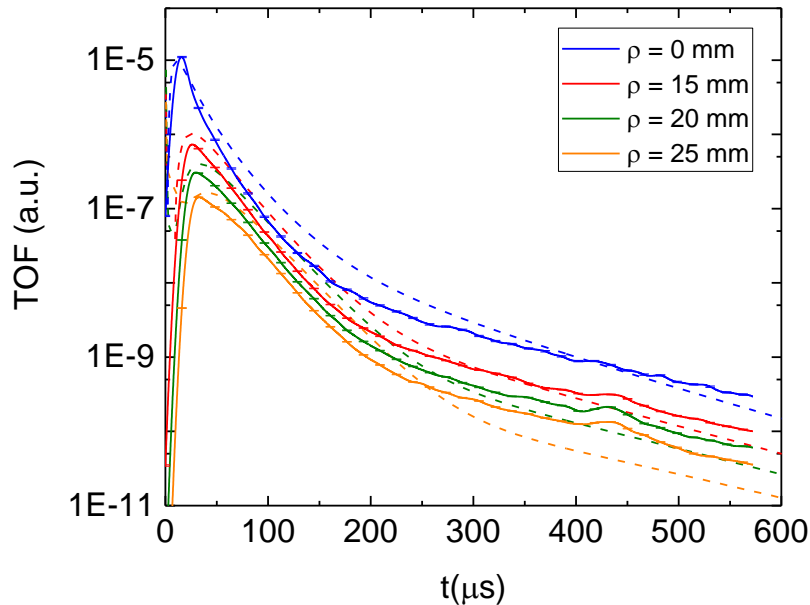


Figure 4.34: Comparison of the experimental values (solid lines) of the time-of-flight profiles at 650 kHz and the theoretical predictions (dashed lines) for four different values of ρ . The colors have the same meaning for experiment and theory.

There is one more parameter that is needed in order to predict the time-of-flight profiles: the absorption time τ_a . By definition, the width squared does not depend on the absorption, which is the reason why this absorption parameter has not been discussed until now. However, the time dependence of the transmitted intensity *is* affected by absorption, which reduces the transmission by the factor $\exp(-t/\tau_a)$. The absorption time used to plot the theoretical results in Figure 4.34 is $\tau_a = 1000 \mu\text{s}$. Since the absorption could be non-uniform, and therefore affect the two components differently, it could be an oversimplification to characterize the absorption by a single absorption time τ_a . However, this simple approximation is likely sufficient to

characterize the global effects of absorption, and going beyond this approximation to a more microscopic approach is challenging and beyond the scope of the thesis.

The theoretical results are able to reproduce the change in the behaviour of the intensity with time, in which two different decay rates are clearly visible. Finding the right parameters to fit perfectly the decay slopes is found to be more challenging.

4.6.2 1000 kHz

The best match between the experimental results and the simulation at 1000 kHz has been obtained for a calculation with $R_1 = 0.666$, $D_{B1}/D_{B2} = 1$, $\theta = 0.01 \mu s^{-1}$, $\gamma = 1/3$ and $L/\xi_1 = -3$. The best time scale was obtained for $D_{B2} = 1.4 \text{ mm}^2/\mu s$. The experimental width squared is compared with this theoretical prediction in Figure 4.35.

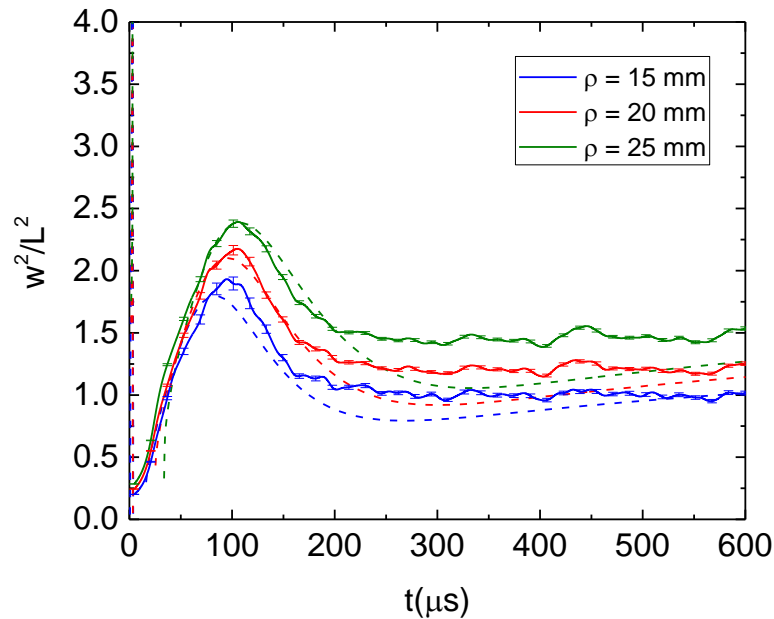


Figure 4.35: Comparison of the experimental values (solid lines) of the width squared at 1000 kHz with a theoretical calculation (dashed lines) for three different value of ρ . The colors have the same meaning for experiment and theory.

As was observed at 650 kHz, the short-time match between the experimental data and the theory is good at 1000 kHz (Figure 4.35), but the long times do not match very well, in particular the spacing between the different curves.

Figure 4.36 shows the measured intensity profiles at 1000 kHz and the theoretical results, using the absorption time $\tau_a = 350 \mu\text{s}$. The ratio between the two decay rates of the intensity is well reproduced, but the initial increase of the theoretical predictions is happening later for the two larger values of ρ compared to the experimental results. In the numerical calculations the behaviour at the shortest times (initial increase of the intensities) is in fact more difficult to obtain as large values of Ω are required. In the numerical calculation, the spacing between adjacent values of this parameter is logarithmic, which means that there is the same number of points in each decade, and therefore a lower resolution at the larger Ω values. As explained in Figure 4.24 and equation (4.38), the Fourier transform of the transmission for a diffusive mode is composed of sharp peaks along the imaginary axis of the frequency, and the short-time behaviour depends strongly on the peaks in $T(q_{\perp}, \alpha)$ obtained for large values of the frequency, which thus may not be sufficiently resolved.

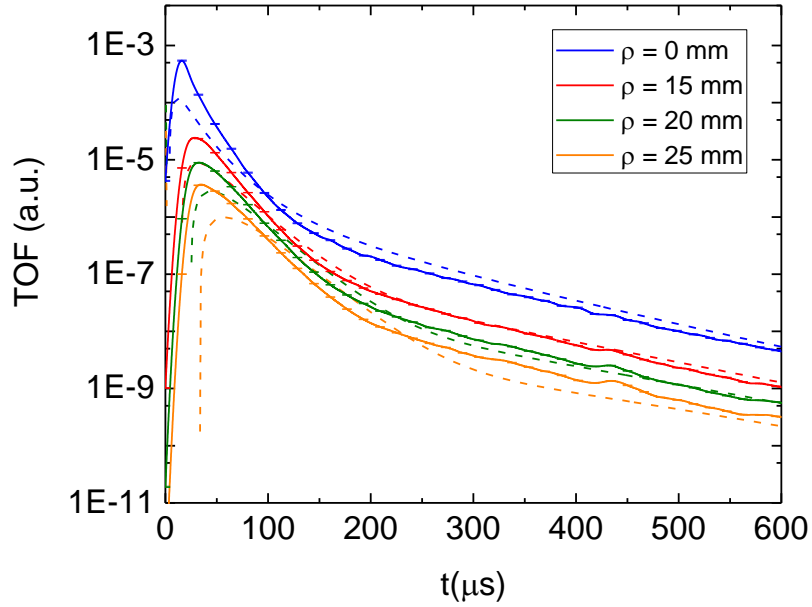


Figure 4.36: Comparison of the experimental values (solid lines) of the time of flight profiles at 1000 kHz with theory (dashed lines) for four different values of ρ . The colors have the same meaning for experiment and theory.

4.6.3 1225 kHz

The best match between the experimental results and the theory at 1225 kHz has been obtained for a numerical calculation with $R_1 = 0.666$, $D_{B1}/D_{B2} = 1$, $\theta = 0.01 \mu\text{s}^{-1}$, $\gamma = 2/5$ and $L/\xi_1 = -2$. The best time scale was obtained for $D_{B2} = 1.3 \text{ mm}^2/\mu\text{s}$. The results are shown in Figure 4.37.

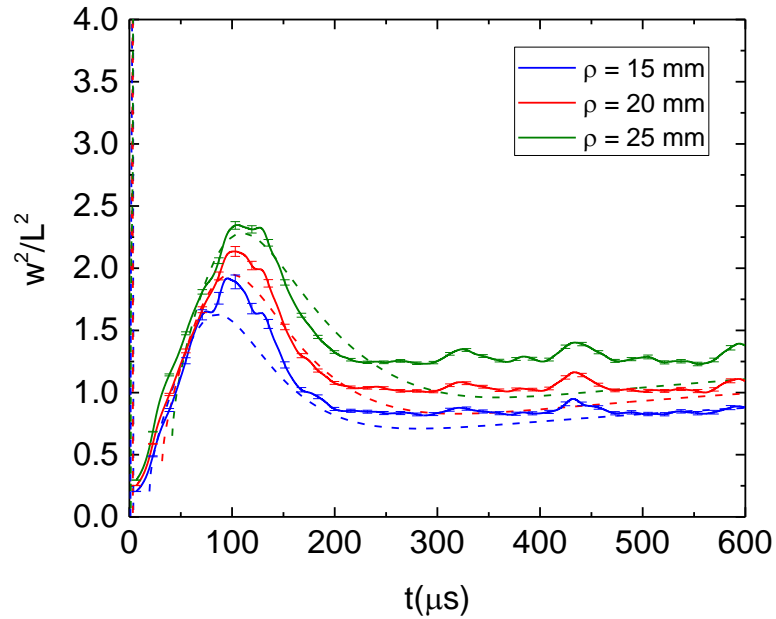


Figure 4.37: Comparison of the experimental values (solid lines) of the width squared at 1225 kHz with theoretical predictions (dashed lines) for three different values of ρ . The colors have the same meaning for experiment and theory.

The same comments can be made for the comparison between the experimental results and the theoretical predictions at 1225 kHz as for the other frequencies: the short-time behaviour is well reproduced but at long times the width squared is too low and the spacing for the different values of ρ too small. There are the same issues for the time-of-flight profile at 1225 kHz (Figure 4.38) as at 1000 kHz (Figure 4.36). The absorption time used in the simulation is here $\tau_a = 500 \mu\text{s}$.

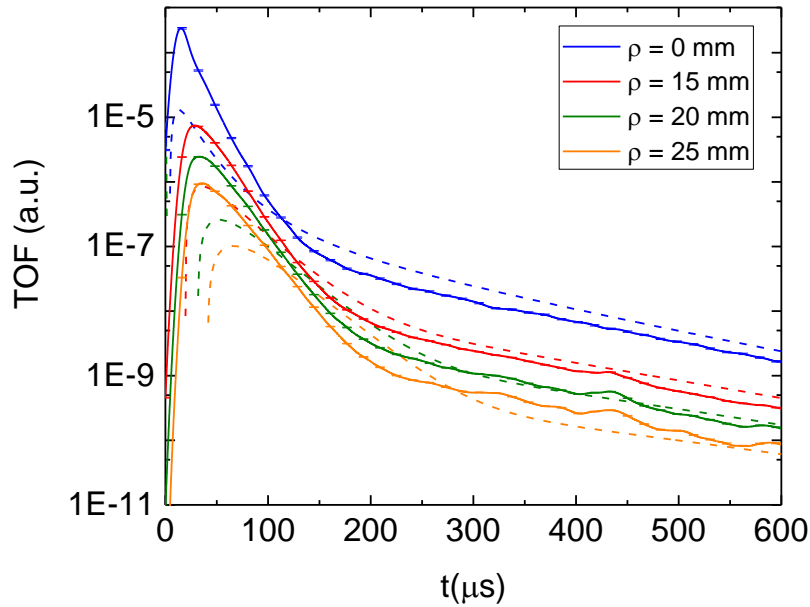


Figure 4.38: Comparison of the experimental values (solid lines) of the time of flight profiles at 1225 kHz with theoretical predictions (dashed lines) for four different ρ values. The colors have the same meaning for experiment and theory.

4.7 Conclusions

The wave transport in a sample composed of disordered aluminum beads in a liquid can have two different behaviours depending on the frequency. The transport depends on the density of states of the network of beads. At low frequencies below the resonances of the beads, and also for higher frequency where the density of states is low because these frequency ranges occur in gaps between the resonant frequencies, diffusive transport is observed, similar to the one observed in a sample made of glass beads in water [1]. In this case, there is no measureable transport through the beads and the observed diffusive transport can be described by a wave travelling in the liquid scattering off the beads. This behaviour is analogous to the diffusion of light in a medium of scatterers, and is responsible, for example, for reduced visibility in fog - a scattering medium composed of small water droplets. When the density of states is non-zero in

the network of beads, a component of the wave can travel through this network and will couple with the component travelling in the liquid.

This work showing the propagation of two components travelling through a sample is the very first observation of two mixed multiply scattered waves in a sample. Unlike other situations in which two wave components travel together in a sample, such as in bones [43] or bread crumbs [47], here the propagation times of the two components overlap, which makes the interpretation of this phenomenon challenging. However, the interpretation of the experimental data has been successfully done with the help of a theoretical model, which gives a good overall explanation of the phenomenon. The only possibility to obtain theoretical predictions that look like the experimental data is to treat the propagation through the network of beads as renormalized transport, in which the diffusion coefficient is renormalized by interference. Thus, the second component is renormalized as is the observed transport in samples of brazed aluminum bead in vacuum, but contrary to this case, it is only sub-diffusive and not localized. This renormalized transport is successfully described in the model using the self-consistent theory of localization. The absence of localization in the overall transport in my sample is due to the introduction of a leakage mechanism from the coupling between the two components (the component propagating in the network of beads and the diffusive component travelling only in the liquid).

The observation of the maximum in the width squared was the first clue that unusual wave propagation was happening. If there is only one mechanism by which energy can be transported across a sample, the width squared is expected to grow at all times and maybe saturate at long times in the case of localization. The observation of the reduction of the width squared is due to

the two components propagating and more particularly to a transition at a given time in the domination of one of the components over the other.

Even though the theoretical model, as demonstrated by the extensive series of numerical calculations that I have carried out, is successful in giving a good overall interpretation of the experimental data, the agreement between theory and experiment is imperfect. This means that some phenomena happening in the sample might not be perfectly taken into account. I will suggest some possible causes for the origin of this disagreement. First, in all the calculations, it has been supposed that the coupling between the two modes is symmetric, which might not be the case. The transfer from the beads to the liquid might indeed be higher than from the liquid to the beads, for a wave going from the liquid to the solid, a critical angle exists reducing the possibility for the energy to enter the beads. There is no critical angle in the other direction (solid to liquid). But on the other hand, it is also possible that the transfer from the liquid to the beads is the highest one as an individual bead can trap the energy for a long time (see Simsonic simulation in chapter 3). Even if this aspect has not been investigated extensively, the trapping time of the energy could also be even larger for multiple beads in contact with each other. The absence of solid links between the beads affects the transport of the solid component and it might not be right to consider the transport through the solid part of the sample as a single component. The bumpy surface of the sample might also lead to some unaccounted for effects. The sample is also covered by a thin plastic wall that has not been considered in the calculations, as it should be thin enough, but it could nonetheless affect somewhat the estimated reflection coefficients both for waves entering and leaving the sample.

Despite the lack of perfect agreement between the theoretical predictions and the experiments, all the main features and behaviour seen experimentally, especially at short times,

are recovered by the model over the entire range of frequencies investigated. I am therefore very confident that the model and interpretation of the data it leads to are satisfactory. I have interesting ideas to improve the model, among which the introduction of two different coupling rates between the two modes seems promising, as has been done for the model with two perfectly diffusive components [equations (4.8) and (4.9)]. Other ideas are the inclusion of different absorption times for each component instead of a single one for the overall intensity, and an improvement of the resolution of the calculations at short times (or large ω). Experimentally, it would be interesting to influence the strength of the contact between the beads, for example by applying different known pressures on the sample, in order to vary the coupling constant between the two components. Another interesting possibility would be to create a suspension of non-touching aluminum beads in silicone oil using a fluidized bed to suppress the slow renormalized component travelling through the network of beads and to study the diffusive component by itself.

Chapter 5

Propagation of ultrasound in a single-layer sample of beads

5.1 Introduction

This experiment has been designed to study two different wave propagation phenomena in complex media: the position dependence of the diffusion coefficient in the case of strong scattering, and the equipartition of energy in multiple scattering media. The dependence of the diffusion coefficient with position has been introduced in the self-consistent theory (SCT) [29]; taking its dependence on position into account is necessary to correctly describe sub-diffusive or localized behaviour of waves in open media. The equipartition of energy in random media is a property of diffuse waves, *i.e.*, waves which have undergone a lot of scattering events [56]. For such a wave, the directions of propagation cannot be defined as energy is going in all directions, but it is still possible to calculate the energy due to the compressional part of the wave and the shear energy [12,57]. In this situation, the ratio between these two energies is predicted to be constant, and equal to the ratio of the number of modes of shear waves to the number of modes of compressional waves [56].

The study of these two phenomena requires knowing the wave field in the sample to access the energies in it, as the calculation of the diffusion coefficient requires the total energy. In the three-dimensional case studied in the previous chapter, it is not possible to measure the field inside the sample. For a “two-dimensional” sample, it is sufficient to measure the displacement field “only” on the surface of the sample, which is possible to do. Therefore, to study these phenomena, experiments were done on a 2D sample of brazed aluminum beads (one layer of beads). The measurement of the field was done using a laser-interferometer, which gives access to the three components of the displacement field on the surface of the sample. This experiment was performed in air, unlike the previous experiment done in water, which means that there was

an almost perfect reflectivity at most of the boundaries of the sample and virtually no loss of energy through these boundaries to the outside medium¹⁵.

5.2 Measurement Technique

Before presenting a description of the sample and method of preparation, I will explain the measurement technique and experimental setup. In order to perform the experiment, I needed the sample to be as isolated as possible, meaning that this experiment could not be performed under water as was done for the experiments on the 3D sample of aluminum beads in a fluid (chapter 0). Because the difference in impedance for longitudinal waves between aluminum (~ 17 MRayl) and air (~ 500 Rayl) is large, performing the experiment in air prevented any significant energy loss to the outside medium, and therefore the sample was isolated. Recall that the transmission from one medium to the next depends on the difference of the two impedances, and that the farther apart they are, the less efficient is the transmission between the two media. Moreover, as explained in the introduction, the field had to be measured on the surface of the entire sample. This led us to use a laser interferometer as the measuring tool to perform the experiment. With the interferometer, the spatially resolved displacement field can be measured by scanning the entire surface of a 2D sample and experiments can be performed in air.

5.2.1 Experimental setup

The experiment was performed on a waveguide-like sample that had the form of a rectangle (Figure 5.1). The elastic wave entered the sample along one of the short sides of the sample. During the experiments, a transducer was in contact with the sample in order to inject the wave.

¹⁵ The only coupling of energy in or out of the sample occurred at the top and bottom interfaces where two transducers were placed (see Figure 5.1).

A second transducer, not active, is placed in contact with the sample on the opposite sides, which allowed having the same reflection coefficient on both ends of the sample, and therefore the same boundary conditions on both ends. The two other sides of the sample (long sides) as well as the surfaces of the 2D sample were in contact only with air, so these boundaries can be considered as free boundary and the reflection is total.



Figure 5.1: Picture of the sample between the two transducers. In this chapter, we will define the x -axis as the axis going along the long side of the sample, the y -axis along the short side of the sample and the z -axis as being perpendicular to the surface of the sample.

One of the surfaces of the rectangle was sanded and polished in order to obtain a flat side on which the measurement using the laser was performed. The sample holder was mounted on a motorized stage so that a scan of the surface can be performed. The typical separation between two acquisition points was 0.25 mm in both directions. The wave propagated parallel to the long side of the sample (x -axis), and the emission occurred on a short side of the sample (y -axis).

5.2.2 Laser Interferometer

The laser interferometer used in this experiment was the TEMPO from Bossa Nova Technologies. The interferometer uses a Nd-YAG laser with a wavelength of 532 nm. This interferometer uses a photorefractive crystal to mix the probe beam with the acquisition beam, making the setup of the system easier than a classic Michelson interferometer. An attractive feature of this interferometer is that it can measure the displacement in two directions [58], the out-of-plane displacement (displacement along the z -axis) and an in-plane displacement (along x or y -axis). To obtain the three components of the displacement, the acquisition has to be done twice with the system being rotated by 90 degrees between the two acquisitions.

The laser signal is focused on the sample using a lens with a focal length of 3 cm, so the interferometer needs to be positioned approximately 3 cm away from the sample. The interferometer contains an array of 16 photodiodes, which allows the measurement of the in-plane component, taking advantage of the different angles of incidence collected by the lens. For this technique to work, the surface of the sample needs to have some roughness to scatter some light away from the incidence angle (Figure 5.2).

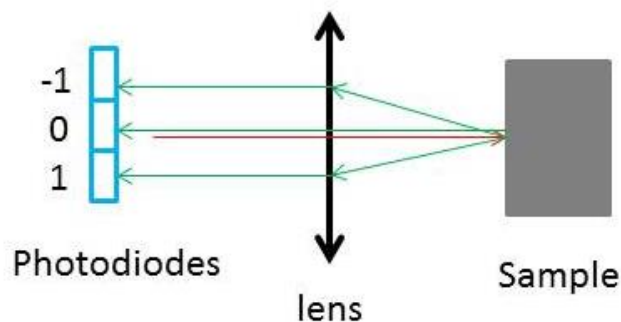


Figure 5.2: The interferometer measures the reflected signal and also the scattered light due to the roughness of the surface. An array of photodiodes acquires the signal: the array is symmetric with the axis of the lens. The elements of the array are numbered from $-i$ to i .

The signal s measured on each photodiode depends on both components of the displacement [59]:

$$s_{\pm i} = u_z \cos(\theta_i) \pm u_x \sin(\theta_i) \quad (5.1)$$

In equation (5.1), θ_i represents the angle of reflection needed to reach the photodiode i . u_z and u_x are the displacements in the z -axis (out-of-plane) and the x -axis (in-plane), respectively. From equation (5.1), both displacements can be obtained:

$$u_z = \frac{s_i + s_{-i}}{2 \cos(\theta_i)} \quad (5.2)$$

and

$$u_x = \frac{s_i - s_{-i}}{2 \sin(\theta_i)}. \quad (5.3)$$

As we can see in equation (5.3), the measurement of the in-plane component u_x uses the scattered signals which are small, and this signal is divided by the sine of a small angle (division by a small number). Therefore the fluctuations of the signal are amplified. These two facts mean that the noise for the in-plane component is much larger than the noise for the out-of-plane u_z [equation (5.2)] component as shown in Figure 5.3.

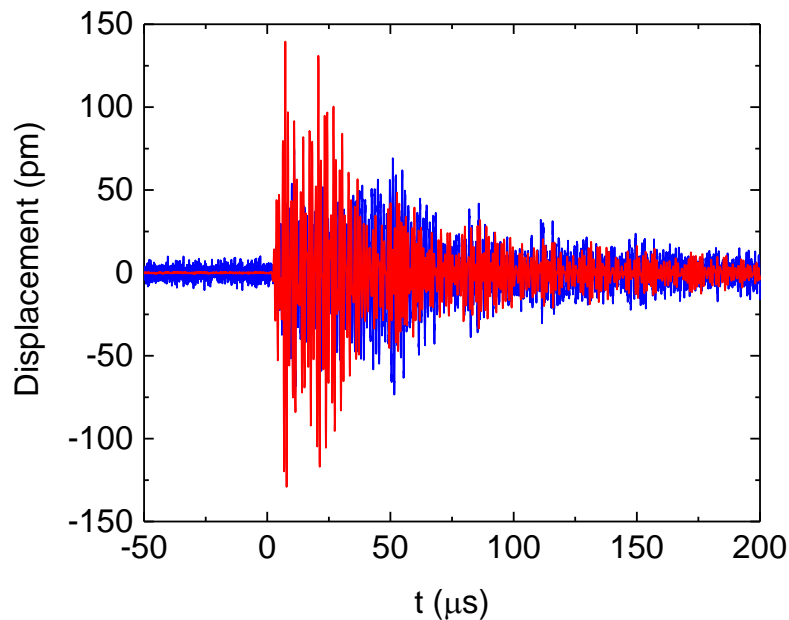


Figure 5.3: Example of an in-plane signal, displacement along the x -axis (blue), and an out-of-plane signal, along the z -axis (red). The pre-trigger signals allow the noise levels to be compared.

There are two more values which are recorded at each acquisition: the DC light level and the calibration value. The DC light signal gives the amount of light collected by the lens. If this value is too low, below the threshold set in the acquisition program, the acquisition is not performed. The calibration signal is a value in V/mm allowing the conversion of the signal measured in Volts to a displacement in mm, as shown in Figure 5.3. If the calibration level is small, the conversion might be inaccurate and some data points might have to be discarded (the recorded signal has to be divided by the calibration signal leading to large fluctuation when it is too small).

The experiment is completely controlled by a computer using the software Matlab. The computer is equipped with a GaGe Compuscope CS14200/CSE1621 digital oscilloscope card for

signal acquisition and is able to control the motor moving the sample. The Figure 5.4 represents a block diagram of the different electronic equipment used in the experiment.

The computer was used to define the waveform, which was exported and stored in the AWG¹⁶. The signal emitted by the AWG was amplified in the E&I power amplifier before being sent to the piezoelectric transducer used to launch the ultrasonic signal in the sample. Then, the TEMPO interferometer detected the ultrasonic displacements and sent the corresponding voltage signals to the compuscope card in the computer. All the electronics were synchronized with the AWG, meaning that the synchronization time corresponded to the time of emission of the ultrasonic wave.

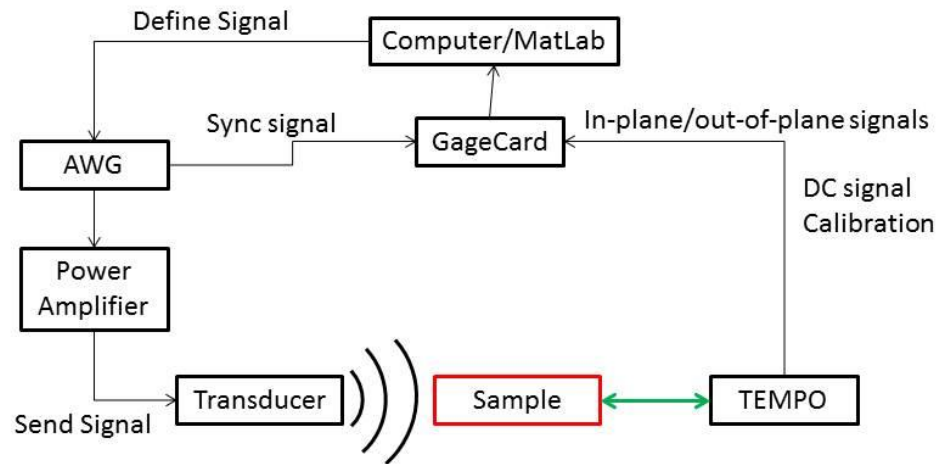


Figure 5.4: Diagram representing the electronic equipment used during the experiment. The black lines represent the connection between the different pieces of equipment. The green line represents the laser light.

¹⁶ The AWG and the E&I power amplifier were identical to the ones used in the experiment described in chapter 4 (description in section 4.3.2).

5.3 Sample fabrication

The experiment was performed on a sample made of brazed aluminum beads arranged in a single plane to obtain a 2D sample. In order to make the sample, a template to determine the positions of the beads was needed. This template pattern of holes to locate the bead positions needed to be as random as possible, as the goal is not to study an ordered sample, and it also needed also to be compact: in order to be able to braze the beads together, they had to be in contact with each other. In the next sections, I will describe how the 2D pattern was obtained next, I will discuss the actual fabrication of the sample.

5.3.1 How to obtain a 2D-random compact system

The most compact lattice in 2D, giving an ordered structure, is the triangular lattice which has a packing fraction of 90.7 %. For this experiment, we are looking to obtain a 2D disordered sample with a packing fraction of about 80 %. Even if this packing fraction is lower than the ordered triangular lattice case it is still very high, and as a consequence the two easiest methods usually employed to create a random pattern could not be used.

The easiest way to create a random 2D pattern is to choose random coordinates where to put a new disk. This cannot work in the case of a high-packing fraction, as gaps between the disks, which are too small to accommodate a new object, are created. There will therefore be a lot of voids and the probability of achieving a high-packing fraction is very small (Figure 5.5 a). The second technique which is easy to implement, but does not allow very high packing fractions to be obtained, consists of starting with some disks (two or three) placed randomly at a certain distance from each other, and then adding disks touching them. Each new disk is placed close to one of the existing disks (the initial one or one already added during the process), the position of

this neighbouring disk being chosen randomly. The placement around this disk is done by choosing randomly the location of the contact point between the two disks, or in other words the angle between the horizontal and the line joining the centres of the two disks. To obtain a high-packing fraction, we need to have several disks close to each other: the choice of angle might limit the number of objects around a given disk. A lot of “lines” of beads are created in which beads touch only one or two other beads (Figure 5.5 b)

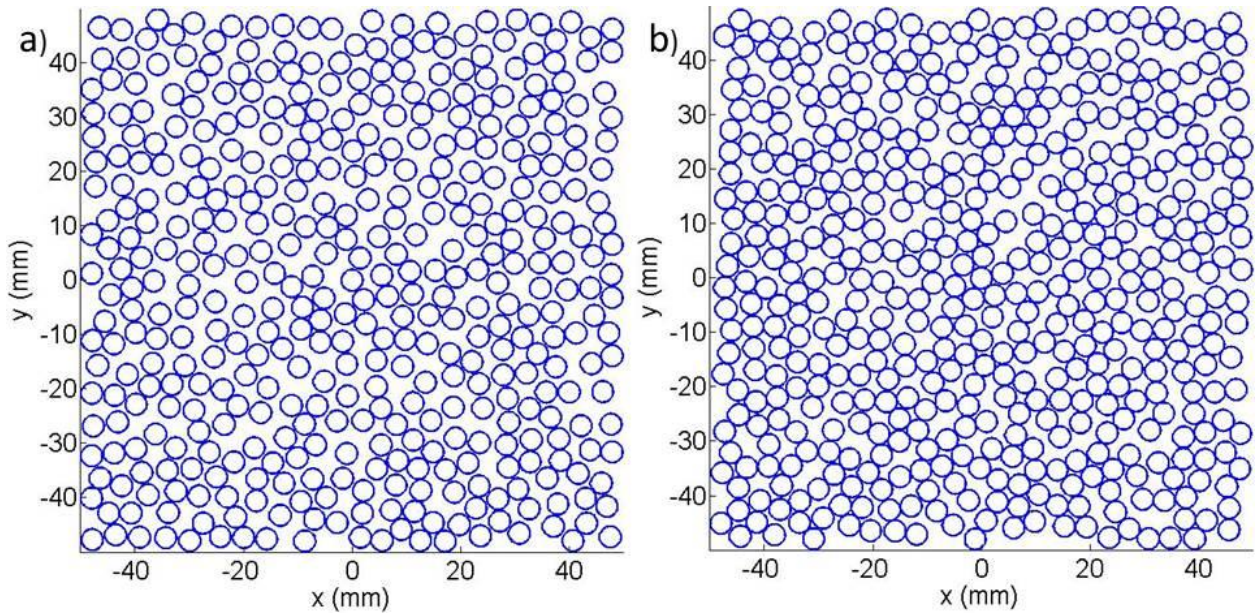


Figure 5.5: Example of patterns obtained with the “classic” techniques used to create 2D random patterns. On a) the final packing fraction is 54 % and in b) 61 %. For both cases, the programs stop after trying 10^6 times to add a new disk.

Finally, because of the impossibility of using the easy most common methods to create a compact 2D pattern, I decided to write an algorithm inspired by the one proposed by Lubachevsky and Stillinger [60], but in a simplified version, designed to meet the needs of this project. The main idea of this algorithm is to create a 2D pattern by simulating the collisions of particles. The parameters of this algorithm are the size of the pattern at the end (size of the box), the number of particles and the final packing fraction. The algorithm starts by placing the

particles randomly and randomly assigning a velocity to each of them. At the beginning, the particles are just points (radius equal to zero). Then, for increasing simulation time, the particles move according to their velocities with their radii increasing simultaneously. Once the particle has a non-zero radius, collisions between different particles have to be taken into account. The collisions are considered as perfectly elastic. The boundaries of the box are periodic: if a particle reaches a boundary, a duplicate of this particle is added on the other side of the box. Sometimes, the system stays stuck in a configuration: a few particles are colliding back and forth in fixed trajectories that are constrained by other neighbouring particles. To avoid this problem, the velocities of the particles are redefined randomly after a given number of time steps, the new configuration of velocities then allowing the system to continue to evolve. The simulation is terminated when the desired packing fraction is reached. An example of the result obtained from this algorithm is shown in Figure 5.6 with 650 disks and a final packing fraction of 80 %.

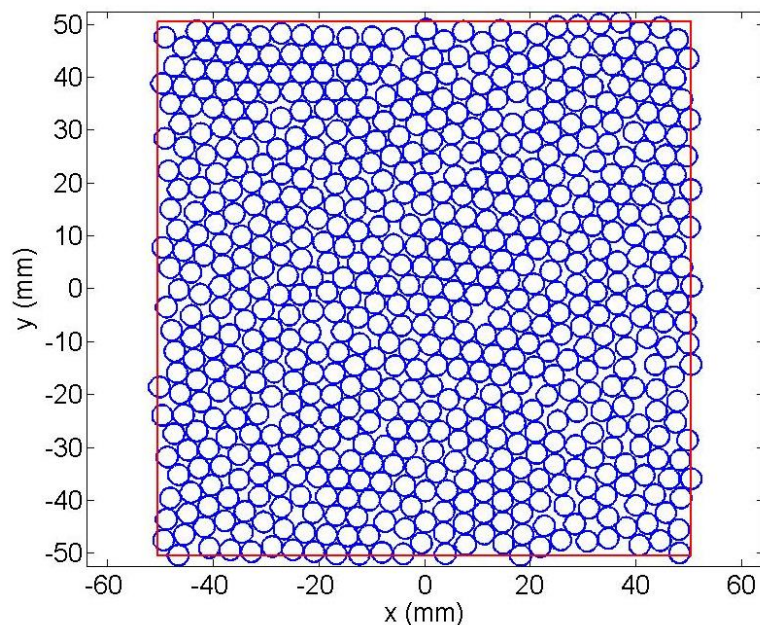


Figure 5.6: Example of a pattern obtained with 650 4-mm-diameter disks with a final packing fraction of 80 %. The red lines represent the box in which the simulation was performed.

A good way to judge the randomness of such a pattern is to look at the distribution of distances between each pair of beads as shown in Figure 5.7.

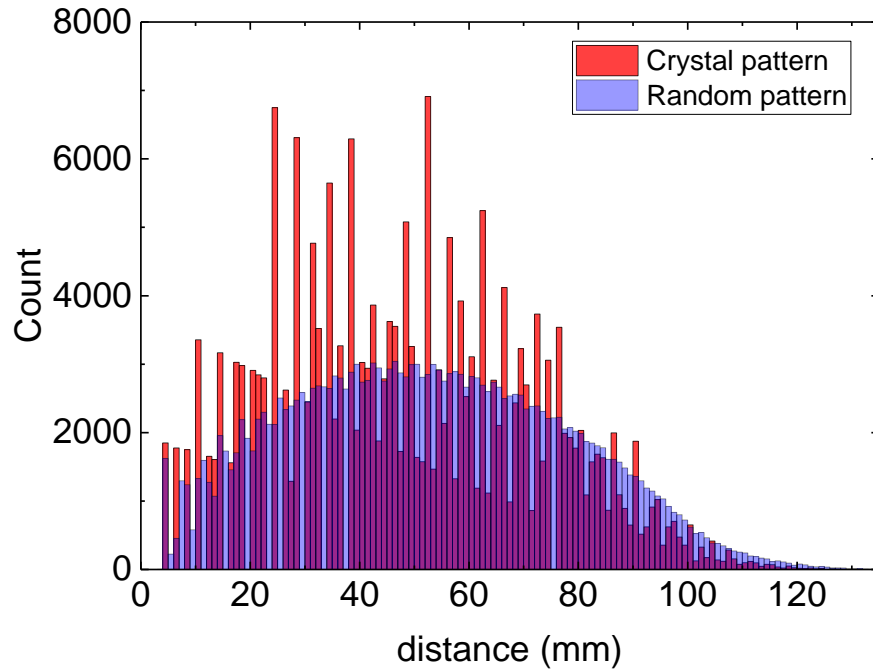


Figure 5.7: Histogram of the distances between each pair of beads for two patterns of 650 4-mm-diameter disks, with each bin representing 1 mm, and the number of distances between pairs of disks being 210925. In red, histogram for a perfect arrangement of beads (hexagonal compact), for which some sharp peaks appear. In blue, histogram obtained for the pattern shown in Figure 5.6.

The two histograms shown in Figure 5.7 emphasize the differences between the patterns for ordered and disordered configurations. In the case of the crystal, there are a lot of sharp peaks corresponding to the different distances in the hexagonal compact pattern: $2r$, $2\sqrt{3}r$, $4r$, $2\sqrt{7}r, \dots$ with r the radius of a disk. For the random pattern, there are two peaks at short distances. These peaks are close to the distances of the two nearest neighbours of the hexagonal compact pattern (around 4 mm and 7 mm as $r = 2$ mm). For the largest distances, there is no

distinct feature; the presence of the maximum, around 50 mm, is only due to an edge effect: there are more beads at intermediate distances than large distances due to the size of the box.

From the histograms, we can see that there is no long distance order, and consequently, the pattern is disordered even though some clusters might form (short distance order).

5.3.2 How the sample is made

5.3.2.1 Mold

We wanted to make a sample of one layer of beads using the random pattern that had been created. First, spherically shaped depressions were milled in a steel plate following the pattern using a Computer Numerical Control (CNC) milling machine, and then used to make the sample using a brazing technique.

In order for the beads to stay in a given position, the holes were drilled so that a quarter of the beads was below the flat surface of the mold, which means that the holes must have a diameter approximately equal to 3.5 mm and be at least 1 mm deep. I wanted the mold to be as big as possible for the furnace (9 in x 9.5 in); so the pattern has been repeated four times to cover the entire surface.

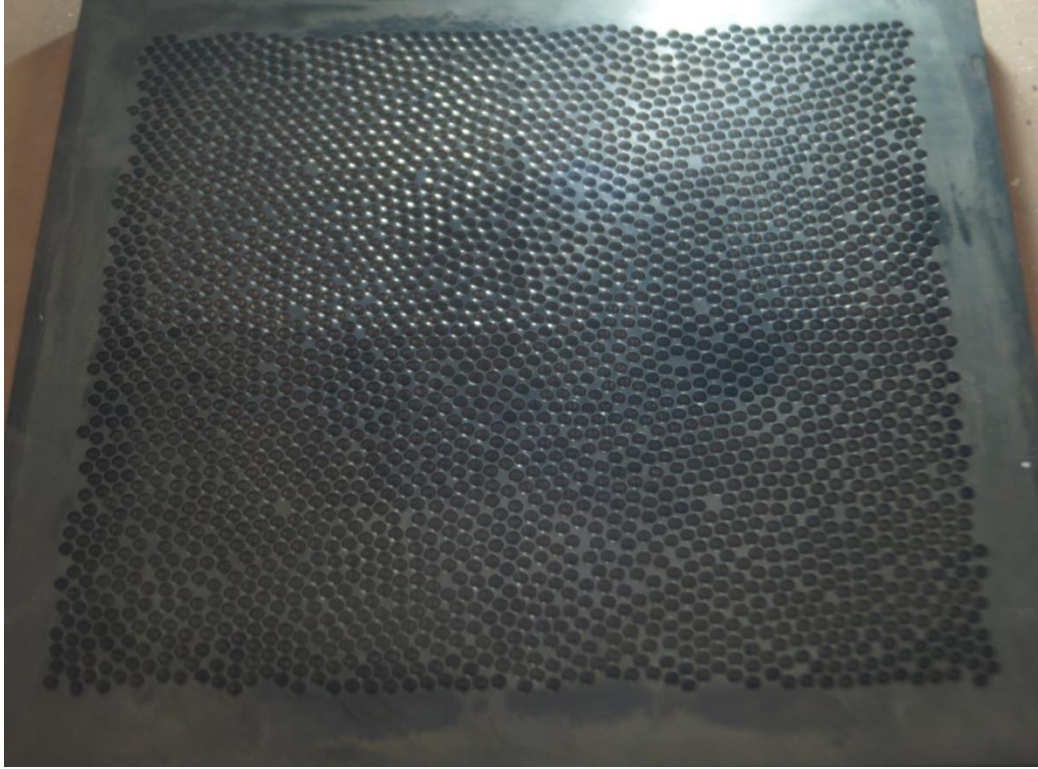


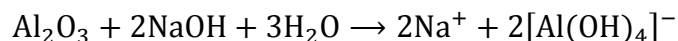
Figure 5.8: Picture of the mold used in the furnace to make the one-layer of beads sample

5.3.2.2 *Brazing*

Before doing the brazing of the aluminum beads [61,62,63], they had to be cleaned. I started by removing the layer of aluminum oxide on the outer edge of the beads. I used this process also to reduce slightly the size of the beads. The beads were indeed on average 4.11 mm in diameter, but the mold had been made for 4-mm-diameter beads. These two steps (removing the oxide layer and reducing the size of the beads) were done the same way, by putting the beads in a solution of sodium hydroxide. By looking at the solution while the beads were in it, it is possible to know if it is the oxide layer which was removed or if the sodium hydroxide (NaOH) was reducing the size of the beads. As long as there was a layer of oxide, there was no creation of

bubbles but when the NaOH was in contact with the aluminum, there was creation of hydrogen gas, as shown in the chemical equations below.

Reaction with the aluminum oxide:



Reaction with the aluminum:



As we can see, in the second reaction, there is creation of hydrogen (H_2) which is not present in the first reaction. Thanks to the presence of bubbles, it is possible to know if the oxide layer (Al_2O_3) has been removed, as there is no creation of gas in the first reaction. Once the oxide layer had been removed, the reaction was stopped by adding water to the beaker and by rinsing the beads.

As mentioned, the beads needed to be reduced to fit inside the mold, and this step was done in two steps using the second reaction. The reaction was done with 15 g of beads (around 150 beads). For the first step, the beads were put in water in which 1.3 g of NaOH was dissolved and this reaction took around 2 hours to be completed. Then the same reaction was repeated but with 1 g of NaOH. During these two reactions, the solution and beads mixture was stirred using a magnetic stirrer.

The brazing process was started after the beads had been cleaned (no oxide layer) and had the right size. The first step is the coating of the beads with a layer made of a mixture of two powders: Silicon powder and NOCOLOK® flux. The general idea of the brazing process is to create a layer, around the objects to be fused, which has a lower melting point than the bulk of

the object. By melting the outside layer and then by cooling it down, two objects are fused, without deforming them.

The flux is a potassium aluminum fluoride salt of general formula $K_{1-3}AlF_{4-6}$. The role of the flux is to dissolve the thin aluminum oxide layer that has reformed after the cleaning process. This layer has to be removed as the melting point of Al_2O_3 is very high, around 2000 °C [64], and would have therefore prevented the beads from fusing together. The silicon powder (Si) is used to create an alloy with the aluminum on the surface of the beads; this alloy has a melting point lower than the melting point of aluminum (just under 600 °C [65] compared with the melting temperature of aluminum, around 650 °C).

For 100 g of beads (around 1000 beads), the coating was made of 1 g of silicon and 2 g of flux [39]. The two powders were mixed in a little bit of water and put over the beads in a frying pan. Then the beads were gently moved around in order to have an even coating on all the beads. The water was slowly evaporated during the process, leaving at the end a dry dense powder coating on the aluminum beads. Once the beads were ready, they were placed in the mold that was then put inside the furnace.

The air inside the furnace was evacuated and replaced by nitrogen that flows continuously inside the furnace during the brazing process, to obtain an inert atmosphere while the temperature was high. For the brazing to occur, the temperature needed to be higher than the melting temperature of the alloy of aluminum and silicon but under the melting point of aluminum. The temperature inside the furnace was increased to 630 °C at a rate of 200 °C/h, and the temperature was held for 90 minutes. The furnace was then cooled down at room temperature, and the mold was removed. After the sample was brazed, it was stuck to the steel

plate (mold), but it was possible to take it out by flowing some dilute nitric acid (HNO_3) between the mold and the sample.

5.4 Theory: position-dependent diffusion coefficient and equipartition

As mentioned in the introduction, I am interested in two phenomena: the position dependence of the diffusion coefficient in the case of renormalized transport [29] and the equipartition of energy due to the multiple scattering in the sample [56]. Experimentally we can access the field on the surface of the sample. We know moreover perfectly well the boundary conditions of the sample. It is therefore technically possible to link our experimental results to some theoretical predictions.

5.4.1 Position-dependent diffusion coefficient

5.4.1.1 Theory

In the second chapter of the thesis, the self-consistent theory (SCT) was presented as a way to describe the sub-diffusive transport or Anderson localization in samples having strong enough disorder [equations (2.89) and (2.90)]. An important characteristic of the SCT that was developed for open media is the existence of a diffusion coefficient that depends on position in the sample. In the previous chapters, the SCT is written for three-dimensional media and for a time-dependent experiment. It can be rewritten in the case of a monochromatic experiment for a quasi-1D waveguide¹⁷ [66]. A quasi-1D waveguide is defined by the condition $w \gtrsim l_s \ll L$, where w is the width of the waveguide, L is its total length and l_s is the scattering mean free

¹⁷ Monochromatic experiments or continuous wave experiments lead to the absence of Ω in equation (5.4) and (5.5) as there is no time-dependence for these experiments. Nonetheless, all the quantities depend on the actual frequency of the wave ω , but it is not explicitly written in the equations (5.4) to (5.7).

path. The length of the waveguide being much larger than its width, a position in it is defined only by one parameter x (along the length of the sample). In these conditions, the SCT becomes (in dimensionless units):

$$\left[\beta^2 - \frac{\partial}{\partial \zeta} d(\zeta) \frac{\partial}{\partial \zeta} \right] \tilde{C}(\zeta, \zeta') = \delta(\zeta - \zeta') \quad (5.4)$$

with

$$\frac{1}{d(\zeta)} = 1 + \frac{2}{\tilde{g}_0} \tilde{C}(\zeta, \zeta). \quad (5.5)$$

In equation (5.4) and (5.5), ζ is the dimensionless position in the waveguide ($\zeta = x/L$). $\tilde{C}(\zeta, \zeta')$ is the dimensionless intensity Green's function observed at the position ζ with a point source at ζ' [$\tilde{C}(\zeta, \zeta') = (wD_B/L)C(x, x')$], $d(\zeta)$ is the diffusion coefficient D normalized by the Boltzmann diffusion coefficient D_B , and β represents the absorption in the sample. \tilde{g}_0 is the dimensionless conductance, which is proportional to the number of modes in the waveguide N [$\tilde{g}_0 = (\pi/2) Nl_s/L$]. The number of modes depends on the wavelength λ in the sample ($N = 2w/\lambda$). The same boundary conditions as the one used in chapter 0 [equation (4.29)] can be defined for the two short sides of the waveguide (*i.e.*, the ends of the waveguide) by the introduction of the extrapolation length. It is assumed that there is total reflection on the other boundaries of the waveguide. These boundary conditions correspond to the experimental conditions presented in the introduction of this chapter.

An expression for the diffusion coefficient $d(\zeta)$ as a function of position can be obtained from equations (5.4) and (5.5). The expression for d depends on whether the transport in the sample is in the weak localization regime ($\tilde{g}_0 \gg 1$) or in the strong localization regime ($\tilde{g}_0 \ll 1$).

When the absorption is neglected ($\beta = 0$), the diffusion coefficient in the weak localization regime is (expressed in terms of non-normalized variables):

$$D(x) = D_B \left[1 - \frac{2}{g_0} \frac{x}{L} \left(1 - \frac{x}{L} \right) \right]. \quad (5.6)$$

In the case of the strong localization regime, the expression for the diffusion coefficient is different:

$$D(x) = D_B \left[\exp\left(-\frac{x}{\xi}\right) + \exp\left(-\frac{L-x}{\xi}\right) \right]^2. \quad (5.7)$$

The localization length ξ has been introduced in equation (5.7): $\xi = g_0 L$.

In the weak localization regime, the renormalization of D follows a parabolic profile whereas in the strong localization regime, the profile of D is a decreasing exponential. As expected, in this latter regime, the renormalization is stronger. For both cases, the minimum value of the diffusion coefficient is obtained in the middle of the waveguide. In these expressions, the absorption has been neglected. If the absorption were taken into account, it would increase the minimum value that can be reached by the renormalized diffusion coefficient due to a decrease of the return probability.

5.4.1.2 Experimental determination of the diffusion coefficient

The diffusion coefficient is obtained using Fick's Law of diffusion linking the "diffusive flux" of energy \vec{j} to the energy density W via the diffusion coefficient D :

$$\vec{j} = -D\vec{\nabla}W. \quad (5.8)$$

For the diffusion of acoustic waves, the flux corresponds to the Poynting vector and the energy density is the sum of the kinetic energy E_k and the elastic potential energy E_p . These three quantities can be expressed in terms of the displacement field, u_i , and some properties of the material; the mass density, ρ , and the components of the stiffness tensor, $c_{\alpha\beta\gamma\delta}$. Using the Einstein notation for summation, we have:

$$J_\alpha = -\frac{1}{2} c_{\alpha\beta\gamma\delta} \left(\frac{\partial u_\gamma}{\partial x_\delta} + \frac{\partial u_\delta}{\partial x_\gamma} \right) \frac{\partial u_\beta}{\partial t}, \quad (5.9)$$

$$E_k = \frac{1}{2} \rho \left(\frac{\partial u_\alpha}{\partial t} \right)^2 \quad (5.10)$$

and

$$E_p = \frac{1}{2} c_{\alpha\beta\gamma\delta} \left(\frac{\partial u_\alpha}{\partial x_\beta} + \frac{\partial u_\beta}{\partial x_\alpha} \right) \left(\frac{\partial u_\gamma}{\partial x_\delta} + \frac{\partial u_\delta}{\partial x_\gamma} \right). \quad (5.11)$$

In the equations (5.9) to (5.11), the subscripts α, β, γ and δ go from 1 to 3 and represent the three directions x, y and z . The two energies, the flux and the displacement field are position and time-dependent quantities, like the diffusion coefficient. The diffusion coefficients in equations (5.6) and (5.7) are defined for a given frequency, so the equations (5.9) to (5.11) need to be rewritten as a function of frequency instead of time:

$$J_\alpha = \mathcal{Re} \left[i\omega \frac{1}{2} c_{\alpha\beta\gamma\delta} \left(\frac{\partial u_\gamma}{\partial x_\delta} + \frac{\partial u_\delta}{\partial x_\gamma} \right) u_\beta^* \right], \quad (5.12)$$

$$E_k = \mathcal{Re} \left[\frac{1}{2} \rho \omega^2 u_\alpha u_\alpha^* \right] \quad (5.13)$$

and

$$E_p = \mathcal{Re} \left[\frac{1}{2} c_{\alpha\beta\gamma\delta} \left(\frac{\partial u_\alpha}{\partial x_\beta} + \frac{\partial u_\beta}{\partial x_\alpha} \right) \left(\frac{\partial u_\gamma^*}{\partial x_\delta} + \frac{\partial u_\delta^*}{\partial x_\gamma} \right) \right]. \quad (5.14)$$

In equations (5.12) to (5.14), the displacements u are function of position and frequency, and they are the Fourier transform in time of the measured displacement. The star symbol $*$ in superscripts represents the complex conjugate of a quantity.

In the case of an isotropic material such as aluminum, a lot of the components of the stiffness tensor are equal to zero, and the remaining ones are linked together. There are only two independent components in the stiffness tensor. Using Voigt Notation, the non-zero components are [12]:

$$\begin{aligned} c_{11} &= c_{22} = c_{33} \\ c_{44} &= c_{55} = c_{66}, \\ c_{12} &= c_{13} = c_{23} \end{aligned} \quad (5.15)$$

and these three values are linked with the equation:

$$c_{44} = \frac{1}{2}(c_{11} - c_{12}). \quad (5.16)$$

Experimentally, my goal is to investigate the variation of the diffusion coefficient with x , so only the x component of the Poynting vector is useful. Moreover, it is assumed that the field is “on average” uniform across the width of the waveguide, due to the quasi-1D hypothesis. The three quantities calculated with equations (5.12) to (5.14) are averaged along the y -axis (width) of the waveguide to reduce the fluctuations (this averaging is represented in the following equations by $\langle \cdot \rangle$). At the end, the diffusion coefficient is obtained using:

$$D(x, \omega) = -\frac{\langle J_x(x, \omega) \rangle}{\frac{\partial}{\partial x} [\langle E_k(x, \omega) + E_p(x, \omega) \rangle]}. \quad (5.17)$$

Equations (5.12) to (5.14) require derivatives with respect to position, but as the acquisition is done only on the surface, there is no direct access to the derivative with respect to z (the direction normal to the surface of the sample). It is possible to evaluate the z -derivatives with the hypothesis of a stress-free boundary on this surface, as there is no load on the sample¹⁸. This hypothesis can be written as [57]:

$$\frac{\partial u_x}{\partial z} = -\frac{\partial u_z}{\partial x}, \quad (5.18)$$

$$\frac{\partial u_y}{\partial z} = -\frac{\partial u_z}{\partial y} \quad (5.19)$$

and

$$\frac{\partial u_z}{\partial z} = -\frac{c_{11} - 2c_{44}}{c_{11}} \left(\frac{\partial u_x}{\partial x} + \frac{\partial u_y}{\partial y} \right). \quad (5.20)$$

In equation (5.20), the notation of the components of the stiffness tensor has been simplified using the Voigt notation (appendix 8.2). The diffusion coefficient can be calculated with equations (5.12) to (5.20).

All these equations used derivatives in space, which can lead to some issues with the experimental data. First, the spacing of the acquisition points has to be small enough for the discretized derivative to be accurate. The spacing has then to be smaller than the typical fluctuation of the field which is usually of the order of λ (the wavelength in aluminum, the typical fluctuation distance in the speckle pattern). Another issue comes from the level of noise of the experimental data which can lead to errors in the derivatives. The calculation of the diffusion coefficient using the equation (5.17) has to be performed with averaged values of the flux and the energy densities. The averaging of these quantities should help to smooth out the

¹⁸ It is assumed that there is no energy going from the sample to the air

fluctuations due to interference effects for a particular realization of a sample. This is done in our case by performing an average across the width of the sample (see section 5.6.2).

5.4.2 Equipartition of the energy

After an elastic wave is incident on a scatterer, the amplitude of the incident wave is distributed along all directions in space, with the distribution depending on the shape and the material of the scatterer and on the frequency of the wave. In a case of a multiple scattering medium, the wave field is randomized after a few scattering events. This randomized field, also called the diffuse field, contains information about the scattering in the medium. For elastic waves, a remarkable property of the diffuse field is the equipartition of the energy of compressional waves with the energy of shear (or transverse) waves. The ratio of these two energies becomes constant with time and depends only on the mechanical properties of the medium [56,57].

Usually, for elastic waves, the compressional wave is the component of the wave for which the displacement of the particles is parallel to the direction of propagation of the total wave, and the transverse waves are the waves for which the displacement of the particles is perpendicular to the direction of propagation. In an isotropic solid, two transverse waves exist, perpendicular to each other, with the same properties (same velocity of propagation). Unlike the transverse waves, the compressional wave leads to a variation of volume in the solid while travelling.

In the case of a diffuse field, it is not possible to define a unique direction of propagation, and consequently the distinction between the two types of waves cannot be made by looking at the direction of the particle displacements. However, the distinction is in the energies. In the diffuse field, the compressional wave is defined as the part of the energy E_c leading to a variation of

volume (curl-free), and the transverse wave is the divergence-free (no variation of volume) part of the energy, E_t (see appendix 8.3). This results in an alternative expression for the potential energy [equation (5.11)], separating the two energies [57,67]:

$$E_p = \frac{c_{11}}{2} (\vec{\nabla} \cdot \vec{u})^2 + \frac{c_{44}}{2} (\vec{\nabla} \times \vec{u})^2 + I = E_c + E_t + I. \quad (5.21)$$

The term I in equation (5.21) is an interference term involving some cross derivatives of the field, but on average this term is equal to zero, except close to a boundary [57]. The equipartition of energy involves the ratio of the two first terms of the right-hand side of the equation (5.21).

In the scattered wave field, the ratio of the two energies depends on the number of modes (phonons) for each type of wave existing in the medium. The number of modes for each wave can be determined using the Debye model counting the number of phonons in a given volume per frequency band, *i.e.*, the density of states. The number of modes for a three-dimensional medium of volume V is [56,68]:

$$dN_c = \frac{1}{2\pi^2} \frac{\omega^2}{v_c^3} V d\omega \quad (5.22)$$

and

$$dN_t = 2 \frac{1}{2\pi^2} \frac{\omega^2}{v_t^3} V d\omega. \quad (5.23)$$

The number of modes of the compressional waves N_c and of the transverse wave N_t depends on the frequency, the volume of the medium V and on the velocity of each wave (v_c and v_t). The factor 2 in equation (5.23) is due to the presence of two orthogonal transverse waves in the medium. The theory for three-dimensional media is used, even though the sample is a

monolayer of beads, as the objects are 3D and the thickness of the sample and the wavelengths are comparable.

Finally, the ratio of the two energies \mathcal{R} , which is equal to the ratio of the numbers of modes, is equal to:

$$\mathcal{R} = \frac{E_t}{E_c} = \frac{dN_t}{dN_c} = 2 \frac{v_c^3}{v_t^3} = 2 \left(\frac{c_{11}}{c_{44}} \right)^{3/2} \quad (5.24)$$

The velocity of the compressional wave is always larger than the velocity of shear waves, so the ratio \mathcal{R} of the energy of transverse wave to the energy of compressional wave is bigger than 1 for scattered waves in a three-dimensional medium. In the case of a two-dimensional sample all the powers in equations (5.22) and (5.23) are reduced by one, so the ratio of the energy involves the square of the velocities instead of the cube of the velocities. In the case of 2D samples, surface and or plate waves, such as Rayleigh waves or Lamb waves, need to be considered and will affect the value of the ratio. The stress-free boundary condition used to evaluate the derivative along z affects the ratio \mathcal{R} . By considering the energy densities of the acoustic wave with the stress free boundary condition, the ratio becomes [69]:

$$\mathcal{R} = \frac{E_t}{E_c} = \frac{\frac{c_{44}}{2} (\vec{\nabla} \times \vec{u})^2}{\frac{c_{11}}{2} (\vec{\nabla} \cdot \vec{u})^2} = \frac{1}{4} \frac{c_{11}}{c_{44}} \frac{4 \left[\left(\frac{\partial u_z}{\partial x} \right)^2 + \left(\frac{\partial u_z}{\partial y} \right)^2 \right] + \left(\frac{\partial u_x}{\partial y} - \frac{\partial u_y}{\partial x} \right)^2}{\left(\frac{\partial u_x}{\partial x} + \frac{\partial u_y}{\partial y} \right)^2} \quad (5.25)$$

Equation (5.25) shows that the equipartition ratio at a free surface depends on the elastic properties of the material as well as the displacement field on the surface. The reflection of the field at a free surface changes the repartition of energy between shear waves and compressional waves due to mode conversion.

Equipartition being a time-dependent phenomenon, the calculations are performed with the data that depends on time and space, unlike what is done for the calculation of the position-dependent diffusion coefficient which is done using frequency-dependent data. The derivatives with respect to the z-direction are obtained with equations (5.18) to (5.20).

5.5 Experimental results

The laser interferometer measures the displacement on the surface of the sample. The experiment was done using the setup shown in Figure 5.1 and the signal sent with the top transducer was a Gauss2 pulse as shown in Figure 4.6. Two experiments had to be done, one for each orientation of the sample to measure the two in-plane displacements. Thus the out-of-plane signal (z-direction) was measured twice. From these two measurements, the three components of the displacement were recovered. For all the acquisitions, the scanning grid was composed of pixels of size $0.25 \times 0.25 \text{ mm}^2$. The signal was recorded for a duration of 1 ms with a sampling frequency of 25 MHz.

5.5.1 In-plane signal filtering

Before looking at a full scan result, it is instructive to look at an individual time-dependent signal recorded at one position of the sample. The signals represented in Figure 5.3 were recorded for the sample shown in Figure 5.1, 4 mm away from the generating transducer. At this distance, the amplitude was still quite high, as it did not go through a lot of scattering events, which have the effect of reducing the amplitude. As explained in section 5.2.2, the noise level is much higher for the in-plane signal than for the out-of-plane signal, but fortunately, most of the noise is at high frequencies (above the frequencies of interest), and therefore it is easy to reduce the noise level by filtering the signals. In Figure 5.9, a filtered signal is compared with the

original signal. The filtering was performed in the Fourier domain, with a Gaussian filter centred at 1 MHz (corresponding to the central frequency of the transducer), and a filter bandwidth (standard deviation) of 400 kHz. The filter bandwidth was wide enough so that the actual signal was not modified and was sufficiently narrow to get rid of most of the noise.

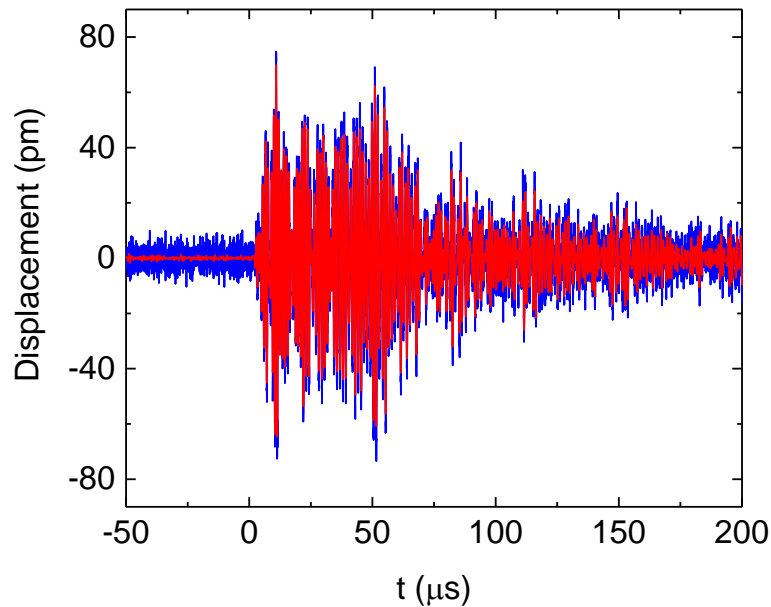


Figure 5.9: In-plane signal measured 4 mm away from the transducer, before (blue) and after (red) filtering. The blue signal is identical to the blue signal in Figure 5.3. The central frequency of the filter is 1 MHz and its bandwidth 400 kHz.

The pre-trigger signals in Figure 5.9 give a good indication of the efficiency of the filtering to reduce the overall noise level of in-plane signals. This reduction of the noise level is important for measuring the signal at long-times or at positions farther away from the generating transducer, where the amplitude of the signal is smaller.

5.5.2 Scan of the entire sample

A scan of the full surface of the sample (Figure 5.1) was performed for only one of the orientations, so only one of the in-plane components, the one polarized in the y -direction, has been measured along with the out-of-plane component. I present in section 5.5.3 some results obtained from measurements on a smaller area for the two different sample orientations. The full acquisition was performed only for one orientation due to the high noise level at long distances from the generating transducer in the sample (section 5.5.2.1). Figure 5.10 and Figure 5.11 show the absolute value of the displacement for both components at four different times in order to view the time-evolution of the field in the sample. The white line in Figure 5.10, Figure 5.11 and Figure 5.15 to Figure 5.19 around $x = 30$ mm is an area of the sample which has not been scanned.

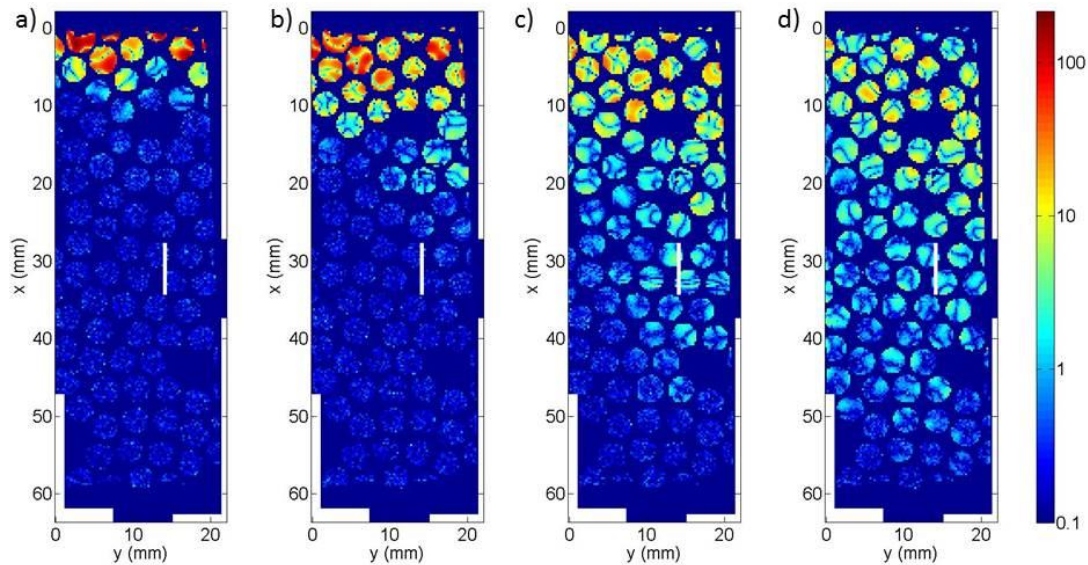


Figure 5.10: Absolute value of the out-of-plane displacement in pm at four different times: a) $5 \mu\text{s}$, b) $20 \mu\text{s}$ c) $100 \mu\text{s}$ and d) $250 \mu\text{s}$. The pulse is emitted at the top of the sample. The color scale is logarithmic. The central frequency and bandwidth are 1 MHz and 400 kHz, respectively.

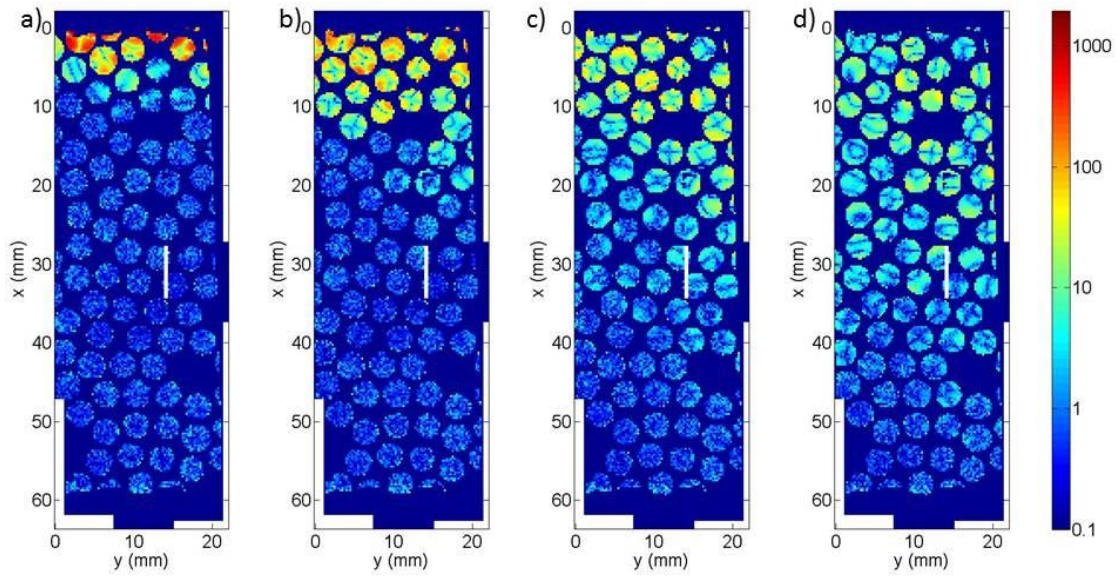


Figure 5.11: Absolute value of the in-plane displacement signals in the y -direction in pm at four different times: a) $5 \mu\text{s}$, b) $20 \mu\text{s}$ c) $100 \mu\text{s}$ and d) $250 \mu\text{s}$. The experimental data have been filtered to remove the high frequency noise.

5.5.2.1 Evaluation of the noise level

By comparing the measurements on beads at large values of x , far from the transducer, at a time before the ultrasonic signal could have arrived, it is clear that the noise level is higher for the in-plane signal than for the out-plane signal, even after the filtering. For example, by comparing the plots in Figure 5.12, the in-plane noise signal is “brighter” than the out-of-plane noise signal. A better estimate of the noise level can be obtained by looking at the signals on some specific beads. Two beads with coordinates ($x = 46.5 \text{ mm}$, $y = 10 \text{ mm}$) and ($x = 50.5 \text{ mm}$, $y = 10.25 \text{ mm}$) have been chosen to calculate some properties of the noise at a time of $5 \mu\text{s}$. These two beads were too far from the transducer for any ultrasonic signal to have reached them at such a short time as shown in Figure 5.10 to Figure 5.12. The averaged displacement and the standard deviation of the displacement have been calculated for these two beads (the calculation has been done on 288 pixels). The results are in Table 5.1.

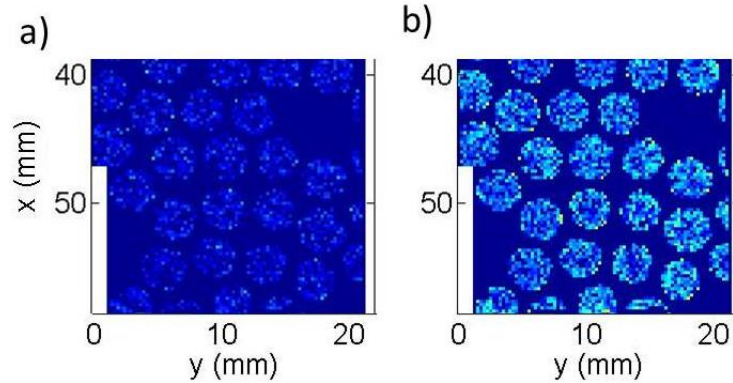


Figure 5.12: Absolute value of the amplitude of the out-of-plane displacement (a) and the in-plane displacement (b) $5 \mu\text{s}$ after the emission of the pulse for the beads far away from the transducer (the color scale is identical for both pictures and is the identical to the one of Figure 5.10).

	Out-of-plane	In-plane
Average (pm)	-0.043	-0.047
Standard deviation (pm)	0.23	1.6

Table 5.1: Average and standard deviation of the noise for two components.

In Table 5.1, the properties of the noise of the two displacement components have been calculated. As expected, the average of the noise for each component is similar and close to zero. It is in this case negative (the displacement is going in the negative direction), but because of its random nature, the noise can be negative or positive (as can the displacement). The main difference comes from the standard deviation which is 7 times larger for the in-plane component. This result shows that the noise fluctuations are much larger for the in-plane component even after the filtering was performed to remove the high frequency noise (section 5.5.1), and this makes it harder to detect small signals, for example, at long times or at long distances.

5.5.2.2 *Transmission along the sample*

As shown in Figure 5.10, the signal was able to travel across the entire sample after 250 μ s, but we will see that it is not the case for all the frequencies. The transmission in the sample depends indeed on the frequency and some pass bands and transmission dips (band gaps) are visible. As explained in chapter 0, these frequency bands depend on the resonant frequencies of the coupled bead resonators constituting the sample (see section 5.7.1). The amplitude transmission coefficient as a function of frequency and distance from the transducer can be calculated from the data measured with the laser interferometer, and is shown in Figure 5.13 and Figure 5.14. To obtain the transmission coefficient, the averaged amplitude was calculated by doing the average of the absolute value of the Fourier transform of the displacement over a 1-mm-wide region along the x -direction (4 pixels) and across the sample in the y -direction. The transmission coefficient at a given distance was estimated by taking the ratio of the averaged amplitude at this distance with the averaged amplitude between 0 and 1 mm away from the transducer (first region)¹⁹. Transmission coefficients have been calculated for both the out-of-plane and the in-plane displacements.

¹⁹ This ratio explains why the transmission at 1 mm is equal to one for all frequencies.

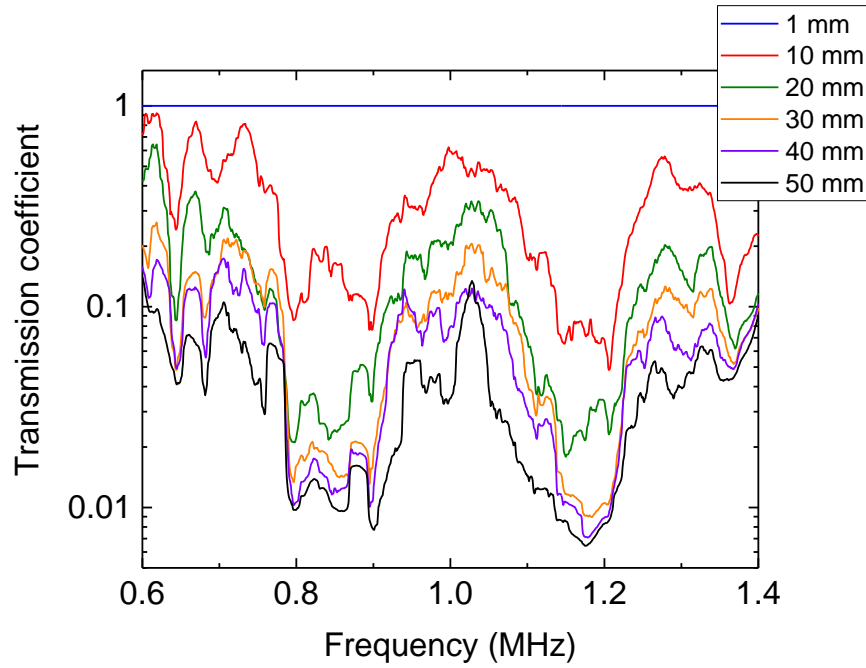


Figure 5.13: Transmission coefficients of the out-of-plane displacements for different distances from the transducer.

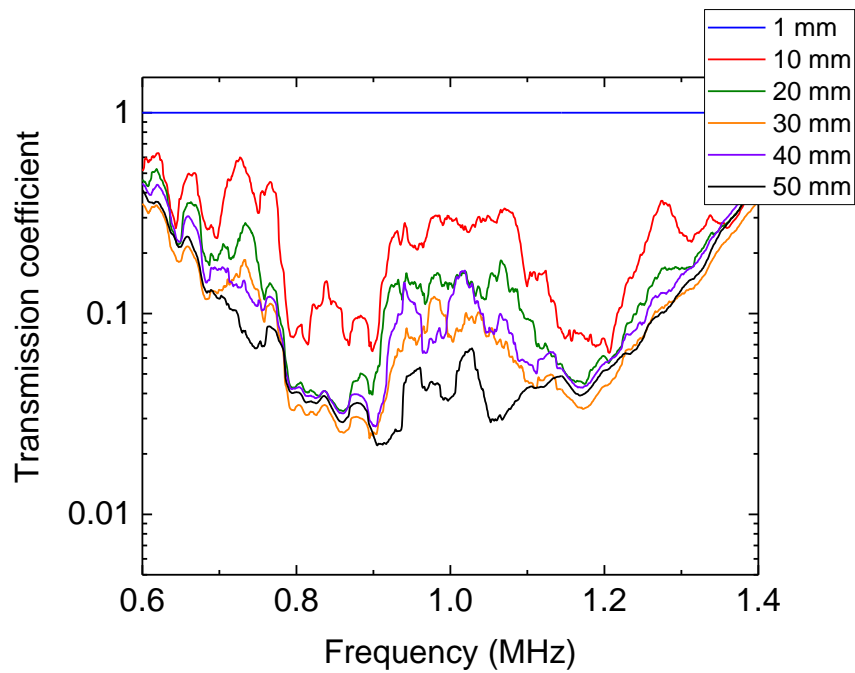


Figure 5.14: Transmission coefficients of the in-plane displacements for different distances from the transducer.

Figure 5.13 and Figure 5.14 show clearly the existence of two band gaps between 600 kHz and 1.4 MHz, the first one between 800 and 900 kHz and the second one from 1.1 to 1.2 MHz. These two band gaps are comparable to the ones observed in the 3D samples made with brazed aluminum beads (see Figure 3.12). Beads constituting the current sample have been sanded on one side, so the resonances of each constituent (a sanded bead) are slightly shifted compared to a single spherical bead, due to the change of symmetry and shape of the resonator. However, these resonant frequencies are not so different (section 5.7.1) which explains the similarities of the band gaps observed for this sample and the ones observed for a collection of non-sanded beads.

The depth of the band gaps is different in Figure 5.13 and Figure 5.14. This observation can be explained by the noise level, since the minimum value of the transmission coefficient in a band gap is limited by the amplitude of the noise in these measurements. It also explains why less variation of the signal with distance from the generating transducer is observed in the case of the in-plane component compared to the out-of-plane component. For example, at 850 kHz there is no variation of the transmission for the in-plane component after 20 mm, which means that here the noise signal is already higher than the acoustic signal, whereas some variation of the transmission of the out-of-plane components is still visible 30 mm away from the generating transducer.

The experimental data can be filtered with a narrow bandwidth to look at the time dependence at different frequencies. More specifically, the time-dependence behaviour for central frequencies inside and outside a band gap can be compared. The data displayed in Figure 5.15 to Figure 5.18 have been obtained with a filter having a bandwidth of 25 kHz and are centered at 850 kHz (inside a band gap) or at 1000 kHz (outside a band gap).

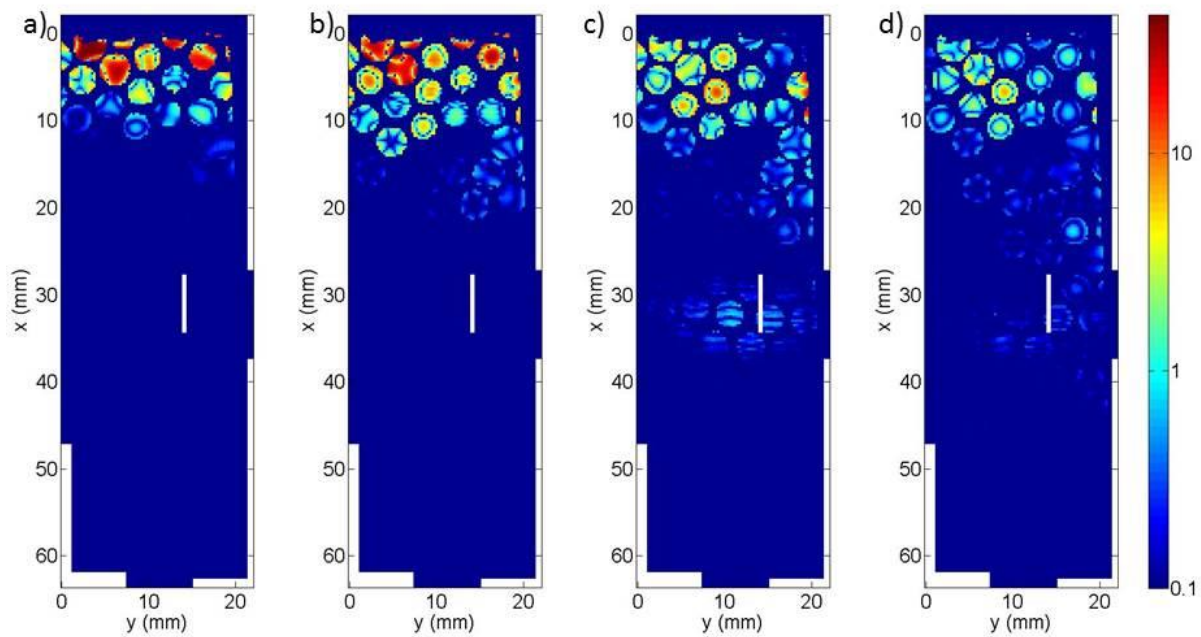


Figure 5.15: Absolute value of the out-of-plane displacement, in pm, for a frequency inside a band gap (850 kHz) at four different times: a) 5 μ s, b) 20 μ s c) 100 μ s and d) 250 μ s. The pulse is emitted at the top of the sample. The color scale is logarithmic.

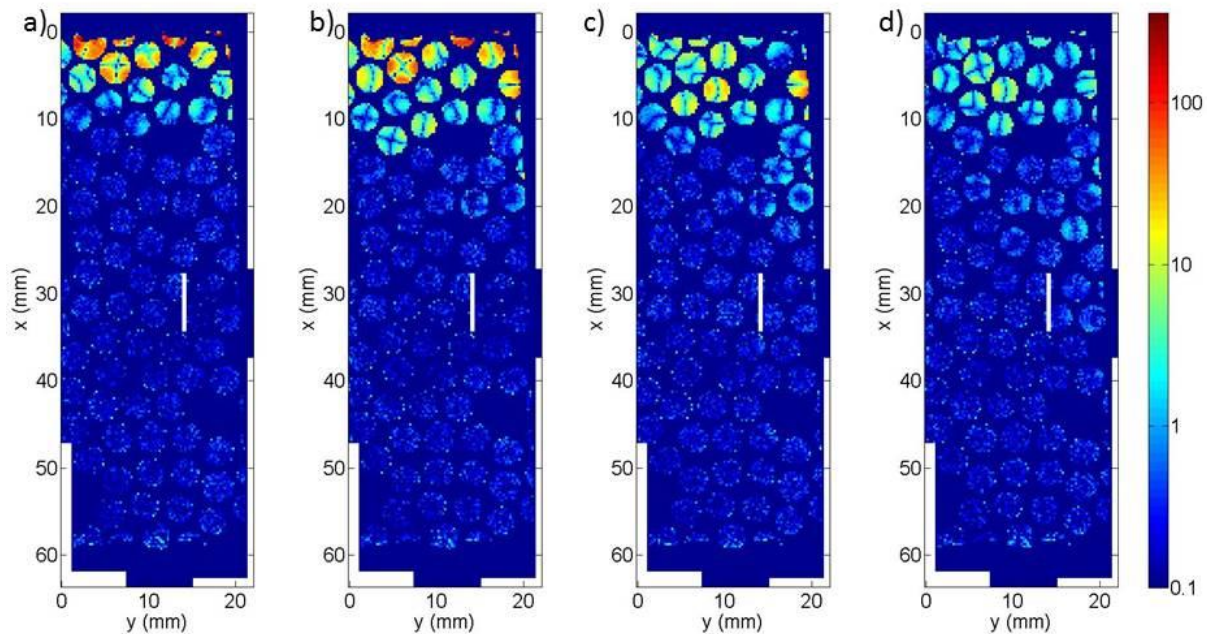


Figure 5.16: Absolute value of the in-plane displacement, in pm, for a frequency inside a band gap (850 kHz) at four different times: a) 5 μ s, b) 20 μ s c) 100 μ s and d) 250 μ s. The pulse is emitted at the top of the sample. The color scale is logarithmic.

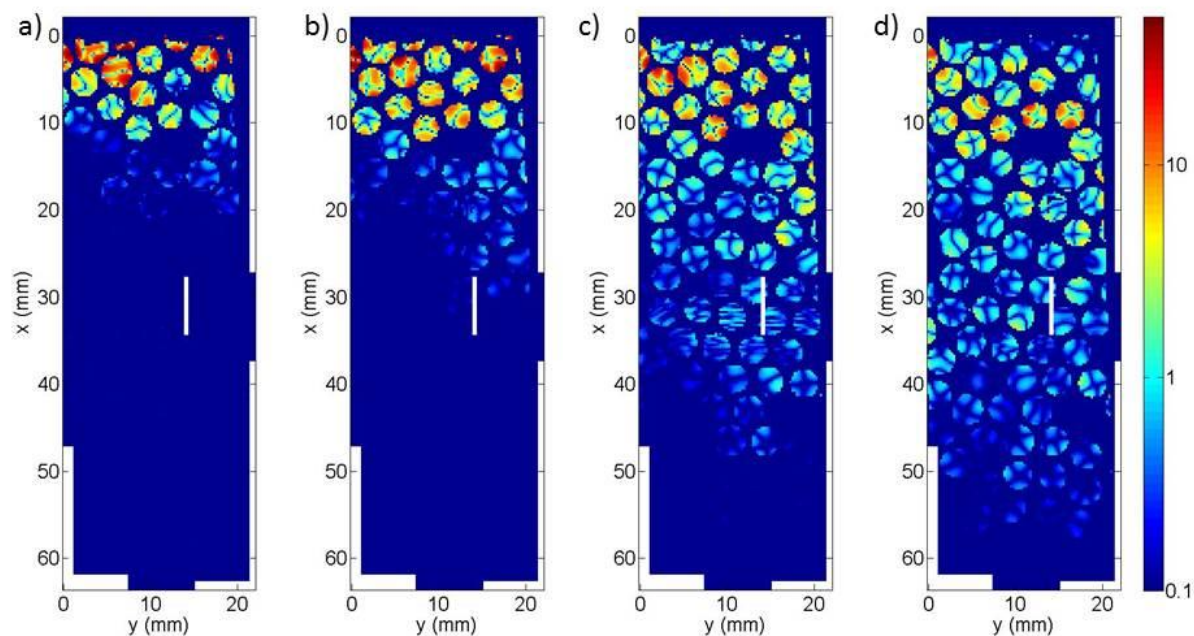


Figure 5.17: Absolute value of the out-of-plane displacement, in pm, for a frequency inside a pass band (1000 kHz) at four different times: a) 5 μs , b) 20 μs c) 100 μs and d) 250 μs . The pulse is emitted at the top of the sample. The color scale is logarithmic.

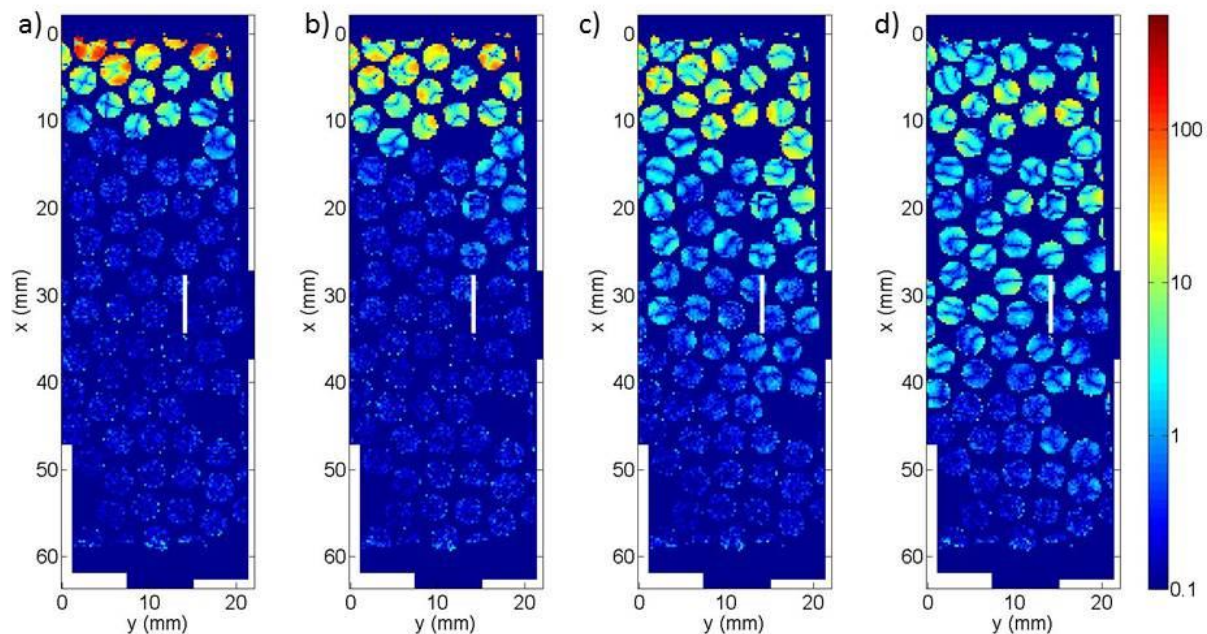


Figure 5.18: Absolute value of the in-plane displacement, in pm, for a frequency inside a pass band (1000 kHz) at four different times a) 5 μs , b) 20 μs c) 100 μs and d) 250 μs . The pulse is emitted at the top of the sample. The color scale is logarithmic.

In the two figures representing the signal inside a band gap (Figure 5.15 and Figure 5.16), the signal was not able to travel beyond a distance equal to three or four beads away from the generating transducer even at long times (250 μ s). At this frequency the amplitude of the signal decreased rapidly with distance inside the sample due to scattering, leaking back to the transducer (for which there is a reflection coefficient different from 1) and eventually by dissipation. By contrast, unlike the transport inside the band gap, in the two figures representing the transport in a pass band (Figure 5.17 and Figure 5.18), the signal can be seen to travel across the full length of the sample. For long distances, the amplitude of the measurable signal is, once again, limited by the noise level for the in-plane signal.

One effect of narrow band filtering is to reduce the noise level considerably. For the out-of-plane signal, this has the effect of reducing the noise to the same level as the background signal at positions where there are no beads. As can be seen in Figure 5.15 and Figure 5.17, it makes it impossible to distinguish the “shape” of the sample, the image being a uniform blue at long distances. This can be compared with Figure 5.16 and Figure 5.18 in which all the beads of the sample can be seen due to the noise.

In Figure 5.15 c), a parasitic signal can be observed around 30 mm away from the transducer. This signal corresponds in fact to a signal travelling in the air in front of the sample, as was deduced from the speed (~ 340 m/s) at which this signal travels. As we can see in Figure 5.1, the sample did not cover the entire surface of the transducer, so a small signal was emitted into the air in front and behind the sample. The variation of air density due to the acoustic wave was enough to change the travel time of the laser light and the signal was detected due to the reflection of the laser light from the sample. This signal is more visible in Figure 5.15 because the signal of the elastic wave in the sample is smaller than the amplitude of the signal in air.

5.5.2.3 Spatial distribution of the elastic waves at different frequencies

It is also interesting to look at the spatial distribution of the amplitude of the signal for some specific frequencies, and in particular, to compare the signals at frequencies inside or outside of the band gap. In Figure 5.19, the amplitudes of the Fourier transform of the displacements at three different frequencies are displayed. The first image (a) is for the frequency 850 kHz, inside a band gap, the second image (b) is at 880 kHz, inside and close to the edge of a band gap, and the third image (c) represents the amplitude at 1000 kHz in a pass band.

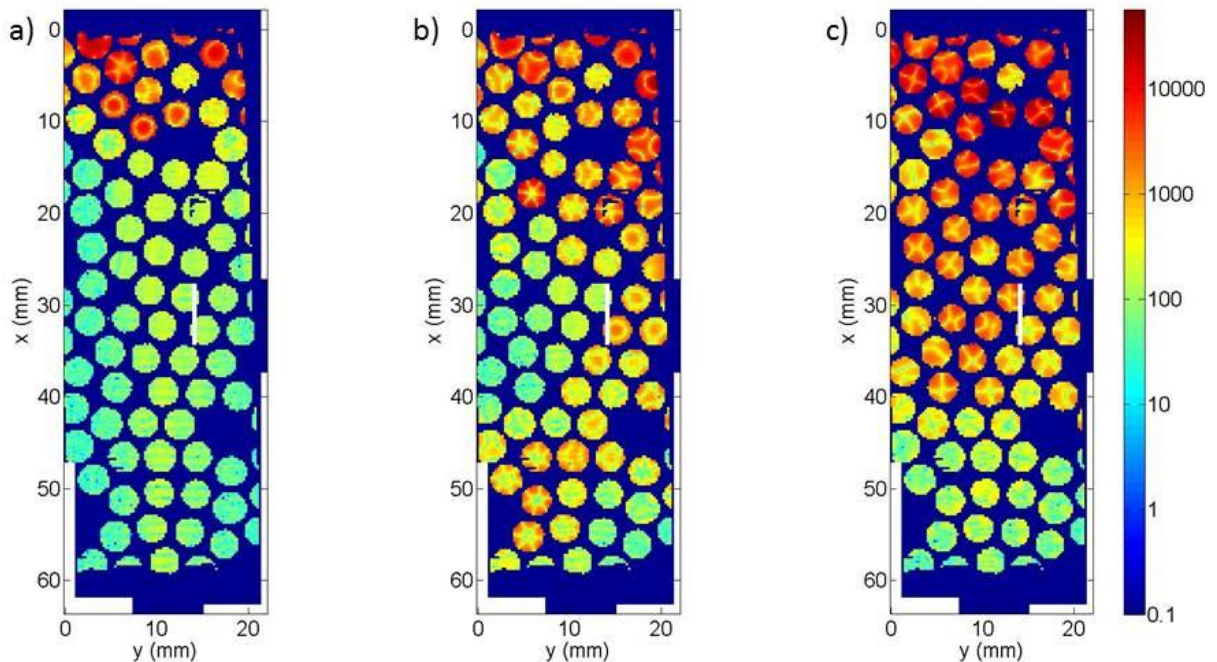


Figure 5.19: Absolute value of the amplitude (a. u.) of the Fourier transform of the out-of-plane displacement for three different frequencies: a) 850 kHz, b) 880 kHz and c) 1000 kHz. The color scale is logarithmic.

The images in Figure 5.19 give information on how waves at a specific frequency can travel inside the sample; they correspond to the steady state or to a continuous wave experiment, in which only one frequency is sent into the sample instead of a wide frequency-band pulse used

here. Three different patterns can be observed for the three different frequencies. The simplest one is observed at 1000 kHz (image c) where the sample was excited uniformly across its top edge by the transducer and the amplitude decreases with the distance. At 850 kHz (image a), there was barely any signal going beyond 10 mm away from the transducer; nonetheless, there was a chain of beads, around $y = 10$ mm, which had an amplitude slightly above the noise level all along the sample (beads in yellow-green instead of blue-green for the noise level). At 880 kHz (image b), the amplitude was approximately uniform across the width of the sample up to 20 mm away from the generating transducer, but beyond this distance, a channel with a width of two beads appeared. It is particularly visible from a position defined by $(x = 30$ mm, $y = 20$ mm) to $(x = 50$ mm, $y = 0$ mm). The amplitude on both sides of this channel was at the noise level.

For the two lowest frequencies (850 kHz and 880 kHz), the signal observed in the lower part of the sample, where there is only noise at nearby frequencies in this band gap, might correspond to some “open channels” of the disordered waveguide sample at a given frequency [70,71]. These open channels appear via the coupling of resonances of several scatterers. The presence of these channels means that if I were able to shape the input signal in an optimum way, I could control the field inside the sample and activate a given channel. These activated channels would have an almost total transmission, unlike the one observed in Figure 5.19 where the amplitude of the signal on the beads far away from the generating transducer is small. Controlling the input means varying the amplitude and the phase of the input signal of each bead on the input side. In the current experimental setup, this is not possible, as a single transducer was used to excite the entire top of the sample at once, but using small transducer elements, for example in an array of transducers, will make this experiment possible.

The optimum shape of an input signal to activate a given channel would be obtained by using the interferometer to measure the field obtained in the sample when each element of the transducer array is used individually and then performing a linear sum of these fields [71]. From one element to the next one, both the amplitude and the phase can be varied to shape the field inside the sample. An optimisation algorithm would need to be created to find the best combination of signals from each element.

5.5.3 Acquisition of three components of the displacement

Two more experiments have been performed on the same sample at two different central frequencies (500 kHz and 1 MHz) by using the appropriate transducers. These acquisitions of the field have been performed for the three components: the two in-plane displacements and the out-of-plane displacement. The acquisition of the third component is done by measuring the field of the same sample rotated by 90°.

In section 5.5.2, it has been shown that the noise level for the in-plane components is significantly higher than the noise of the out-of-plane component, making the signal difficult to detect above the noise at a distance far from the transducer. Consequently, only the first 2 cm of the sample have been scanned in these two experiments. In Figure 5.20, the three components of the field obtained with a 1 MHz transducer are displayed for four different times. Figure 5.21 displays the same quantities but obtained with the 500 kHz transducer. In these two figures, it is possible to see, one more time, that the noise level is higher for the in-plane components, but also that the overall signal is higher.

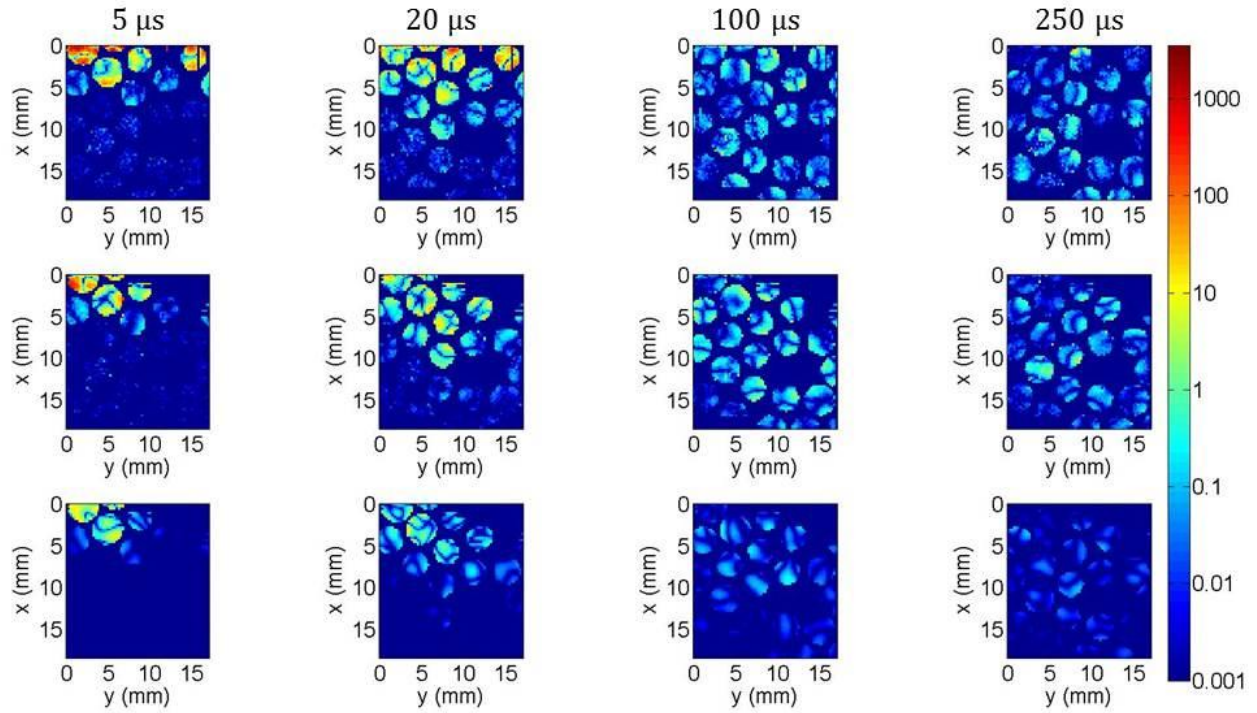


Figure 5.20: Absolute value of the three components of the field for four different times (time value indicated at the top of each column) obtained with a 1 MHz transducer. First and second rows show the x and y components (in-plane); the third row shows the z -component (out-of-plane). The color scale is in pm.

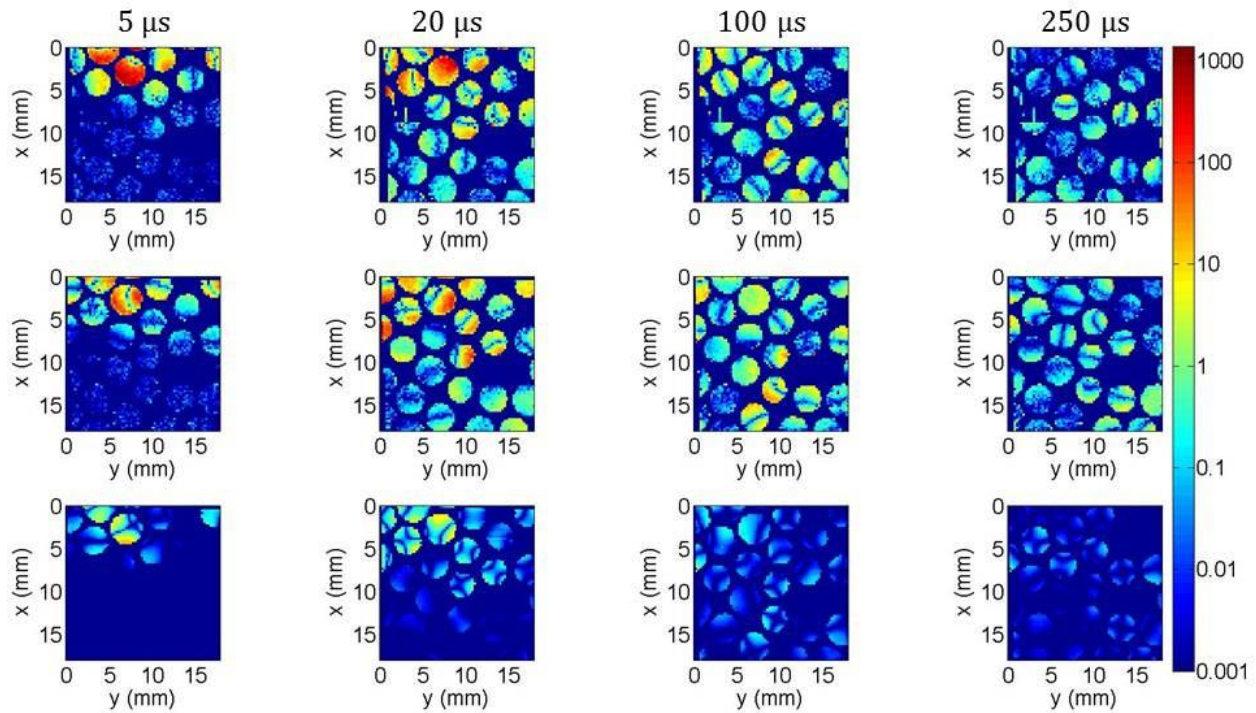


Figure 5.21: Absolute value of the three components of the field for four different times (time value indicated at the top of each column) obtained with a 500 kHz transducer. First and second rows show the x and y components (in-plane); the third row shows the z -component (out-of-plane). The color scale is in pm.

The data obtained at 500 kHz gave information about the transmission for a new frequency-band. By using the same technique as previously (Figure 5.13 and Figure 5.14), the transmission is calculated 17 mm away from the transducer for the three components (Figure 5.22), and shows that another band gap exists in this sample, between 325 and 525 kHz.

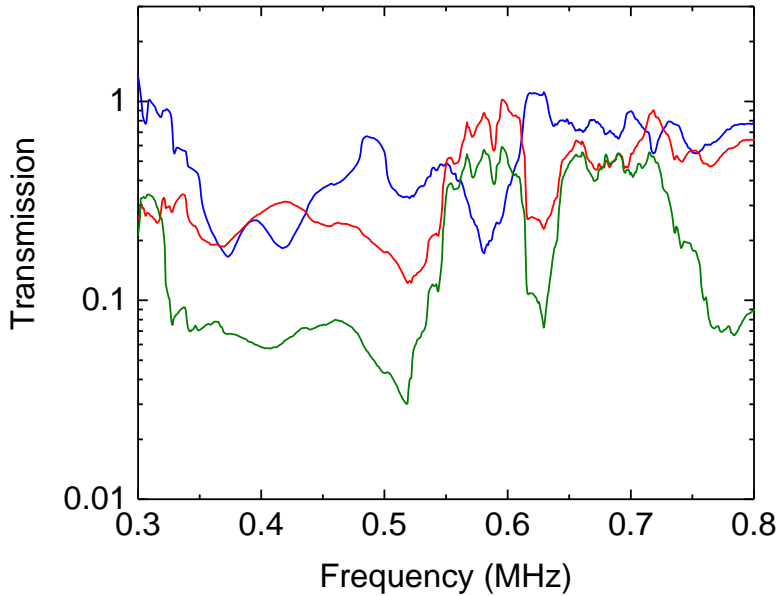


Figure 5.22: Transmission for each component obtained with the 500 kHz transducer 17 mm away from the transducer. Blue: x -component (in-plane), red: y -component (in-plane) and green: z -component (out-of plane).

5.6 Analysis of the results

5.6.1 Estimation of the scattering mean free path

In section 5.4.1, describing the position-dependent diffusion coefficient, the hypothesis of a quasi-1D waveguide is made. For equations (5.6) and (5.7) giving the value of the diffusion coefficient as a function of position to be valid, the sample needs to respect the condition $w \gtrsim l_s \ll L$, where w is the width of the sample, L its length and l_s the scattering mean free path of the wave in the sample. As was done in chapter 4 for the sample of aluminum beads in liquid and explained in chapter 2, the scattering mean free path can be found by looking at the attenuation of the ballistic signal of the wave. Usually it is measured by comparing the amplitude of a reference signal, a signal acquired when there is no sample between the emitter

and the receiver. For this experiment, a reference cannot be measured, but I can compare the amplitude of the ballistic signal at two positions inside the sample with a known separation. The scattering in the sample being strong (the field is losing coherence rapidly according to the field images), these two positions cannot be far from the transducer, otherwise, the ballistic signal will not be visible.

Figure 5.23 represents the averaged out-of-plane signal at the beads touching the transducer (blue) and 10 mm away from the transducer (red). The signals are averaged along the width of the sample for one value of the distance (one line of acquisition). The ballistic pulse is extracted from these two signals. The amplitude ratio is calculated to obtain the attenuation, and then the scattering mean free path is determined as a function of frequency (Figure 5.24).

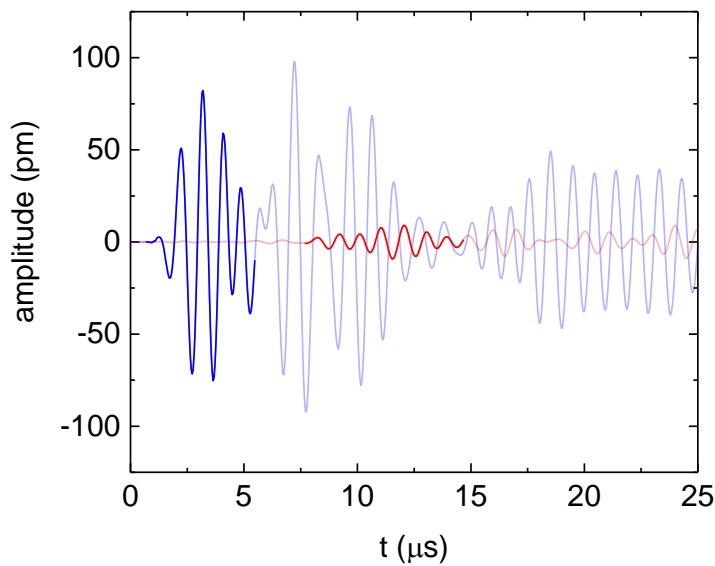


Figure 5.23: Averaged amplitude of the out-of-plane signal at the output of the transducer (blue) and 10 mm away from the transducer (red). The thicker, darker solid lines represent the ballistic signals; the thinner, lighter colored lines, represent the scattered signal. Experiments are performed at 1 MHz.

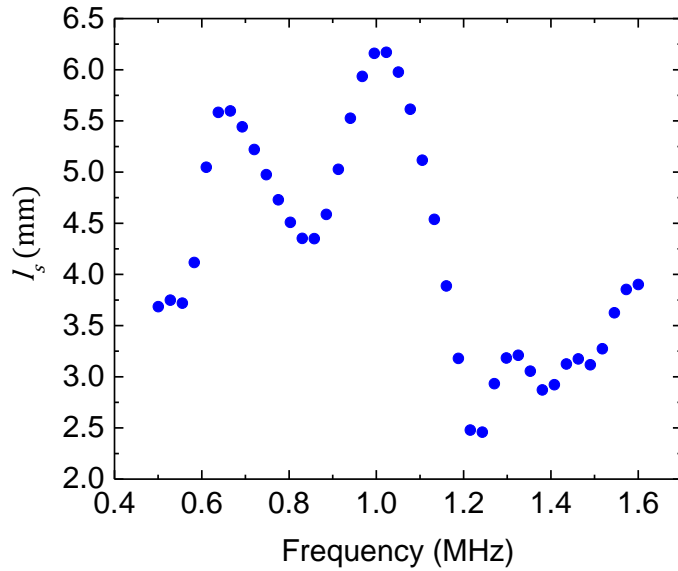


Figure 5.24: Scattering mean free path obtained from the out-of-plane signal for the 1 MHz experiment.

The value of the scattering mean free path is between 2.5 and 6 mm and l_s is minimum for the frequencies at which band gaps have been observed in Figure 5.13, *i.e.*, at around 850 kHz and around 1.2 MHz.

Even though the values obtained for l_s may not be very accurate, their values are far enough from the value of the width (~ 4 mm compared to 20 mm) to indicate that the approximation of a quasi-1D waveguide cannot be assumed in this sample, *a priori*. However, the input signal from the transducer is uniform across the top of the sample (no x and y dependence) and the perfect reflectivity on the sides of the sample further limits the possibility of transport across the width of the sample so that a transverse component of the transport is not expected.

5.6.2 Position-dependent diffusion coefficient

In section 5.4.1 the calculation of the position-dependent diffusion coefficient has been explained. One of the hypotheses made in these calculations is to consider the sample as a quasi-

1D waveguide in order to neglect any transport in the transverse direction (y -direction). As shown in the section 5.6.1, this quasi-1D hypothesis is not entirely respected. Nonetheless, calculations have been performed to assess the possibility to determine the values of the diffusion coefficient as a function of position along the length of the sample, and to have a better idea of what kind of sample would be needed to obtain more accurate results. It is worth emphasizing that position dependence of D is expected in the localized regime for other sample geometries, such as a slab of finite width with open boundaries on the faces of the slab.

According to the quasi-1D hypothesis, the averaging of the energy is done on the entire width of the sample, and this is performed every millimeter in the propagation direction x corresponding to an average over 4 pixels (4 lines of acquisition). As these calculations require having the three components of the displacement, they are performed only on the first 2 cm of the sample, corresponding to the acquisitions shown in Figure 5.20. In order to reduce the fluctuations, an average over a frequency bandwidth of 25 kHz is also performed; this corresponds to 33 adjacent values of frequencies. It is assumed that the behaviour from one frequency to the next one is not too different, as observed in the transmission profiles (Figure 5.13).

In Figure 5.25, the energy density, calculated with equations (5.10) and (5.11), as a function of the distance from the transducer is plotted for three different frequencies, one frequency in the first band gap (850 kHz) a frequency in a pass band (1000 kHz) and a frequency inside the second band gap (1170 kHz). The decrease of the energy with distance is greater for the two frequencies in the band gaps. The calculation of the diffusion coefficient is done using Fick's law. According to this law, the energy density has to decay monotonically with the distance from the source. In Figure 5.25, we can clearly see that it is not the case. For some frequencies,

at some distances the energy density is increasing, this is due to interference effects which increase the energy in a given bead. These fluctuations in the energy density are amplified when the derivative as a function of position is taken to calculate the diffusion coefficient.

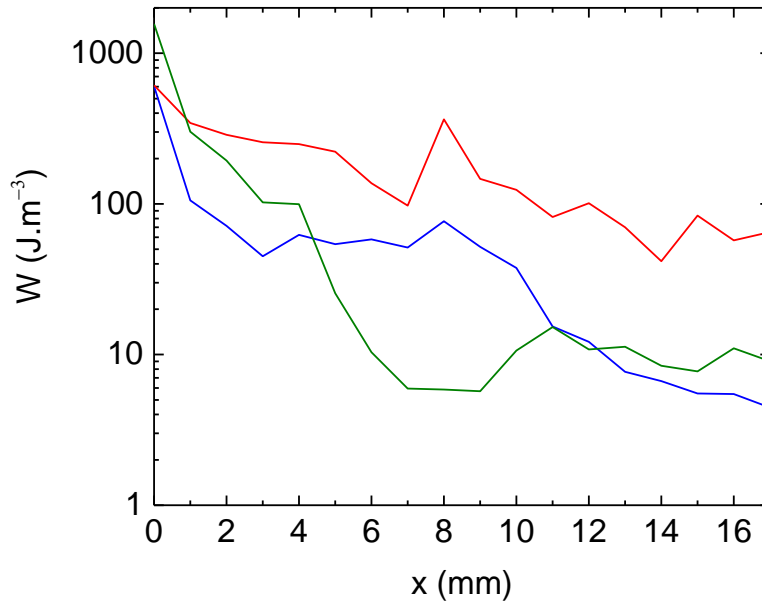


Figure 5.25: Energy density for three different frequencies as a function of the distance from the transducer (blue: 850 kHz, red: 1000 kHz and green: 1170 kHz).

In Figure 5.26, the component of the flux (Poynting vector) along the x -direction is shown for the same three frequencies. As for the energy density (Figure 5.25), the variation of the flux is not smooth with the distance. All these fluctuations lead to estimates of the diffusion coefficient (Figure 5.27) that fluctuate wildly, with many values being not physical (for example, negative values).

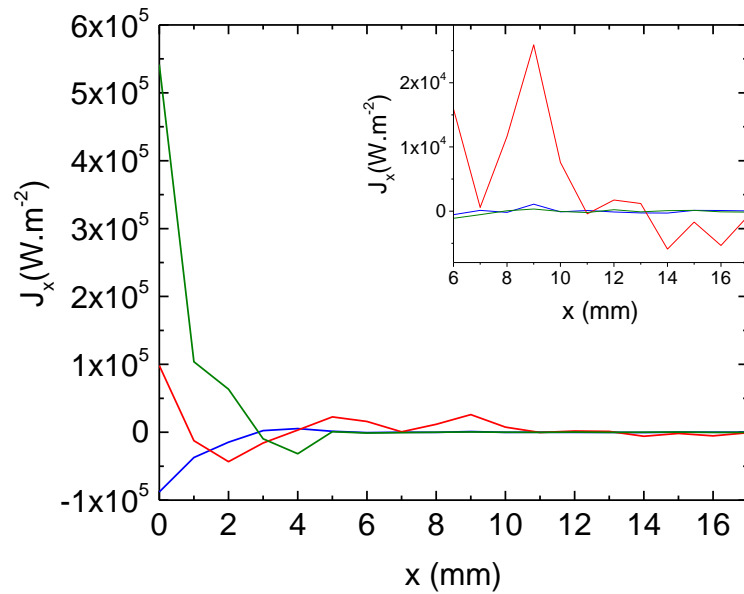


Figure 5.26: x -component of the flux (Poynting vector) for three different frequencies as a function of the distance from the transducer (blue: 850 kHz, red: 1000 kHz and green: 1170 kHz). The inset is a zoom at the long distances.

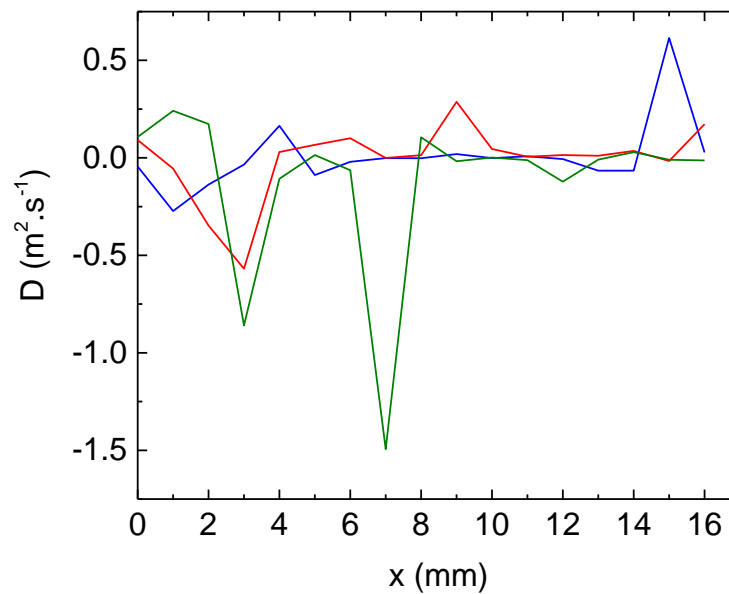


Figure 5.27: Diffusion coefficient calculated as a function of distance away from the transducer for three different frequencies (blue: 850 kHz, red: 1000 kHz and green: 1170 kHz).

It is therefore not possible in this sample made of a single layer of aluminum beads to calculate correctly the diffusion coefficient as a function of position. Several phenomena can explain why I was not able to do it. First, the hypothesis of a quasi-1D waveguide is not respected, which could lead to some transverse transport in the sample. Secondly, the amount of ensemble averaging that is possible with one sample is not enough to have an idea of the “average” behaviour in this kind of experiment. Some averaging over position and frequency has been done, but it is not sufficient to compensate for the effects of the large fluctuations that are intrinsic to wave transport in this type of highly disordered sample that contains a small number of beads, where, for example, some beads might store more energy than others at a given frequency. If we want to perform this analysis on this kind of sample, we will need to have samples with different arrangements of beads, with the same average properties, such as the density of beads and the geometry. It would also be useful to have a narrower sample to get closer to the quasi-1D approximation, but these samples cannot be too narrow, otherwise the number of configurations existing for such a sample will be reduced dramatically. If we want to keep the possibility to have a good number of configurations, these samples should be at least 3 beads wide. Another possibility is to perform this experiment on another kind of sample. Instead of the aluminum beads as being both the scatterers and the medium of propagation, a plate with holes in it can be used. In this case, the holes are the scatterers and the medium of propagation is the plate. In such a sample, some other complications might appear such as the presence of Lamb waves, which are resonant modes of a plate. These waves are highly dispersive and as a consequence introduce other physical phenomena which would need to be taken into account. Also the nature of the scattering would be different, and this would affect the possibility of reaching a localization regime. Such a sample would be closer to samples used in a

similar experiment done in optics [72], where the waveguide was a silicon membrane with air holes in it acting as scatterers (no example of such a measurement exists for acoustic waves).

5.6.3 Equipartition of the energy

For the equipartition of energy to exist, the wave needs to undergo several scattering events for the amplitude and the phase to be randomized [56]. For a scattering medium, the distance necessary for the wave field to have lost information about its original direction and phase is the transport mean free path l_B^* (defined in section 2.5.3). The transport mean free path is proportional to the scattering mean free path l_s and depends on the directivity of the scatterers. The short values of l_s obtained in section 5.6.1 are for this analysis an advantage to satisfy this condition rapidly, after a few microseconds.

In order to obtain usable data, the fluctuations of the signal in space and time due to interferences need to be reduced, so it is necessary to average over nearby positions and times. In section 5.6.2, I was interested in the variation of the energy with distance away from the transducer, so the averaging was performed on 1-mm-thick lines (4 pixels in x). For the calculation of the equipartition of energy, the distance from the transducer does not play an important role, but since the repartition of total energy between shear energy and compressional energy should be similar in a given bead, the average over the surface of each bead was taken. All the signals are averaged in time using a sliding window of 40- μ s width.

The calculation was performed for different frequencies. The experimental signal has been filtered with a bandwidth of 25 kHz at different central frequencies (same filter as the one used to plot Figure 5.15 to Figure 5.18). Figure 5.28 to Figure 5.31 show the shear and compressional energies for two different beads at two different frequencies. The first bead is relatively close to

the transducer (centre of the bead is 8 mm away from the transducer), so a lot of energy is reaching it, and it is farther away than the scattering mean free path, so scattering events happen before the energy reaches this bead. The second bead is farther away from the source (14 mm), so less energy is reaching it. The two chosen frequencies are 850 kHz, inside one of the band gap, and 1000 kHz, outside the band gaps.

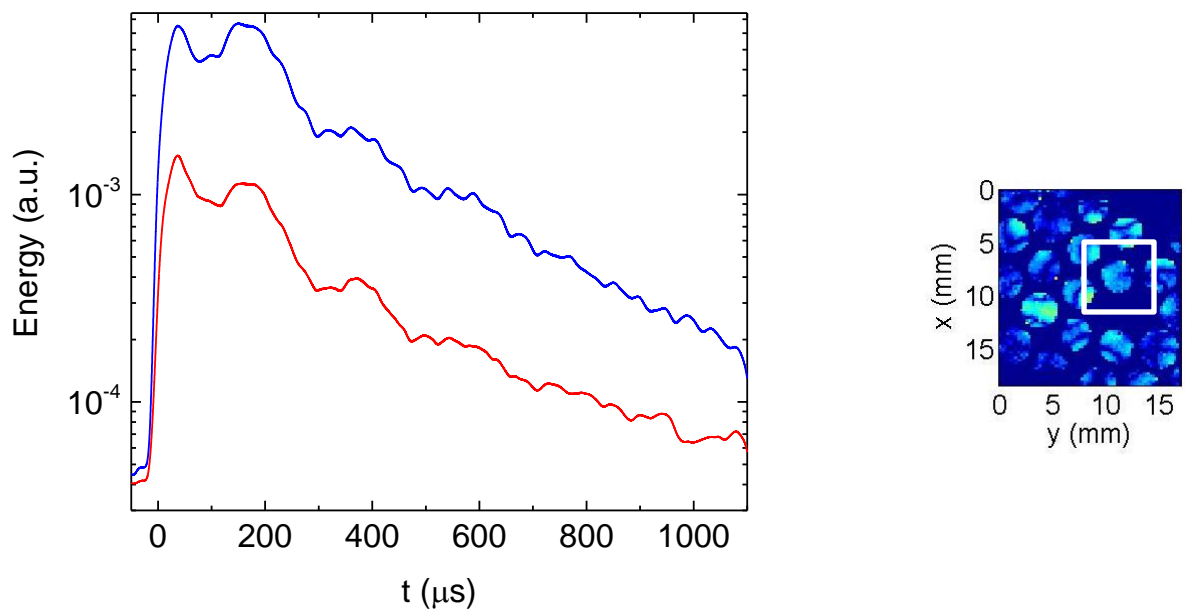


Figure 5.28: Shear (blue) and compressional (red) energies as a function of time in the bead in the centre of the white square in the right image (emitting transducer is at the top of the image) at 850 kHz.

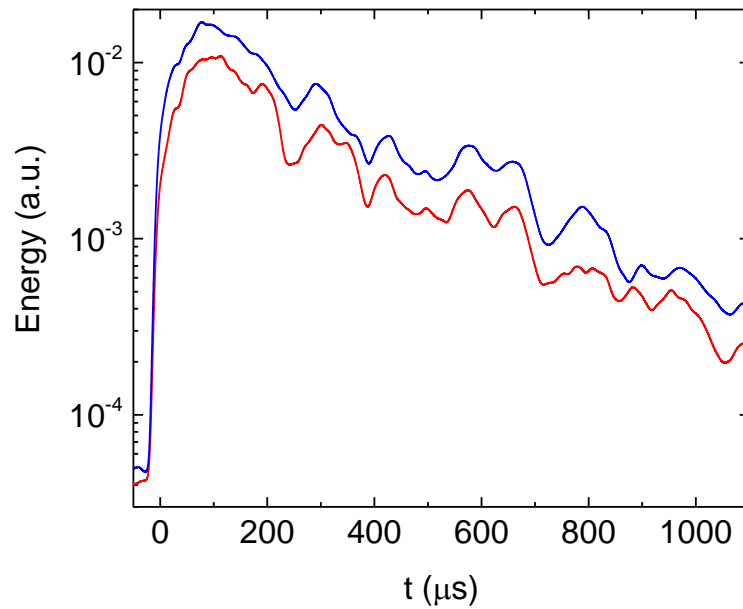


Figure 5.29: Shear (blue) and compressional (red) energies in the same bead as Figure 5.28 at 1000 kHz, as a function of time.

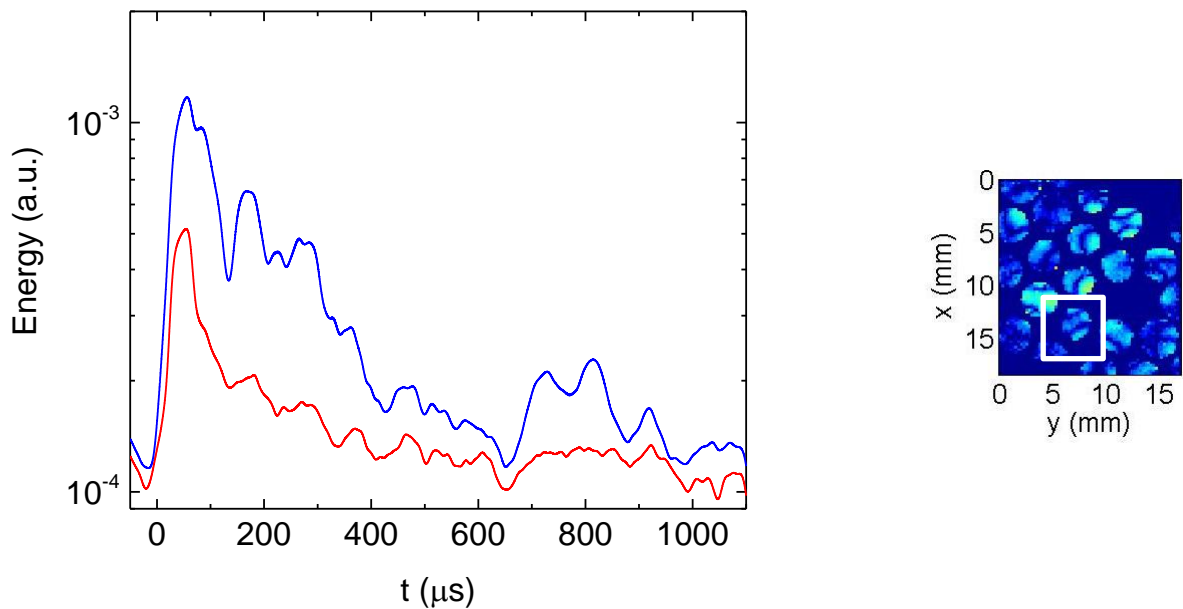


Figure 5.30: Shear (blue) and compressional (red) energies in the bead in the centre of the white square on the right image (transducer is at the top of the image) at 850 kHz, as a function of time.

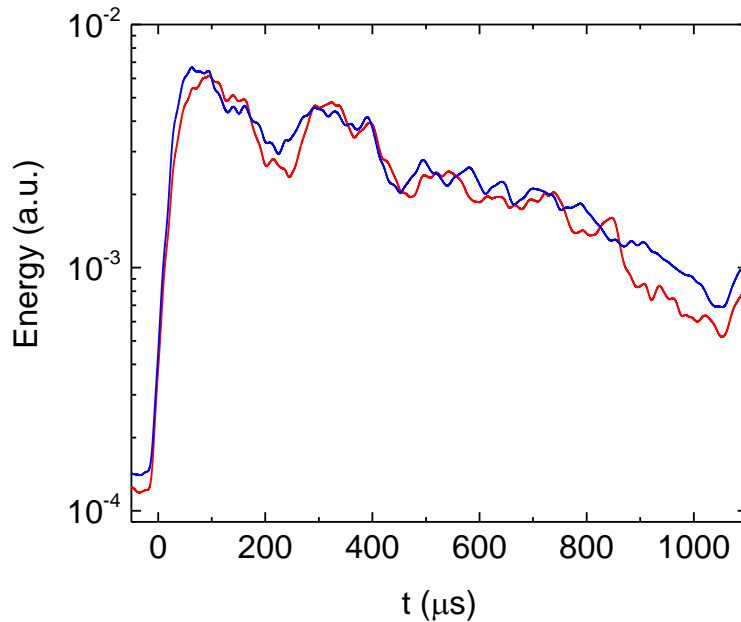


Figure 5.31: Shear (blue) and compressional (red) energies in the same bead as Figure 5.30 at 1000 kHz, as a function of time.

In Figure 5.28 and Figure 5.30 representing the energies at frequencies inside the band gap, the shear energy is higher at all times than the compressional energy, but in Figure 5.29, for the energy at a frequency outside of the band gap, the two energies have comparable magnitude. This is clearly visible in Figure 5.32 and Figure 5.33 which represent the ratio of the two energies for both beads and both frequencies. Also, in Figure 5.30, the maximum of the energies is lower than in the three other figures and the decay is faster. This low energy can be explained easily, as this figure represents the energies inside the band gap for a bead several mean free paths away from the transducer.

As expected from Figure 5.28 to Figure 5.31 representing the compressional and shear energies as a function of time, the ratio of these two energies is higher for the frequency inside the band gap (850 kHz). The decrease of the two blue curves (ratio at 850 kHz in Figure 5.32 and Figure 5.33) is likely due to the noise, as the compressional energy is getting closer to the

noise level and therefore is artificially increased by it. The ratio at 1000 kHz is close to one for both beads. Here, the results have been shown for two different beads, but these observations are the same for all the beads in the sample.

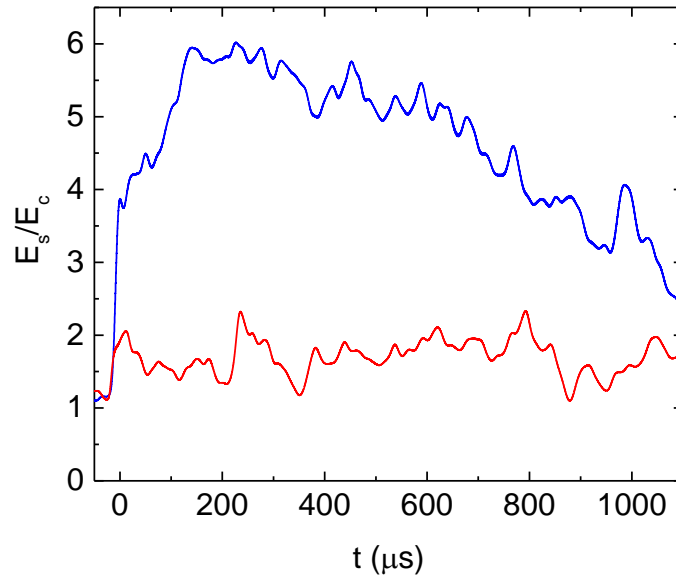


Figure 5.32: Ratio of the shear energy to the compressional energy for a bead at 8 mm from the source at 850 kHz (blue) and at 1000 kHz (red).

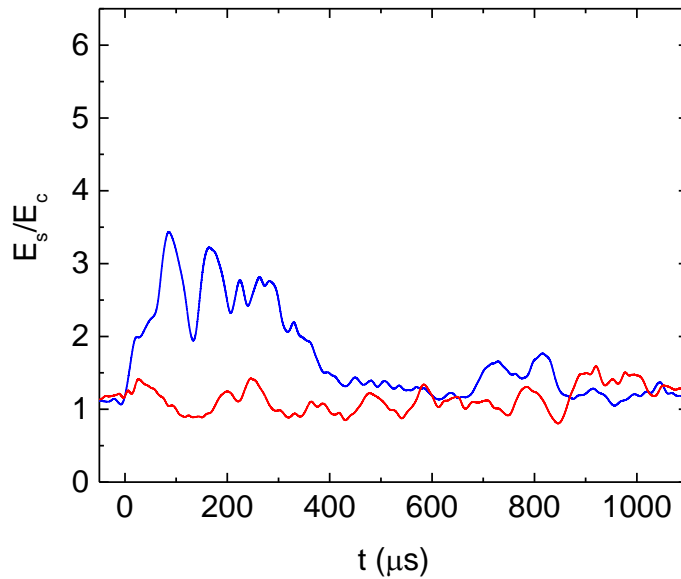


Figure 5.33: Ratio of the shear energy to the compressional energy for a bead at 14 mm from the source at 850 kHz (blue) and at 1000 kHz (red).

According to Figure 5.32 and Figure 5.33, it looks like the band gaps in the sample have an influence on the repartition of energy. The difference between the energy ratio for a frequency in a band gap or outside of the band gap can even be seen for a bead close to the transducer (Figure 5.32), for which the maximum of energy for the frequency inside the band gap is not so different to the maximum of energy for the frequency outside the band gap (see Figures 5.28 and 5.29).

The theoretical value of the equipartition ratio has been obtained for multiply scattered waves in a 3D medium filled with scatterers; for aluminum the theoretical value of the equipartition is 17.3 (it would be 8.4 in the case of a 2D sample) [56,57]. In the case of the sample used in this experiment, this 3D theoretical value cannot be recovered, due possibly to surface effects. It has been shown that in the case of semi-infinite media the surface effects reduce the theoretical ratio between the two energies due to mode conversion of mode after the reflection off the surface and the possibility of generation of surface waves (Rayleigh waves) [57,73]. The 1-layer aluminum beads sample being finite and having free surfaces on different sides, we can reasonably assume that the ratio will be reduced even more. This might explain the very low value (between 1 and 2) of equipartition obtained in this sample. The part of the energy due to a surface wave cannot be determined directly from the measurement of the field. In addition, the resonances of the beads have a strong influence on the transport properties in the sample; the resonances of the beads influence the number of shear and longitudinal modes and can change the value of the equipartition. Figure 5.32 and Figure 5.33 show this difference in behaviour for the two studied frequencies. Even though the actual value of the ratio cannot be explained, the two last figures show that equipartition is reached by the system at 1000 kHz.

5.7 Finite Element Simulations

5.7.1 Resonance frequencies of truncated beads

The laser interferometer measurements can be performed only on flat surfaces, so the beads in the sample used for this experiment were polished to obtain flat top surfaces. Approximately one quarter of the diameter of each bead, along the direction perpendicular to the surface of the sample, had to be removed. This change in geometry implies that the resonant frequencies of the truncated beads are different from the resonant frequencies of a spherical bead. This new object has less symmetry than the full bead, so we expect more resonant frequencies but a lower degree of degeneracy of each resonant frequency. As it was done in chapter 3, Comsol was used to calculate the resonant frequencies of a truncated bead.

These Comsol simulations were performed using the same mechanical parameters as the one used in chapter 3. The bead studied in the Comsol simulations had a radius of 2.07 mm and has been truncated 1.035 mm away from its centre (a quarter of the diameter is removed). Table 5.2 shows the first few resonance frequencies of the truncated bead.

Frequency (MHz)	Degeneracy
0.492	2
0.630	2
0.638	2
0.677	1
0.703	2
0.704	1
0.751	1
0.804	2
0.905	2
0.943	2
0.951	2
0.975	2
1.02	2
1.05	1
1.06	2

Table 5.2: First resonance frequencies of a truncated bead

Table 5.2 shows the lowest resonant frequencies of a truncated bead. By comparison with the case of a spherical bead (chapter 3), this object has more resonant frequencies and their degeneracy is less, as the maximum value for the degeneracy in this frequency range is 2, compared to 11 for a non-truncated bead. Except for the very lowest frequency in Table 5.2 which has a lower value than any frequency of the full bead, the resonances are happening in general at higher frequencies, which is logical as the volume of the truncated bead is smaller than the volume of the full bead.

Figure 5.34 and Figure 5.35 show the displacement field for the two first resonant frequencies having a degeneracy of 1 (0.677 MHz and 0.704 MHz). For both of these frequencies, the y -axis (axes are defined at the bottom left corner of the images) is an axis of symmetry of the field, explaining the degeneracy of 1. Figure 5.36 shows the displacement for the lowest resonant frequency of the truncated bead (0.492 MHz). This resonance has a degeneracy of 2, with the second resonance at the same frequency having the same field rotated by 90° around the y -axis. The scale on these three figures represents the displacement due to the

resonances, the scales on the different figures are in arbitrary displacement units, but the units are the same for all these figures so that the scales can be reliably compared.

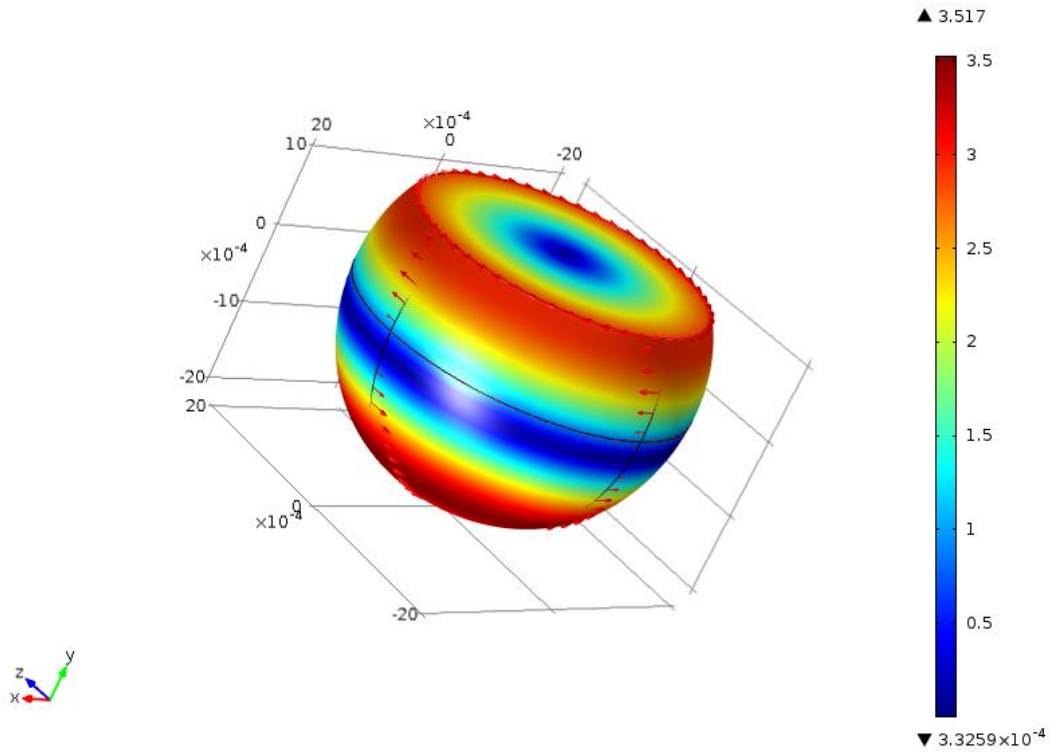


Figure 5.34: Simulation of the displacement field of the 0.677 MHz resonance of a truncated bead. The displacement field is completely along the surface of the object.

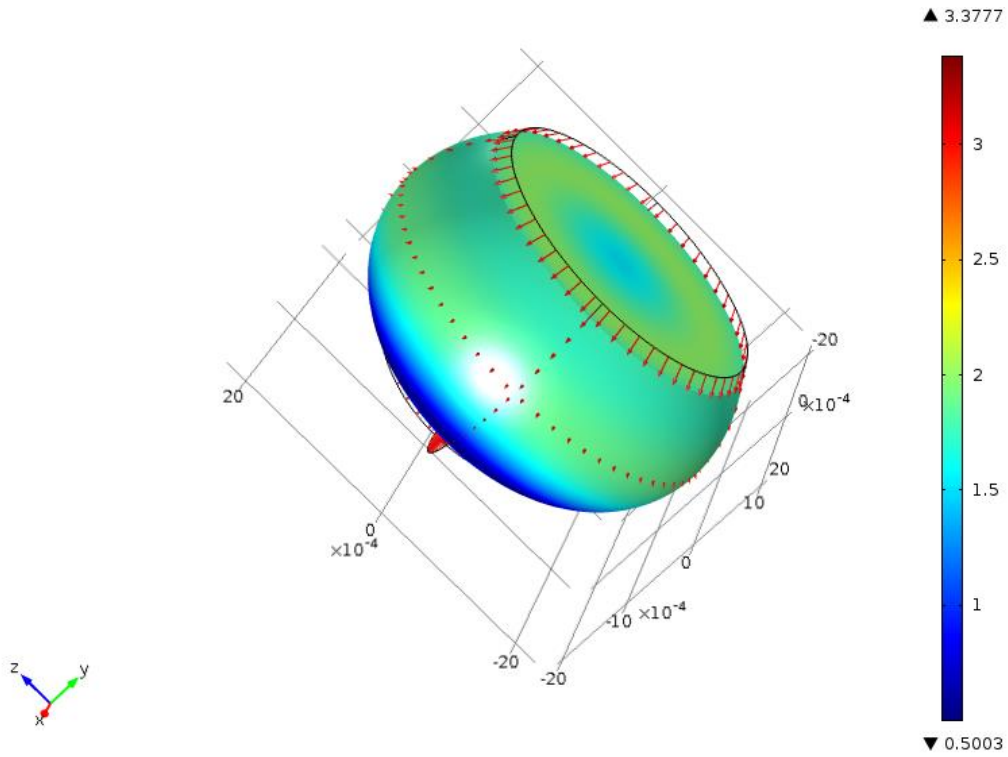


Figure 5.35: Simulation of the displacement field of the 0.704 MHz resonance of a truncated bead. The displacement field is mainly radial at this frequency.

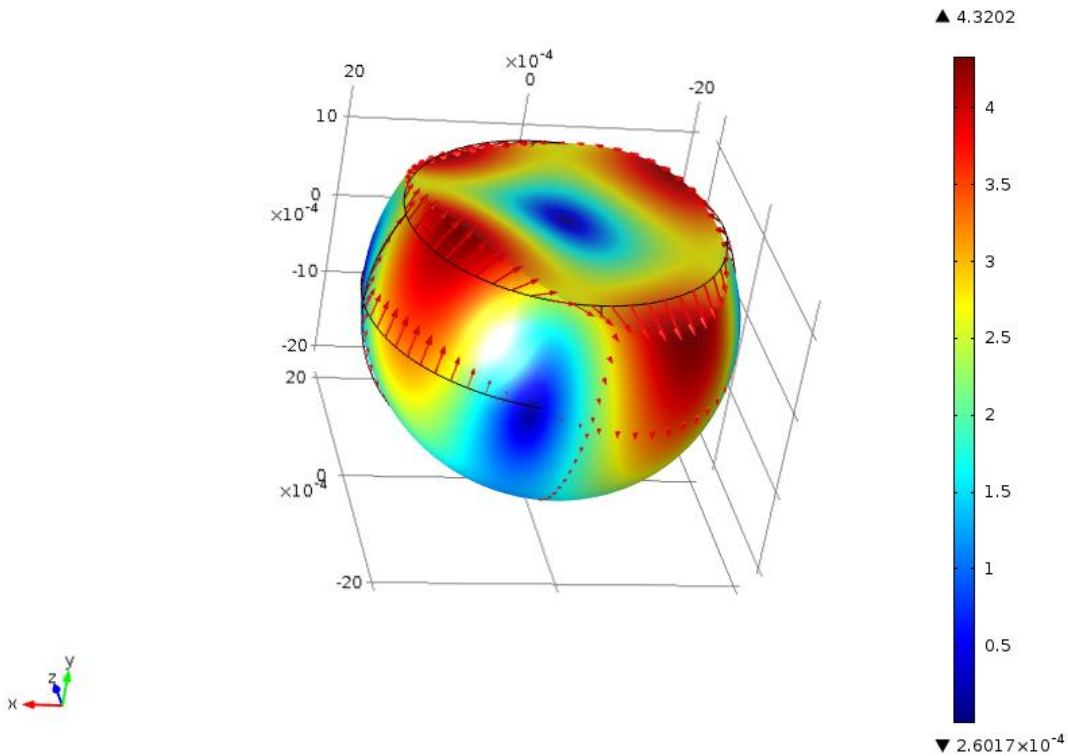


Figure 5.36: Simulation of the displacement field of the 0.492 MHz resonance of a truncated bead. At this frequency, the flat part of this object is deformed.

5.7.2 Simulation of the propagation in a 2D sample

Comsol can also be used to simulate the propagation inside a sample similar to the experimental one as a complex geometry can be defined. Comsol is mainly programmed to perform frequency-dependent simulations, so instead of propagating a pulse containing several frequencies, the simulation is done frequency by frequency. This would correspond to a continuous wave experiment. Several limitations exist with these simulations. First, as the simulations are frequency-dependent, it is not simple to compare with time-dependent experimental data. Secondly, the size of the simulated sample is limited by the quantity of memory accessible on the computer. The memory needed to perform the simulation depends on the size of simulated geometry and on the size of the mesh (size of the simulation elements). Small geometrical elements, such as the necks linking the beads, need to have several mesh elements in them in order to perform a reliable simulation, and this requirement constitutes an important constraint. The maximum mesh size in the sample has been fixed at 0.3 mm, which leads to a usage of 32 Gb of memory on the computer (maximum amount of memory available) for a sample composed of 30 beads.

Figure 5.37 shows the displacement fields in the three directions at the surface of a simulated sample at 750 kHz. We can see that the displacement has a higher value for the two in-plane directions than for the out-of-plane direction.

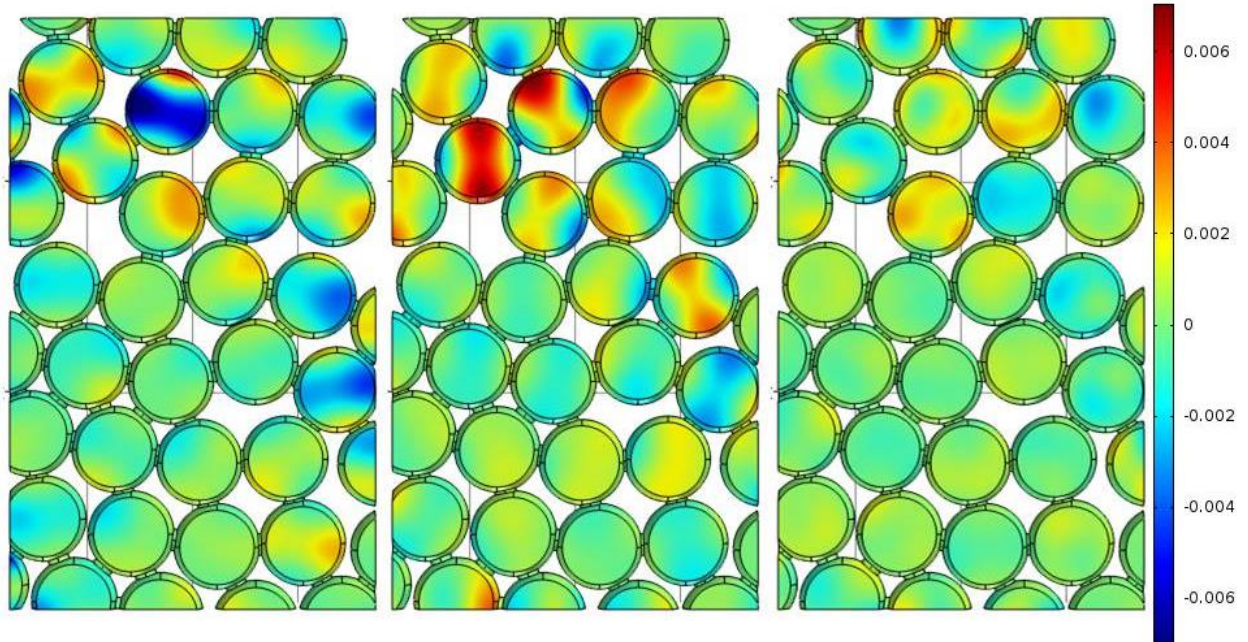


Figure 5.37: Displacement fields at 750 kHz in the three directions: along x (left), along y (centre) and along z (right). Here, the y direction is going from top to bottom of the images, and the z direction is the out-of-plane direction. The color scale is expressed in arbitrary units of displacement.

The generation of waves in simulations is not normally done using a transducer as in the experiment, but by imposing a harmonic displacement at one of the boundaries of the sample, creating a continuous wave in the sample. All the other boundaries of the sample have a “free boundary” condition, meaning that there is no load on them (so the beads are surrounded by vacuum or, to an excellent approximation, by air). This difference in the generation between experiment and simulation means that it is not possible to study the position-dependence of the diffusion coefficient with the simulation data as this quantity depends on the boundary condition: in particular to observe this phenomenon, a leakage mechanism must exist at, at least, one of the boundaries of the sample, which is not the case in these simulations. In the experiment this leakage is coming from the contact with the transducer.

The transmission profiles can be reproduced using the simulation. In Figure 5.38, the transmission of the out-of-plane displacement is plotted. Values larger than one are due to two effects: the interferences and the reflection at the boundary. In the simulation, there is a perfect reflection at the end of the sample.

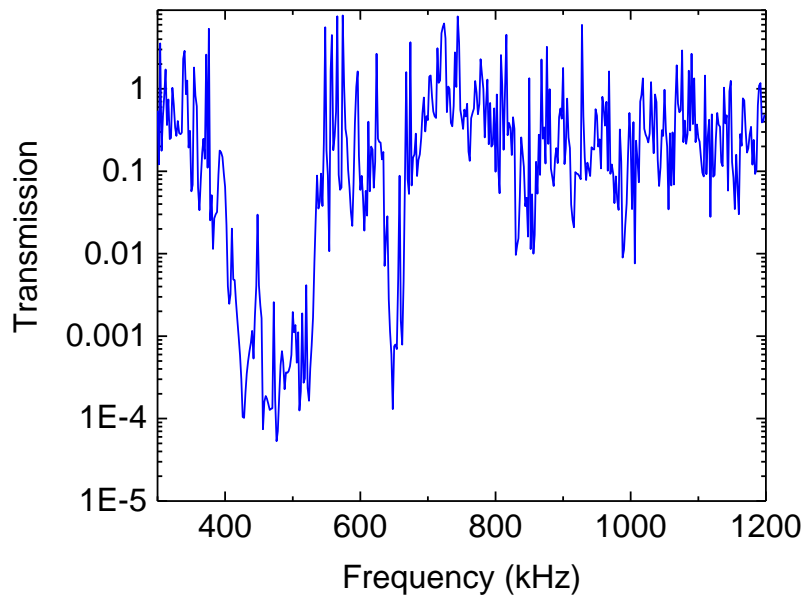


Figure 5.38: Amplitude transmission coefficient of the magnitude of the out-of-plane displacement obtained from the Comsol simulation. The transmission is obtained 27 mm away from the transducer.

In Figure 5.38, the two low frequency band gaps (centered at 500 kHz and 650 kHz) are reproduced as we can see by comparing with Figure 5.22. A drop in the transmission just above 800 kHz can be seen in the simulation data, but it is not as large as the band gap observed experimentally. In the dip in transmission between 800 and 900 kHz, there are two peaks which might correspond to the open-channels discussed in section 5.5.2.3. The experimental sample cannot be as perfect as the one in the simulation, where all the beads are perfectly identical, on the same plane and the links between beads have the same strength. Differences in the sample

will change the transmission properties. For example, as all the beads are not exactly in the same plane in the experiment, they were not sanded evenly, and the difference in bead truncations will shift the resonant frequencies of each of the resonators. If each resonator has slightly different resonant frequencies, they will not couple in the same way as if the resonant frequencies were completely identical and this will change the transmission profiles.

5.8 Conclusions

The sample made of a single layer of brazed beads used in this experiment is a new kind of sample designed to study previously unexplored aspects of the propagation of ultrasound in disordered media in which Anderson localization can be reasonably expected to occur. Such a sample is not easy to make, as the positions of the beads need to be as close to random as possible but the beads also need to be in contact with each other, which makes it more difficult to construct a disordered sample. The propagation in this sample is strongly linked to the resonances of the beads. The two main objectives of this experiment were the study of the dependence in position of the diffusion coefficient in the case of strong scattering (sub-diffusive transport or Anderson Localization) and to look at the partition of the total energy between shear and longitudinal energies.

The measurements of the diffusion coefficient as a function of the distance from the source were not conclusive. There are several reasons for this result. First, the geometry of the sample may not have been ideal, as it is probably too wide compared to the scattering mean free path l_s (20 mm compared to ~ 5 mm) to satisfy the quasi-1D geometry that simplifies the analysis. (Note that prior to making the sample and conducting measurements on it, it was not possible to know the actual value of the scattering mean free path for this sample.) Secondly, I did not get

enough statistics to obtain a reliable estimate value of the ensemble-averaged energy density and the flux that are needed to determine the diffusion coefficient. The spatial fluctuations of wave properties are strong in this sample, so a “bright bead” (*i.e.*, a bright spot of the speckle pattern) can modify the averaged quantities too much. The scattering mean free path of the wave in the sample depends on the diameter of the beads and the strength of the mechanical links between them, so it is difficult to modify it, meaning that to solve the first issue, the width of the sample needs to be reduced. If the width of the sample is reduced, the amount of disorder that can be introduced is also reduced, as the number of beads across the width will be very low. The second problem described in this paragraph can be solved by performing the experiments on many different samples, which are statistically equivalent but are different enough to change the speckle pattern and sample different configurations of the disorder. Then, the different calculated quantities derived from the measured displacements can be averaged sufficiently to extract more meaningful results. However, performing experiments on a large number of statistically equivalent samples is a very time-consuming process, and was unfortunately beyond the scope of this thesis.

The values obtained experimentally for the equipartition of energy are not equal to the values that have been predicted theoretically and observed experimentally in 3D media. My experimental results thus constitute a new finding that has not been anticipated previously. In my new system consisting of a single layer of brazed aluminum beads, the ratio of the two energies is indeed close to 1 for most of the frequencies. However, the equipartition ratio is different for the frequencies inside the band gaps of the sample. Since it is likely that Anderson localization occurs inside the band gaps, this result may be the first experimental indication that equipartition can be different for localized waves. Overall, there are several possible

explanations for the different behaviour found for my sample. First, the resonant nature of the constituents (beads) of the sample might be expected to influence the energy ratio. Also, surface waves, such as Rayleigh waves, have not been considered and could influence the repartition of energy, as the energy is then distributed between compressional, shear and surface waves.

Measurements of the diffusion coefficient and of the equipartition of energy could be both done on a different type of 2D sample made of a (thin) plate with holes in it. However, for such a sample, the feasibility of achieving Anderson localization in a sample of reasonable size would also need to be assessed before it would make sense to look for a position dependence of the diffusion coefficient. If this were successful, there could be advantages for measuring a position-dependent diffusion coefficient, as controlling the magnitude of the scattering mean free path via the size of the holes and their concentration could be easier. Depending on the number of holes, this might also help to obtain better measurement statistics as there could be more positions on which to perform the acquisition (as the displacement field would be then measured on the plate). The variation of the scattering mean free path would give more liberty in designing an optimum geometry of the sample, in particular for its width. For the equipartition of energy such a sample might reduce the influence of Rayleigh waves but would also create also some issues, as using a plate will introduce plate modes (Lamb waves) [74].

Another unexpected and interesting result emerged from this experiment. Depending on the working frequency, some channels composed of specific beads appeared to be opened or not. All the experiments were performed using a single element transducer, meaning that there was no real control over the wave front of the injected wave in the sample. If a multi-element transducer were used instead to inject the wave into the sample, the spatial distribution of

amplitude and phase of the emitted signal could be adjusted and might lead to an accurate control of open or closed channels in the wave field inside the sample [71].

Chapter 6

Measurement of the mechanical properties of noodle dough with ultrasound

6.1 Introduction

In this chapter, I am interested in the propagation of ultrasound in Asian noodle dough. Noodle dough mechanical properties are linked to its texture and are a very important aspect of final product quality [75,76,77]. Ultrasound is a very convenient technique to assess the mechanical properties [78,79]. Until now, ultrasound was used in a contact setup (the dough was compressed between two plates). To go beyond this limitation for product quality assessment, a new non-contact technique is presented in this chapter. Non-contact ultrasonic techniques have already been used on food products [80], including porous food materials such as bread [47]. The samples used for the experiments presented here are very different to the samples described in the two previous chapters: the noodle dough is not an artificial material as were the samples made from aluminum beads. Noodle dough is a very complex material with a microstructure that cannot be easily controlled. In the case of aluminum bead samples, the material was chosen to have small absorption, allowing access to the long-time propagation of multiply scattered waves. Noodle dough on the contrary has a high attenuation due to absorption. Noodle dough is a complex media from the point of view of acoustic wave propagation, and different constituents can act as scatterers for the waves. Bubbles [81] in the dough can scatter the wave and also exhibit a resonance which will affect greatly the propagation. In noodle dough, the hydrated gluten molecules are forming a network in which starch granules are entrapped [76], making the dough a composite material. Noodle dough is a viscoelastic medium exhibiting a variety of characteristic relaxation times depending on the different constituents of the dough [82,83]. The acoustic waves undergo a lot of scattering events in the dough but, unlike the sample of aluminum beads, a long-time coda cannot be observed in an acoustic signal going through a noodle dough, as the absorption is too high in the dough for the long-time multiply-scattered

signal to be detectable. Only the ballistic (coherent) signal is visible and the noodle can be seen as an effective medium (see section 2.4).

Asian noodles are made of three constituents: water, flour and salt [76]. These three elements are mixed and then the dough is sheeted multiple times with a sheeting rolls machine. The final dough is a rectangle that can be several tens of centimeters in length and width and less than 2 mm in thickness, with the dimensions depending on the machine used and roll gap sizes. The mixing conditions [84], the sheeting process [85] and the proportion of each ingredient [78,86] affect the texture and hence the final quality of the noodle. Since ultrasound is sensitive to the mechanical properties of the medium in which it is travelling, it is an efficient technique to characterize the texture of the dough. The characteristics of the wave transport, the phase velocity and the attenuation, are measured for different doughs to study the influence of each parameter on the texture. All the experiments described in this chapter are done with air-coupled transducers, meaning that the measurement of the mechanical properties of the dough is done directly in air, with no need to place the noodle between plastic blocks or in water, and therefore making this technique interesting for on-line non-destructive quality control in the noodle dough manufacturing industry. One of the objectives of the project is indeed to apply this technique during the sheeting process in a pilot production plant.

In section 6.2, the influence of bubbles and of the viscoelastic nature of noodle dough on mechanical properties is discussed, and how this is reflected in the ultrasonic signal. Then the experimental technique is presented, and in particular the method to take into account the large impedance mismatch between noodle dough and air. In the last section 6.5, the mechanical properties measurements for different noodle doughs are presented and discussed.

6.2 Influence of the dough properties on the ultrasonic signal

The propagation of ultrasound in a medium is characterized by its phase velocity v and its attenuation α ; these two quantities are, in complex media, frequency dependent (angular frequency ω) and are used to define the complex wave number k :

$$k = \frac{\omega}{v} + i \frac{\alpha}{2}. \quad (6.1)$$

The acoustic properties of a medium are known once the wave number is known. In the following sections, I will present the effect on the wave number of the presence of bubbles in the medium in which the wave propagates and of the existence of relaxation times linked to the visco-elastic nature of the medium.

6.2.1 Effect of bubbles in the propagation of acoustic waves

Bubbles are strong scatterers exhibiting a resonance at low-frequency [87,88,89]. The resonant frequency of a bubble ω_M , called the Minnaert frequency [90], depends on the radius of the bubble R_0 , the sound velocity in the gas of the bubble v_g , the shear velocity in the medium surrounding the bubble v_s , the density of the gas ρ_g and the density of the medium ρ_0 :

$$\omega_M = \frac{\sqrt{3v_g^2 \rho_g / \rho_0 + 4v_s^2}}{R_0}. \quad (6.2)$$

When a plane wave [described by $p \exp(-i\omega t + ik_0 x)$, p being the amplitude of the wave, ω its angular frequency and k_0 the wave number in the surrounding medium] excites a single bubble, a spherical wave centered on the bubble is generated. Its amplitude is:

$$\frac{f(\omega, R_0)}{r} p \exp(-i\omega t + ik_0 x), \quad (6.3)$$

with f the scattering function

$$f(\omega, R_0) = \frac{R_0}{\left(\frac{\omega_M}{\omega}\right)^2 - 1 + i\Gamma(\omega)}. \quad (6.4)$$

As the scattering function [equation (6.4)] is complex, it describes at the same time the changes in amplitude and in phase induced by the presence of a bubble. $\Gamma(\omega)$ represents the damping rate of the wave which comes mainly from scattering losses and the viscosity of the medium. The attenuation of the wave scattered by a bubble is much higher for frequencies close to the Minnaert frequency [equation (6.2)].

In a noodle, as in a lot of different food materials, there is more than one bubble. The scattering of waves by each bubble has to be taken into account, so an effective medium model is used (chapter 2 equation 2.42). In Foldy's model, an effective wave number k can be obtained, depending on the scattering function and the number of bubbles per unit volume n [87]:

$$k^2 = k_0^2 + 4\pi n f(\omega, R_0). \quad (6.5)$$

The Foldy's model is equivalent to the Independent Scatterer Approximation (ISA) for a scatterer having only a monopolar resonance. In this model, the influence of all the bubbles on a given bubble is taken into account only via an average field coming from all the bubbles. Moreover, it is assumed that there is no correlation between the positions of each bubble. Equation (6.5) assumes that all the bubbles have the same size, but an effective wave vector can also be calculated when there is a distribution of bubble sizes:

$$k^2 = k_0^2 + 4\pi \int n(R_0) f(\omega, R_0) dR_0. \quad (6.6)$$

$n(R_0)$ is the number of bubbles of radius R_0 per unit of volume. The modification of the wave number due to the bubbles can have some important effects on the properties of the materials (see Figure 6.1 and Figure 6.2). In particular, it has been shown that the attenuation and the phase velocity of the acoustic wave exhibit maxima and that the velocity of the wave in a bubbly medium can be very small [91] (smaller than the velocity of the gas and of the surrounding medium) below the resonant frequency, as shown in Figure 6.1.

Leroy et al. [92] used equation (6.6) to explain ultrasonic data obtained in bread dough. In order to use this equation, a distribution of bubble size $n(R_0)$ has to be defined. It has been shown that the bubble size distributions in bread dough are well characterized by lognormal distributions [93,94,95]. This type of distribution depends on two parameters: median radius and width (which is the polydispersity of bubbles). The number of bubbles depends on the fraction of gas inside the medium and on the size of the bubbles. The matrix is characterized by its density, the velocity of propagation without bubbles and the complex shear modulus G . The real part of G (or G') is related to the shear velocity needed to calculate the Minnaert frequency and the imaginary part of G (or G'') is involved in the viscous damping term in $\Gamma(\omega)$. The parameters used in [92], typical of a bread dough, that are also used to obtain Figure 6.1 and Figure 6.2 are shown in Table 6.1.

Median radius of the distribution (μm)	14
Lognormal distribution width	0.46
Volume fraction of gas	0.12
Real part of G (kPa)	$25.14 \times f^{1/3}$
Imaginary part of G (kPa)	$17.54 \times f^{1/3}$
Density (g. cm^{-3})	1.29
Velocity ($\text{mm. } \mu\text{s}^{-1}$)	1.6

Table 6.1: Parameters used to obtain Figure 6.1 and Figure 6.2. f is the frequency in Hz.

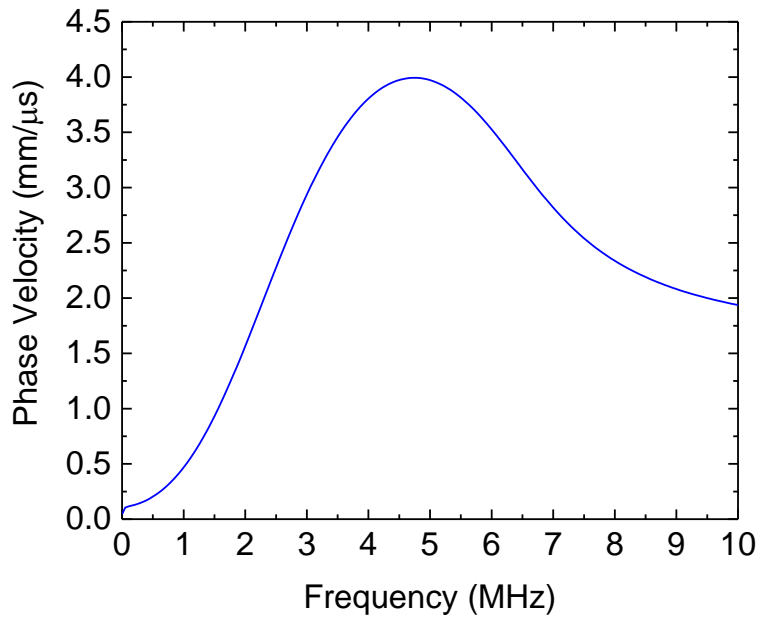


Figure 6.1: Phase velocity obtained using the model described by equation (6.6) with the parameters of Table 6.1.

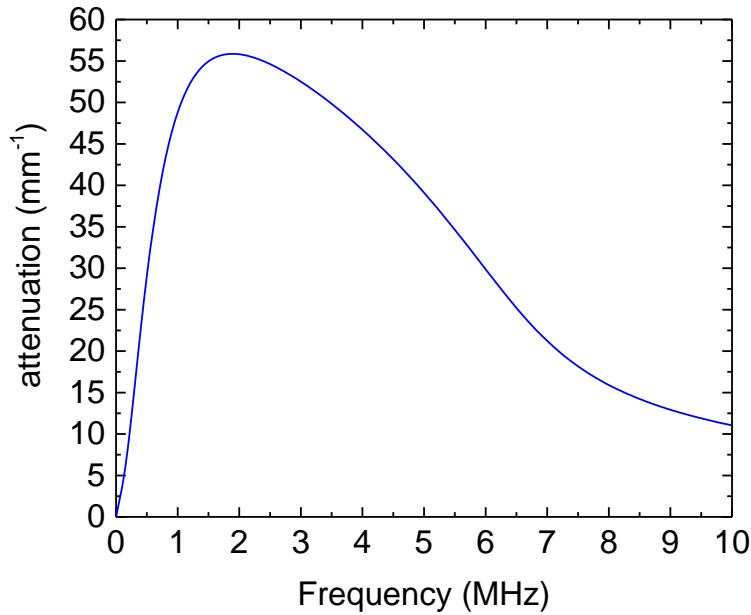


Figure 6.2: Attenuation obtained using the model described by equation (6.6) with the parameters of Table 6.1.

Some models have also been developed to take into account the possibility of correlation in the bubble positions or the effect of the scattered waves from a bubble on the others (multiple scattering) [89].

6.2.2 Propagation of ultrasound in a viscoelastic medium

The viscosity of a medium introduces dissipation of waves and dispersion, *i.e.*, a dependence of the phase velocity on frequency. In the case of a non-scattering medium, dissipation is the only source of attenuation, as there is no scattering event to decrease the amplitude of the wave. For frequencies much higher than the Minnaert frequency, the coherent wave is not affected by the bubbles, and therefore the viscous effects are the main mechanism of energy loss. In such a situation, the wave equation for a longitudinal wave can be written as

$$\rho \frac{\partial^2 \varphi(\vec{x}, t)}{\partial t^2} - M \vec{\nabla}^2 \varphi(\vec{x}, t) = 0, \quad (6.7)$$

where M is the longitudinal modulus of the medium and φ can be any physical quantity which can propagate (e.g., displacement of the particle due to the wave or stress). In a solid, the longitudinal modulus M depends on the bulk modulus K and on the shear modulus²⁰ G , because shear waves can propagate in a solid. All these moduli are complex. The imaginary part describes the delay existing between an excitation and the response of a system to this excitation, due to the viscosity. The equation linking these moduli is [96]

$$M = M' + iM'' = K + \frac{4}{3}G. \quad (6.8)$$

The moduli used in equation (6.8) are frequency dependent, and depend on the properties of the materials. It is possible to introduce characteristic times of relaxation for compressional waves, τ_c , and for shear waves, τ_s . For example in a viscous liquid, the bulk and shear modulus can be expressed as [97]

$$K = K_0 + \frac{K_2 i \omega \tau_c}{1 + i \omega \tau_c}, \quad G = \frac{G_\infty i \omega \tau_s}{1 + i \omega \tau_s}. \quad (6.9)$$

K_0 , K_2 and G_∞ are three frequency-independent moduli. The dispersion relation, the equation linking the wave number with the frequency, is obtained from the wave equation [equation (6.7)] assuming a monochromatic plane wave propagating inside the medium. The dispersion relation is

$$\rho \omega^2 - M k^2 = 0. \quad (6.10)$$

²⁰ The shear modulus G is equal to the second Lamé parameters μ used in the previous chapters.

By using the definition of the wave number [equation (6.1)] in the dispersion relation, the storage modulus (real part of M) and loss modulus (imaginary part of M) can be expressed as a function of the phase velocity, the attenuation and the frequency [96,98]:

$$M' = \rho v_p^2 \frac{1 - \left(\frac{\alpha v_p}{2\omega}\right)^2}{\left[1 + \left(\frac{\alpha v_p}{2\omega}\right)^2\right]^2} \quad (6.11)$$

and

$$M'' = \frac{2\rho v_p^2 \left(\frac{\alpha v_p}{2\omega}\right)}{\left[1 + \left(\frac{\alpha v_p}{2\omega}\right)^2\right]^2}. \quad (6.12)$$

The velocity and attenuation of the wave in the visco-elastic medium can be expressed using equations (6.9), (6.11) and (6.12). Expressions for the velocity of propagation and attenuation of waves depending on the viscoelastic properties of the medium (the relaxation times and the moduli) can then be obtained.

The longitudinal modulus can be used to define a relationship between the element of the deformation tensor S_{ij} and the element of the stress T_{ij} induced by the wave in the material, and the moduli M and G (see Appendix 8.3):

$$T_{ij} = 2GS_{ij} + (M - 2G)S_{kk}\delta_{ij} \quad (6.13)$$

In the case of a uniaxial deformation (for example only S_{11} is different from zero) and for a harmonic excitation [$S_{11} = S \exp(i\omega t)$], the associated stress component is equal to:

$$T_{11} = (M' + iM'')S \exp(i\omega t) = |M|S \exp[i(\omega t + \delta)], \quad (6.14)$$

where $|M|$ is the modulus of the complex number M (longitudinal modulus) and δ its argument ($\tan \delta = M''/M'$). In equation (6.14), a phase-shift is introduced between the stress and the deformation, or in other words, there is delay between the deformation and the stress in the medium due to the viscosity. For a purely viscous medium (Newtonian fluid), this phase shift is equal to $\pi/2$ and for perfectly elastic medium it is equal to zero [it is not possible to have a shear wave travelling in a purely viscous (fluid) medium].

Since the longitudinal modulus M depends on the bulk modulus K and the shear modulus G , the viscosity measured with a longitudinal wave in a visco-elastic medium depends on the two characteristic viscosities of the medium: the bulk viscosity η_b and the shear viscosity η_s . The imaginary part of the modulus is equal to [96]

$$M'' = \omega \left(\eta_b + \frac{4}{3} \eta_s \right), \quad (6.15)$$

following the same relationship defined between the moduli in equation (6.8).

6.3 Experimental setup

All the measurements on noodle dough were performed in a transmission setup, meaning that there is one transducer on each side of the dough (see Figure 6.3), one being the emitter and the other one the receiver. Noodle dough is a sheet, with a thickness of approximately 2 mm. Three different pairs of air-coupled transducers were used during the project, all of them were mounted the same way. For a proper and accurate transmission experiment the two transducers need to be as parallel as possible, as the parallelism of the transducers helps to maximize the recorded signal. It is also important that the noodle dough sheet is wide enough to ensure that no signal can go around it. Experiments were performed in two different contexts: laboratory and pilot-

plant environments. First, to assess the feasibility of the technique, measurements were done in a laboratory environment with a static sheet of dough in a closed box in which the humidity was increased to around 70 % (the dough dries rapidly otherwise). Once these experiments had shown the feasibility of the experimental method - in particular, the possibility to measure some signal through the noodle and to detect changes in the mechanical properties of dough with different compositions, measurements were done in a more realistic situation for process control applications on an industrial sheeting machine during the production of noodles at the Canadian International Grains Institute (CIGI). Different pairs of transducers have been used depending on the experimental context; each of these pairs uses their own electronic equipment and are described in the following sections.

6.3.1 Transducers

6.3.1.1 Microacoustics BAT-1

The BAT-1 transducers (see Figure 6.3) manufactured by Microacoustics are capacitive transducers with a very large bandwidth. Unlike a classic piezoelectric transducer in which the waves are generated from the deformation of a piezoelectric crystal due to a variation of applied voltage, there is no crystal in a capacitive transducer.

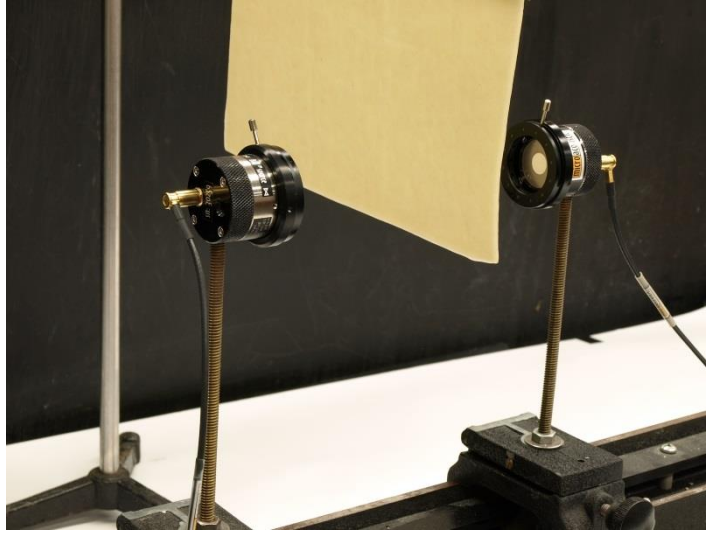


Figure 6.3: Transducers from Microacoustics.

These transducers are made of two electrodes separated by a dielectric material (air); this system forms a capacitor. One of the two electrodes is free to move, which allows the generation or the detection of sound waves. To operate the capacitive transducer, a static polarization between the two electrodes needs to be applied, typically a 200 V bias. This bias sets up the equilibrium position of the transducer. To generate a sound wave, an AC signal corresponding to the emitted wave signal is added to the static voltage. This second signal modifies the capacitance of the transducer by changing the distance between the two electrodes; the moving electrode creates a sound wave in the air. The detection of a sound wave works the same way; the sound wave moves one of the two electrodes which modifies the value of the capacitance and a voltage signal is then measured.

These transducers are broad-band, so the central frequency for the emitted pulse has to be chosen. The best way to do it is to use an arbitrary wave generator (AWG). The AWG is able to emit a Gaussian pulse at a chosen central frequency, but the maximum amplitude is only 10 Vpp which is not enough to drive the transducer. Associated with the AWG, a power amplifier (E & I

2200L, see section 4.3.2.2) is used, and this has a gain of 53 dB. The maximum possible amplitude used with the transducer is 400 V_{pp}. A typical signal obtained with the pair of Microacoustics transducers is shown in Figure 6.4.

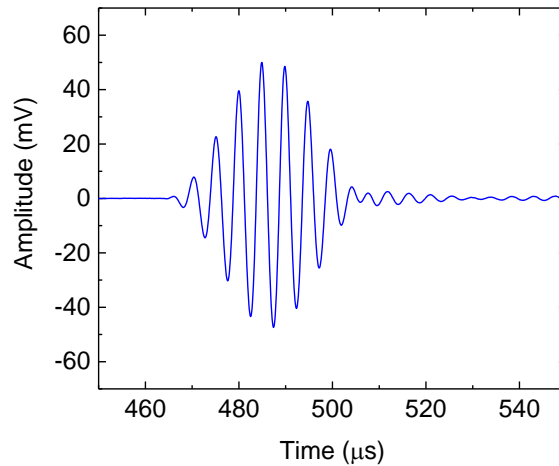


Figure 6.4: Typical signal obtained with the BAT-1 transducers (central frequency: 200 kHz).

The high amplitude DC voltage on top of the AC signal is applied by two dedicated electronic boxes: the V-pole and the Q-amp. On the emitter side, the V-pole superimposes the DC voltage to the signal that will be sent by the transducer. The level of the DC bias can be chosen, 200 V or 400 V. On the receiver side, the Q-amp applies the DC voltage to the transducer and it is also a pre-amplifier for the small signal that is detected. The acquisition can be done either with an oscilloscope or a Gage-card computer (see section 4.3.2.6).

6.3.1.2 *The Ultran Group transducers*

The transducers purchased from the Ultran Group are piezoelectric transducers that uses a gas matrix piezoelectric (GMP™) (Figure 6.5), which helps emission in air. As for all piezoelectric

transducers, the thickness of the piezoelectric material determines the central frequency of the transducer and gives a limited bandwidth. The transducers used during this experiment have a central frequency of 200 kHz, and the bandwidth is approximately 40 kHz around the central frequency.



Figure 6.5: Air-coupled transducer from the Ultrason Group.

The bandwidth being so narrow, the best solution to drive the transducer is to use a pulser (model 5058PR from Panametrics), allowing the maximum possible bandwidth of the transducer to be used. The main problem arising from this small bandwidth is the presence of some ringing following the real signal as shown in Figure 6.6, which makes the analysis more complicated. Unlike the BAT-1 transducer, it is possible to do reflection measurements using the Ultrason transducers and the pulser as the receiving and emitting sides are symmetric.

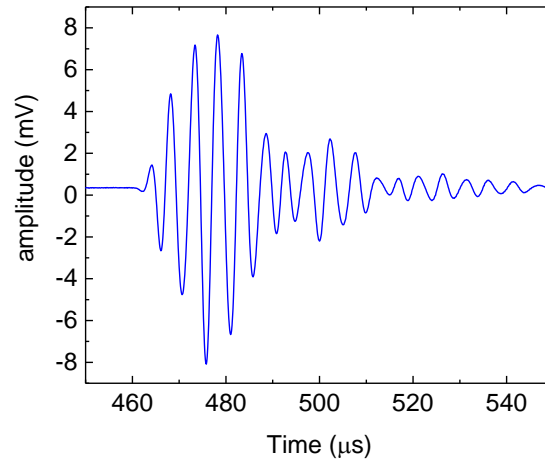


Figure 6.6: Typical signal obtained with the Ultran transducers (central frequency: 200 kHz).

6.3.1.3 VN Instruments

a) Transducers

Three pairs of transducers from VN-instruments (see Table 6.2) were tested for measurements on noodles. These transducers are capacitive transducers, as are the BAT-1 transducers from Microacoustics. Compared to the BAT-1, the effective surface is larger, leading to a better sensitivity. VN Instruments supplies all the electronics necessary to use their transducers.

Transducer	Central Frequency (kHz)	Bandwidth (kHz)
CAP 2-1	113	77
CAP 2-2	100	89
CAP 3-1	200	169
CAP 3-2	205	187
CAP 5-1	666	1090
CAP 5-2	766	1330

Table 6.2: Characteristics of VN instrument transducers



Figure 6.7: VN instruments transducer.

b) SIA-7

The SIA-7 is the main component of the VN system. It is used to synthesize the signal, to emit the high voltage AC signal and it also acts as the receiver. Between the SIA-7 and the transducer, remote modules are used to apply the high DC voltage to the transducer.

The SIA-7 can act at the same time as a computer, an AWG, a power amplifier and a receiver. Signals generated by the system are chirps: the frequency varies with time inside the envelope of the signal. The chirp allows for a better signal to noise ratio (SNR) to be obtained after signal processing (pulse compression). This is a very common process in radar technology. A chirp is defined by a central frequency, a bandwidth and a duration over which the frequency is varied (see appendix 8.4).

The pulse compression technique consists in cross-correlating the received signal with the emitted signal. This leads to a better SNR, and compressing the signal in time will also help to distinguish two echoes very close in time. After this process, the envelope of the signal is

calculated to help the signal analysis (see appendix 8.4). Even if only the envelope is displayed, there is still information about the phase, as the recorded signal is complex (example in Figure 6.8).

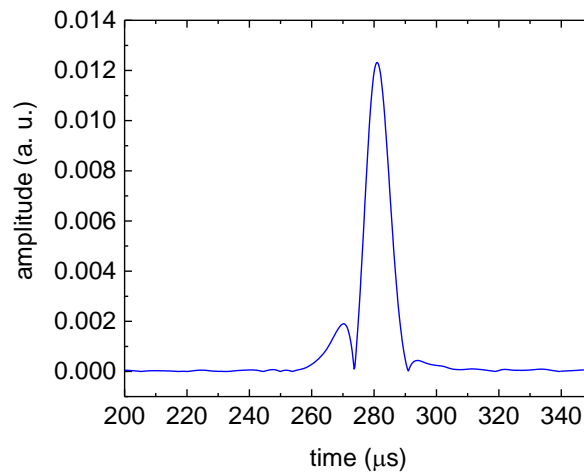


Figure 6.8: Typical signal obtained with the pair of CAP 3 transducers.

6.4 Analysis

The recorded signals have propagated through the noodle dough sheet, so they contain information about the mechanical properties of the dough. From the ultrasonic signal, the phase velocity and the ultrasonic attenuation are obtained. These two quantities can be used to obtain the elastic moduli of the dough, which, since they relate directly stress and strain, give information that is easier to interpret from a mechanical point of view.

6.4.1 Theory

The dough sheet can be seen as a layer. At each dough-air interface, part of the sound is transmitted and the other part is reflected. This happens when the sound enters the dough, but also after the wave has traveled through the dough and arrives at the other interface. The

reflected part inside the noodle can then undergo another reflection (see Figure 6.9). As a consequence, there are several reflected waves inside the layer.

The amplitude of the transmission and reflection coefficients at each interface are, with medium 1 being the air and medium 2 the noodle,

$$t_{1 \rightarrow 2} = \frac{2Z_2}{Z_1 + Z_2} \quad (6.16)$$

and

$$r_{1 \rightarrow 2} = \frac{Z_2 - Z_1}{Z_1 + Z_2}. \quad (6.17)$$

Z_1 is the impedance of the medium from where the wave is coming (air) and Z_2 is the impedance of the second medium (noodle dough). The corresponding quantities when the wave originates in medium 2, $t_{2 \rightarrow 1}$ and $r_{2 \rightarrow 1}$, are defined by swapping the indices 1 and 2 on the right-hand side of equations (6.16) and (6.17).

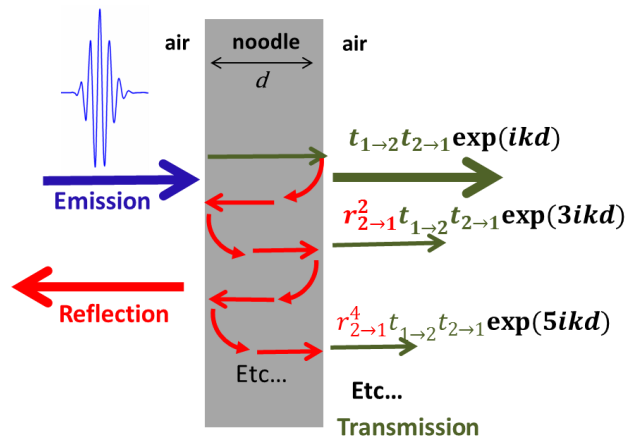


Figure 6.9: Multiple reflections inside a layer of noodle dough (image courtesy of R.-M. Guillermic).

The total amplitude transmission coefficient T through the sheet of noodle dough can be calculated [99]:

$$T = t_{1 \rightarrow 2} t_{2 \rightarrow 1} e^{ikd} (1 + r_{2 \rightarrow 1}^2 e^{2ikd} + r_{2 \rightarrow 1}^4 e^{4ikd} + r_{2 \rightarrow 1}^6 e^{6ikd} + \dots) \quad (6.18)$$

The term inside the parentheses is a geometric sequence, so the transmission coefficient is equal to

$$T = \exp(ikd) \frac{t^2}{1 - r^2 \exp(2ikd)}, \quad (6.19)$$

where $t^2 = t_{1 \rightarrow 2} t_{2 \rightarrow 1} = 4Z_1 Z_2 / (Z_1 + Z_2)^2$, $r^2 = r_{2 \rightarrow 1}^2 = [(Z_2 - Z_1) / (Z_1 + Z_2)]^2$, k is the wave number in the noodle and d is the thickness of the sheet.

The impedance Z depends on the phase velocity and the attenuation. Using equation (6.1), the impedance is:

$$Z = \rho \frac{\omega}{k} = \frac{\rho v}{1 + i \alpha v / 2\omega}, \quad (6.20)$$

where ω is the angular frequency ($\text{rad} \cdot \text{s}^{-1}$), v the phase velocity ($\text{m} \cdot \text{s}^{-1}$), α the attenuation (m^{-1}) and ρ the density ($\text{kg} \cdot \text{m}^{-3}$).

Equation (6.19) needs to be inverted in order to extract the phase velocity and the attenuation. But first, the simplifying assumption is made that the denominator of equation (6.19) is equal to one. This assumption means that the multiple reflections inside the dough sheet are not taken into account. For this to be true, there are two possibilities. First the dough sheet is thick enough so the multiple reflections are well separated in time. To be in this situation, the thickness of the noodle needs to be large compared to the wavelength of the wave inside the noodle ($d \gg \lambda$).

The second possible situation for this assumption to be true is that the attenuation in the noodle is large enough that no measurable signals are able to do a complete round-trip inside the noodle ($\alpha d \gg 1$). In the case of the noodle dough, the second situation is almost always true at the frequencies of interest. With this assumption equation (6.19) becomes:

$$T = t^2 \exp(ikd). \quad (6.21)$$

6.4.2 Experimental technique

For a given experiment, two acquisitions must be performed, one of the signals going through the noodle sheet, and one reference signal through air. The comparison of these two signals is used to get the actual amplitude change and phase-shift due to the noodle dough. The Fourier transform of the first signal is divided by the Fourier transform of the second signal to obtain the relative transmission through the noodle sheet.

$$T_r = \frac{FT(\text{noodle})}{FT(\text{reference})} = \frac{At^2 \exp(ikd)}{A \exp(ik_a d)} \quad (6.22)$$

In equation (6.22), A represents the amplitude of the emitted wave and k_a is the wave number in air. The factor $\exp(ik_a d)$ accounts for the phase shift of the reference through the layer of air which will be replaced by the noodle for the measurement on the dough sheet.

The transmission T_r in equation (6.22) is the actual value that is measured during an experiment. The absolute value of T_r yields the wave attenuation in the noodle dough, and the phase (φ) determines the phase velocity.

$$T_r = \frac{4Z_a Z}{(Z_a + Z)^2} \exp(i(k - k_a)d), \quad (6.23)$$

$$|T_r| = \left| \frac{4Z_a Z}{(Z_a + Z)^2} \right| \exp\left(-\frac{\alpha}{2}d\right) \quad (6.24)$$

and

$$\varphi = \gamma + \left(\frac{1}{v} - \frac{1}{v_a}\right) \omega d. \quad (6.25)$$

γ is the phase of t^2 , and Z_a and v_a are the impedance and the velocity of sound of air.

The impedance is a function of both phase velocity (v) and attenuation (α) [equation (6.20)], so it is not possible to directly invert equations (6.24) and (6.25) to extract v and α . In order to obtain these values from the experiment, an iteration process is done. First, the two last equations are solved for v and α as a function of all the other parameters (including Z). The two new equations are:

$$v = \frac{v_a}{1 + (\varphi - \gamma) \frac{v_a}{\omega d}} \quad (6.26)$$

and

$$\alpha = -\frac{2}{d} \ln \left(|T_r| \left| \frac{(Z_a + Z)^2}{4Z_a Z} \right| \right). \quad (6.27)$$

Equations (6.26) and (6.27) can be used to do an iterative process on the impedance of the dough, Z . The set of equations used for the iteration is:

$$v^{(n+1)} = \frac{v_a}{1 + (\varphi - \gamma^{(n)}) \frac{v_a}{\omega d}}, \quad (6.28)$$

$$\alpha^{(n+1)} = -\frac{2}{d} \ln \left(|T| \left| \frac{(Z_a + Z^{(n)})^2}{4Z_a Z^{(n)}} \right| \right) \quad (6.29)$$

and

$$Z^{(n)} = \frac{\rho v^{(n)}}{1 + i \alpha^{(n)} v^{(n)} / 2\omega}. \quad (6.30)$$

The iterative process starts with a first “guess” of the velocity $v^{(1)}$ and the attenuation $\alpha^{(1)}$ in the noodle. A first value of the impedance $Z^{(1)}$ is calculated with equation (6.30), and from the impedance, the next values of the velocity and the attenuation are calculated with equations (6.28) and (6.29), leading to a new value of the impedance. This iterative process converges rapidly; usually 20 steps are enough to obtain the final values of velocity and attenuation.

6.5 Results and Interpretation

The objectives of the first part of the project were to assess the feasibility of using air-coupled transducers to study the properties of noodle dough, *i.e.*, to establish if the signal going through noodle is large enough to detect, and if the detection of differences in composition/mechanical properties is possible. Despite the very large reflection coefficient at the interface between air and noodle dough [the amplitude t^2 of equation (6.21) has a value around 10^{-4}], the signal going through the noodle is detectable and has a good signal-to-noise ratio, and therefore it can be used to measure mechanical properties. The ultrasonic technique has been used on different dough samples, varying in their composition or by the manufacturing process.

6.5.1 Noodle dough making [76,100]

Noodles are made from three ingredients: flour, water and salt. The masses of water and salt used in the dough are weighed with respect to the mass of flour. To obtain noodle dough, the typical range of water content is from 32% to 38% of the flour weight (%fwb: % flour weight basis) giving a very dry dough (in bread dough, the quantity of water is typically 65 %fwb). Two types of salt are used to make noodles, sodium chloride (NaCl) or kansui salt. The kansui is an alkaline salt containing sodium carbonate (Na_2CO_3) or potassium carbonate (K_2CO_3) salt.

The noodles used during the first part of the project, experiments in a laboratory environment, were made at the Grain Research Laboratory. Flour, water and salt were mixed using a centrifuge mixer for 30 seconds at 3000 rpm [100]. The flour used was milled from a Canada Western Red Spring (CWRS) wheat. At the end of the mixing, the dough crumbs (see Figure 6.10) were gathered together and formed into a sheet. This sheeting process started by feeding the crumbs in between two counter-rotating sheeting rolls of the noodle machine using a roller gap of 3 mm. At the end of this first pass, all the crumbs were aggregated together and formed the noodle sheet. At this stage, at least one lamination step was performed (Figure 6.10). Lamination consists of folding the sheet in two and letting it pass again through the rolls with the same roll separation as the first pass. The number of lamination steps performed on the dough is one of the parameters that was studied and is presented later in this section. The number of laminations was varied from 1 to 9 and they were all done at constant roller separation. After the laminations, 6 reduction passes were done with a decreasing roll gap (Table 6.3) [100]. The thickness of the noodle was therefore progressively reduced, while its length increased. The thickness of the noodle after each reduction step is larger than the separation between the rolls,

as the noodle dough sheets spring back, due to the large constraint applied on them and their viscoelastic character.

Reduction step	Separation between the rolls (mm)
1	2.55
2	2.15
3	1.85
4	1.57
5	1.33
6	1.10

Table 6.3: Separation between the rolls of the noodle machine for the different reduction steps (after the lamination steps).



Figure 6.10: Left: dough crumbs at the end of mixing. Right: Dough going through the rolls during a lamination step (the dough has been folded in two). Pictures taken at the Grain Research Laboratory by Dr. Daiva Daugelaite.

Noodle dough is a complex material composed of a network of gluten with embedded starch granules. Gluten development (formation of the gluten network) happens at all stages of production: the mixing, lamination and elongation steps. During the mixing, the flour is hydrated by the water in the mixer bowl. Most gluten development, however, takes place during

lamination and sheeting rather than during mixing [76]. The gluten is composed of two proteins, the glutenins and the gliadins. In the dry flour, these molecules are folded and the different processing steps have the effect of aligning the molecules due to forces applied on the dough [82]. A network of protein is created thanks to the cross-links between the different molecules, including disulfide bonds or hydrogen bonds, leading to an increase of the strength of the matrix and, as a result, of the dough itself. The different molecules of different lengths in the network experience different relaxation times [101], which can be linked to the model developed in the section 6.2.2. If too much force is applied on the dough during a reduction step, these bonds may break, damaging the gluten structure [102]. The type and the quantity of salt influence the number of these bonds and hence, the strength of the dough [103]. The quantity of added water is also an important factor in the gluten development and influences the viscoelastic properties of the final dough [102].

6.5.2 Comparison of the acoustical properties of different doughs

The ultrasonic signal going through a noodle sheet is reduced drastically, as explained in section 6.4. As an example, Figure 6.11 shows a signal going through air (reference signal) and Figure 6.12 shows a signal going through a dough sheet. The ratio between the vertical scales of these two figures is around 10^{-4} .

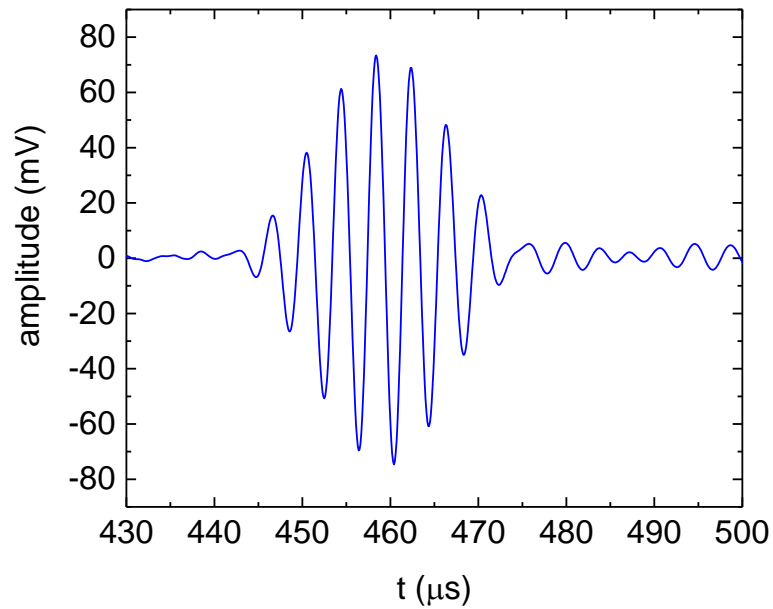


Figure 6.11: Reference signal obtained with the Microacoustics transducers at 250 kHz. The separation between the two transducers is 16 cm.

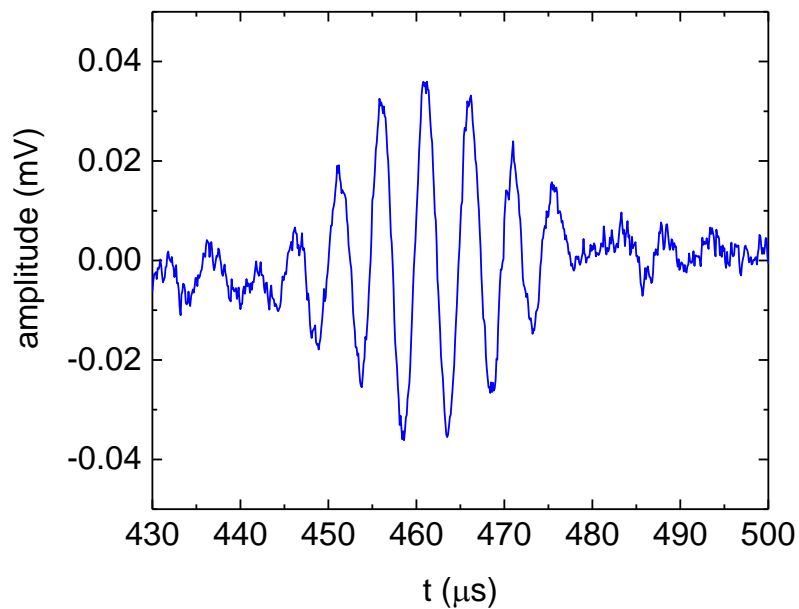


Figure 6.12: Signal going through a noodle dough made with a water absorption level of 34%, 1% of NaCl salt and 1% of kansui salt. This dough was made with 9 lamination steps. The thickness of the dough was 1.75 mm.

The density of each noodle dough sample was measured with two different techniques. The first method uses a specific gravity bottle, and consists in measuring the weight of water displaced by the sample. For this method, the specific gravity bottle is initially full of water and is weighed by itself, then a piece of sample of known weight is put inside and the bottle is weighed again after carefully wiping off the overflowed water. The volume of the object can then be deduced and the density can be easily calculated. The second technique consists in taking a picture of small (typically a few cm^2) subsamples of dough sheets with a constant thickness. An image analysis software, ImageJ, is used to determine the area of the sample, the thickness is measured using a calliper, and the mass of the dough piece is measured using a precision balance. Hence the volume and then the density were determined. The density of all the doughs is approximately $\rho = 1280 \pm 50 \text{ kg/m}^3$. The specific gravity bottle method is the one that is commonly used in food science as it is very precise, but it requires training in order to get good quality measurements. One common source of error is the warming up of the bottle due to too many manipulations, and this leads to an erroneous density. The image analysis method on the other end has to be done carefully with a controlled lighting in order to obtain good quality images that are easy to process.

The influence of different parameters on phase velocity and attenuation has been studied and will be presented in the following subsections.

6.5.2.1 Influence of the water content and of the number of lamination steps

In this section, four different dough sheets are characterized: two sheets with different water contents (34% or 38% of flour weight) and two sheets with a different numbers of lamination steps (1 or 9). All the doughs were made with 1% of NaCl salt and 1% of kansui salt. Figure

6.13 to Figure 6.20 (on the next four pages) show the velocity and attenuation in these four noodle doughs by comparing them two-by-two. The measurements were done on 6 different batches of noodle dough with the same processing and composition, and each dough sheet was cut in three pieces. Therefore, for each dough, 18 measurements were done. The error bars are the error of the mean obtained from these 18 different acquisitions.

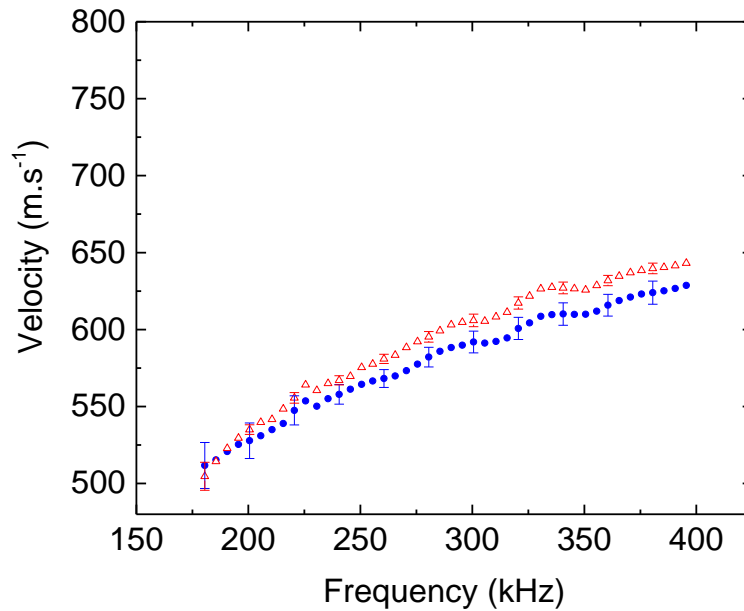


Figure 6.13: Velocity of ultrasound as a function of frequency for dough with 38% water made with 1 lamination step (blue circles) and 9 lamination steps (red open triangles). The thickness of the 1-lamination noodle dough was 1.64 ± 0.03 mm and the thickness of the 9-lamination noodle dough was 1.69 ± 0.03 mm.

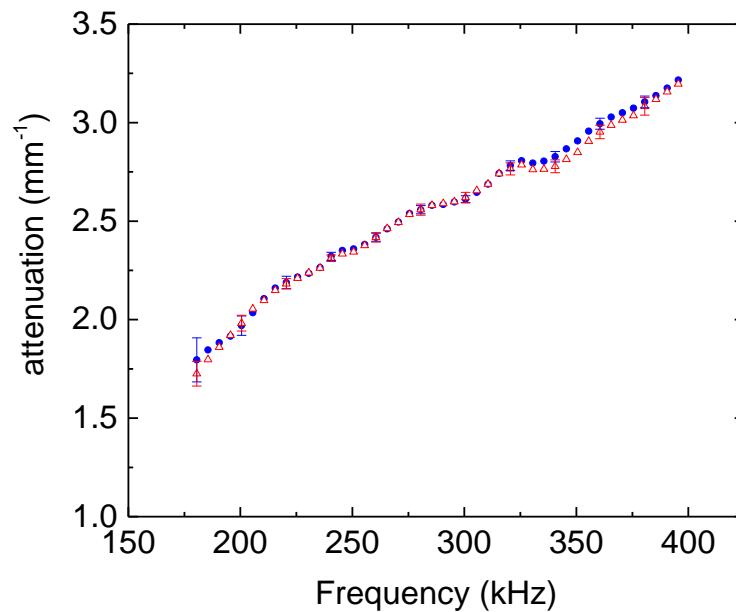


Figure 6.14: Attenuation of ultrasound as a function of frequency for dough with 38% water and 1 lamination step (blue circles) and 9 lamination steps (red open triangles).

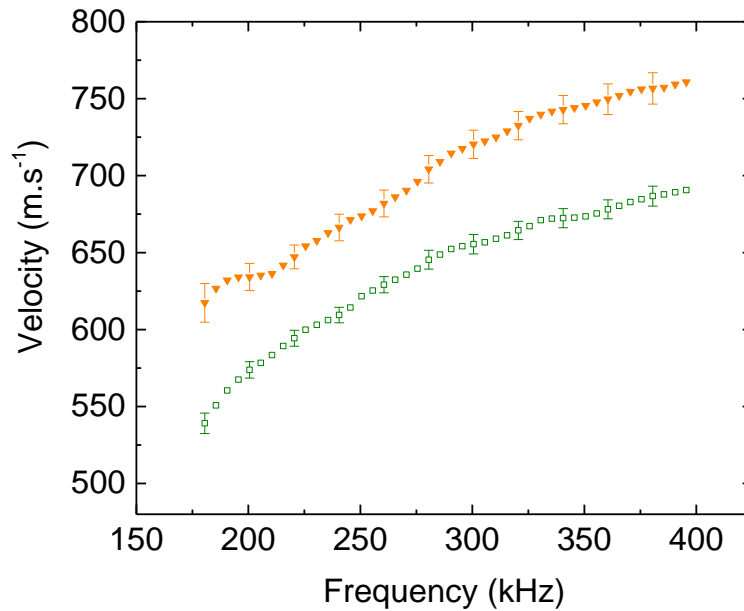


Figure 6.15: Velocity of ultrasound as a function of frequency for dough with 34% water and 1 lamination step (orange triangles) and 9 lamination steps (green open squares). The thickness of the 1-lamination noodle dough was 1.72 ± 0.03 mm and the thickness of the 9-lamination noodle dough was 1.80 ± 0.05 mm.

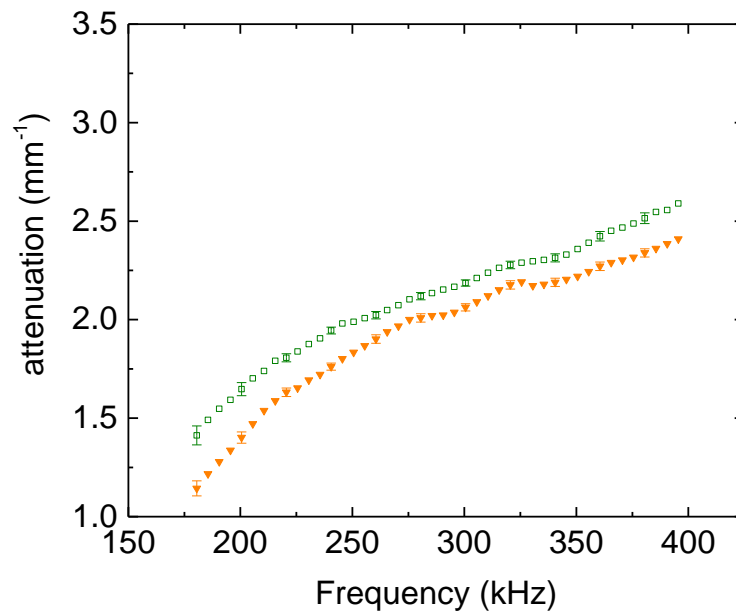


Figure 6.16: Attenuation of ultrasound as a function of frequency for dough with 34% water and 1 lamination step (orange triangles) and 9 lamination steps (green open squares).

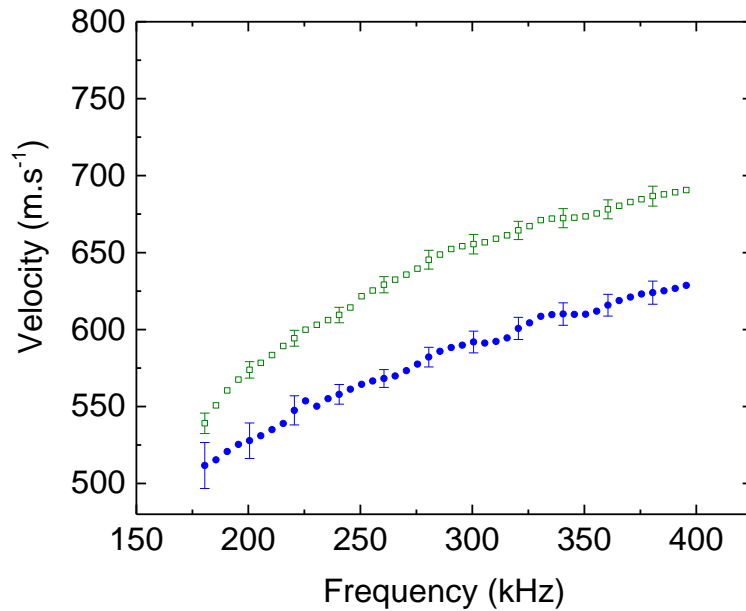


Figure 6.17: Velocity of ultrasound as a function of frequency for dough with 34% (green open squares) and 38 % (blue circles) water and 9 lamination steps. The thickness of the 34% water noodle dough was 1.80 ± 0.05 mm and the thickness of the 38% water noodle dough was 1.69 ± 0.03 mm.

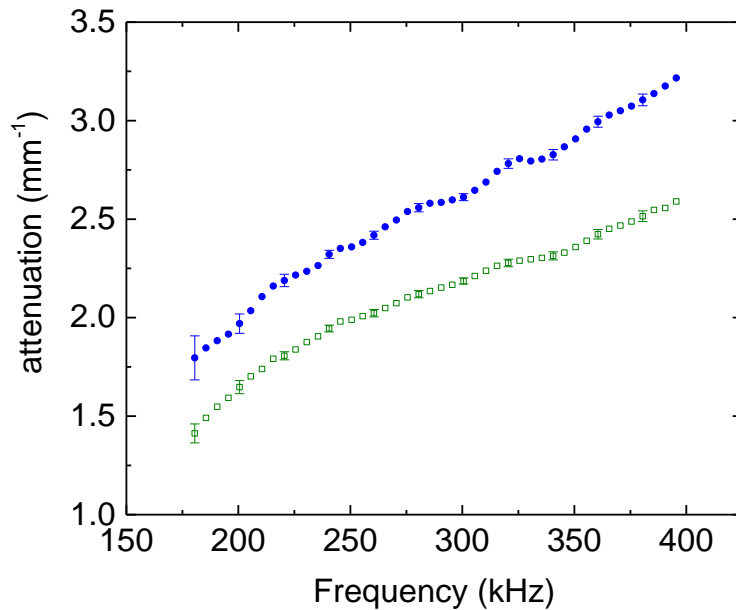


Figure 6.18: Attenuation of ultrasound as a function of frequency for dough with 34% (green open squares) and 38 % (blue circles) water and 9 lamination steps.

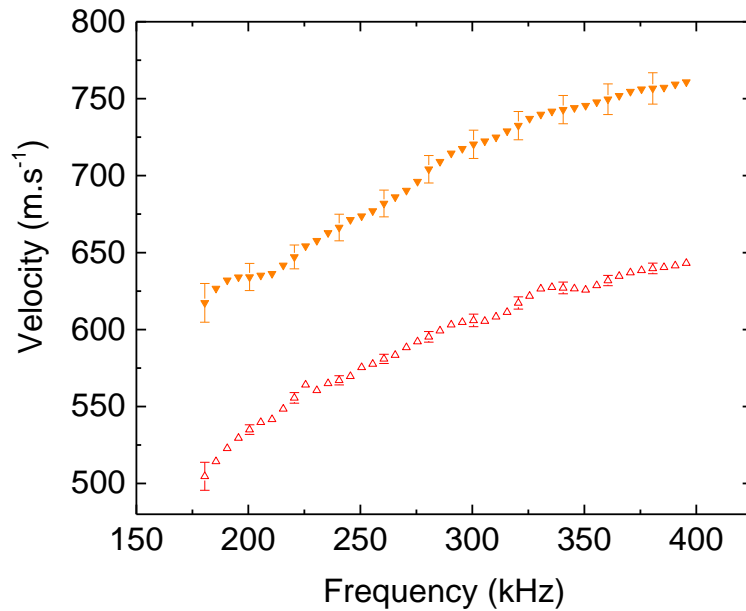


Figure 6.19: Velocity of ultrasound as a function of frequency for dough with 34% (orange triangles) and 38 % (red open triangles) water and 1 lamination step. The thickness of the 34% water noodle dough was 1.72 ± 0.03 mm and the thickness of the 38% water noodle dough was 1.64 ± 0.03 mm.

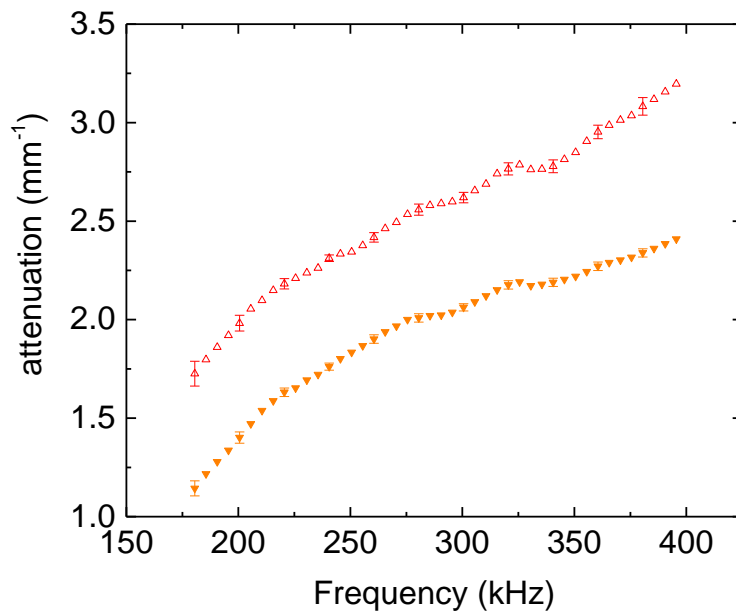


Figure 6.20: Attenuation of ultrasound as a function of frequency for dough with 34% (orange triangles) and 38 % (red open triangles) water and 1 lamination step.

According to Figure 6.13 and Figure 6.14, the number of lamination steps does not influence the mechanical properties of dough with a high level of water (38%). However, Figure 6.15 and Figure 6.16 show that the number lamination steps influences significantly the mechanical properties of a dryer (34%) noodle dough. For the dryer noodle dough, the velocity of sound is lower for the high number of lamination steps while the attenuation is larger.

When the number of lamination steps is kept constant, the quantity of water has an influence on the mechanical properties of the dough (Figure 6.17 to Figure 6.20) [82,83,104]. For wet or dry noodle dough, whatever the number of laminations, the dry noodle has always a higher velocity and a lower attenuation than the wet noodle for the range of frequencies studied with these transducers. These effects are discussed in more detail in section 6.5.2.4.

In Figure 6.13 to Figure 6.20, whether or not a difference in the value of the velocity and attenuation can be observed, the slopes of both curves in each figure are similar. The number of lamination steps or the quantity of water does not change the evolution with frequency of the velocity or attenuation. The large frequency dependence observed in these figures is consistent with previous observations either at the lower frequency of 40 kHz, where the velocity and attenuation were found to be smaller [78], or at the higher frequencies of 1 MHz and 11 MHz, where larger velocities and attenuation were measured [79,105].

The quantity of water added to the dough has an effect on the mechanical properties of the dough. In particular the water quantity influences the gluten development which, as a result, affects the rheological (and mechanical) properties of the dough. It is more convenient to look at the modulus to assess the mechanical properties of the dough. The complex longitudinal

modulus can be calculated using equations (6.11) and (6.12); the error bars in Figure 6.21, Figure 6.22 and Figure 6.23 are obtained using standard propagation of error formulas.

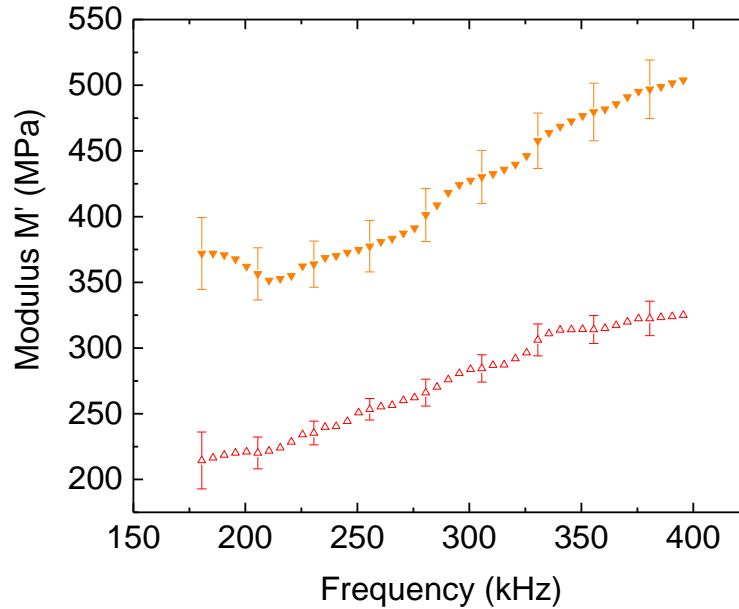


Figure 6.21: Real part of the complex longitudinal modulus (storage modulus) as a function of frequency for dough with 34% (orange triangles) or 38 % (red open triangles) water and 1 lamination step.

The higher value of the storage modulus M' of the dryer noodle (34%), shown in Figure 6.21, indicates that this noodle is firmer than the wet noodle (38%). The imaginary part of M (Figure 6.22) and the ratio of the two components (Figure 6.23) of M give more information about the viscous properties of the noodle.

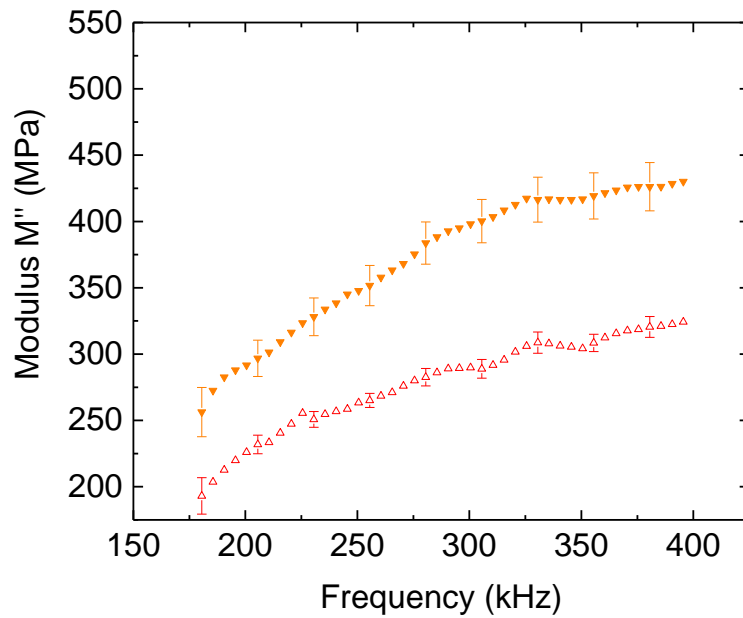


Figure 6.22: Imaginary part of the complex longitudinal modulus (loss modulus) as a function of frequency for dough with 34% (orange triangles) or 38 % (red open triangles) water and 1 lamination step.

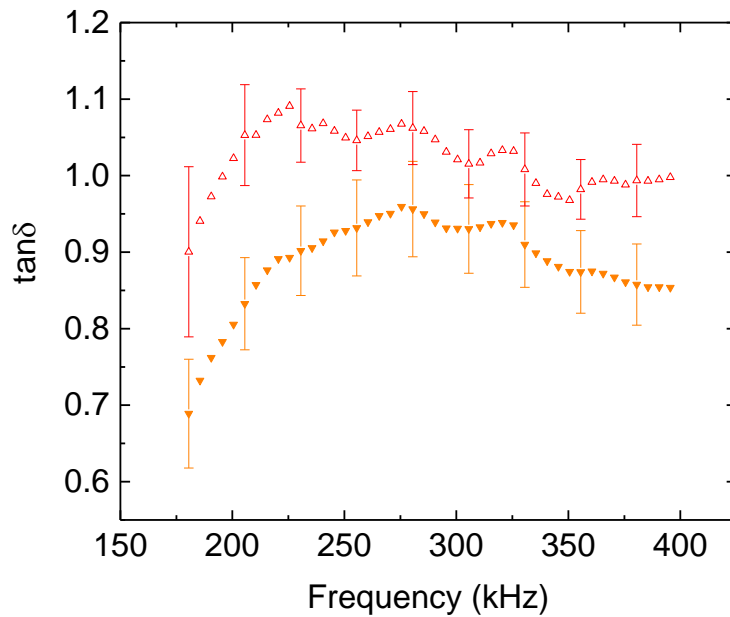


Figure 6.23: Ratio of the imaginary and real parts of the longitudinal modulus, $\tan(\delta) = M''/M'$ as a function frequency for dough with 34% (orange triangles) or 38 % (red open triangles) water and 1 lamination step.

As explained in section 6.2.2, $\tan(\delta)$ plotted in Figure 6.23 represents the phase-shift introduced by the effects of the viscosity of the medium. The $\tan(\delta)$ of the dough with 38% water is higher than for the 34% water dough, meaning the viscous effects in the dough with the highest water content are more pronounced than in the dryer dough.

6.5.2.2 Influence of the salt

Two different noodle dough types are discussed in this section. Both of them were made with a 37% water level and with 1 lamination step. In one of the doughs, there is 1% NaCl salt and in the second dough 1% kansui is added with the 1% NaCl salt. Figure 6.24 and Figure 6.25 show the velocity and attenuation for these two doughs.

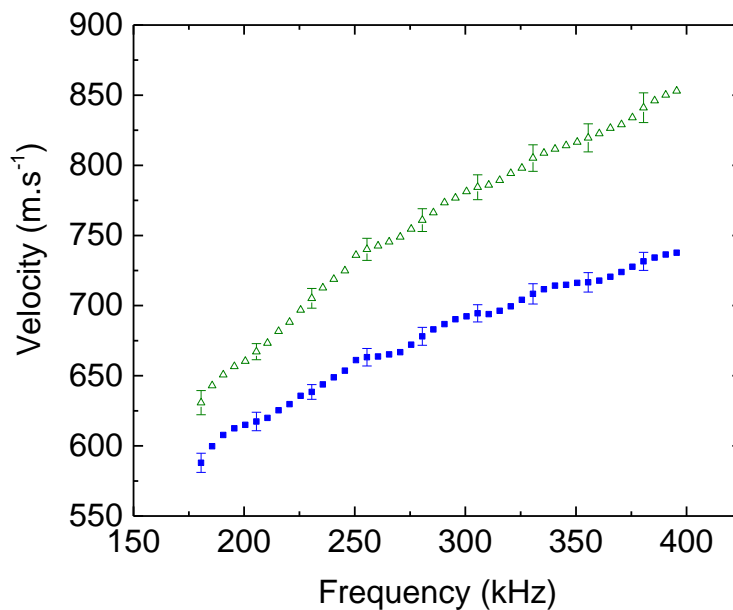


Figure 6.24: Velocity of ultrasound as a function of frequency for dough with 1% NaCl salt (green open triangles) or 1% kansui + 1% NaCl salt (blue squares).

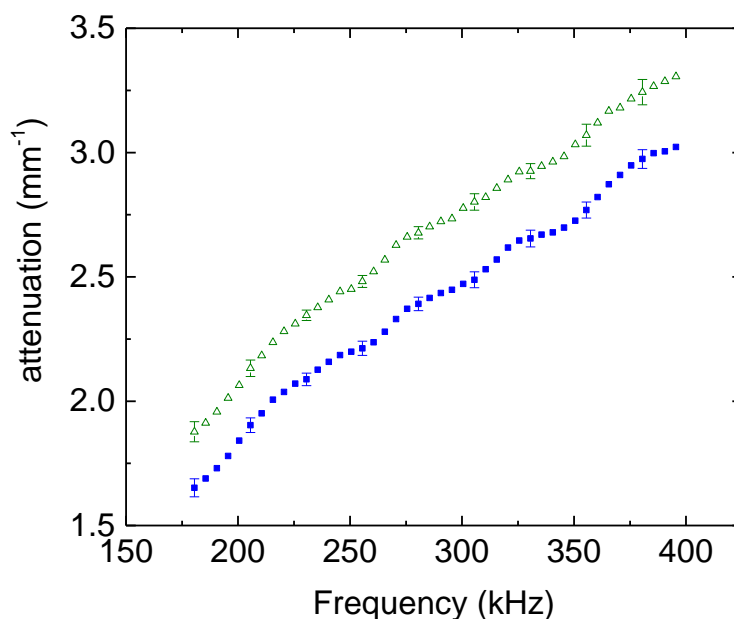


Figure 6.25: Attenuation of ultrasound as a function of frequency for dough with 1% NaCl salt (green open triangles) or 1% kansui + 1% NaCl salt (blue squares).

The addition of the kansui salt has the effect of decreasing both the velocity and the attenuation in the dough sheets. This behaviour is different from what has been observed in section 6.5.2.1, in which a higher velocity is always associated with a lower attenuation when two doughs are compared. It is known that both the type of salt and the quantity of salt have an influence on the gluten network, in particular on the disulphide and hydrogen bonds in the network [103]. As was done in section 6.5.2.1, the longitudinal modulus can be calculated for these two doughs. The storage modulus M' is displayed in Figure 6.26, the loss modulus M'' in Figure 6.27 and their ratio in Figure 6.28.

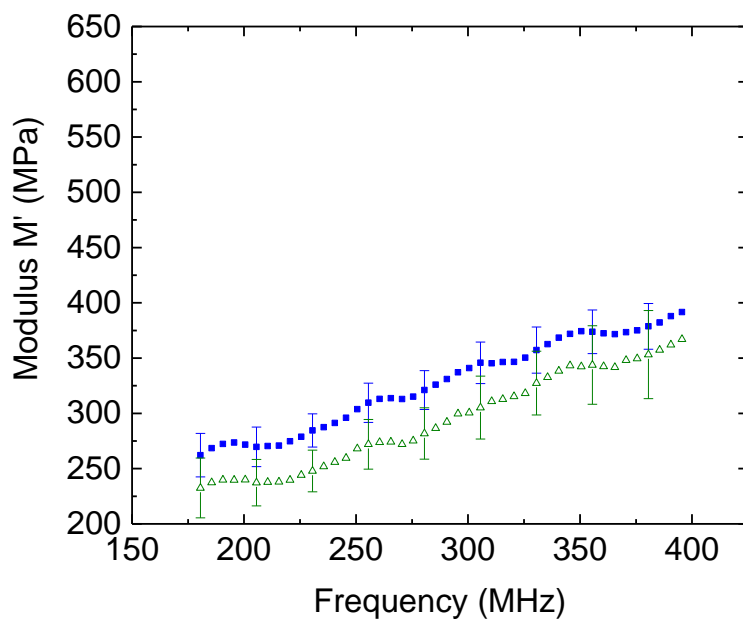


Figure 6.26: Real part of the longitudinal modulus M' as a function of frequency for dough with 1% NaCl salt (green open triangles) or 1% kansui + 1% NaCl salt (blue squares).

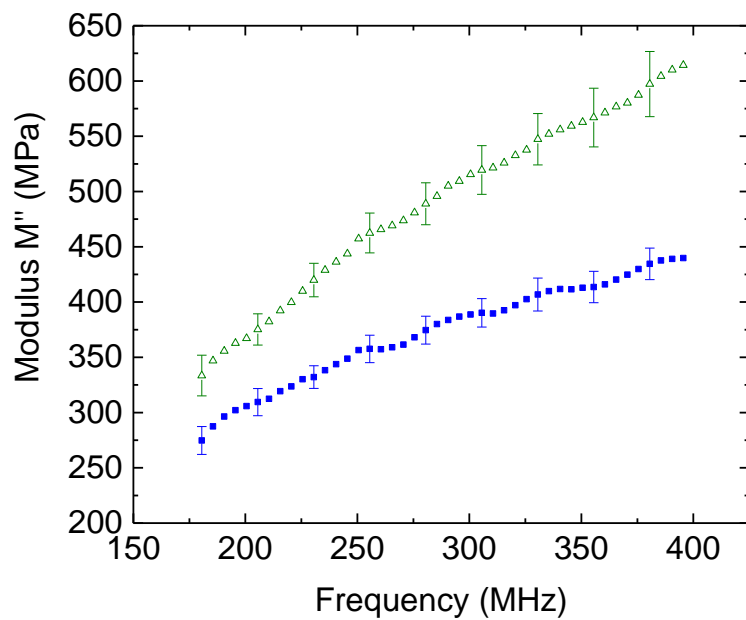


Figure 6.27: Imaginary part of the longitudinal modulus M'' as a function of frequency for dough with 1% NaCl salt (green open triangles) or 1% kansui + 1% NaCl salt (blue squares).

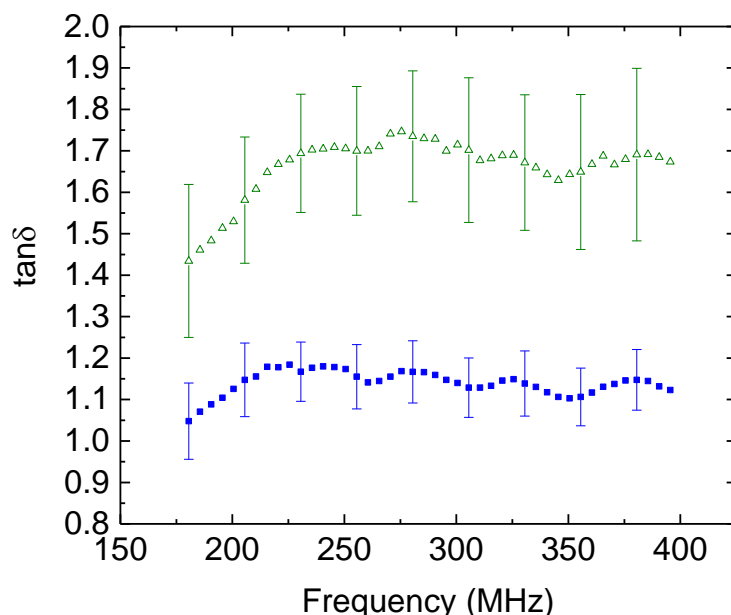


Figure 6.28: Ratio of the imaginary and real parts of the longitudinal modulus, $\tan(\delta) = M''/M'$ as a function of frequency for dough with 1% NaCl salt (green open triangles) or 1% kansui + 1% NaCl salt (blue squares).

The two storage moduli shown in Figure 6.26 are similar, meaning that the firmness of these two doughs is comparable. Unlike the storage moduli, the loss moduli are different for the two doughs (Figure 6.27), leading to different values of $\tan(\delta)$ in Figure 6.28. These results can be interpreted to mean that viscous effects [equation (6.14)] are more important in the dough with 1% kansui + 1% NaCl compared to the dough with only 1% NaCl. This observation confirms the important influence of the salt on the properties of the gluten network of the dough.

6.5.2.3 Results obtained during the production of the dough

The air-coupled ultrasound system has been used on-line on a pilot plant noodle sheeting machine at CIGI. Acquisition of ultrasonic signals was done during the production of the noodle (the dough was moving), between two sets of rolls, after the second reduction step (Figure 6.29). Since these experiments were performed on the pilot plant noodle sheeting machine, the number

of reduction steps and roller gaps were different to those reported in Table 6.3 (four reduction steps in total). During these experiments, the transducers from the company Ultrasonics were used (section 6.3.1.2) as they have a better sensitivity than the Microacoustics transducers and they are more robust, and these experiments were performed before the VN Instruments system had been purchased. The bandwidth of these transducers does not allow frequency-dependent results to be obtained over a significant bandwidth, so only the values at the central frequency of the transducers, 200 kHz, are shown in Figure 6.30 and in Figure 6.31. During these experiments, results at two different pressure levels during the mixing were studied: mixing at atmospheric pressure or at 25% of atmospheric pressure [76] (called “vacuum mixing” in the figures). In all the doughs tested during this set of experiments, sodium chloride (NaCl) salt was used. During the experiment at CIGI, a pin-mixer was used instead of the centrifuge mixer. The thickness of the dough was measured during the production, between the different set of rolls, by stopping them for a short instant. A piece of dough was extracted in order to perform the density measurements (thanks to Ali Salimi). These results are summarized in Table 6.4.



Figure 6.29: Ultrasonic transducers placed on opposite sides the dough sheet as it moves between two sets of rolls at the CIGI pilot plant. The transducers used are the Ultrasonics transducers (section 6.3.1.2).

Dough type	Thickness (mm)	Density (kg.m ⁻³)
Atm, Salt 2%, water 32%	3.40	
Atm, Salt 2%, water 34%	3.22	
Atm, Salt 5%, water 32%	3.62	1293
Atm, Salt 5%, water 34%	3.54	1290
Vac, Salt 2%, water 32%	3.32	1290
Vac, Salt 2%, water 34%	3.20	1293
Vac, Salt 2%, water 36%	3.18	1293
Vac, Salt 5%, water 34%	3.52	1296
Vac, Salt 5%, water 36%	3.31	1302

Table 6.4: Thickness and density of the different doughs on which ultrasonic measurement was performed during the production (Atm: Atmospheric mixing, Vac: Vacuum mixing).

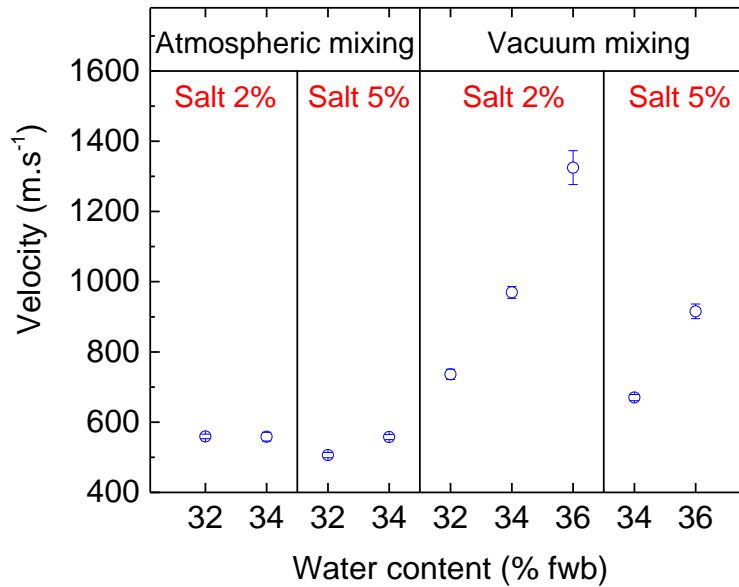


Figure 6.30: Velocity measured at 200 kHz for different noodle doughs measured during production.

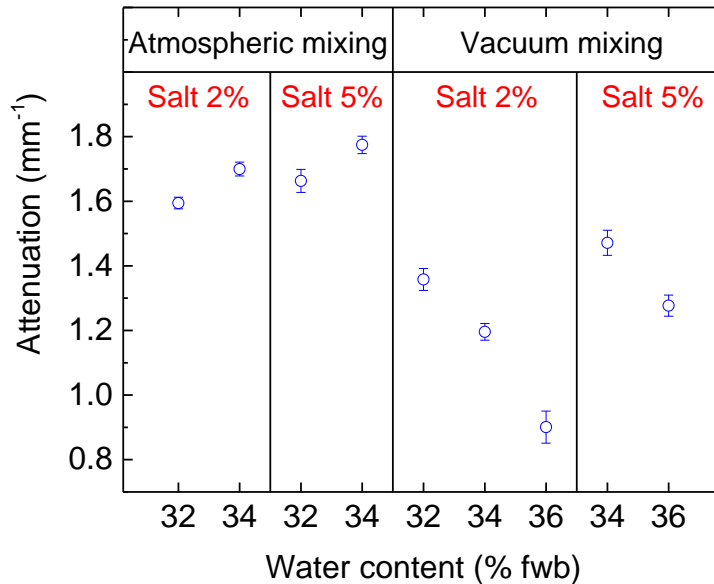


Figure 6.31: Attenuation measured at 200 kHz for different noodle doughs measured during production.

Figure 6.30 and Figure 6.31 show the strong impact of the pressure during mixing on the dough properties. Mixing under reduced pressure leads in fact to a more uniform hydration of the flour, resulting in a continuous network of gluten instead of a thread-like network found in the dough mixed under atmospheric pressure [84]. The mobility of the water molecules is reduced [84], even though the recommended amount of water to be added to the flour for the doughs mixed under vacuum is higher. Thus, for the vacuum doughs, the highest water content was 36%, as opposed to 34% for atmospheric mixed doughs (Figure 6.30 and Figure 6.31). Another observation is that, for all the noodles tested during the on-line trial at CIGI, a higher value of the velocity is associated with a smaller value of the attenuation, and this finding is similar to what has been observed in most of the previous results obtained in lab measurements.

Another series of measurements done during the processing of the noodle dough at CIGI was performed using the transducers from VN instruments. Figure 6.32 shows the results of the raw signals obtained with this setup of transducers. Because the signal processing is implemented directly in the acquisition system (see Appendix 8.4), the signal-to-noise ratio is much better than the results shown in Figure 6.12, making the analysis easier to perform. During the measurement, acquisitions were performed on noodle sheets up to 7 mm thick, after only one elongation step. My contributions to these measurements were the setup of the experiment, the programming to perform the acquisitions with these transducers, the subsequent operation of the data acquisition system during the experiment, and development of the software to do the data analysis. However, all the analysis performed after the experiments were completed by Huiqin (Mia) Wang and the results will be included in her M.Sc. thesis [106]

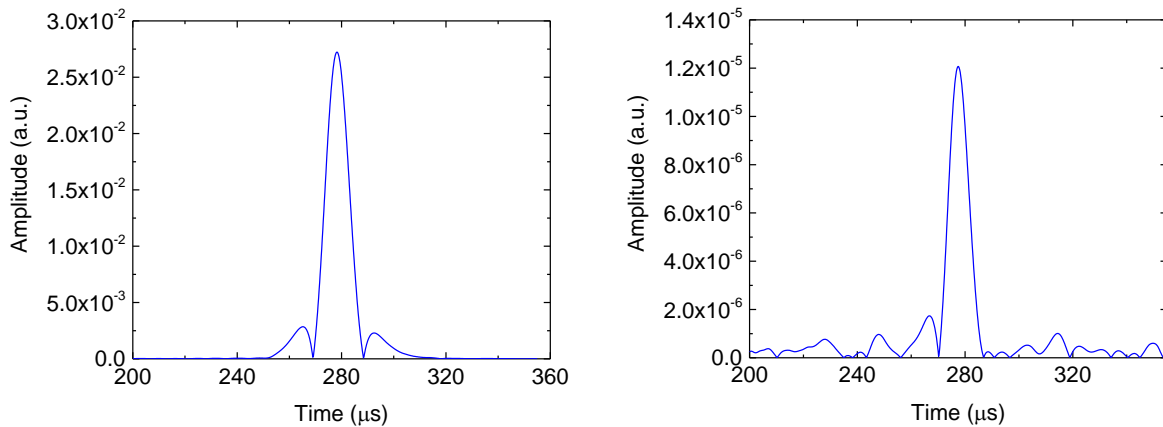


Figure 6.32: Signals obtained with the 200-kHz transducers from VN instruments. Left: reference signal through air. Right Signal through a noodle dough with a thickness of 1.31 mm and containing 36 %fwb of water and 2% of salt. 1 lamination step was performed.

6.5.2.4 Presence of air bubbles in the dough

The frequency-dependent results shown in sections 6.5.2.1 to 6.5.2.3 can be compared to the low frequencies region of Figure 6.1 and Figure 6.2. In these two figures, the slopes of the velocity and attenuation are large at low frequencies below the resonance peak compared to the variation of velocity and attenuation in a medium without any bubbles. For the data on noodles shown in the previous sections, the slope of both the attenuation and the phase velocity are consistent with the presence of peaks at higher frequencies as in Figure 6.1 and Figure 6.2 (noodle dough and bread dough are very different so it is not possible to do a direct comparison). It has recently been shown that there are bubbles in noodle dough (Figure 6.33) [81], and, in particular, that the fraction of gas is higher and the mean radius of the bubbles is lower when the number of lamination steps is larger. These observations should lead to a lower velocity and higher attenuation for the larger number of lamination steps, and this is observed in the noodle dough results shown in Figure 6.15 and Figure 6.16. The increase of volume fraction is probably due to the trapping of air during the multiple lamination steps between the two folds of the noodle. Additionally, each lamination step has the effect of breaking up the bubbles [81], leading to a smaller mean radius when the number of lamination steps increases.

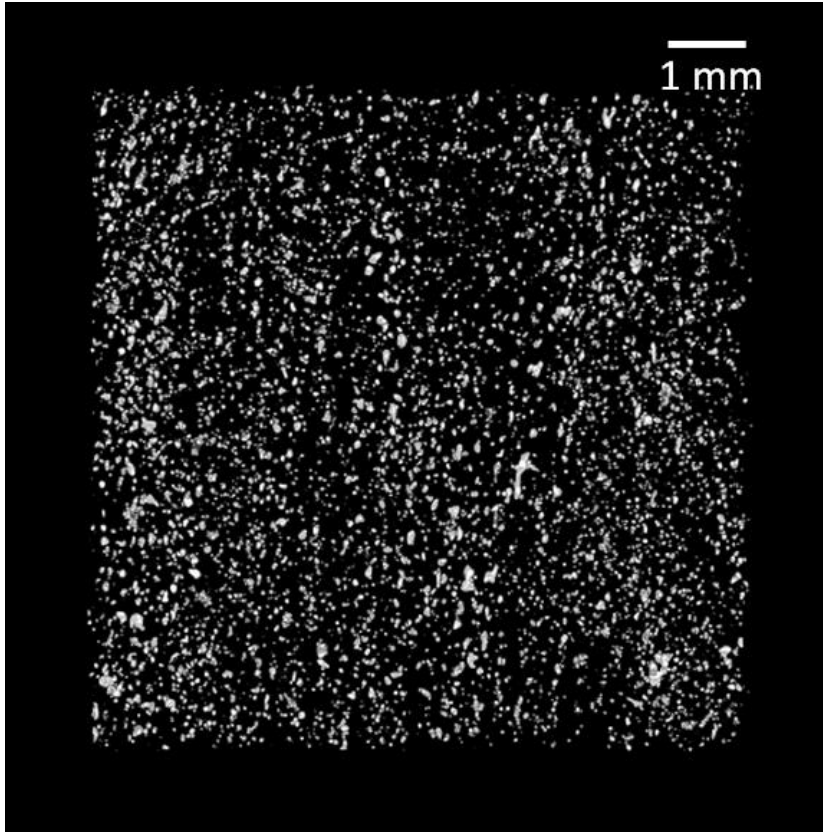


Figure 6.33: Image of a noodle dough sheet obtained by X-ray microtomography (experiment done at the Canadian Light Source in Saskatoon). The white elements of the image represent the voids (air) inside the noodle. The noodle was made with 34% water, 1% salt and 1 lamination step (picture courtesy of R.-M. Guillermic).

In order to see more clearly the influence of bubbles on the acoustic properties, an experiment in contact has been performed over a large frequency band. The contact experiment allows studying a larger frequency range compared to experiments in air, due to the large attenuation of ultrasound in air. Figure 6.34 and Figure 6.35 show the velocity and attenuation obtained on dough similar to the dough shown with the green open triangles in Figure 6.24 to Figure 6.28: in both cases the noodle is made with 1% NaCl salt, 37% water absorption level and 1 lamination. The noodle dough used for the experiment in contact was made in the Ultrasonics Research Laboratory with parameters as similar as possible to the one (that was made at the

GRL) used to perform the air-coupled transducer experiments, but there are still some manufacturing differences, since, in particular, the mixer, the flour batch and the sheeting roll stand are different (even though both noodle doughs were made with CWRS flour). For contact experiments, the piezoelectric transducers are placed against a polystyrene (Rexolite) delay line. To ensure good contact between the noodle dough and the delay lines, a small stress has to be imposed on the dough sheet.

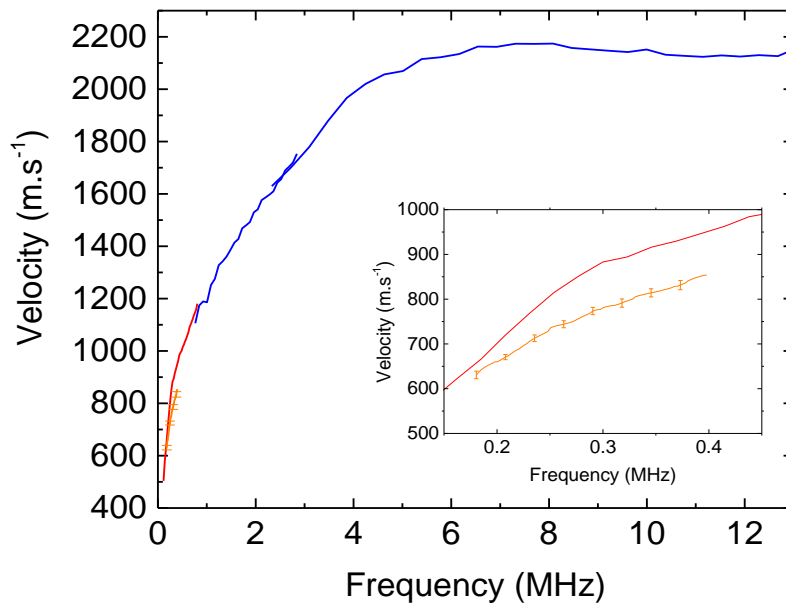


Figure 6.34: Velocity obtained over a large frequency band with contact experiments (red: 500 kHz transducers, blue: 10 MHz transducers). The inset is a zoom at low frequency to compare the air-coupled results (orange) obtained on a similar dough.

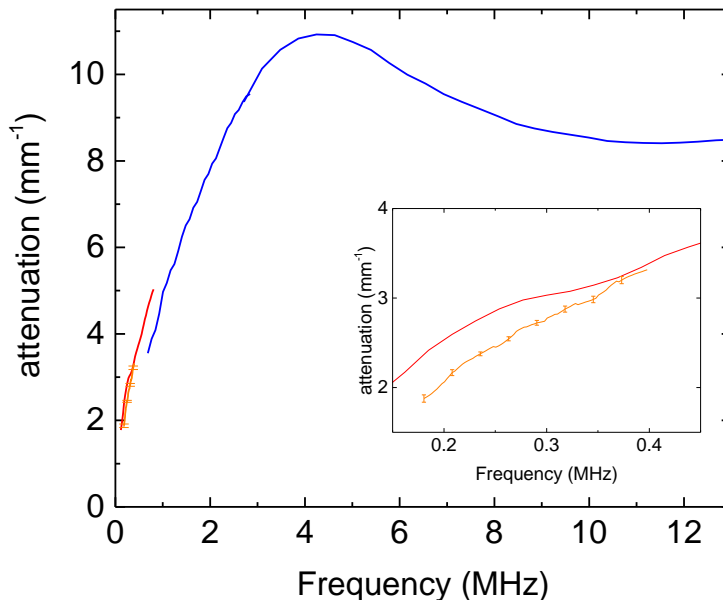


Figure 6.35: Attenuation obtained over a large frequency band with contact experiments (red: 500 kHz transducers, blue: 10 MHz transducers). The inset is a zoom at low frequency to compare the air-coupled results (orange) obtained on a similar dough.

The results shown in Figure 6.34 and Figure 6.35 show that the acoustic properties of the dough obtained with a contact measurement or without contact are similar (12% differences for the velocity and 9% for the attenuation at 300 kHz) despite the differences in the processing of the dough. The behaviour of the velocity and the attenuation at high frequency (above 2 MHz) is one more indicator of the presence of bubbles inside the dough, as can be seen, in particular, by comparing the frequency dependence of the attenuation in Figure 6.2 and Figure 6.35.

6.6 Conclusions

This project shows not only that the detection of an air-coupled ultrasonic signal going through a sheet of noodle dough is possible, but that the quality of this signal is sufficiently good that differences in the mechanical properties of different doughs can be detected. The manufacturing of noodle dough involves a lot of different physical and chemical processes which

are not fully understood. Some parameters can be controlled and they are either processing parameters such as the mixing conditions and number of laminations, or composition parameters. The final raw noodle product is composed of an inhomogeneous gluten network with starch granules embedded in it. Air bubbles are furthermore trapped inside the dough. During the sheeting process, bubbles have the tendency to elongate [81] and the elastic properties of the dough tend to prevent the bubbles from recovering their spherical shape.

All the parameters of the dough sheets studied during this project have an influence on the development of the gluten network. As has been discussed, the quantity and the type of salt influence the number of bonds between the different proteins constituting the network, the mixing under vacuum leads to a more homogenous dough structure, the quantity of water changes the final texture of the dough, and the amount of work input needed to obtain the dough sheets also affects the dough texture. The gluten network being the main structural component of the dough, all these modifications affect the mechanical properties and consequently modify the propagation of acoustic waves. I was able to detect these modifications with the air-coupled transducer setup. As there are a lot of physical and chemical processes happening in the dough during the manufacturing, it is very difficult to link a given modification of the acoustic signals to a given parameter of the dough. Consequently, it will be challenging to implement an on-line system for a direct quality control of the dough. A parameter for which the ultrasonic technique is very sensitive, but was not studied extensively, is the thickness of the noodle sheet. During online production, if the thickness of a dough sheet varies by a small amount during the sheeting (0.1 mm), the variation is very rapidly visible on the acoustic signal. For example, if the spring-back ratio of the dough is different to the expected one, it might mean that the dough was not made optimally, and the ultrasonic technique may prove to be a useful way of detecting such

thickness variations. Furthermore, since it has been shown that the spring-back ratio depends, *e.g.*, on the number of lamination steps or the type of salt added in the dough [100], the sensitivity of the ultrasonic technique to variations in thickness due to spring-back fluctuations could be useful for quality control.

Another outcome of this project is the design and the creation of software to analyse these data rapidly. At first, I developed this program specifically for this project, with the objective of making it as user-friendly as possible, but this code is now used for some other applications such as the study of the ballistic signal analyzed in the previous chapters (sections 4.4.1 and 5.6.1). This program was developed in Matlab and calculates the velocity and attenuation of ultrasound in the sample from information about the sample (density, thickness) and the outside medium (air, water,...), and the signal obtained in transmission and a reference signal. More explanations of this program are provided in appendix 8.5.

The research reported in this chapter has laid a foundation that has facilitated additional research on noodle dough at the University. More experiments have been performed by Dr. Reine-Marie Guillermic and Huiqin (Mia) Wang (MSc student in Food Science), some in a laboratory context, some at CIGI, using the third type of transducers provided by VN instruments. These experiments are aimed at obtaining more systematic measurements on some types of noodle dough, in order to study with more statistics the influence of different formulation and processing parameters. The analysis is more convenient with this set of transducers as the signal-to-noise ratio is higher due to the processing done directly within the electronic system provided by VN instruments with the transducers. In addition to these measurements, Dr. Guillermic is currently doing measurements over a much larger range of frequency (from 200 kHz to 15 MHz) to characterize the bubble size distribution in the dough.

Figure 6.34 and Figure 6.35 are an example of results obtained from these experiments. These measurements are done with a contact setup, the noodle being between two plastic plates as it is not possible to perform experiments in air for high frequencies due to the large attenuation. Huiqin (Mia) Wang, for her M.Sc. thesis, did experiments with a sensory panel in order to compare the "mouth feel" of the cooked noodle with the mechanical properties measured via the ultrasound experiments. All these additional experiments should help to determine criteria for the mechanical properties of the raw noodle dough that the noodle manufacturer should look for to obtain a "good" noodle. This project has potential to lead to industrial applications for on-line quality control during production of sheeted noodle dough.

Chapter 7

Conclusions

In this thesis, the results of several experiments using ultrasound have been presented, all of them focusing on explaining or investigating propagation of waves in heterogeneous media. Each of the three sets of experiments focused on a specific type of sample: two of them were specifically designed to examine effects due to strong multiple scattering on wave transport in samples made from aluminum beads, and the third set of experiments was performed on noodle dough, for which I was interested in looking at the mechanical properties. The ultrasonic properties of the two samples made of aluminum beads were investigated in the strong scattering regime where $l_s \approx \lambda$. In these two samples, the analysis focused mainly on the properties of the coda corresponding to the signal which has been scattered a large number of times. On the other hand, the experiments on noodle dough focused on the properties of the ballistic signal, as a coda could not be recorded. The scattering is still strong but the absorption is much larger than in the other samples.

Resonances have an important role in the wave properties of all three types of sample. In the case of noodle dough, bubbles inside the noodle lead to a modification of the acoustic properties compared to the same material without bubbles in it. Indeed, the variations with frequency of wave velocity and attenuation in a medium with bubbles have an important impact on the measurable signal through the dough. Depending on the frequency, it can be hard to measure any signal due to high attenuation; however, the frequency dependence of the attenuation is also a useful characteristic, since it can provide information on the bubble sizes and concentration. For the two samples constructed with aluminum beads, resonances are also important as they define the frequency pass bands and band gaps of the sample. The resonances of an individual bead have been calculated and measured. When several beads are assembled together in contact, the degeneracy of these resonances is lifted, increasing the number of distinct frequencies of the

modes travelling through the beads. When the number of beads is large enough, the frequencies of the coupled resonant modes of the beads are shifted to form an almost continuous spectrum over finite ranges of frequencies, leading to the pass bands. How the coupled modes are distributed in frequency determines the density of states.

Through experimental observations and modeling of the propagation of acoustic waves in the sample made of aluminum beads in a liquid, there is the first clear evidence that multiply scattered waves can travel simultaneously via two coupled pathways through the medium was observed. For all the samples previously studied acoustically in the literature, for example in bones, when two wave components were observed to be travelling together in a given sample, only ballistic signals were detected, facilitating the separation of the two components via their distinct arrival times. In my new and unusual sample, the initial arrival time of the slower component cannot be measured as it is hidden by the coda of the faster component. The first sign of this anomalous behaviour was observed in the time-dependent width squared $w(t)^2$, characterizing the expansion of the multiply scattered wave energy in the sample; the width squared exhibited a maximum followed at later times by a plateau. If there were only a single component propagating, the width would have to grow at all times (or saturate in the case of localization). The second proof of the existence of two components comes from the comparison of the transport characteristics for frequencies inside and outside the band gaps of the network of beads. At low frequencies below the resonances of the beads, and at frequencies in these band gaps, the transport is diffusive, consistent with the transport expected for waves travelling in liquid and scattering off beads. Consequently, at frequencies where the anomalous transport occurs, it can be deduced that the additional slow component uses the network of beads as the medium of propagation. Furthermore, calculations have confirmed the existence of two

propagating components: a fast diffusive component travelling in the liquid, and a slower sub-diffusive component travelling in the bead network. While the agreement between the experimental data and the theoretical predictions is not perfect yet, the results obtained by the theoretical calculations are sufficiently close to the experimental results that one can be confident in this explanation of the wave propagation in this biphasic sample.

The two-dimensional sample was designed to study two effects: the position dependence of the diffusion coefficient in the case of renormalized transport (sub-diffusive or localized) and the equipartition of elastic wave energy. Unfortunately, the calculations performed on the experimental data to obtain the diffusion coefficient did not allow conclusive results to be obtained. Different effects can explain this outcome, the main one being the limited amount of averaging that could be performed on data for a single sample. The position dependence of the diffusion coefficient is an average property of the wave transport, so it is necessary to average over different realizations of the disorder (different samples). An average was performed over the width of the waveguide-like sample, but it was clearly not enough to smooth out all fluctuations in the data due to the interference effects that lead to speckle; at some frequencies, some beads have more energy than their neighbours. In particular, when, at a particular frequency, a bead further away from the source has a higher energy than beads closer to the emitting transducer, it leads to a negative value of the diffusion coefficient, which is not physical.

The main outcome of the analysis of the experimental data to investigate the equipartition of energy is that the resonances of the beads have an influence on the ratio of the shear energy to the compressional energy at long times. The long-time value of the ratio of the two energies is close to one for frequencies in a pass band, and seems to be different in a band gap. The exact

value of the ratio in a band gap is harder to determine due to the noise level of the acquired data, but it is none-the-less clear that the ratio is higher at these frequencies. The value of the equipartition is far from the expected values inside a 3D diffusive sample, and this difference might be due to the part of energy taken by the surface waves (Rayleigh waves) which is not accounted for and is difficult to obtain. This experiment also revealed an unexpected result: the observation of transmission channels through the sample. At some specific frequencies, chains of beads were “active” while the measured amplitude of the displacement in the surrounding beads was close to the noise level. These chains of beads correspond to open channels in the disordered waveguide-like sample. Theoretically, it should be possible to control which beads of the sample are excited by using an array of transducers instead of a single element transducer. This array would allow a precise shaping of the emitted signal into the sample, in space and in time.

The investigation of noodle dough was a project with two distinct objectives. One of them was to assess the feasibility of creating an on-line quality control technique using ultrasound. An ultrasonic technique is a perfect candidate for such an application as it can be non-destructive and provide rapid results. The key to developing this technique is the use of non-contact, air-coupled transducers. Through an extensive series of tests, I determined not only that air-coupled transducers have enough sensitivity to make reliable ultrasonic measurements on noodle dough, but also that ultrasound at the frequencies accessible in the air-coupled transducer measurements can detect differences between different types of noodle dough (formulation or processing differences). Ultrasound gives access to the mechanical properties of the dough, as expressed either in terms of the directly measured quantities of velocity and attenuation, or in terms of the

complex dynamic longitudinal modulus, which can be easily calculated from these directly measured quantities.

In order to have a useful industrial application of this technique, a range of parameters characterizing a “good” noodle dough has to be determined. The second main objective was to understand what affects the mechanical properties that are measured with ultrasound. For this purpose, different doughs were made with a range of different formulation and processing parameters. In noodle dough, the ingredients that were adjusted were the quantity and type of salt and the quantity of water. The processing parameters that were adjusted were the mixing conditions and the number of lamination steps. The experiments that I performed on these noodle doughs showed that air-coupled ultrasonic measurements are capable of determining changes in mechanical properties coming from changes in these different parameters. A recent interest has emerged in the presence of bubbles in the dough [81]. The resonances of the bubbles influence a lot the acoustic properties of the dough, even at frequencies well below the resonances. An important extension of the research on noodle dough reported in this thesis will be more measurements, over a larger frequency range, to obtain more information about the quantity of air and the bubble size distribution. Such measurements are currently being performed in the laboratory.

All the results obtained during my thesis research show the impact of structure and constituents on the transport of acoustic and elastic waves in disordered heterogeneous materials. For the first time, the propagation of two coupled multiply scattered waves has been observed and characterized. The propagation in a 2D sample shows the possibility of controlling wave propagation via the open channels. Ultrasound can also be used to characterize the mechanical

properties of viscoelastic materials. These three experimental studies have also shown the crucial role of the resonances of the scatterers on the acoustic properties.

Bibliography

1. J.H. Page, H.P. Schriemer, A.E. Bailey, and D.A. Weitz. Experimental Test of the Diffusion Approximation for Multiply Scattered Sound. *Physical Review E* 52(3), 3106-3114 (1995).
2. H.P. Schriemer, M.L. Cowan, J.H. Page, P. Sheng, Z. Liu, and D.A. Weitz. Energy Velocity of Diffusing Waves in Strongly Scattering Media. *Physical Review Letter* 79(17), 3166 (1997).
3. H. Hu, A. Strybulevych, J.H. Page, S.E. Skipetrov, and B.A. van Tiggelen. Localization of Ultrasound in a Three-Dimensional Elastic Network. *Nature Physics* 4(12), 945-948 (2008).
4. S. Faez, A. Strybulevych, J.H. Page, A. Lagendijk, and B.A. van Tiggelen. Observation of Multifractality in Anderson Localization of Ultrasound. *Physical Review Letters* 103(15), 155703 (2009).
5. W.K. Hildebrand, A. Strybulevych, S.E. Skipetrov, B.A. van Tiggelen, and J.H. Page. Observation of Infinite-Range Intensity Correlations above, at, and below the Mobility Edges of the 3D Anderson Localization Transition. *Physical Review Letters* 112(7), 073902 (2014).
6. A. Aubry, L.A. Cobus, S.E. Skipetrov, B.A. van Tiggelen, A. Derode, and J.H. Page. Recurrent Scattering and Memory Effect at the Anderson Localization Transition. *Physical Review Letters* 112(4), 043903 (2014).
7. L.A. Cobus, S.E. Skipetrov, A. Aubry, B.A. Van Tiggelen, A. Derode, and J.H. Page. Anderson Mobility Gap Probed by Dynamic Coherent Backscattering. *Physical Review Letters* 116(19), 193901 (2016).
8. P. Sheng, *Introduction to Wave Scattering, Localization and Mesoscopic Phenomena* (Springer, Berlin, 2006).
9. E. Akkermans and G. Montambaux, *Mesoscopic Physics of Electrons and Photons* (Cambridge University Press, Cambridge, 2007).
10. P.W. Anderson. Absence of Diffusion in Certain Random Lattices. *Physical Review* 109(5), 1492-1505 (1958).
11. J.H. Page, Anderson Localization in Three Dimensions. In R. Kaiser, D.S. Wiersma, L. Fallani, and Societa Italiana di Fisica, *Nano Optics and Atomics: Transport of Light and Matter Waves : proceedings of the International School of Physics "Enrico Fermi", course CLXXIII, Varenna on Lake Como Villa Monastero, 23 June - 3 July 2009* (IOS Press, Amsterdam).
12. D. Royer and E. Dieulesaint, *Elastic Waves in Solids* (Springer, Berlin, 1996).
13. A. Tourin, *Diffusion Multiple et Renversement Du Temps Des Ondes Ultrasonores* (Ph.D. Thesis, Université Paris VII, 1999).

14. A. Lagendijk and B.A. van Tiggelen. Resonant Multiple Scattering of Light. *Physics Reports* 270(3), 143-215 (1996).
15. B.A. Van Tiggelen, A. Lagendijk, M.P. van Albada, and A. Tip. Speed of light in random media. *Physical Review B* 45, 12233 (1992).
16. B. Tallon, T. Brunet, and J.H. Page. Impact of Strong Scattering Resonances on Ballistic and Diffusive Wave Transport. *Physical Review Letters* 119, 164301 (2017).
17. H.S. Carslaw and J.C. Jaeger, *Conduction of Heat in Solids* (Oxford University Press, London, 1959).
18. P.W. Anderson. The Question of Classical Localization: A Theory of White Paint? *Philosophical Magazine Part B* 112(4), 505 (1985).
19. S. John, H. Sompolinsky, and M.J. Stephen. Localization in a Disordered Elastic Medium near Two Dimensions. *Physical Review B* 27(9), 5592 (1983).
20. J.T. Edwards and D.J. Thouless. Numerical Studies of Localization in Disordered Systems. *Journal of Physics C: Solid State Physics* 5(8), 807 (1972).
21. D.J. Thouless. Electrons in Disordered Systems and the Theory of Localization. *Physics Reports* 13(3), 93 (1974).
22. E.P. Abrahams, P.W. Anderson, D.C. Licciardello, and T.V. Ramakrishnan. Scaling Theory of Localization: Absence of Quantum Diffusion in Two Dimensions. *Physical Review Letters* 42(10), 673 (1979).
23. D. Vollhardt and P. Wölfle. Diagrammatic, Self-Consistent Treatment of the Anderson Localization Problem in $d \leq 2$ Dimensions. *Physical Review B* 22(10), 4666 (1980).
24. D. Vollhardt and P. Wölfle. Anderson Localization in $d \leq 2$ Dimensions: a Self-Consistent Diagrammatic Theory. *Physical Review Letters* 45(10), 842 (1980).
25. D. Vollhardt and P. Wölfle, Self-Consistent Theory of Anderson Localization. In W. Hanke and Y.V. Kopaev, *Electronic Phase Transitions* (Elsevier Science Publishers, Singapore, 1992). p. 1-78.
26. D. Vollhardt and P. Wölfle. Scaling Equations from a Self-Consistent Theory of Anderson Localization. *Physical Review Letters* 48(10), 699-702 (1982).
27. B.A. van Tiggelen, A. Lagendijk, and D.S. Wiersma. Reflection and Transmission of Waves near the Localization Threshold. *Physical Review Letters* 84, 4333 (2000).
28. S.E. Skipetrov and B.A. van Tiggelen. Dynamics of Weakly Localized Waves. *Physical Review Letters* 92(11), 113901 (2004).

29. S.E. Skipetrov and B.A. van Tiggelen. Dynamics of Anderson Localization in Open 3D Media. *Physical Review Letters* 96(4), 043902 (2006).
30. A.F. Ioffe and A.R. Regel. Non-Crystalline, Amorphous and Liquid Electronic Semiconductors. *Progress in Semiconductors* 4, 237-291 (1960).
31. N. Cherroret, S.E. Skipetrov, and B.A. van Tiggelen. Transverse Confinement of Waves in Three-Dimensional Random Media. *Physical Review E* 82(5), 056603 (2010).
32. E.J.S. Lee, *Ultrasound Propagation through Complex Media with Strong Scattering* (Ph.D. Thesis, University of Manitoba, 2014).
33. C. Croënne, E.J.S. Lee, H. Hu, and J.H. Page. Band gaps in phononic crystals: Generation mechanisms and interaction effects. *AIP Advances* 1, 041401 (2011).
34. B.A. Auld, *Acoustic Fields and Waves in Solids* (Wiley & Sons, New York, 1973).
35. W.K. Hildebrand, *Density of States of Elastic Waves in a Strongly Scattering Porous "Mesoglass"* (M.Sc. Thesis, University of Manitoba, 2009).
36. M.C. Maliepaard, J.H. Page, J.P. Harrison, and R.J. Stubbs. Ultrasonic Study of the Vibrational modes of sintered Metal Powders. *Physical Review B* 32(10), 6261-6271 (1985).
37. E. Bossy, M. Talmant, and P. Laugier. Three-dimensional simulations of ultrasonic axial transmission velocity measurement on cortical bone models. *Journal of the Acoustical Society of America* 115, 2314-2324 (2004).
38. J.A. Turner, M.E. Chambers, and R.L. Weaver. Ultrasonic Band Gaps in Aggregates of Sintered Aluminum Beads. *Acoustica* 84, 628-631 (1998).
39. L.A. Cobus, *Anderson Localization and Anomalous Transport of Ultrasound in Disordered Media* (Ph.D. Thesis, University of Manitoba, 2016).
40. R.H. Hackman, *Acoustic Scattering from Elastic Sphere*. In A.D. Pierce and R.N. Thurston, *Physical Acoustics XXII* (Academic Press, New York, 1993). p. 1-195.
41. W.K. Hildebrand, *Ultrasonic Waves in Strongly Scattering Disordered Media: Understanding Complex Systems Through Statistics and Correlations of Multiply scattered Acoustic and Elastic Waves* (Ph.D. Thesis, University of Manitoba, 2015).
42. A. Hosokawa and T. Otani. Ultrasonic Wave Propagation in Bovine Cancellous Bone. *Journal of the Acoustical Society of America* 101(1), 558-562 (1997).

43. Z.E.A. Fellah, J.Y. Chapelon, S. Berger, W. Lauriks, and C. Depollier. Ultrasonic Wave Propagation in Human Cancellous Bone: Application of Biot Theory. *Journal of the Acoustical Society of America* 116(1), 61-73 (2004).
44. T.J. Plona. Observation of Second Bulk Compressional Wave in a Porous Medium at Ultrasonic Frequencies. *Applied Physics Letters* 36(4), 259-261 (1980).
45. M.A. Biot. Theory of Propagation of Elastic Waves in a Fluid Saturated Porous Solid I. Low-Frequency Range. *Journal of the Acoustical Society of America* 28(2), 168-178 (1956).
46. M.A. Biot. Theory of Propagation of Elastic Waves in a Fluid Saturated Porous Solid II. Higher Frequency Range. *Journal of Acoustical Society of America* 28(2), 179-191 (1956).
47. B. Lagrain, L. Boeckx, E. Wilderjans, J.A. Delcour, and W. Lauriks. Non-Contact Ultrasound Characterization of Bread Crumb: Application of the Biot-Allard Model. *Food Research International* 39, 1067-1075 (2006).
48. M.D. Abramoff, P.J. Magalhaes, and S.J. Ram. Image Processing with ImageJ. *Biophotonics International* 11(7), 36-42 (2004).
49. H. P. Schriemer, *Ballistic and Diffusive Transport of Acoustic Waves in Random Media* (Ph.D. Thesis, University of Manitoba, 1997).
50. M.L. Cowan, K. Beaty, J.H. Page, Z. Liu, and P. Sheng. Group Velocity of Acoustic Waves in Strongly Scattering Media: Dependence on the Volume Fraction of Scatterers. *Physical Review E* 58(5), 6626-6636 (1998).
51. T. Sperling, W. Buehrer, C.M. Aegerter, and G. Maret. Direct Determination of the Transition to Localization of Light in Three Dimensions. *Nature Photonics* 7(1), 48-52 (2013).
52. N. Cherroret and S.E. Skipetrov. Microscopic Derivation of Self-Consistent Equations of Anderson Localization in a Disordered Medium of Finite Size. *Physical Review E* 77(4), 046608 (2008).
53. L.A. Cobus, W.K. Hildebrand, S.E. Skipetrov, B.A. van Tiggelen, and J.H. Page. to be published. ,.
54. X.J. Zhu, D.J. Pine, and D.A. Weitz. Internal Reflection of Diffusive Light in Random Media. *Physical Review A* 44(6), 3948-3959 (1991).
55. Sergey Skipetrov. private communication. ,.
56. R.L. Weaver. On Diffuse Waves in Solid Media. *Journal of Acoustical Society of America* 71(6), 1608-1609 (1982).

57. R. Hennino, N. Tregoures, N.M. Shapiro, M. Campillo, B.A. van Tiggelen, and R.L. Weaver. Observation of Equipartition of Seismic Waves. *Physical Review Letters* 86(15), 3447-3450 (2001).
58. B. Pouet, N. Lefaudeux, P. Clemenceau, and S. Breugnot. Laser Ultrasonic Inspection Based in In-Plane Detection and Shear Wave Generation. 1st International Symposium on Laser Ultrasonics: Science, Technology and Applications, July 16-18 2008, Montrea, Canada ,.
59. T.E. Blum, K. van Wijk, B. Pouet, and A. Wartelle. Multicomponent Wavefield Characteriation with a Novel Scanning Laser Interferometer. *Review of Scientific Instruments* 81(7), 073101 (2010).
60. B.D. Lubachevsky and F.H. Stillinger. Geometric Properties of Random Disk Packings. *Journal of Statistical Physics* 60(5-6), 561-583 (1990).
61. A. Baldantoni, B.J. Janeway, D.C. Lauzon, M.J. Purdon, and R.S. Timsit. NOCOLOK TM Sil Flux - A Novel Approach for Brazong Aluminum. SAE Technical Paper 7, 940502 (1994).
62. J. Bobowski. Summer Student Report for 2000 and 2001. Ultrasonics Research Laboratory, University of Manitoba ,.
63. H. Hu, Localization of Ultrasonic Waves in an Open Three-Dimensional system (MSc. Thesis, University of Manitoba, 2006).
64. P. Patnaik, Handbook of Inorganic Chemicals (McGraw-Hill, New York, 2002).
65. T.H. Chuang, M.S. Yeh, L.C. Tsao, T.C. Tsai, and C.S. Wu. Development of a Low-Melting-Point Filler Metal for Brazing Aluminum Alloys. *Metallurgical and Materials Transactions A* 31(9), 2239-2245 (2000).
66. B. Payne, A. Yamilov, and S.E. Skipetrov. Anderson Localization as Position-Dependent Diffusion in Disordered Waveguides. *Physical Review B* 82(2), 024205 (2010).
67. P.M. Morse and H. Feshbach, *Methods of Theoretical Physics* (McGraw-Hill, New-York, 1953).
68. C. Kittel, *Introduction to Solid State Physics*. 8th ed. (Wiley & Sons, New York, 2005).
69. L. Margerin, *Diffusion Multiple des Ondes Elastiques dans la Litosphère* (Ph.D. Thesis, Université Joseph Fourier - Grenoble I, 1998).
70. A. Goetschy and A.D. Stone. Filtering Random Matrices: The Effect of Incomplete Channel Control in Multiple Scattering. *Physical Review Letters* 111(6), 063901 (2013).

71. B. Gerardin, J. Laurent, A. Derode, C. Prada, and A. Aubry. Full Transmission and Reflection of Waves Propagating through a Maze of Disorder. *Physical Review Letters* 113(17), 173901 (2014).
72. A.G. Yamilov, R. Sarma, B. Redding, B. Payne, H. Noh, and H. Cao. Position-Dependent Diffusion of Light in Disordered Waveguides. *Physical Review Letters* 112(2), 023904 (2014).
73. R.L. Weaver. Diffuse Elastic Waves at a Free Surface. *Journal of the Acoustical Society of America* 78(1), 131-136 (1985).
74. R.L. Weaver. Diffuse Waves in Finite Plates. *Journal of Sound and Vibration* 94(3), 319-335 (1984).
75. A.S. Ross. Instrumental Measurement of Physical Properties of Cooked Asian Wheat Flour Noodles. *Cereal Chemistry* 83(1), 42-51 (2006).
76. G.G. Hou, *Asian Noodles: Science, Technology, and Processing* (Wiley, Hoboken, NJ, 2010).
77. J. Smewing. Navigating Noodle Texture: Taking the Rheological Route. *Cereal Foods World* 61(3), 92-95 (2016).
78. S. Diep, D. Daugelaite, A. Strybulevych, M. Scanlon, J. Page, and D. Hatcher. Use of Ultrasound to Discern Differences in Asian Noodles Prepared Across Wheat Classes and Between Varieties. *Canadian Journal of Plant Science* 94, 1-10 (2014).
79. D. Daugelaite, A. Strybulevych, M.G. Scanlon, J.H. Page, and D.W. Hatcher. Use of Ultrasound to Investigate Glucose Oxidase and Storage Effects on the Rheological Properties of Cooked Asian Noodles. *Cereal Chemistry* 93(2), 125-129 (2016).
80. R. Saggin and J.N. Coupland. Non-Contact Ultrasonic Measurements in Food Materials. *Food Research International* 34, 865-870 (2001).
81. R.-M. Guillermic, F. Koksel, X. Sun, D.W. Hatcher, M.T. Nickerson, G.S. Belev, M.A. Webb, J.H. Page, and M.G. Scanlon. Bubbles in Noodle Dough: Characterization by X-ray Microtomography. *Food Research International* 105, 548-555 (2018).
82. C. Létang, M. Piau, and C. Verdier. Characterization of Wheat Flour-Water Doughs. Part I: Rheometry and Microstructure. *Journal of Food Engineering* 41, 121-132 (1999).
83. C. Létang, M. Piau, C. Verdier, and L. Lefebvre. Characterization of Wheat Flour-Water Doughs: a New Method Using Ultrasound. *Ultrasonics* 39, 133-141 (2001).

84. M. Li, K.-X. Zhu, J. Peng, X.-N. Guo, T. Amza, W. Peng, and H.-M. Zhou. Delineating the Protein Changes in Asian Noodles Induced by Vacuum Mixing. *Food Chemistry* 143, 9-16 (2014).
85. N.M. Edwards, M.G. Scanlon, J.E. Kruger, and J.E. Dexter. Oriental Noodle Dough Rheology: Relationship to Water Absorption, Formulation, and Work Input during Dough Sheeting. *Cereal Chemistry* 73, 708-711 (1996).
86. D.W. Hatcher, A. Salimi, D. Daugelaite, A. Strybulevych, M.G. Scanlon, and J.H. Page. Application of Ultrasound to the Evaluation of Rheological Properties of Raw Asian Noodles Fortified with Barley Beta-Glucan. *Journal of Texture Studies* 45, 220-225 (2014).
87. V. Leroy, A. Strybulevych, J.H. Page, and M.G. Scanlon. Sound Velocity and Attenuation in Bubbly Gels Measured by Transmission Experiments. *Journal of Acoustical Society of America* 123(4), 1931-1940 (2008).
88. V. Leroy, A. Strybulevych, M.G. Scanlon, and J.H. Page. Transmission of Ultrasound Through a Single Layer of Bubbles. *European Physical Journal E* 29, 123-130 (2009).
89. V. Leroy, A. Strybulevych, J.H. Page, and M.G. Scanlon. Influence of Positional Correlations on the Propagation of Waves in a Complex Medium with Polydisperse Resonant Scatterers. *Physical Review E* 83, 046605 (2011).
90. M. Minnaert. On Musical Air-Bubbles and the Sounds of Running Water. *The London, Edinburgh, and Dublin Philosophical Magazine and Journal of Science* 16(104), 235-248 (1933).
91. A.B. Wood, *A Text Book of Sound* (Bell and Sons, London, 1941).
92. V. Leroy, Y. Fan, A.L. Strybulevych, G.G. Bellido, J.H. Page, and M.G. Scanlon, Investigating the Bubble Size distribution in Dough using Ultrasound. In G.M. Campbell, M.G. Scanlon, and D. Leo Pyle, *Bubbles in Food 2* (Eagan press, St. Paul, MN, 2008). p. 51-61.
93. G.G. Bellido, M.G. Scanlon, J.H. Page, and B. Hallgrimson. The Bubble Size Distribution in Wheat Flour Dough. *Food Research International* 39, 1058-1066 (2006).
94. F. Koksel, S. Arıtan, A. Strybulevych, J.H. Page, and M.G. Scanlon. The Bubble Size Distribution and its Evolution in Non-Yeasted Wheat Flour Doughs Investigated by Synchrotron X-ray Microtomography. *Food Research International* 80, 12-18 (2016).
95. Y. Shimiya and K. Nakamura. Changes in Size of Gas Cells in Dough and Bread During Breadmaking and Calculation of critical size of Gas Cells that Expand. *Journal of Texture Studies* 28(3), 273-288 (1997).

96. T.A. Livovitz and C.M. Davis, Structural and Shear Relaxation in Liquids. In W.P. Mason, *Physical Acoustics II Part A* (Academic Press, New York, 1965). p. 282-348.
97. J.L. Hunter, C.J. Montrose, and J.H. Shively. Viscoelastic Constants of a Short-Chain Polymer. *Journal of the acoustical Society of America* 36(5), 953-960 (1964).
98. C. Verdier, P.-Y. Longin, and M. Piau. Dynamic Shear and Compressional Behavior of Polydimethylsiloxanes: Ultrasonic and Low Frequency Characterization. *Rheol. Acta.* 37(3), 234-244 (1998).
99. J. Pierre, F. Elias, and V. Leroy. A Technique for Measuring Velocity and Attenuation of Ultrasound in Liquid Foams. *Ultrasonics* 53, 622-629 (2013).
100. A.K. Salimi, Use of Ultrasound to Determine the Effects of Sheeting and Barley B-Glucan Addition on Mechanical Properties of Asian Wheat Noodles (Ph.D. Thesis, University of Manitoba, 2014).
101. J. Gasparoux, Étude rhéo-acoustique de gels polymères (Ph.D. Thesis, Université Montpellier II, 2007).
102. G.G. Hou, Noodle Processing Technology. In G.G. Hou, *Asian Noodles: Science, Technology, and Processing* (Wiley, Hoboken, NJ, 2010). p. 99-140.
103. I. Rombouts, K.J.A. Jansens, B. Lagrain, J.A. Delcour, and K.-X. Zhu. The Impact of Salt and Alkali on Gluten Polymerization and Quality of Fresh Wheat Noodles. *Journal of Cereal Science* 60, 507-513 (2014).
104. D.W. Hatcher, J.E. Kruger, and M.J. Anderson. Influence of Water Absorption on the Processing and Quality of Oriental Noodles. *Cereal Chemistry* 76(4), 566-572 (1999).
105. D.W. Hatcher, A. Salimi, D. Daugelaite, A. Strybulevych, M.G. Scanlon, and J.H. Page. Application of Ultrasound to the Evaluation of Rheological Properties of Raw Asian Noodles Fortified with Barley Beta-Glucan. *Journal of Texture Studies* 45, 220-225 (2014).
106. H. Wang, M.Sc. Thesis, University of Manitoba (, in progress).

Chapter 8
Appendices

8.1 Einstein notation

The Einstein notation or Einstein summation convention is commonly adopted to simplify equations involving summation. The summation over repeated indexes is implied. For example:

$$y = \sum_{i=1}^3 c_i x_i = c_1 x_1 + c_2 x_2 + c_3 x_3 \quad (8.1)$$

will be written:

$$y = c_i x_i. \quad (8.2)$$

8.2 Voigt notation

The Voigt Notation is used to simplify the notation of tensor. A number is associated with each component of the system coordinate. For example, for Cartesian coordinates and for spherical coordinates, the Voigt notation will be:

$$\begin{array}{ll} x \leftrightarrow 1 & r \leftrightarrow 1 \\ y \leftrightarrow 2 \text{ and } \theta \leftrightarrow 2 & \\ z \leftrightarrow 3 & \varphi \leftrightarrow 3 \end{array}$$

Each element of the tensor is defined by two numbers, defining the position of an element in the tensor (line and column of the matrix). For example, in the case of the stress tensor in Cartesian coordinate, the stress applies in the direction x on a surface of normal y is written T_{xy} or T_{12} . As the different tensors defined are symmetric, the notation can be simplified by associating one number to any pairs of numbers:

$$\begin{aligned}
(11) &\leftrightarrow 1 \\
(22) &\leftrightarrow 2 \\
(33) &\leftrightarrow 3 \\
(23) &\leftrightarrow 4 \\
(13) &\leftrightarrow 5 \\
(12) &\leftrightarrow 6
\end{aligned}$$

Using this notation, the stress tensor can be written:

$$\mathbf{T} = \begin{bmatrix} T_{rr} & T_{r\theta} & T_{r\varphi} \\ T_{r\theta} & T_{\theta\theta} & T_{\theta\varphi} \\ T_{r\varphi} & T_{\theta\varphi} & T_{\varphi\varphi} \end{bmatrix} = \begin{bmatrix} T_{11} & T_{12} & T_{13} \\ T_{21} & T_{22} & T_{23} \\ T_{31} & T_{32} & T_{33} \end{bmatrix} = \begin{bmatrix} T_1 & T_6 & T_5 \\ T_6 & T_2 & T_4 \\ T_5 & T_4 & T_3 \end{bmatrix}. \quad (8.3)$$

The stiffness tensor $c_{\alpha\beta}$ used in equation (3.27) is a tensor of rank four, but can be reduced to a tensor of rank two, thanks to the symmetry of the system and with the Voigt Notation. The use of Einstein Convention and the Voigt notation simplify the way of writing some equations.

For example equation (3.27) linking the stress and the strain tensors is

$$T_{ij} = \sum_{k=1}^3 \sum_{l=1}^3 c_{ijkl} S_{kl} \quad (8.4)$$

and becomes in the simplified notation

$$T_i = c_{ij} S_j, \quad (8.5)$$

with i and j going from 1 to 6.

8.3 Wave equation in a solid

In a solid, the wave equation is obtained using the fundamental elastodynamic equation [equation (8.6)], which is the application of the Newton's second law on a small volume element on which internal stress forces are applied and the generalized Hooke's law [equation (8.7)].

$$\frac{\partial^2 u_i}{\partial t^2} = \sum_j \frac{\partial T_{ij}}{\partial x_j} \quad (8.6)$$

$$T_{ij} = \sum_{k,l} c_{ijkl} \frac{\partial u_k}{\partial x_l} \quad (8.7)$$

Here, ρ is the density ($\text{kg}\cdot\text{m}^{-3}$), u_i are the displacements (m), T_{ij} are the components of the stress tensor (Pa) (see Figure 8.1) and c_{ijkl} are the components of the stiffness tensor (rank 4) (Pa).

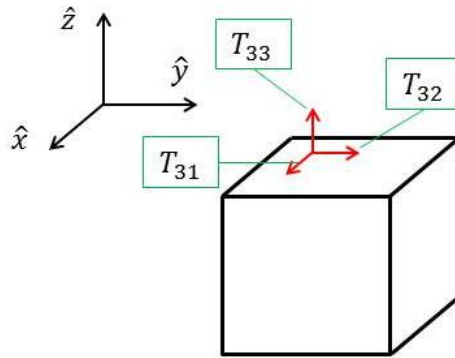


Figure 8.1: Definition of the components of the stress tensor.

The volume forces, such as the weight have been neglected in equation (8.6). The generalized Hooke's law [equation (8.7)] can be applied to any kind of solid, isotropic or not, as long as the displacements are small, $(\partial u_i)/(\partial x_j) \ll 1$. Equations (8.4) and (8.7) are equivalent due to the symmetry of the strain tensor and of the stiffness tensor. The stiffness tensor quantifies the magnitude of the deformation in all the directions in a crystal.

From equations (8.6) and (8.7), the wave equation is obtained:

$$\rho \frac{\partial^2 u_i}{\partial t^2} = \sum_{j,k,l} c_{ijkl} \frac{\partial^2 u_k}{\partial x_j \partial x_l}. \quad (8.8)$$

Equation (8.8) can describe the propagation of waves in any solid, including anisotropic solids. With some symmetries in the medium (like many crystals) or in a case of a completely isotropic medium, the wave equation can be simplified.

Due to symmetry of the stress and strain tensor, there are 36 independent components of the stiffness tensor (instead of 81). Symmetries in a solid will reduce the number of independent elements of the tensor. In the case of an isotropic medium, there are only two components left. The two remaining components of the stiffness tensor are, using Voigt notation, c_{11} and c_{12} ²¹. There are several other pairs of coefficients that can be used to describe an isotropic elastic medium: the Lamé parameters (λ, μ) , the Young modulus and Poisson's ratio (E, ν) , or the bulk and shear moduli (K, G) ²².

Using the Lamé parameters, the elastic wave equation in an isotropic medium is

$$\rho \frac{\partial^2 u_i}{\partial t^2} = \sum_j (\lambda + \mu) \frac{\partial^2 u_j}{\partial x_i \partial x_j} + \mu \frac{\partial^2 u_i}{\partial x_j^2}. \quad (8.9)$$

or, in vector form:

$$\rho \frac{\partial^2 \vec{u}}{\partial t^2} = (\lambda + \mu) \vec{\nabla} \cdot (\vec{\nabla} \cdot \vec{u}) + \mu \nabla^2 \vec{u}. \quad (8.10)$$

It is possible to decompose the displacement \vec{u} into a divergence-free vector \vec{u}_T and an irrotational vector \vec{u}_L , so $\vec{u} = \vec{u}_T + \vec{u}_L$. This decomposition leads to two wave equations:

²¹ In the case of the isotropic solid, there are more than two components different from zero, but they can all be expressed using only two independent parameters: $c_{11} = c_{22} = c_{33}$, $c_{12} = c_{13} = c_{23}$, and $c_{44} = c_{55} = c_{66} = (c_{11} - c_{12})/2$.

²² The second Lamé parameters and the shear modulus are equal $\mu = G$.

$$\rho \frac{\partial^2 \vec{u}_L}{\partial t^2} = (\lambda + 2\mu) \nabla^2 \vec{u}_L \quad (8.11)$$

$$\rho \frac{\partial^2 \vec{u}_T}{\partial t^2} = \mu \nabla^2 \vec{u}_T \quad (8.12)$$

Equations (8.11) and (8.12) correspond to the wave equations for displacements with the different polarizations of elastic waves. The first one describes a longitudinal wave in a solid with velocity of propagation of $v_L = \sqrt{(\lambda + 2\mu)/\rho}$. The second describes the shear (or transverse) waves with a velocity $v_T = \sqrt{\mu/\rho}$.

For a longitudinal wave, the displacement of the particles of the solid occurs in the same direction as the direction of propagation of the wave; there is a compression of the solid due to this wave. For a shear wave, the displacement of the particles is perpendicular to the direction of propagation of the wave; the shear waves do not involve any variation of volume during the propagation - hence the definitions of the compressional and transverse energy in chapter 0.

In the case of an isotropic solid, the generalized Hooke's Law [equation (8.7)] can be simplified. It depends on the components and the strain tensor S_{ij} and on the dilation S .

$$S_{ij} = \frac{1}{2} \left(\frac{\partial u_i}{\partial x_j} + \frac{\partial u_j}{\partial x_i} \right) \quad (8.13)$$

and

$$S = S_{11} + S_{22} + S_{33}. \quad (8.14)$$

There are different ways to write the stress tensor, depending on which elastic constants are chosen:

$$\begin{aligned}
T_{ij} &= c_{12}S\delta_{ij} + (c_{11} - c_{12})S_{ij} \\
&= \lambda S\delta_{ij} + 2\mu S_{ij} \\
&= \left(K - \frac{2}{3}G\right)S\delta_{ij} + 2GS_{ij}.
\end{aligned}
\tag{8.15}$$

The last expression of equation (8.15) is equivalent to the equation (6.13), in which the relation between stress and strain is expressed in terms of the longitudinal modulus rather than the bulk modulus, and which is used in the case of a uniaxial strain (only S_{11} different from 0).

8.4 Signal processing in SIA-7

Signal processing in SIA-7 is done in two steps. First a “pulse compression” is performed in order to improve the signal-to-noise ratio, and then the envelope of the signal is calculated, leading to a signal more convenient to analyse.

Pulse compression uses a modulated signal, a signal for which the frequency is not constant in time. A typical signal used is the chirp, in which the frequency varies linearly with time. In Figure 8.2, a chirp multiplied by a Gaussian envelope is shown (blue curve), where we can see clearly that the frequency of oscillation is higher at longer times. The pulse compression is performed by doing the cross-correlation of the recorded signal with the emitted signal. The result of the cross-correlation of the chirp signal by itself is shown in Figure 8.2 (red curve). The two main effects of the cross-correlation are to reduce the length in time of the signal and to increase its amplitude.

Figure 8.3 shows the improvement of the signal-to-noise ratio obtained using pulse compression. The blue curve is a chirp signal with an added random signal (corresponding to

experimental noise). On this blue curve, it is barely possible to distinguish a signal. The red curve is the result of the cross correlation of the same noisy signal with the original chirp signal. The red signal has become clearly visible over the noise background.

Finally, the envelope is obtained by performing a demodulation of the signal which removed the oscillatory part of the signal and kept only the low frequency variation of the envelope. The amplitude of the signal is extracted from the carrier wave by removing the high-frequency component. The frequency of the carrier wave corresponds to the central frequency of the original chirp. An example of envelope detection using this technique is shown in Figure 8.4.

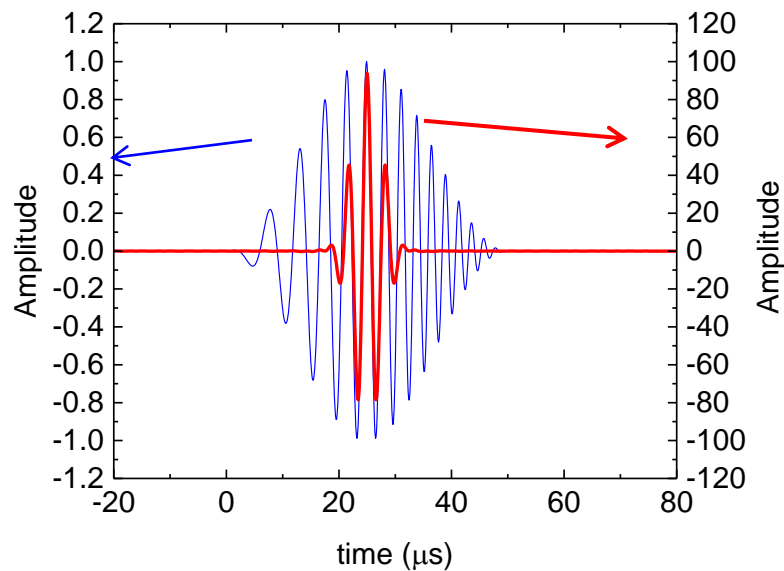


Figure 8.2: A chirp signal (blue, left scale) and the results of the cross-correlation of the chirp by itself (red, right scale).

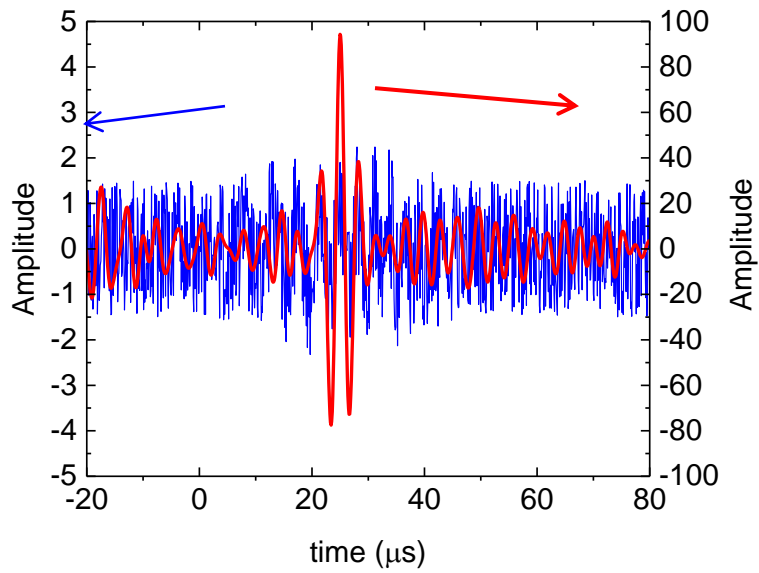


Figure 8.3: Example of the improvement of the signal-to-noise ratio, using the pulse compression technique. In blue, a random signal has been added to a chirp. In red, the cross-correlation of the blue signal with the chirp from Figure 8.2 is shown.

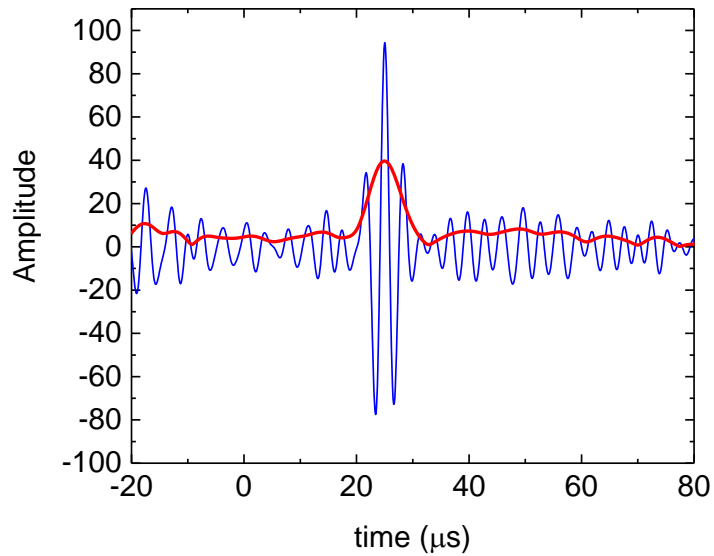


Figure 8.4: Example of the envelope detection using demodulation. Blue: experimental signal after pulse compression; red: envelope of the blue signal obtained by demodulation.

8.5 Transmission analyser

As mentioned in chapter 6, during my thesis research, I developed my own software to analyse ballistic transmitted pulses, using the Graphic User interface (GUI) engine of Matlab. This software has two main purposes. I needed an efficient way to analyse a large quantity of data and I wanted other people to be able to perform the analysis easily. These two objectives led to the use of the GUI.

There are two panels for the GUI, the first one with the time signals (Figure 8.5) and the second one with the velocity and attenuation (Figure 8.6). Each panel is divided into six boxes, four of which remain the same when switching between panels.

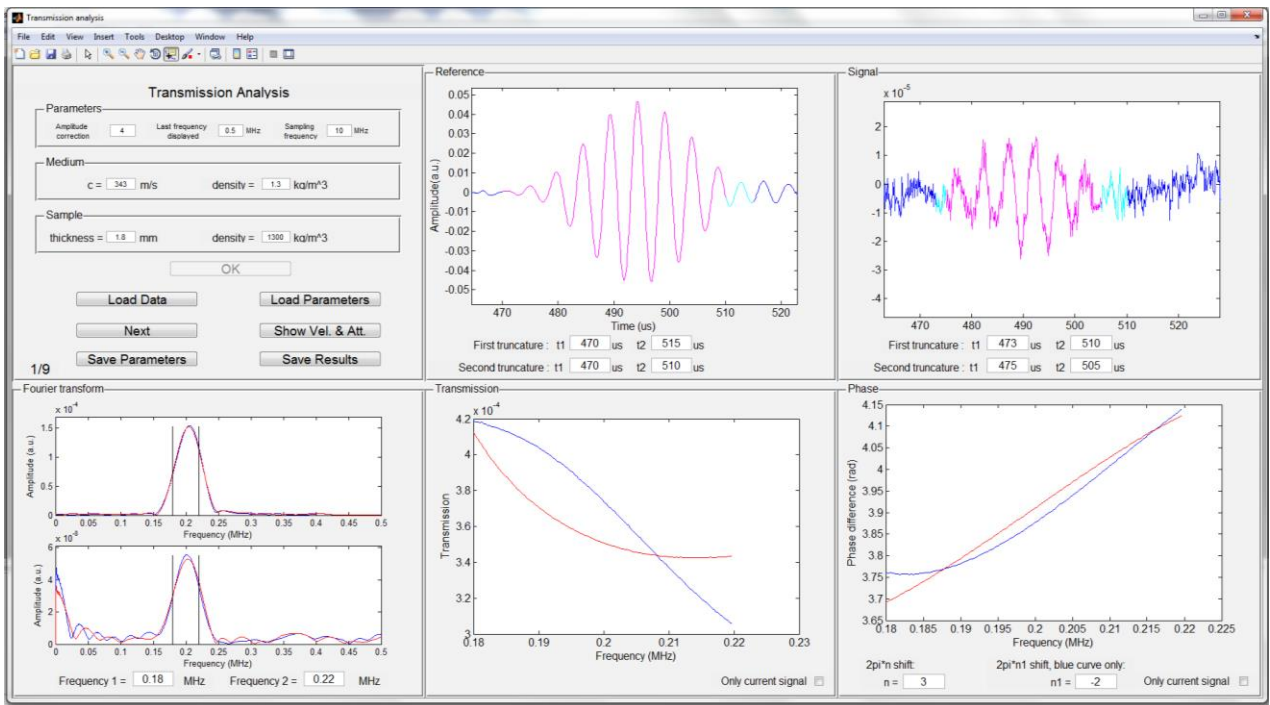


Figure 8.5: First panel of the GUI displaying the time signals.

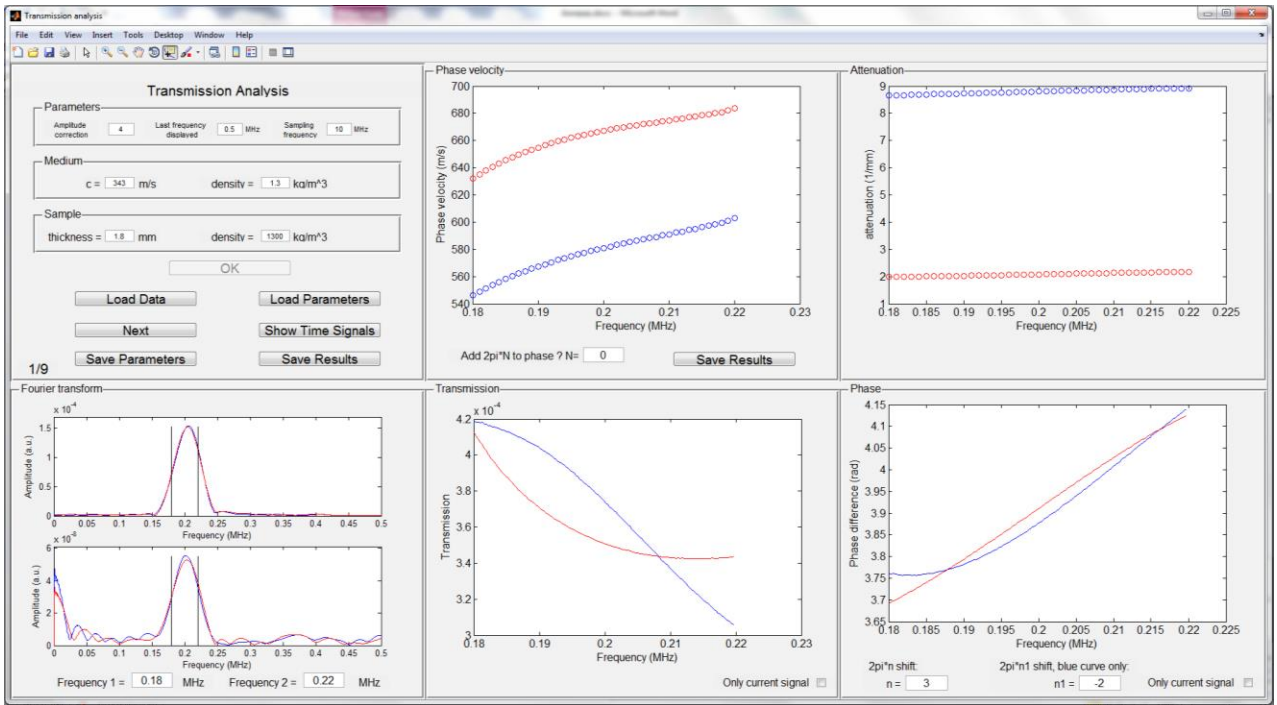


Figure 8.6: Second panel of the GUI displaying the velocity and attenuation.

The four boxes that are identical in the two panels are the boxes for the parameters, the Fourier transforms, the transmission coefficient and the phase-shift. The parameters box (top left) has all the information of the experiment, properties of the sample (thickness and density), properties of the propagating medium between the two transducers and the sample (velocity and density), which is air in the case for the noodle project, and the characteristics of the acquisition (sampling frequency and amplitude ratio between the two acquisitions). The Fourier transform box (bottom left) displays the Fourier transform of the reference signal and of the signal going through the sample. The transmission box (bottom centre) displays the magnitude of the ratio of the two Fourier transforms and the phase-shift box (bottom right) represents the phase difference

between the transmitted signal and input signal²³. There is the possibility to add or subtract 2π times an integer due to the uncertainty in the cumulative phase of each signal²⁴.

In Figure 8.5, the top central box displays the reference signal and the top right box displays the signal going through the sample. For these two signals, there is the possibility to perform truncations in time to choose the appropriate part of the signal and to limit the noise. It is possible to do two different truncations (magenta and cyan) to analyse the influence of the choice of the beginning or the end of the chosen part of the signal.

In Figure 8.6, the two time-signal boxes have been replaced by the velocity box (top centre) and the attenuation box (top right). In both of these boxes, there are two sets of points plotted. There is the calculated velocity or attenuation before (blue) and after the iteration (red) as explained in section 6.4.2. In the example shown in Figure 8.6, the differences between before and after the iteration are large due to the large difference in acoustic properties of the air compared to the noodle (large impedance mismatch).

At the end of the analysis, it is possible to save different results: either the transmission and the phase shift as a function of frequency or the phase velocity and attenuation. Different add-on features have been implemented depending on some specific needs of different projects. It is possible to analyse different acquisitions done on the same sample at different frequencies and “stitch” the results together. For another project, in which acquisitions were done at different positions of the sample using a motorized stage, a “map” of the acquisitions can be displayed to

²³ The input signal is determined from the reference signal by subtracting the time needed for the wave to travel a distance L (thickness of the sample) through water.

²⁴ The phase-shift is supposed to go to 0 for a frequency equal to 0. It is, most of the time, a good indication to find the right value of the phase shift.

choose which one to analyse (it might be useful, for example, to discriminate acquisitions based on whether or not they were done too close to the edge of a sample).

I created this program for the project on the mechanical properties of the noodle dough, but now it has been used on different projects. The analysis of the ballistic signals in chapter 4 and 5 was done using this software as it gives access to the velocity and attenuation (and then the scattering mean free path). It was also used for contact measurements on noodle dough. Finally, it has been used by a variety of persons with different backgrounds in physics or food science demonstrating how convenient and easy this software is to use.